Insights into Tropical Oceanic Convection Relationships with Local Environments from Recent Field Campaigns and Through Idealized Numerical Modeling

By

Benjamin D. Rodenkirch

A dissertation submitted in partial fulfillment of

the requirements for the degree of

Doctoral of Philosophy

(Atmospheric and Oceanic Sciences)

at the

UNIVERSITY OF WISCONSIN–MADISON

2026

Date of final oral examination: 04/13/2026

The dissertation is approved by the following members of the Final Oral Committee:

Angela K. Rowe, Assistant Professor, Atmospheric and Oceanic Sciences
Ángel F. Adames Corraliza, Associate Professor, Atmospheric and Oceanic Sciences
Larissa E. Back, Professor, Atmospheric and Oceanic Sciences
Tristan S. L'Ecuyer, Faculty Affiliate, Nelson Institute for Environmental Studies
Rosimar Rios-Berrios, Scientist V, NSF National Center for Atmospheric Research

Abstract

Deep tropical oceanic convection (TOC) is an integral component of the tropical atmosphere and plays key roles in modulating regional and global weather and climate. Yet, a lack of understanding persists regarding how TOC is impacted by local environmental parameters, including tropospheric moisture and vertical wind shear that are primary influences on TOC. Inconclusive results across studies pertaining to the degrees of influence of moisture and shear are partly owed to limits of satellite, reanalysis, and modeling capabilities that together have motivated historical field campaigns. Consequent field campaign studies still convey inconsistent findings that are likely attributed to suggested regional variabilities and inconsistent tropospheric vertical layer definitions over which local moisture and shear are calculated. To address these limitations, this dissertation leverages rare, coincident, high-resolution near-storm measurements from modern-day, regionally diverse airborne TOC field campaigns to provide an extensive interregional evaluation of local moisture and wind shear relationships with TOC using consistent tropospheric vertical layer definitions.

Similar suites of near-storm airborne observations from the recent three-part NASA Convective Processes Experiment (CPEX) field campaign series and Cloud, Aerosol, and Monsoon Processes Philippines Experiment ($CAMP^2Ex$) are analyzed to investigate TOC-environment relationships across the tropical West Atlantic, East Atlantic, and Northwest Pacific using similar methodologies. Focusing on convective inflow regions, statistically significant wind shear relationships between single-core and multi-core convective types exist in different tropospheric

vertical layers across regions, signaling regional variability. Meanwhile, similar statistically insignificant moisture relationships with convective type prevail across regions that suggest more nuanced moisture relationships with TOC than prior studies contend. Coupled with observed regionally ubiquitous large near-storm environmental variabilities both within and across TOC systems, these results highlight potential conditionally dependent moisture and shear relationships with TOC on each other. Further examination of this theory using idealized numerical modeling sensitivity simulations constrained by CPEX near-storm dropsonde observations supports the contention. Auxiliary analysis discussing additional dynamical convergence, gravity wave, and aerosol influences on TOC further complicate suggested conditionally dependent moisture and shear relationships that, in addition to regionally distinct synoptic-scale influences on local environments, warrant future expanded interregional TOC-environment research involving coordinated field campaign and modeling efforts.

Acknowledgements

I am incredibly fortunate to be surrounded by so many amazing people that have supported me during these past six years and throughout my life. First and most importantly, I would like to thank my advisor, Dr. Angela Rowe, for accepting me into her research group and providing invaluable guidance, mentorship, and support throughout my academic journey. She has provided me the opportunities of a lifetime, and her work ethic is truly inspirational. She is a great scientist, but most importantly, she is a great person. I also thank the other members of my advising committee, Dr. Tristan L'Ecuyer, Dr. Ángel Adames Corraliza, Dr. Larissa Back, and Dr. Rosimar Rios-Berrios for their valuable input and feedback for my research. Additionally, I am grateful for the exceptional faculty and staff at the AOS department, along with fellow students. Their intellect, drive, and kindness are inspiring and make the department as distinguished and welcoming as it is. I want to thank my family and friends for their love and support throughout the years and for encouraging my decision to return to school after a three-year hiatus working professionally. I am truly blessed to have all these people in my life, and without them I would not be where I am today.

This research was supported by NASA Awards 80NSSC20K0894 and 80NSSC23K1303, as well as the NSF National Center for Atmospheric Research Advanced Study Program Graduate Visitor Program (NCAR ASP GVP) fellowship. I thank all NASA CPEX, CPEX-AW, CPEX-CV, and CAMP^{2}Ex participants, for which this research would not be possible without. I am especially grateful for all the wonderful people in mission management from the CPEX field campaign series for fostering such an inclusive and welcoming environment for everyone, especially students.

Contents

List of Tables

List of Figures

Chapter 1

Introduction

Deep convection is a prevailing feature of the atmosphere over tropical oceans and plays key roles in driving Earth's weather and climate on both regional and global scales. Deep tropical oceanic convection (TOC) influences the large-scale tropical atmospheric circulation through three-dimensional (3-D) redistribution of mass, heat, moisture, and momentum (e.g., Zipser 1977; Alexander & Young, 1992; Young et al., 1995; Brown & Zhang, 1997; LeMone et al., 1998; Saxen & Rutledge, 1998; Saxen & Rutledge, 2000; Tompkins, 2001; Cetrone & Houze, 2006; Mechem et al., 2006; Liu & Liang, 2010; Grant et al., 2020; Mulholland et al., 2021; Chen et al., 2023; Maybee et al., 2024). Associated convective clouds, particularly near cloud-top levels, also have considerable impacts on radiative fluxes that affect Earth's radiation budget (e.g., Hartmann et al., 2001; Tobin et al., 2012; Del Genio & Chen, 2015; Hartmann, 2016; Grant et al., 2020; Bony et al., 2020; Pilewskie & L'Ecuyer, 2022; Pilewskie & L'Ecuyer, 2026), while convectively generated cold pools locally alter the planetary boundary layer (PBL), modify air-sea exchange, and can initiate new convection (e.g., Esbensen & McPhaden, 1996; Saxen & Rutledge, 1998; Feng et al., 2015; Rowe & Houze, 2015; Chandra et al., 2018; Houze, 2018; Touzé-Peiffer et al., 2021; Sakaeda & Torri, 2023).

1.1 Seminal Efforts to Understand TOC

Given the notable influences of TOC on both regional and global weather and climate, TOC has been a targeted focus of research in the tropics for many decades. One of the most seminal research efforts involving TOC began in the 1950s, wherein the role of deep cumulus convection in the maintenance of the tropical heat and energy budget aloft was investigated (Riehl & Malkus, 1958). Through this work, Riehl & Malkus (1958) proposed one of the first seminal theories relating TOC to atmospheric circulation–the "hot tower" hypothesis. The hot tower hypothesis argued that turbulent mixing of moist static energy (MSE) and equivalent potential temperature from the PBL to the upper troposphere arises via narrow, undiluted (i.e., no entrainment) convective updrafts (i.e., "hot towers") embedded within deep tropical cumulus convection, ultimately to balance observed upper-tropospheric heat and energy loss (Riehl & Malkus, 1958). The hot tower hypothesis was a groundbreaking theory in tropical convective research, and though its validity has since been challenged by subsequent observations and observation-informed model simulations (e.g., Zipser, 2003; Fierro et al., 2009; Romps & Kuang, 2010; Fierro et al., 2012), it helped inspire future TOC research.

A notable example of motivated future TOC research occurred in the 1970s, with the 1974 GARP Atlantic Tropical Experiment (GATE) field campaign. GATE is widely recognized as the seminal TOC field campaign, wherein a coordinated network of ship and airborne observations in the tropical East Atlantic sought to improve limited understanding of TOC and its interactions with the surrounding environment (Houze & Betts, 1981). GATE succeeded tremendously in this endeavor, with the in situ radar and sonde observations leading to one of the first detailed conceptual models of a TOC mesoscale convective system (MCS) squall (Figure 1.1; Houze,

1977), including its cloud microphysics, anvil structure, stratiform melting band (i.e., brightband) structure, convective core structure, and mesoscale circulations (e.g., updrafts and downdrafts) (Zipser & LeMone, 1980; Houze & Betts, 1981).

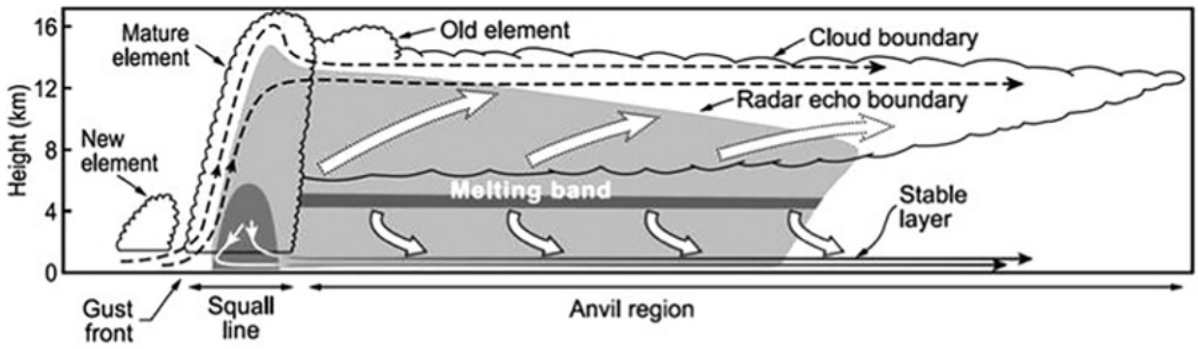

Figure 1.1: Conceptual model of a tropical oceanic MCS squall-line, based on ship- and aircraft-based radar and sonde observations from GATE. From Jenney et al. (2025) adapted from Houze (1977).

The conceptual model highlights the prototypical structure of a TOC squall line, with a leading line of deep convective elements trailed by stratiform precipitation that primarily forms from detrained ice particles from old leading line convective elements and broad mesoscale ascent within the anvil cloud region (Figure 1.1; Houze, 1977; Houze & Betts, 1981; Houze, 1982; Houze, 1989). Below the melting band of the stratiform precipitation, where falling ice particles and rimed graupel transition to rain, weak broad mesoscale descent of stable unsaturated air prevails (Figure 1.1) and sits atop a shallow near-surface layer of cool, near-saturated air introduced by outflow from the deep convective regions (Figure 1.2; Zipser 1977; Houze & Betts, 1981). This cool, near-surface outflow layer (i.e., gust front) also propagates out ahead of the leading line deep convection, with its imposed vertical wind shear providing continued lift for the narrow convective-scale updrafts and potentially initiating new convective elements ahead of the pre-existing squall (Figure 1.1; Houze, 1977; Houze & Betts, 1981). Now commonly known as cold pools, identification of these convective-scale downdraft features and their influences on TOC

foreshadowed the influence of local tropospheric vertical wind shear on TOC that is still a subject of research focus today. Meanwhile, subsequent GATE studies of TOC draft intensities (LeMone & Zipser, 1980; Zipser & LeMone, 1980) noted weaker convective-scale updraft vertical velocities than expected based on the hot tower hypothesis from Riehl & Malkus (1958). Coupled with observed updraft vertical velocity minima near the melting level (Zipser & LeMone, 1980), dilution of TOC updrafts via entrainment of environmental air was postulated, which challenged the hot tower hypothesis and motivated future research on TOC regarding its relationships with local tropospheric moisture.

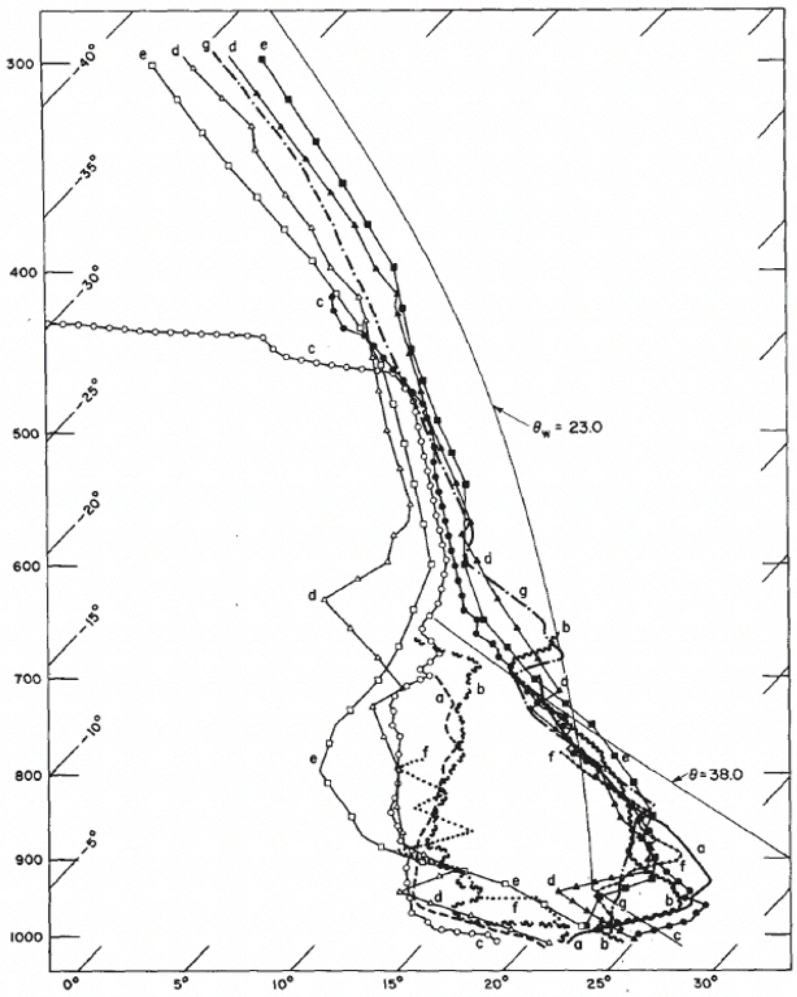

Figure 1.2: Characteristic thermodynamic soundings of post-squall stratiform regions during GATE. From Zipser (1977).

1.2 Historical Efforts to Understand TOC-Environment Relationships

Motivated by the seminal work of Riehl & Malkus (1958) and GATE, TOC research efforts have long focused on TOC representation in global models by relating its structure and intensity to grid-scale environmental parameters, both indirectly through convective parameterization of sub-grid scale cloud and mesoscale processes (e.g., Arakawa, 1969; Arakawa & Schubert, 1974; Tiedtke, 1993; Randall & Fowler, 1999; Randall et al., 2003; Arakawa, 2004; Rio et al., 2019) and directly through cloud-resolving models (CRMs) and superparameterization (e.g., Grabowski & Smolarkiewicz, 1999; Grabowski, 2001; Randall et al., 2003; Rio et al., 2019; Satoh et al., 2019). Satellite remote sensing, reanalysis, and CRM studies using newer technology since the days Riehl & Malkus (1958) and GATE have attempted to develop generalized relationships between local environmental parameters and convection across the broader tropics. Confirming the suggestions proposed by GATE literature, these studies note the particular importance of local tropospheric moisture and vertical wind shear (hereafter referred to as "wind shear") in influencing TOC structure and intensity.

1.2.1 Local Tropospheric Moisture Relationships with TOC from Non-In Situ Frameworks and Theory

Satellite (e.g., Bretherton et al., 2004), reanalysis (e.g., Chen et al., 2017; Schiro et al., 2020; Wolding et al., 2022; Chen et al., 2023; Muetzelfeldt et al., 2025), and CRM (e.g., Tompkins, 2001) studies have linked greater mid-tropospheric (e.g., above the PBL) moisture to larger and more intense precipitating areas (e.g., Figure 1.3). Though the impacts of other environmental

parameters (e.g., wind shear) introduce variability in the degree of influence, these findings are generally consistent across studies and are commonly attributed to a moister middle troposphere reducing entrainment-driven negative buoyancy introduction into TOC systems. Meanwhile, low-tropospheric (e.g., within the PBL) moisture relationships with TOC vary in both strength and sign across studies (Tompkins, 2001; Chen et al., 2017; Schiro et al., 2020; Muetzelfeldt et al., 2025). The inconsistencies may in part be due to differing contributions of low- and mid-tropospheric inflow into convection that vary with convective lifecycle stage (Mechem et al., 2002), necessitating lifecycle contextualization of data.

Region	TPWV (mm)	RHLow (%)	RHMid (%)	Shallow wind shear ($m\,s^{-1}$)	Deep wind shear ($m\,s^{-1}$)	CIN ($J\,kg^{-1}$)	CAPE ($J\,kg^{-1}$) ($\times 10^3$)	LCL (km)
Tropical ocean	57.8	89.0	75.7	4.0	9.7	7.9	1.12	0.40
	47.1	84.1	47.6	3.6	10.8	8.6	1.06	0.54
INOC	57.4	88.6	78.9	3.5	9.0	7.0	1.1	0.42
	51.4	84.7	60.3	3.3	8.7	7.9	1.2	0.53
GATE	55.7	90.7	72.2	4.4	8.7	6.3	0.8	0.37
	51.1	87.4	57.6	4.1	8.8	7.6	0.9	0.47
EPAC	56.8	92.0	70.3	4.6	9.8	6.3	0.8	0.32
	50.4	88.4	53.2	4.0	10.4	7.4	0.9	0.43
WPAC	59.6	87.9	78.5	3.3	7.8	9.3	1.3	0.44
	53.6	83.9	58.7	3.1	7.1	11.0	1.4	0.55
BBL	63.2	87.2	83.6	3.9	13.4	8.8	1.6	0.41
	58.5	84.4	70.4	3.3	11.4	9.8	1.6	0.5

Figure 1.3: Mean environmental metrics for TOC with rain area greater than 10^4 km^2 (top row) and rain area less than 100 km^2 (bottom row) for each tropical oceanic region. INOC = Indian Ocean, GATE = Eastern Atlantic, EPAC = East Pacific, WPAC = West Pacific, BBL = Bay of Bengal. TOC was observed by TRMM radar and environmental metrics were derived from 1.5° grid ERA-Interim reanalysis. From Chen et al. (2017).

Theoretical studies have found similar moisture links to TOC as well, notably pertaining to plume buoyancy in the low- and mid-troposphere (B_L; e.g., Ahmed & Neelin, 2018; Adames et al., 2021). A proxy for convective instability in the tropics in relation to convective quasi-equilibrium theory (Arakawa, 1969), B_L has been shown to have an exponential relationship with TOC rain rate (Figure 1.4a; e.g., Adames et al., 2021; Wolding et al., 2022) that is directly tied to similar column moisture relationships with TOC (Figure 1.4b; e.g., Bretherton et al., 2004; Wolding et al., 2020;

Padullés et al., 2022). Through analysis of undilute and dilute B_L in a quasi-equilibrium cyclical framework about a critical B_L value (Figure 1.5), the strong relationship is tied to lower free tropospheric entrainment influence, wherein moister lower free tropospheres (i.e., less dilute B_L) reduce negative buoyancy introduction into TOC updrafts that promote TOC development and deepening, while drier lower free tropospheres (i.e., more dilute B_L) enhance negative buoyancy introduction to promote TOC dissipation and weakening (Hannah, 2017; Wolding et al., 2022; Wolding et al., 2024). While B_L and associated entrainment are convenient metrics for gauging convective instability and predicting TOC precipitation rates, they are not all-encompassing predictors of TOC morphology. B_L also does not factor in upper tropospheric thermodynamic influences like ice processes that have been shown to influence convection (e.g., Zipser 2003), nor does it account for dynamical factors like wind shear (Adames et al., 2021). The B_L framework is limited in its usage of plume modeling as well, which inherently assumes single-cell TOC systems whose takeaways do not necessarily translate to larger, multi-cell TOC. Altogether, these shortcomings motivate continued investigation into TOC relationships with moisture throughout the troposphere, including in tandem with variable local tropospheric wind shear conditions and across different TOC morphologies.

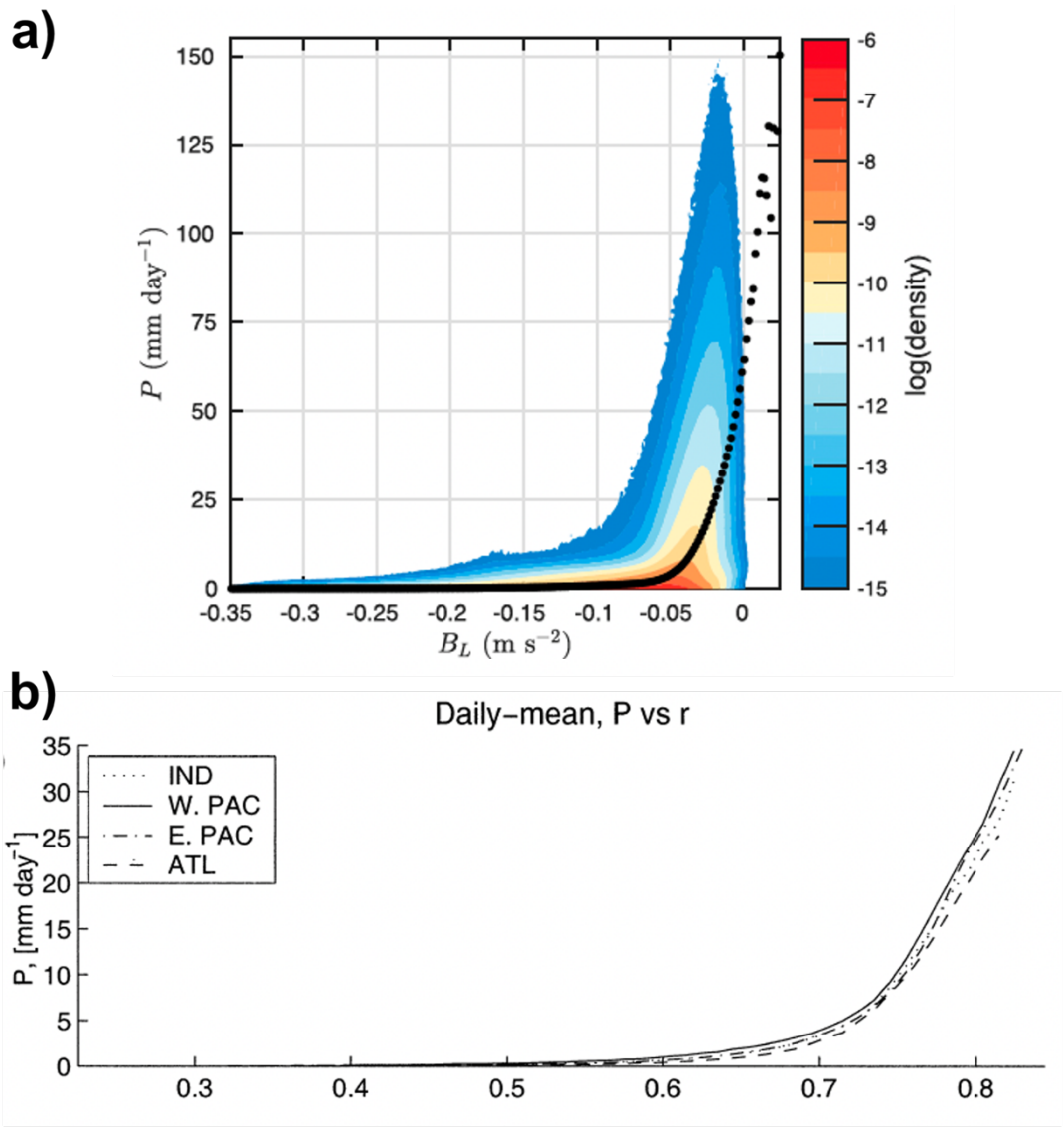

Figure 1.4: Relationship of tropical oceanic precipitation rate with (a) ERA5 B_L and (b) SSM/I and TRMM satellite-derived column relative humidity from Adames et al. (2021) and Bretherton et al. (2004), respectively.

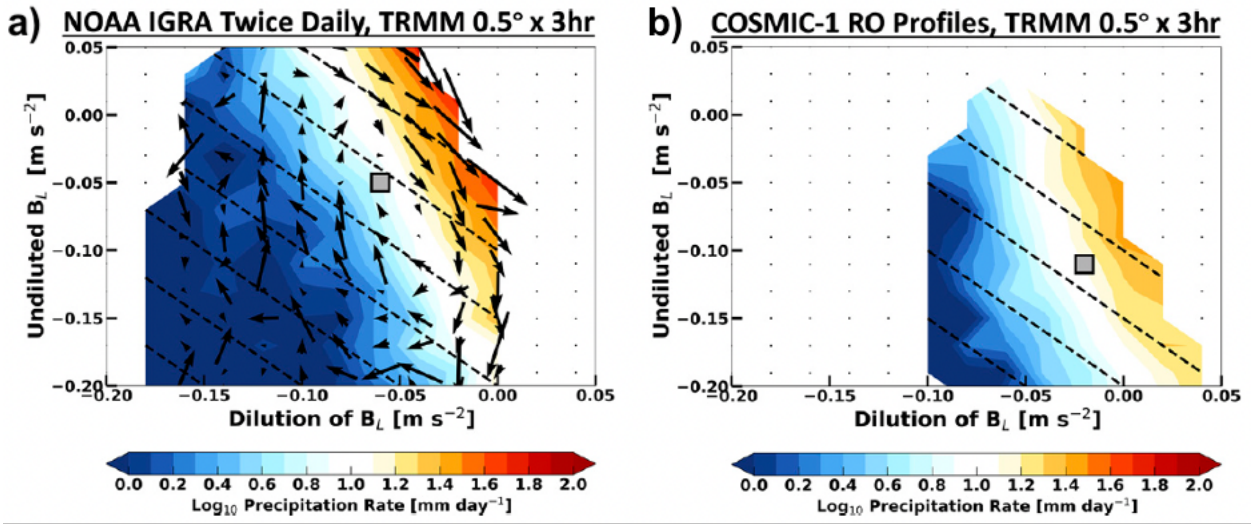

Figure 1.5: Temporal mapping (arrows) of TRMM rainfall rate (fill) about the B_L quasi-equilibrium point (square) in (a) NOAA IGRA sounding B_L space and (b) COSMIC-1 radio occultation profile B_L space. Adapted from Wolding et al. (2022).

1.2.2 Local Tropospheric Wind Shear Relationships with TOC from Non-In Situ Frameworks and Theory

Similar to moisture, some wind shear relationships with TOC are inconclusive in satellite, reanalysis, and CRM studies. While some reanalysis (e.g., Igel & van den Heever, 2015; Chen et al., 2023; Roca et al., 2025) and CRM (e.g., Tompkins, 2001) work finds stronger deep layer shear to promote larger and more intense TOC systems, others suggest alternate relationships that are regionally dependent (e.g., Figure 1.3; Chen et al., 2017; Muetzelfeldt et al., 2025). Likewise, studies exist linking enhanced low-tropospheric shear to enhanced TOC intensity and structure (e.g., Anber et al., 2014; Mulholland et al., 2021), while other studies contend less of an association of TOC structure with low-tropospheric shear (e.g., Grant et. al, 2018; Muetzelfeldt et al., 2025).

Theoretical studies of wind shear relationships with convection may give inclinations toward why TOC-wind shear relationships vary across existing literature. Rotunno et al. (1988) established

RKW theory that remains a prevailing paradigm of convection-wind shear relationships today. RKW theory contends that the balance between low-tropospheric wind shear-induced vorticity and convective cold pool-generated vorticity is a key driver of quasi-linear convective structure and maintenance (Figure 1.6). While RKW theory has proven applicable in some scenarios to TOC (e.g., LeMone et al., 1998), RKW theory is predominantly directed towards land-based mid-latitude quasi-linear convection (i.e., squall lines). Studies such as Grant et al. (2018) have showed RKW theory to not be as applicable to quasi-linear and non-linear TOC due to weaker cold pools over tropical oceans than land from typically moister prevailing environmental conditions and greater entrainment of cold pool air into TOC updrafts.

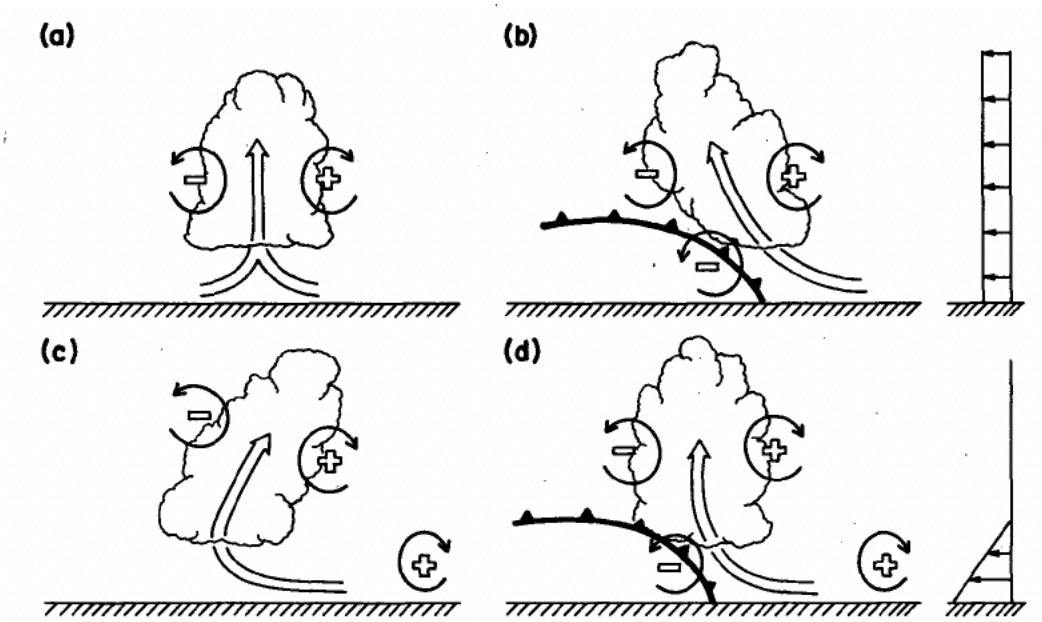

Figure 1.6: Schematic diagrams showing a convective updraft and associated generated vorticity in the presence of (a) no cold pool and no low-tropospheric wind shear, (b) a cold pool and no low-tropospheric wind shear, (c) no cold pool but low-tropospheric wind shear, and (d) a cold cool and low-tropospheric wind shear. From Rotunno et al. (1988).

Other modeling studies like Mulholland et al. (2021) link imposed low-tropospheric wind shear with increased low-tropospheric horizontal convective mass flux via enhanced convective inflow that, in turn, correlates with greater quasi-linear convective updraft areas via mass continuity. The

consequence of these wider convective updrafts is less updraft dilution from entrainment and more intense quasi-linear convection (Mulholland et al., 2021). As such, horizontal convective mass flux theory provides a valuable amendment to RKW theory that highlights the importance of local wind shear interactions with layer inflow thermodynamics to influence quasi-linear convection. While this horizontal convective mass flux theory concurs with some tropical convective intensity studies (e.g., Baidu et al. 2022; Maybee et al. 2024), it is inconsistent with other studies (e.g., Peters 2016; Morrison & Peters 2018; Peters et al. 2019) that show enhanced shear to reduce convective updraft intensity through increased downward dynamic pressure perturbations and enhanced entrainment from increased convective cloud areas and perimeters. However, Peters et al. (2022) and Chen et al. (2023) contend that these detrimental effects of shear on updraft intensity may only apply to weaker, narrower convection, which, coupled with most of these studies being predominantly CRM-based, behoove investigation into how these proposed wind shear relationships manifest in real life observations and with non-linear TOC where the theories are not as well tested.

1.2.3 Benefits of Field Campaigns to Investigate TOC-Environment Relationships

Inconsistencies in the literature pertaining to both wind shear and moisture relationships with TOC are likely due to many factors. Apart from different types of datasets being used (i.e., satellite, reanalysis, CRM), these factors include limited spatiotemporal data resolution, imperfect parameterization of convective-scale processes in models (e.g., Randall et al., 2003; Arakawa, 2004; Satoh et al., 2019; Rio et al., 2019), and inclusion of data from the broad oceanic tropics, wherein more specific regions can have differing underlying trends (e.g., Chen et al., 2017; Galarneau et al., 2023; Muetzelfeldt et al., 2025). Motivated by these issues, field campaign studies within specific tropical oceanic regions have been employed. Field campaigns are unique in their

ability to collect frequent, detailed environmental measurements near TOC systems that cannot be accomplished by satellite remote sensing nor provided by CRMs. In situ observations are superior to reanalysis products as well, in that reanalysis products, like satellites, have limited spatiotemporal resolutions and additionally rely on imperfect underlying models, particularly in data-sparse regions like tropical oceans (Pincus et al., 2017; Chen et al., 2017; Wolding et al., 2022).

1.2.4 Local Tropospheric Moisture Relationships with TOC from Historical Field Campaigns

Prior field studies primarily in the West Pacific (e.g., the Tropical Ocean – Global Atmosphere Coupled Ocean Atmosphere Response Experiment (TOGA COARE) and the Kwajalein Experiment (KWAJEX); Figure 1.7) investigating local moisture relationships with predominantly organized TOC (e.g., MCSs) have linked greater mid-tropospheric moisture with larger and more intense precipitating systems (e.g., Brown & Zhang, 1997; LeMone et al., 1998; Cetrone & Houze, 2006; Holloway & Neelin, 2009; Wolding et al., 2022). The low-troposphere is more complicated, however, with inconsistent low-tropospheric moisture relationships with TOC size and intensity across studies from differing regions within the broader West Pacific (e.g., Brown & Zhang, 1997; Cetrone & Houze, 2006; Holloway & Neelin, 2009). The inconsistent in situ moisture-convection relationships in the low-troposphere reflect aforementioned satellite, reanalysis, and CRM results, but with added regional context that further compels targeted studies in diverse tropical oceanic regions.

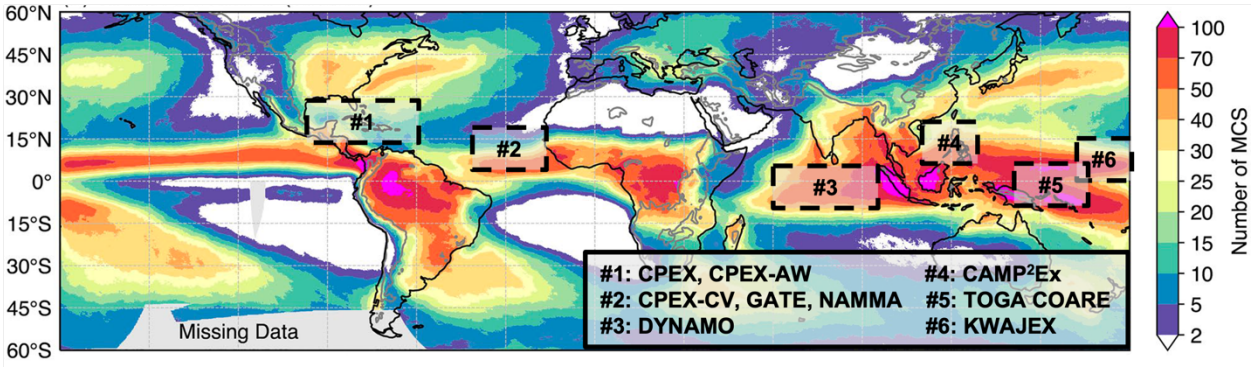

Figure 1.7: Annual mean global distribution of MCS occurrence. Adapted from Feng et al. (2021) to include overlays of TOC field campaign regions discussed herein.

1.2.5 Local Tropospheric Wind Shear Relationships with TOC from Historical Field Campaigns

Similar to moisture, low-tropospheric wind shear relationships with TOC structure are also inconsistent across field campaign studies. Some studies link enhanced low-tropospheric shear to enhanced organized TOC intensity and size in the West Pacific (e.g., Alexander & Young, 1992; LeMone et al., 1998; Chudler & Rutledge, 2021), while studies from the Dynamics of the Madden-Julian Oscillation (DYNAMO) field campaign in the Indian Ocean (e.g., Guy & Jorgensen, 2014; Figure 1.7) show less of an organized TOC relationship with low-tropospheric shear. Likewise, while some field campaign studies in the West Pacific (e.g., Saxen & Rutledge, 2000) find stronger deep layer shear to promote larger organized TOC systems, previously discussed reanalysis studies (e.g., Chen et al., 2017; Muetzelfeldt et al., 2025) find regionally dependent relationships (e.g., Figure 1.3) that discourage assuming application of these relationships to every tropical oceanic region.

1.3 Inconsistent TOC-Environment Relationships in Literature and How it Motivates this Dissertation

Collectively, the frequent, detailed field observations together with satellite, reanalysis, and CRM datasets across tropical oceanic regions convey inconsistent local moisture and wind shear relationships with TOC. These inconsistent findings could be attributed to a multitude of factors. Definitions of tropospheric vertical layers for which local environmental moisture and wind shear are calculated vary across studies, making interstudy comparisons of results difficult. For example, some studies define the low-troposphere as the PBL, while others extend it beyond the PBL into the lower free troposphere. Meanwhile, most modern in situ research on local environmental relationships with TOC has predominately focused on quasi-linear convection and is largely based in the West Pacific (e.g., Alexander & Young, 1992; Brown & Zhang, 1997; LeMone et al., 1998; Saxen & Rutledge, 2000; Cetrone & Houze, 2006; Holloway & Neelin, 2009; Chudler & Rutledge, 2021). Studies focused elsewhere (e.g., from GATE and the NASA African Monsoon Multidisciplinary Analysis (NAMMA) experiment in the East Atlantic; Figure 1.7) occurred decades ago, lacked higher quality modern-day instrumentation, and, in the case of NAMMA, focused more on land-based (e.g., Barthe et al., 2010; Nicholls & Mohr, 2010) or tropical cyclone (TC)-related tropical convection in the context of larger scale synoptic environments (e.g., Zipser et al., 2009; Cifelli et al., 2010; Zawislak & Zipser, 2010). With TOC structure varying across the tropics, including an abundance of non-linear TOC (Houze et al., 2015), proper evaluation of TOC relationships with local environments necessitates focused in situ studies of non-linear TOC morphologies across a variety of tropical oceanic regions. The lack of modern, regionally diverse in situ research is particularly noteworthy, due to aforementioned suggested regional dependencies

in convective-environment relationships using coupled satellite and reanalysis data (Chen et al., 2017; Galarneau et al., 2023).

Regional variability likely stems from differing climatological moisture and wind shear between tropical oceanic regions that leads to different frequencies of TOC morphologies (Chen et al., 2017) and may lead to altered degrees of influence of these variables on TOC (Sakaeda & Torri, 2022). Sources of such regional underlying environmental variability often reside on the synoptic scale. For example, the African Easterly Jet (AEJ), Saharan Air Layer (SAL), West African monsoon, and African Easterly Waves (AEWs) are known to modulate tropical East Atlantic moisture and wind shear, particularly in the boreal summer, that in turn influence TOC prevalence, structure, and intensity (e.g., Cook, 1999; Wong & Dessler, 2005; Cifelli et al., 2010; Nicholls & Mohr, 2010; Guy et al., 2011; Wolding et al., 2020; Vargas Martes et al., 2023; Mayta & Adames Corraliza, 2024). As the AEWs propagate westward across the tropical Atlantic, they can bring copious moisture and even dry, dusty SAL air more characteristic of the boreal summer tropical East Atlantic into the tropical West Atlantic (e.g., Kaufman et al., 2005; Engelstaedter et al., 2006), where they similarly can influence TOC occurrence, morphology, and intensity in an otherwise moister and less sheared region (Dunion, 2011; Chen et al., 2017). Meanwhile, regions like the tropical West Pacific, which is generally moister than the tropical Atlantic (e.g., Chen et al., 2017), are continuously impacted by the Madden-Julian Oscillation (MJO; Madden & Julian, 1971; Madden & Julian, 1972; Zhang, 2005) whose active and inactive phases bring moister and drier conditions, respectively, along with varying wind shear that each influence TOC prevalence, structure, and intensity (e.g., LeMone et al., 1998; Guy & Jorgensen, 2014; Rowe & Houze, 2014; Rowe & Houze, 2015; Chen et al., 2016; Dias et al., 2017; Chandra et al, 2018; Reid et al., 2023).

Additionally, these same regions are affected by large-scale features like the El Niño Southern Oscillation (ENSO) and the Asian monsoon (Chang et al. 2005), with prevailing moister conditions during La Niña and the wet monsoon season (vice versa for El Niño and the dry monsoon season) further influencing regional frequency, morphology, and intensity of TOC (e.g., Qian et al., 2010; Sullivan et al., 2019; Reid et al., 2023).

Satellite and reanalysis datasets can provide the ability to examine an array of tropical oceanic regions separately. However, their limited spatial and temporal resolutions cannot sufficiently capture essential small-scale near-storm environmental variability and convective features (Maddy & Barnet, 2008; Roca et al., 2015; Gelaro et al., 2017; Chen et al., 2017; Adhikari et al., 2019). *Consequently, an encapsulating evaluation of TOC relationships with local environments necessitates targeted in situ regional studies equipped with coincident high-resolution hydrometeor, moisture, and wind measurements, along with successive interregional comparisons with consistent layer definitions for wind shear and moisture*. Motivated by this requirement and associated gap in TOC research, this dissertation leverages recent TOC field campaigns from a diverse array of tropical oceanic regions to address the following overarching research questions:

- How does 3-D TOC structure relate to local environmental moisture and vertical wind shear in different tropospheric layers in differing tropical oceanic regions?
- How do local environmental moisture and vertical wind shear influence collective TOC spatial organization both separately and together?

1.4 Dissertation Chapter Focuses and Hypotheses

1.4.1 Field Campaign Analysis

High-resolution in situ sampling of non-TC deep TOC structure and surrounding environments is particularly rare across the tropical Atlantic and has limited the understanding of local environmental influences on the prevalent TOC in this basin (Figure 1.7). Toward addressing this observational need and research gap, the National Aeronautics and Space Administration (NASA) executed a three-part airborne field campaign series across the tropical North Atlantic, consisting of the Convective Processes Experiment (CPEX, 2017; Chen & Zipser, 2017) and CPEX—Aerosols & Winds (CPEX-AW, 2021; Skofronick-Jackson et al., 2021) campaigns in the West Atlantic and the CPEX—Cabo Verde (CPEX-CV, 2022; Zawislak et al., 2022; Nowottnick et al., 2024) campaign in the East Atlantic. The NASA CPEX series collected rare, coincident, and high-resolution airborne measurements of 3-D TOC structure and near-storm environments suitable to study the structure and intensity of 32 non-linear TOC systems in varying local environmental conditions within two basins on opposite ends of the Atlantic. Given the uniqueness of this suite of airborne observations, the CPEX field campaign series presents an exceptional opportunity to analyze tropical West and East Atlantic local moisture and wind shear relationships with TOC structure, which will be the focuses of Chapters 2 and 3, respectively.

Based upon prior observational (e.g., Brown & Zhang, 1997; LeMone et al., 1998; Bretherton et al., 2004; Cetrone & Houze, 2006; Holloway & Neelin, 2009; Padullés et al., 2022), CRM (e.g., Tompkins, 2001), and reanalysis (e.g., Chen et al., 2017; Schiro et al., 2020; Wolding et al., 2020; Chen et al., 2023; Muetzelfeldt et al., 2025) studies supported by more theoretical literature (e.g., Ahmed & Neelin, 2018; Adames et al., 2021; Wolding et al., 2022), greater TOC size and intensity

are hypothesized to be associated with greater tropospheric moisture, particularly above the PBL through decreased negative buoyancy introduction and dilution from entrainment into convective updrafts (Brown & Zhang, 1997; LeMone et al., 1998; Tompkins, 2001; Cetrone & Houze, 2006; Chen et al., 2016; Chen et al., 2017; Hannah, 2017; Alfaro, 2017; Schiro et al., 2020; Wolding et al., 2022; Chen et al., 2023; Wolding et al., 2024). Enhanced PBL and deep tropospheric wind shear are also predicted to be linked to increased TOC intensity and size, respectively, in line with expectations based on prior studies using observations (e.g., Alexander & Young, 1992; LeMone et al., 1998; Saxen & Rutledge, 2000; Chudler & Rutledge, 2021) and reanalysis (e.g., Igel & van den Heever, 2015; Baidu et al. 2022; Chen et al., 2023; Roca et al., 2025). Chapter 3 will include an interregional comparison of CPEX(-AW) results in the West Atlantic with CPEX-CV results in the East Atlantic as well. In the East Atlantic, expected drier environments introduced by the SAL (e.g., Wong & Dessler, 2005; Dunion, 2011) are hypothesized to produce more robust local wind shear relationships between narrower and larger TOC systems, in accordance with the findings of prior literature (e.g., Sakaeda & Torri, 2022; Peters et al., 2022; Chen et al., 2023) that suggest enhanced suppressive wind shear impacts on narrower TOC systems in drier environments and dampened wind shear impacts on TOC in moister environments that are otherwise already conducive to TOC development and organization.

The interregional analysis of TOC-environment relationships using CPEX series airborne data in the tropical Atlantic in Chapters 2 and 3 will be extended to another tropical ocean basin with considerable TOC presence, namely the Northwest Pacific (Figure 1.7), in Chapter 4. Similar to the tropical West and East Atlantic, the tropical Northwest Pacific basin has the benefit of a recent airborne field campaign—the 2019 NASA Cloud, Aerosol, and Monsoon Processes Philippines

Experiment (CAMP^{2}Ex; Reid et al., 2023)—that sampled numerous non-linear and non-TC deep TOC systems with coincident, high-resolution airborne near-storm environment and 3-D TOC structure profiling. CAMP^{2}Ex TOC systems were sampled within a variety of synoptic environments, including southwesterly and northeasterly Asian monsoons, active and inactive MJO periods, and a prevailing weak El Niño (Reid et al., 2023). Normally, anticipated moister conditions in the tropical Northwest Pacific based on climatology (e.g., Chen et al., 2017) would be hypothesized to produce less robust wind shear relationships between narrower and larger TOC systems than the tropical Atlantic, per the findings of prior studies like (e.g., Sakaeda & Torri, 2022; Peters et al., 2022) suggesting decreased wind shear effects on TOC in moister environments. However, given the prevailing weak El Niño conditions and concomitant anomalously dry sampling period (Reid et al., 2023), CAMP^{2}Ex regional data is predicted to exhibit similar general moisture and wind shear relationships between narrower and larger TOC systems as the CPEX series tropical Atlantic data.

1.4.2 Idealized Numerical Modeling Analysis

The regionally diverse field campaign datasets analyzed in Chapters 2-4 provide unique coincident high-resolution measurements of TOC structure and near-storm environments that will offer valuable insight into local TOC-environment relationships across tropical oceanic regions. However, in situ observations are limited in their sample sizes and are prone to collection biases (e.g., intense TOC cores rarely sampled due to aircraft flight restrictions). It is also difficult to separate individual impacts of moisture and wind shear on TOC within in situ observations, thereby limiting the ability of in situ observational analysis to evaluate the relative influence of either. This constraint is an inherent, prevailing limitation of observational studies in general and

behooves supplementing such with idealized CRM sensitivity simulations, wherein the impacts of moisture and wind shear on TOC can be better isolated from one another. Additionally, prior studies have suggested that the roles of wind shear and moisture in influencing TOC can be dependent on the magnitude of the other (e.g., Sakaeda & Torri, 2022; Peters et al., 2022; Chen et al., 2023). As such, these studies further support supplementing in situ observational analysis with CRM sensitivity simulations that can more effectively elucidate how wind shear and moisture act in tandem to influence TOC structure and intensity.

Supplementing the field campaign analyses of Chapters 2-4 with complementary analysis of CRM sensitivity simulations will be the focus of Chapter 5. Cloud Model 1 (CM1; Bryan & Fritsch, 2002) sensitivity simulations of TOC under different combinations of local wind shear and moisture informed by CPEX series airborne observations will be executed. Influences of wind shear and moisture will not only be assessed relative to individual TOC structure, but with an added focus on collective TOC spatial organization whose impacts on regional and global weather and climate can exacerbate those of individual TOC systems (e.g., precipitation distribution, atmospheric circulations, radiation fluxes). Within the CM1 sensitivity simulations, increased tropospheric wind shear and moisture both together and individually are hypothesized to enhance individual TOC size and intensity, consistent with expected results and logic from the field campaign analyses of Chapters 2-4. More pronounced responses of individual TOC size and intensity, as well as collective TOC spatial organization, to imposed wind shear are hypothesized in drier tropospheric conditions, motivated by studies like Sakaeda & Torri (2022) that suggest enhanced wind shear impacts on TOC spatial organization in drier environments.

1.4.3 Dissertation Publication Breakdown

Each of Chapters 2-5 represents a unique contribution to the field of TOC-environment research. As such, each chapter stands alone as its own individual publication. Chapter 2 was officially published in the *AGU Journal of Geophysical Research: Atmospheres* journal in June 2024. Chapter 3 was submitted for publication to *AGU Journal of Geophysical Research: Atmospheres* in December 2025 and is currently undergoing the first round of edits to reviewer responses. Chapter 4 has not yet been submitted for publication, but submission for publication to *AGU Journal of Geophysical Research: Atmospheres* is planned post-defense. Chapter 5 was submitted for publication to *AGU Journal of Geophysical Research: Atmospheres* in October 2025 and, similar to Chapter 3, is currently undergoing the first round of edits to reviewer responses. Chapter 6 will conclude this dissertation with a synthesis of the results of Chapters 2-5, along with a discussion of the results in the context of the literature to highlight their unique contributions, implications, and guidance for future research.

Chapter 2

Near-storm Environmental Relationships with Tropical Oceanic Convective Structure Observed during NASA CPEX and CPEX-AW

2.1 Introduction

Deep tropical oceanic convection (TOC, equatorward of 30° latitude with radar echo extending to heights above the melting level) is a prevalent feature of the tropical atmosphere and plays key roles in driving both regional and global weather and climate, including influences on the large-scale tropical atmospheric circulation and upper ocean responses (e.g., Zipser 1977; Alexander & Young, 1992; Young et al., 1995; Brown & Zhang, 1997; LeMone et al., 1998; Saxen & Rutledge, 1998; Saxen & Rutledge, 2000; Tompkins, 2001; Cetrone & Houze, 2006; Mechem et al., 2006; Liu & Liang, 2010; Grant et al., 2020; Mulholland et al., 2021; Chen et al., 2023), as well as radiative fluxes particularly near cloud-top levels (e.g., Hartmann et al., 2001; Tobin et al., 2012; Del Genio & Chen, 2015; Hartmann, 2016; Grant et al., 2020; Bony et al., 2020; Pilewskie & L'Ecuyer, 2022). TOC also frequently produces thermodynamically driven cold pools, which can trigger development of non-precipitating cumulus congestus clouds (a further radiative influencer), initiate new deep convection, alter planetary boundary layer (PBL) characteristics, and

---

The following chapter is a reformatted reprint of Rodenkirch, B. D. & Rowe, A. K. (2024). Journal of Geophysical Research: Atmospheres. DOI: 10.1029/2023jd039632

thus further modify air-sea exchange (e.g., Esbensen & McPhaden, 1996; Saxen & Rutledge, 1998; Feng et al., 2015; Rowe & Houze, 2015; Chandra et al., 2018; Houze, 2018; Touzé-Peiffer et al., 2021; Sakaeda & Torri, 2023). Accurate TOC representation and parameterization is therefore critical for the success of weather and climate modeling efforts. However, despite decades of TOC research, an incomplete understanding of TOC structure, initiation, and evolution persists, including how TOC relates to its near-storm environments throughout storm system lifecycle (Cetrone & Houze, 2006; Igel & van den Heever, 2015; Minamide & Posselt, 2022). Studying near-storm environmental relationships is challenging, as it requires frequent, high-resolution measurements to capture fundamental small-scale convective processes, features, and environments. Highly temporally and spatially resolved *in situ* data collection is an ideal means of garnering such measurements.

Observational analysis from field campaigns in the western Pacific basin (e.g., TOGA-COARE, KWAJEX, EMEX, PISTON) has investigated near-storm environmental wind shear relationships with TOC structure using *in situ* sonde deployments. These studies have linked greater low-tropospheric speed shear to a greater degree of spatial organization of west Pacific mesoscale convective systems (MCSs), with quasi-linear convective systems oriented perpendicular to the low-level shear vector (Alexander & Young, 1992; LeMone et al., 1998; Chudler & Rutledge, 2021). Guy and Jorgensen (2014), however, found differing results in the Indian Ocean during the DYNAMO field campaign, with quasi-linear MCSs oriented more parallel to the low-tropospheric shear. Furthermore, quasi-linear MCSs in the west Pacific have also been linked to strong deep layer vertical speed shear owing to more expansive stratiform precipitation and anvil advection (Saxen & Rutledge, 2000). The analysis of these shear-convection relationships has been extended

to the greater tropics using convection-permitting model (CPM), spaceborne remote sensing, European Centre for Medium-Range Weather Forecasts Reanalysis-Interim (ERA-Interim) reanalysis, and ERA5 reanalysis datasets, finding similar deep layer speed shear relationships with tropical squall lines specifically (Tompkins, 2001) and tropical MCSs more generally (Igel & van den Heever, 2015; Chen et al., 2023). However, Tompkins (2001) acknowledges CPM limitations (e.g., limited vertical dimension and unrealistic cyclic boundary conditions), while Igel and van den Heever (2015) acknowledges biases stemming from inconsistent storm-relative CloudSat measurements that are a natural consequence of random chance convective sampling of low Earth orbit satellites. Additionally, much of the *in situ* research has predominately focused on (quasi-) linear convection and is largely based in the west Pacific and Indian Ocean. With TOC structure varying across the tropics, including an abundance of non-linear TOC (Houze et al., 2015), an evaluation of TOC relationships with near-storm wind shear necessitates detailed *in situ* studies in other tropical oceanic regions across different TOC types.

Similar to wind shear, field campaign data in the western Pacific and Indian Ocean basins, along with broader tropical oceanic CPM, ERA-Interim, and ERA5 reanalysis data, have been used to investigate near-storm environmental moisture relationships with TOC structure. Analysis of these datasets have shown mid-tropospheric relative humidity (RH) to positively correlate with TOC precipitation area and intensity due to decreased dry air entrainment (Brown & Zhang, 1997; LeMone et al., 1998; Tompkins, 2001; Cetrone & Houze, 2006; Savarin et al., 2014; Chen et al., 2016; Chen et al., 2017; Schiro et al., 2020; Chen et al., 2023). However, the relationships between low-tropospheric RH and TOC precipitation area and intensity vary, in both strength and sign, across tropical oceanic studies, even within similar regions (Tompkins, 2001; Cetrone & Houze,

2006; Chen et al., 2017; Schiro et al., 2020). The inconsistencies may relate to data collection during differing TOC lifecycle stages, with low-level inflow shown to potentially be more important during early lifecycle stages compared to mid-level inflow for later lifecycle stages (Mechem et al., 2002).

Similarly, inconsistent relationships between environmental CAPE and TOC structure exist across prior studies of the western Pacific basin. Cetrone and Houze (2006) and Chudler and Rutledge (2021) found KWAJEX and PISTON MCSs, respectively, to be associated with lesser CAPE compared to smaller, less organized convective systems, while Kingsmill and Houze (1999) found opposing results using TOGA-COARE data. The conflicting results could stem from negatively biased CAPE measurements caused by asymmetric thermodynamic instability concentration in the lower troposphere in the KWAJEX soundings (Cetrone & Houze, 2006) and low-level cooling and drying by MCSs in the PISTON soundings (Chudler & Rutledge, 2021).

Collectively, both the strength and sign of near-storm mean-layer environmental RH, wind shear, and CAPE relationships with TOC structure are inconsistent across studies. These inconsistent findings could be attributed to a multitude of factors, like differing analysis methods and data sources. However, a lack of regional context may be a major culprit. This lack of modern, regionally diverse, and regionally distinct *in situ* research is an issue, because TOC structure and its relationships with near-storm environments have been shown through TRMM observations and ERA-Interim reanalysis to exhibit regional dependencies (Houze et al., 2015; Chen et al., 2017). Satellite and reanalysis datasets provide the ability to examine each tropical oceanic region separately, but their limited spatial and temporal resolutions cannot sufficiently capture essential

small-scale near-storm environmental variability and convective processes. Consequently, targeted regional *in situ* studies, particularly in understudied areas, equipped with collocated high-resolution hydrometeor, moisture, and wind measurement capabilities are imperative to adequately analyze near-storm environmental relationships with TOC structure.

Two such targeted *in situ* regional studies were the 2017 NASA Convective Processes Experiment and 2021 CPEX – Aerosols & Winds (CPEX-AW) field campaigns based in Ft. Lauderdale, Florida and St. Croix, USVI, respectively. CPEX and CPEX-AW performed a total of 23 science flights aboard the NASA DC-8 research aircraft from 27 May 2017 – 24 June 2017 and 20 August 2021 – 4 September 2021, respectively, to study TOC processes in the Gulf of Mexico, Caribbean Sea, and western Atlantic—regions that were notably lacking recent *in situ*, non-tropical cyclone related deep convective research (Cui et al., 2020). The DC-8 aircraft was equipped with, amongst other instrumentation, a multi-wavelength airborne precipitation radar, a Doppler wind lidar, and dropsondes. Together, these instruments provided rare, coincident, high-resolution profiling of spatial three-dimensional (3-D) convective structure and near-storm winds and moisture for convective systems of different spatial scales and intensities (Turk et al., 2020; Hristova-Veleva et al., 2021). Given the uniqueness of this suite of observations, the CPEX and CPEX-AW field campaigns present an exceptional opportunity to analyze their region's near-storm environmental relationships with tropical oceanic 3-D convective structure, which will be the focus of this chapter. In particular, *how does 3-D TOC structure relate to near-storm environmental RH, vertical speed shear, and CAPE in different tropospheric vertical layers in the CPEX(-AW) observational domain?*

To address this research question, the organization of the chapter is as follows. Section 2.2 offers a description of the CPEX(-AW) instrumentation and data used for the analysis, while Section 2.3 outlines the analysis methodology. Section 2.4 presents the results of the analysis, and Section 2.5 provides a discussion of the results in the context of prior studies. Section 2.6 concludes the chapter with main takeaways from the analysis and next steps for future research.

2.2 Data

2.2.1 CPEX and CPEX-AW Overview

The NASA DC-8 aircraft was equipped with six science instruments during CPEX (Chen & Zipser, 2017) and five during CPEX-AW (Skofronick-Jackson et al., 2021). This chapter will focus on analysis of the higher spatial resolution airborne datasets from the following instrumentation: dropsondes, the Doppler Aerosol WiNd Lidar (DAWN; Kavaya et al., 2014), and the Third-Generation Airborne Precipitation Radar (APR-3; Sadowy et al., 2003). Together, these three instruments provided coincident, detailed measurements of near-storm moisture, winds, and 3-D convective structure (e.g., Figure 2.1) at sufficient resolutions to analyze characteristics of distinct vertical layers. Seventeen of the 23 CPEX(-AW) science flights sampled 20 separate deep precipitating convective systems (hereafter referred to as convective cases) with this instrument payload. As such, only observational data from these 17 science flights were used for analysis for this chapter.

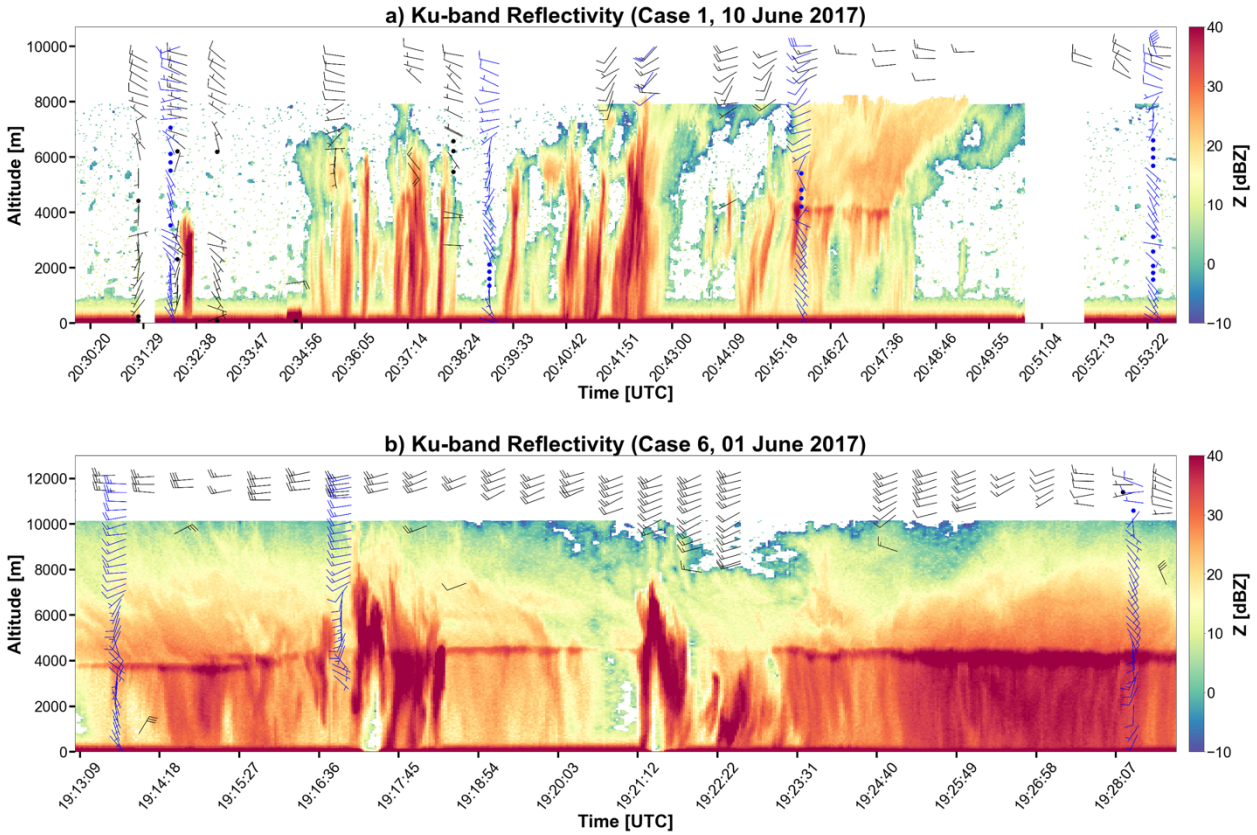

Figure 2.1: APR-3 Ku-band reflectivity profiles (fill), dropsonde wind profiles (blue barbs), and DAWN wind profiles (black barbs) for an (a) isolated and (b) organized TOC system observed during CPEX.

2.2.2 Dropsondes

CPEX vertical profiles of pressure, temperature, horizontal wind velocity, and humidity were collected using Yankee Environmental Systems eXpendable Digital Dropsondes (CPEX Dropsonde, 2019; Black et al., 2017). The dropsondes provided accuracy and resolutions appropriate for the purposes of this chapter (Greco et al., 2018; Black et al., 2017): 1.5 hPa (at 25°C) accuracy at 2.5 hPa resolution for pressure, 0.148°C accuracy with 0.0168°C resolution for temperature, 0.97 kts accuracy with 0.39 kts precision for horizontal winds, and 1.8% (at 25°C) accuracy at 0.1% precision for RH. CPEX-AW released the National Center for Atmospheric Research (NCAR) dropsondes, which used the Airborne Vertical Atmospheric Profiling System

(AVAPS) developed by Vaisala Inc. (AVAPS Dropsondes, 2023). These CPEX-AW dropsondes provide similarly appropriate accuracy and resolutions as the ones used from CPEX (AVAPS Dropsondes, 2023) with the largest differences seen in horizontal wind velocity (0.97 kts accuracy at 0.02 kts resolution) and RH (3% accuracy at 0.01% resolution). Unfortunately, RH accuracies were notably worse in actively precipitating environments from both campaigns as the dropsondes exhibited moisture biases when encountering precipitation, likely due to water ingress (Greco et al., 2018). As such, moisture data from dropsondes deployed in actively precipitating environments was excluded from analysis in this chapter. All the dropsonde data were processed using the NCAR Atmospheric Sounding Processing ENvironment (ASPEN) software (Greco et al., 2018; Vömel et al., 2021; Martin & Suhr, 2021). Post-mission GPS correction was also employed (CPEX Dropsonde, 2019). Dropsonde profiles with frequent, graphically visible anomalous spikes in equivalent potential temperature were excluded from analysis, amounting to 195 usable dropsondes across the 20 convective cases.

2.2.3 Doppler Aerosol WiNd Lidar (DAWN)

High-resolution vertical profiles of wind near convection were collected by the DAWN instrument aboard the NASA DC-8 aircraft during CPEX(-AW). DAWN is equipped with a 2-μm, 10-Hz laser that utilizes atmospheric aerosols to measure horizontal wind components (Kavaya et al., 2014; Turk et al., 2020; Greco et al., 2020). DAWN vertical profiles of horizontal winds were obtained at horizontal resolutions as fine as 3-7 km and a vertical resolution of ~33 m using line-of-sight wind profiles (CPEX DAWN, 2019; Greco et al., 2020). These profiles were severely attenuated when encountering opaque clouds (e.g., convective anvil cirrus), and data gaps frequently existed in the middle troposphere due to low aerosol concentrations (e.g., Bedka et al.,

2021). DAWN wind speed accuracy was < 0.10 kts with < ~2.92 kts precision (Greco et al., 2020) and showed a low bias of < 0.39 kts compared to dropsonde winds (Greco et al., 2020). Given the scales that are being explored for comparing mean-layer wind shear (differences hypothesized to be several kts), the DAWN wind accuracy and precision are adequate for the purposes of this chapter. DAWN data were processed and quality controlled via methods described in Kavaya et al. (2014), CPEX DAWN (2019), Greco et al. (2020), and Bedka et al. (2021).

2.2.4 Third-Generation Airborne Precipitation Radar (APR-3)

Vertical radar reflectivity profiles of 3-D convective hydrometeor structure were collected using the APR-3 instrument (Sadowy et al., 2003). APR-3 mirrors the Global Precipitation Measurement Mission Dual-Frequency Precipitation Radar (GPM-DPR) 13.4-GHz (Ku-) and 35.6 GHz (Ka-) bands, which simultaneously measure co- and cross-polarized reflectivities and vertical Doppler velocities (Durden et al., 2012; Turk et al., 2020; CPEX APR-3, 2018). Only Ku-band reflectivity profiles were used for analysis, as the Ku-band captures precipitation structure better than the Ka-band, which is more quickly attenuated by precipitating hydrometeors. Doppler velocity datasets were corrupted for a majority of CPEX convective cases (i.e., cases prior to 16 June 2017). Therefore, Doppler velocity was not incorporated in subsequent analysis. APR-3 scans at a vertical resolution (i.e., has an along-beam gate spacing) of 60 m (Sadowy et al., 2003; Durden et al., 2012). Ku-band horizontal resolution is ~730 – 800 m at 10-km range with a 10-dBZ sensitivity (Sadowy et al., 2003; Durden et al., 2012). APR-3 data were processed via methods described in Durden et al. (2012), with Ku-band calibration uncertainty for the CPEX and CPEX-AW campaigns estimated at 1 dB (CPEX APR-3, 2018; Turk et al., 2020).

2.3 Methods

2.3.1 Convective Case Characterization

In order to investigate near-storm environmental relationships with TOC structure, each of the 20 CPEX(-AW) convective cases was categorized as either isolated, organized, or scattered based on horizontal precipitation extent and continuity provided by archived half-hourly averaged Integrated Multi-satellitE Retrievals for GPM (IMERG) satellite data (Huffman et al., 2019). Given the small number of cases from the field campaigns, categorization of each convective system was manual. Isolated convective systems were defined as horizontally small, single-core precipitating regions, while organized convective systems were defined as broader, continuous, multi-core precipitating regions. Scattered convection was defined as broad, discontinuous precipitating regions. An example of each type of convection in the context of IMERG is depicted in Figure 2.2 using the CPEX data portal (Hristova-Veleva et al., 2020). The focus of this chapter is on isolated and organized non-tropical cyclone TOC cases, with the exclusion of scattered TOC cases motivated by a lack of observations during time periods of convective development and maturity. With the omission of the 2 scattered and 6 tropical cyclone cases, 12 out of the 20 total convective cases sampled during CPEX(-AW) underwent further analysis (Table 2.1). All but one (i.e., Case 15) of the 12 cases was sampled during a similar time of day (i.e., between 1800 UTC and 0000 UTC, or alternatively between 1400-1500 LT and 2000-2100 LT), so diurnal influences on convective structure are assumed to have been similar across cases.

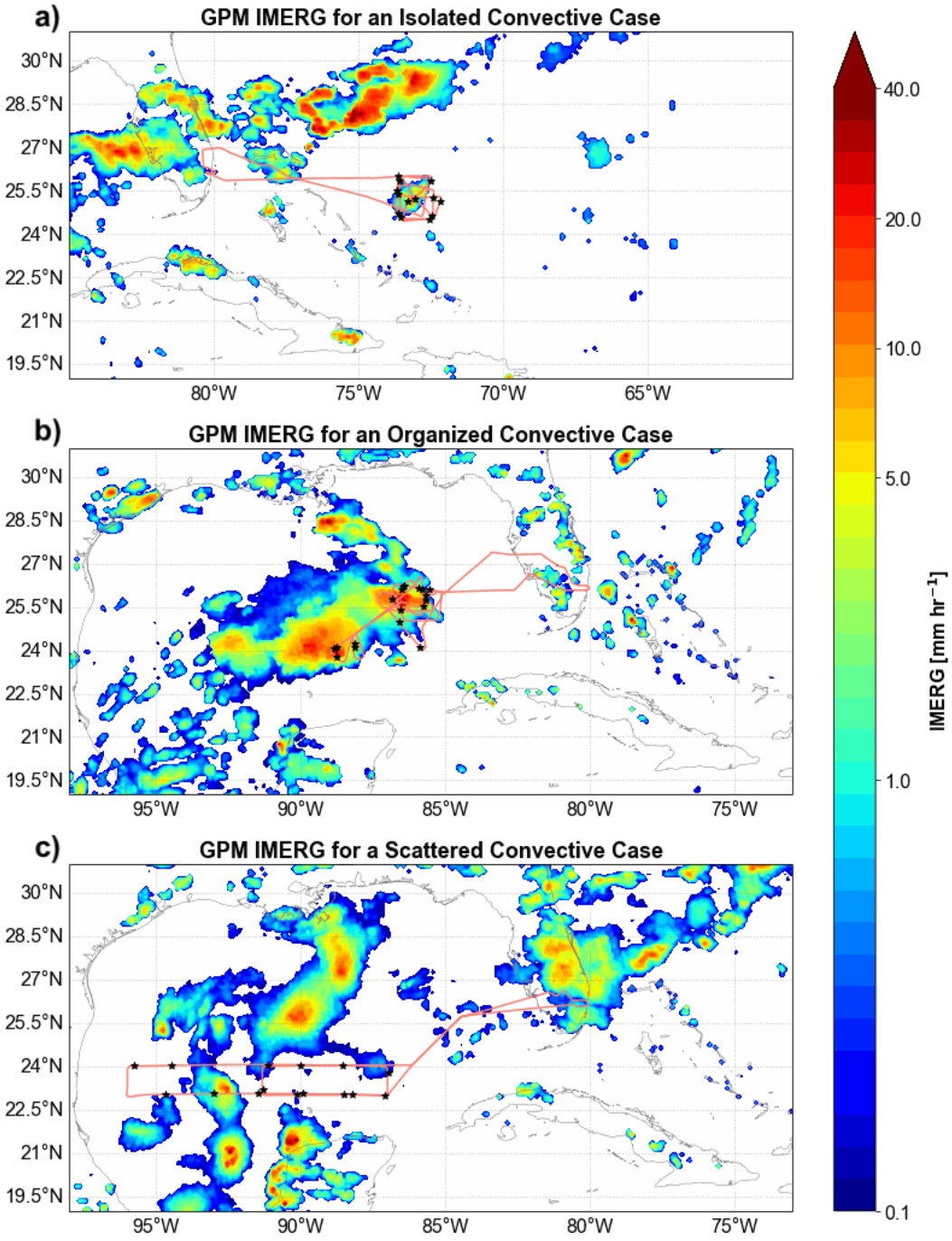

Figure 2.2: An example of (a) isolated, (b) organized, and (c) scattered TOC sampled during CPEX, as defined by GPM IMERG precipitation area and continuity. CPEX science flight tracks are overlaid in pink, with black stars representing dropsonde deployment locations. Thin gray outlines denote land.

Table 2.1: CPEX and CPEX-AW convective cases used for analysis in this chapter, sorted by convective type. The number of associated dropsondes (full and partial) for each case is provided with dropsonde deployment environment.

Case	Date	Field Campaign	Region	Convective Type	Number of Dropsondes (Full)	Number of Dropsondes (Partial)	Clear	In Cloud	In Precip
1	20170610	CPEX	Western Atlantic	Isolated	11	2	9	3	1
2	20170624	CPEX	Caribbean	Isolated	1	2	3	0	0
3	20170624	CPEX	Gulf of Mexico	Isolated	4	0	3	1	0
15	20210822	CPEX-AW	Western Atlantic	Isolated	2	1	2	1	0
4	20170615	CPEX	Caribbean	Organized	2	2	0	3	1
5	20170616	CPEX	Caribbean	Organized	3	16	0	0	19
6	20170601	CPEX	Gulf of Mexico	Organized	6	12	0	1	17
7	20170606	CPEX	Gulf of Mexico	Organized	4	2	4	0	2
8	20170617	CPEX	Caribbean	Organized	0	8	2	0	6
13	20170611	CPEX	Gulf of Mexico	Organized	15	4	10	5	4
14	20210821	CPEX-AW	Western Atlantic	Organized	1	4	4	1	0
16	20210824	CPEX-AW	Caribbean	Organized	4	5	4	0	5

2.3.2 Dropsonde Characterization

Only dropsonde profiles temporally collocated with their respective convective case's APR-3 data (i.e., within or near the anvil region, translating conservatively to within ~150 km of actively precipitating regions) were considered for analysis, amounting to 111 dropsondes. Each dropsonde from the cases identified in Table 2.1 was characterized by the convective type of its respective case, along with the convective-relative environment it was deployed into. Using APR-3 plots overlaid with dropsonde and DAWN wind profiles (e.g., Figure 2.1), the three environmental categories were "Clear" (deployed through a vertical layer with little to no Ku-band radar echo), "In Cloud" (deployed through a vertical layer with Ku-band radar echo present, but not reaching the surface (i.e., a non-precipitating cloud layer)), and "In Precip" (deployed through a vertical layer with Ku-band radar echo present and reaching the surface (i.e., actively precipitating at the surface)). Skew-T diagrams of the dropsonde profiles (not shown) also aided in validation of the environmental categorization. The distribution of dropsondes amongst the three environmental categories for each case is shown in Table 2.1, along with the distribution of full and partial (i.e.,

sparse data coverage in certain layers due to GPS transmission issues) dropsonde profiles for each case. Due to the notable moisture biases of In Precip dropsondes, as previously mentioned in Section 2.2, the only data from In Precip dropsondes used for analysis in this chapter was wind data. Omitting In Precip dropsonde moisture data from analysis amounted to 56 of the 111 total dropsondes being used for subsequent moisture analysis.

Convective lifecycle stage at the time of deployment was determined for each dropsonde, based on convective core evolution using time lapses of archived hourly GOES-East IR COLOR imagery and also APR-3 reflectivity features near the dropsonde profile. Convective lifecycle stage was defined as "growing" for systems composed of deepening convective elements with no stratiform elements, "mature" for systems with a mix of convective and stratiform elements, and "weakening" for systems with only stratiform elements. All near-storm environmental analysis was performed for data from all convective lifecycles and separately excluding dropsondes deployed during weakening convective lifecycle stages. Excluding the weakening lifecycle stage was tested as a means to focus on environments supporting convective development and sustainment. However, the results of the analysis excluding the weakening lifecycle stage data (figures not shown in this chapter) were similar to the results of the analysis that included data from all lifecycle stages, and thus all analysis presented in later sections includes data from all lifecycle stages. Dropsondes deployed within a convective inflow region were also noted, with convective inflow regions determined based on hourly 975 hPa – 925 hPa and 775 hPa – 700 hPa streamline flow near the convection of interest from European Centre for Medium-Range Weather Forecasting (ECMWF) ERA5 hourly reanalysis (Hersbach et al., 2018). Storm propagation was

neglected when determining convective inflow regions due to the slow-moving nature of the convective systems during sampling periods.

2.3.3 Mean-layer, Near-storm Environmental Metrics

Mean RH and vertical wind speed shear were calculated for each dropsonde profile for four distinct layers: the PBL, mid layer, upper layer, and deep layer. The base of the PBL is defined as the profile height nearest to the surface, ranging from 6.5 m to 338.5 m because of dropsonde transmission issues. Metric values were not found to correlate with near-surface height within that range. The top of the PBL is defined as the first height for which the virtual potential temperature exceeds its value nearest to the surface by 0.5 °C (e.g., Blumberg et al., 2017). The mid layer extends from the top of the PBL up to the melting level (i.e., 0 °C), while the upper layer extends from the melting level up to the lowest maximum height of the 111 qualifying dropsondes (7622.5 m), such that a uniform upper layer cap was achieved. The deep layer ranges from the profile height nearest to the surface up to the lowest maximum dropsonde height. Environmental metrics for layers not fully sampled by partial dropsonde profiles (see Table 2.1) were excluded from analysis.

Layer RH calculations use RH data at all height levels within the specified layer thresholds to calculate profile mean-layer RHs. With the assistance of the Sounding/Hodograph Analysis and Research Program in Python (SHARPpy; Blumberg et al., 2017) open-source meteorological package, vertical speed shear was calculated for the four distinct layers using the dropsonde component winds at each layer threshold height (interpolated as necessary). In addition to mean-layer RH and vertical speed shear, both most-unstable convective available potential energy

(MUCAPE, using the most unstable air parcel found within the lowest 300 hPa of the troposphere) and mixed-layer CAPE (MLCAPE, using a parcel with the mean temperature and moisture values from the lowest 100 hPa of the troposphere) were calculated for each dropsonde for the deep layer and the upper layer using SHARPpy, with upper layer CAPE equivalent to the component of deep layer CAPE between the melting level and the 7622.5 m upper layer cap. Upper layer CAPE supplements deep layer CAPE to provide a gauge of where convective instability is greatest in the vertical, though this metric, like deep layer CAPE, can be affected by convective anvils via their temperatures that are typically warmer than the surrounding cloud-free environment.

Similar to the dropsonde data, only DAWN profiles that were temporally collocated with their respective convective case's APR-3 data and conservatively within ~150 km of actively precipitating regions were included in analysis. The DAWN instrument provided much denser wind profiling (both spatially and temporally) in non-anvil regions compared to the dropsondes. That being said, PBL depth and melting level height could not be identified for each DAWN profile owing to temperature and moisture data not available from DAWN. With PBL depth in dropsonde data found to vary appreciably within short geospatial and temporal ranges, only deep layer wind shear could be confidently calculated for the DAWN profiles. The DAWN deep layer, in comparison with the dropsonde deep layer, was similarly capped at the lowest maximum dropsonde height of 7622.5 m. However, the deep layer for the DAWN data slightly varies from the dropsonde deep layer, in that a uniform near-surface value of 500 m was employed to omit low SNR (i.e., noisy) data from DAWN shear calculations. For similar reasons, DAWN profiles, with a vertical resolution of ~33 m, were also required to contain at least 20 data points within the

lowest 1 km of the atmosphere. An equivalent 500 m – 7622.5 m dropsonde deep layer shear was computed for direct comparison with DAWN deep layer shear.

2.3.4 Contoured Frequency by Altitude Diagrams

For analysis of convective intensity, defined in this chapter as radar reflectivity intensity related to hydrometeors as a proxy for convective updraft intensity (e.g., Zipser & Lutz, 1994; Zipser et al., 2006; Heymsfield et al., 2010; Ni et al., 2019), all APR-3 Ku-band reflectivity profiles for an individual case were binned into two-dimensional (2-D) histograms with 5-dBZ and 0.5-km intervals. Reflectivity was binned from -10 dBZ to 60 dBZ, and height bins extend from 1.5 km to 8 km, so as to omit potentially spurious near-surface data (Sadowy et al., 2003; Durden et al., 2003) and provide a uniform upper layer altitude cap to allow for case intercomparison. Each 2-D histogram was normalized by the maximum bin count in *any* height interval to create joint PDFs, allowing for frequency comparisons across height levels (e.g., Zagrodnik et al., 2019). Each 2-D histogram was also separately normalized by the maximum bin count in *each* height interval to create Contoured Frequency by Altitude Diagrams (CFADs) (Yuter & Houze, 1995), allowing for easier frequency comparisons at a given height level. Given the 10-dBZ Ku-band sensitivity of the APR-3 instrument at 10-km range, it is noted that the utilization of Ku-band reflectivity values below 10 dBZ may have increasingly shifted joint PDFs and CFADs toward greater reflectivities in height bins progressively farther from the DC-8 aircraft. The heights from the reflectivity profiles, and thus in each joint PDF and CFAD, were also not adjusted for brightband height, as brightband height across all the convective cases did not vary considerably (i.e., < ~0.5-km, or one height interval).

Subsequent so-called “difference CFADs” were produced by subtracting one case’s CFAD from another. These difference CFADs allow for investigation of convective intensity and storm structure differences between cases with distinct mean-layer environmental metric differences (Yuter & Houze, 1995). Convective case intercomparisons, via difference CFADs, were only performed between cases of similar convective type (i.e., isolated vs. isolated, organized vs. organized), as comparisons across convective type would offer little value due to inherent differences in single-core vs. multi-core storm structure. Convective case intercomparisons were also only performed between cases that were observed during a similar convective lifecycle stage, such that predominantly convective elements were not compared with predominantly stratiform elements. Relatedly, while the CFAD case intercomparisons shown in this chapter incorporate APR-3 Ku-band reflectivity profiles from each case’s convective and stratiform regions combined, similar case intercomparisons were performed separating each case’s convective and stratiform regions. The objective convective-stratiform partitioning of each case’s Ku-band reflectivity profiles was achieved using the Echo Classification from COnvectivity for Vertically pointing radars (ECCO-V) algorithm (Dixon & Romatschke, 2022; Romatschke & Dixon, 2022), and it notably produced the same conclusions as the analysis including both convective and stratiform components discussed in this chapter.

2.4 Results

2.4.1 Near-storm Environmental Relationships with Convective Type

To analyze potential near-storm environmental relationships with TOC type (i.e., isolated versus organized), mean-layer dropsonde metrics are presented as box-and-whisker plots (e.g., Figure 2.3). Particular focus is placed on dropsonde metrics collected within convective inflow regions,

as these regions are more representative of environments influencing convection. Therefore, subsequent quantitative discussion relates to dropsonde metrics collected only within convective inflow regions. However, due to the limited dropsonde sampling within convective inflow regions, analogous metrics that include dropsondes deployed outside of convective inflow regions are also provided for reference in subsequent figures. While a majority of the quantitative analysis is not statistically significant (as denoted by overlapping "notches" in the box-and-whisker plots), predominantly due to the aforementioned limited sample sizes of the CPEX(-AW) data, the results still provide insight into potential relationships between TOC structure and near-storm environments.

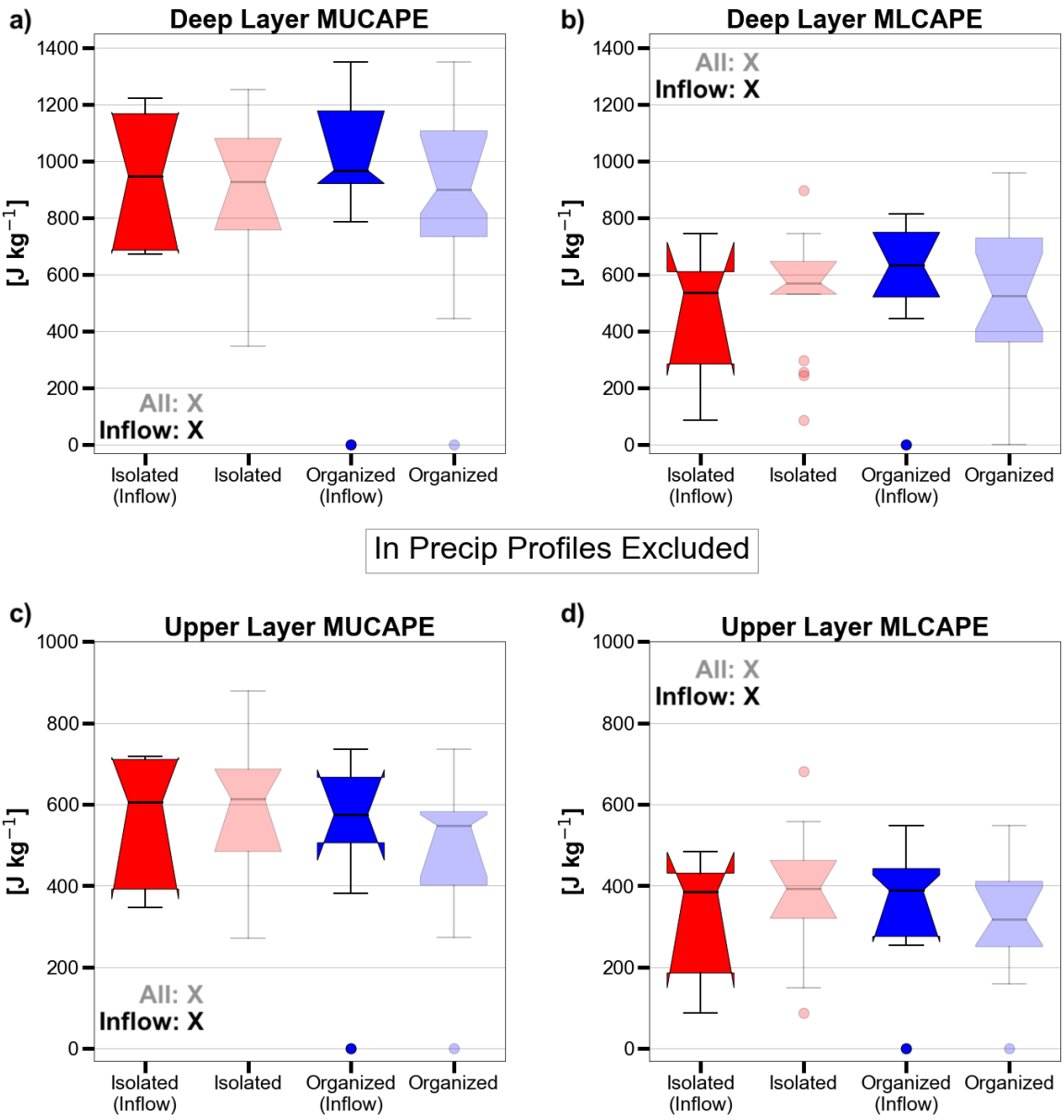

Figure 2.3: Dropsonde-derived (a) deep layer MUCAPE, (b) deep layer MLCAPE, (c) upper layer MUCAPE, and (d) upper layer MLCAPE for isolated (red) and organized (blue) TOC systems sampled during CPEX and CPEX-AW (In Precip profiles excluded). Faded boxes denote observations collected both within and outside of convective inflow (i.e., all) regions, while saturated boxes denote observations collected only within convective inflow regions. Each box extends from the first quartile to the third quartile of the data, with a black line at the median. Whiskers extend from the box by up to 1.5 times the inter-quartile range, and outlier points are points beyond the whiskers. Notches denote statistical significance with a 95% confidence level via bootstrapping the median 10,000 times and using a Gaussian-based asymptotic approximation. Extended notches are the result of the confidence interval bounds extending beyond the first quartile or the third quartile. Statistically significant medians between sets of observations of similar convective inflow categorization are denoted by a check mark, while statistically insignificant medians are denoted by an X.

CAPE is first analyzed, showing that organized convection has slightly greater median deep layer MUCAPE (968 J kg^{-1} vs. 948 J kg^{-1}, Figure 2.3a) and MLCAPE (632 J kg^{-1} vs. 537 J kg^{-1}, Figure 2.3b) compared to isolated convection. Meanwhile, isolated convection is observed to have slightly greater median upper layer MUCAPE (605 J kg^{-1} vs. 575 J kg^{-1}, Figure 2.3c), though median upper layer MLCAPE is comparable between the two convective types (386 J kg^{-1} for isolated vs. 388 J kg^{-1} for organized, Figure 2.3d). Large CAPE variability exists within each convective type, motivating further subdivision by case. Figure 2.4 reveals large CAPE variability within each case as well, even when accounting for location of the dropsonde relative to the precipitating system. This result is not surprising, as like many prior observational studies of CAPE and TOC structure (e.g., Chudler & Rutledge, 2021), CPEX(-AW) likely sampled near-storm environments where CAPE was both unrealized and separately already realized. *Large intra-case variability may also partly be attributed to flight duration and spatial extent, but some cases have large metric variabilities (e.g., Figure 2.4) despite convective flight legs covering small areas (e.g., Case 1 (Figure 2.2a) and Case 15) and/or having small observation periods (e.g., Case 15).* Therefore, despite no clear general relationship between convective type and MUCAPE/MLCAPE in either layer in the CPEX(-AW) region, some cases—even of similar convective type—do have distinctly different CAPE magnitudes compared to others (e.g., isolated Cases 1 and 3 with non-overlapping upper layer CAPE ranges in Figure 2.4d), which will be investigated more as individual case comparisons in Section 2.4.2 and Section 2.4.3.

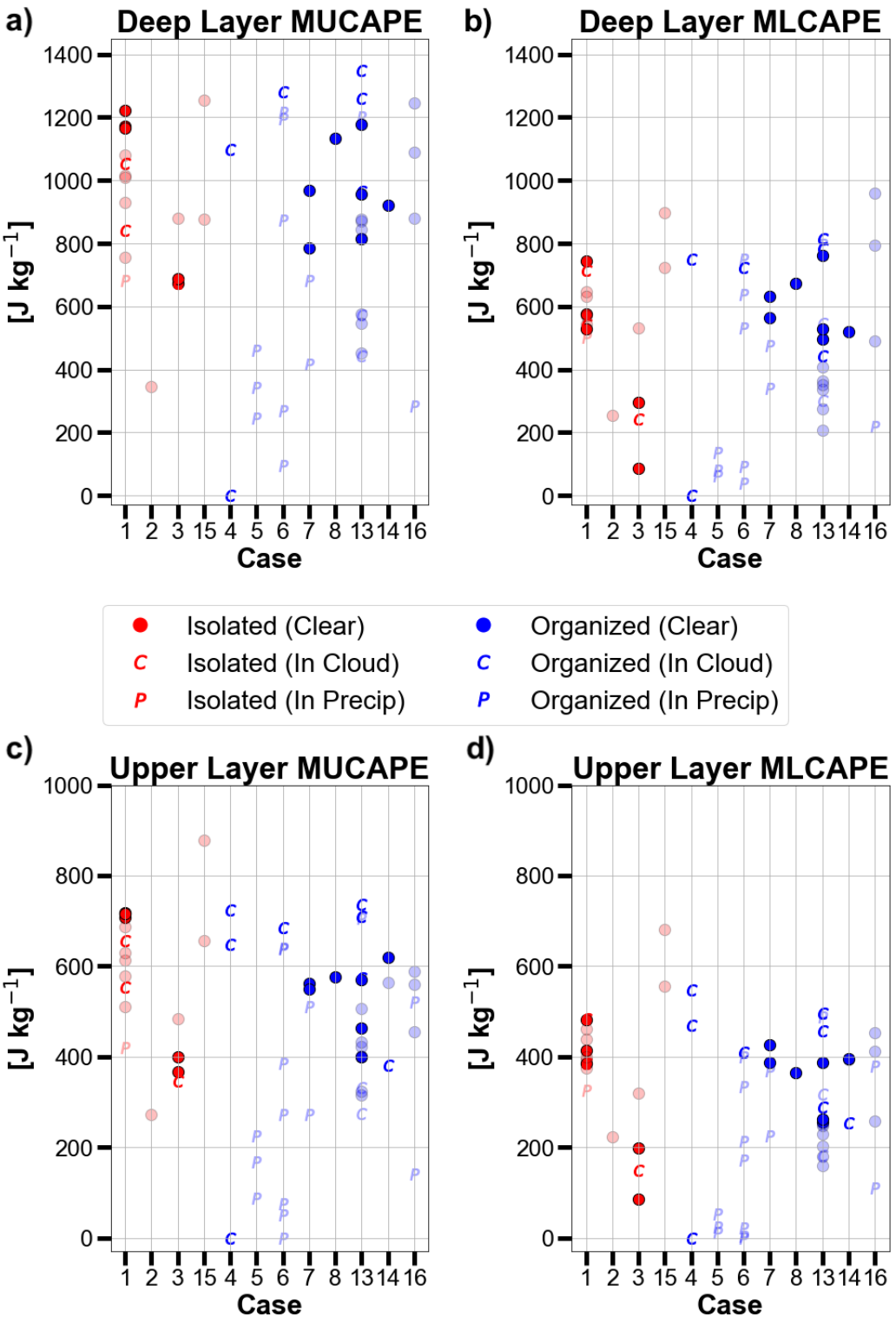

Figure 2.4: Same data as Figure 2.3, except dropsonde observations are further sorted by convective case (In Precip profiles included as well). Faded points denote observations not collected within convective inflow regions. Markers denote the convective-relative environment the dropsonde was deployed into.

RH appears to have a clearer distinction between convective types, with organized convection associated with greater median RH in each layer: 71.3% vs. 65.7% in the deep layer (Figure 2.5a), 89.1% vs. 86.5% in the PBL (Figure 2.5b), 73.4% vs. 67.5% in the mid layer (Figure 2.5c), and 66.8% vs. 57.3% in the upper layer (Figure 2.5d). These results align with west Pacific studies that consistently link greater mean-layer RH to more organized convection via greater convective buoyancy potential and reduced updraft dilution from dry air entrainment. As with CAPE, large mean-layer RH spreads exist for both convective types, particularly for organized convection (Figure 2.5), and within individual cases (Figure 2.6), especially Cases 1, 13, and 16. Organized Cases 13 and 16, in particular, record some of the lowest deep, mid, and upper layer RH values of any case and will be investigated further in Section 2.4.4. When comparing only the clear air dropsondes for each case across convective type, deep and mid layer RH spread is similar for isolated and organized convection (Figure 2.6a), while PBL RH is generally greater for organized convection (Figure 2.6b). Distinct mean-layer RH differences between cases of similar convective type also exist, which further motivates case comparisons in Section 2.4.2 and Section 2.4.3.

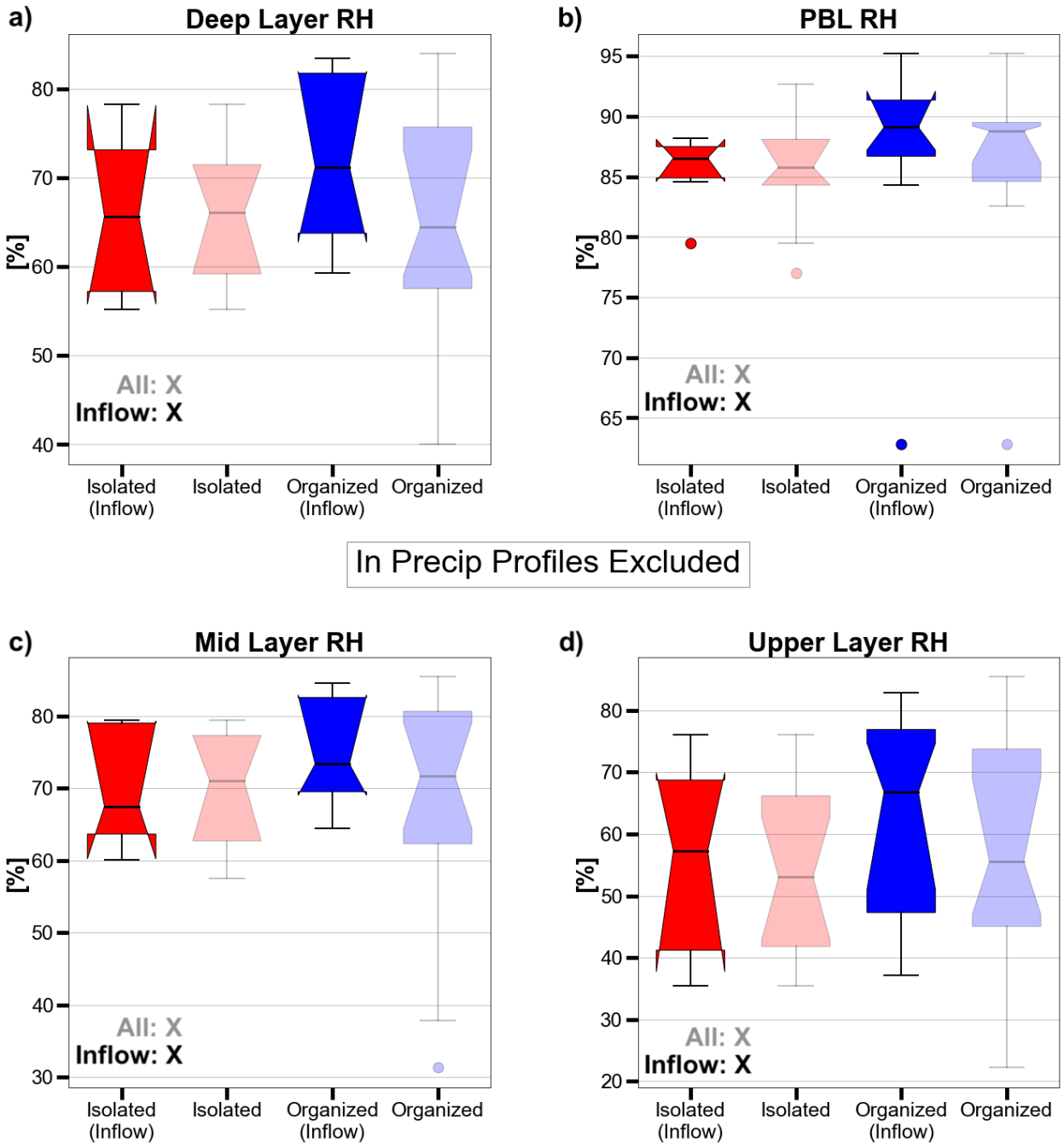

Figure 2.5: Same as Figure 2.3, except showing (a) deep layer RH, (b) PBL RH, (c) mid layer RH, and (d) upper layer RH.

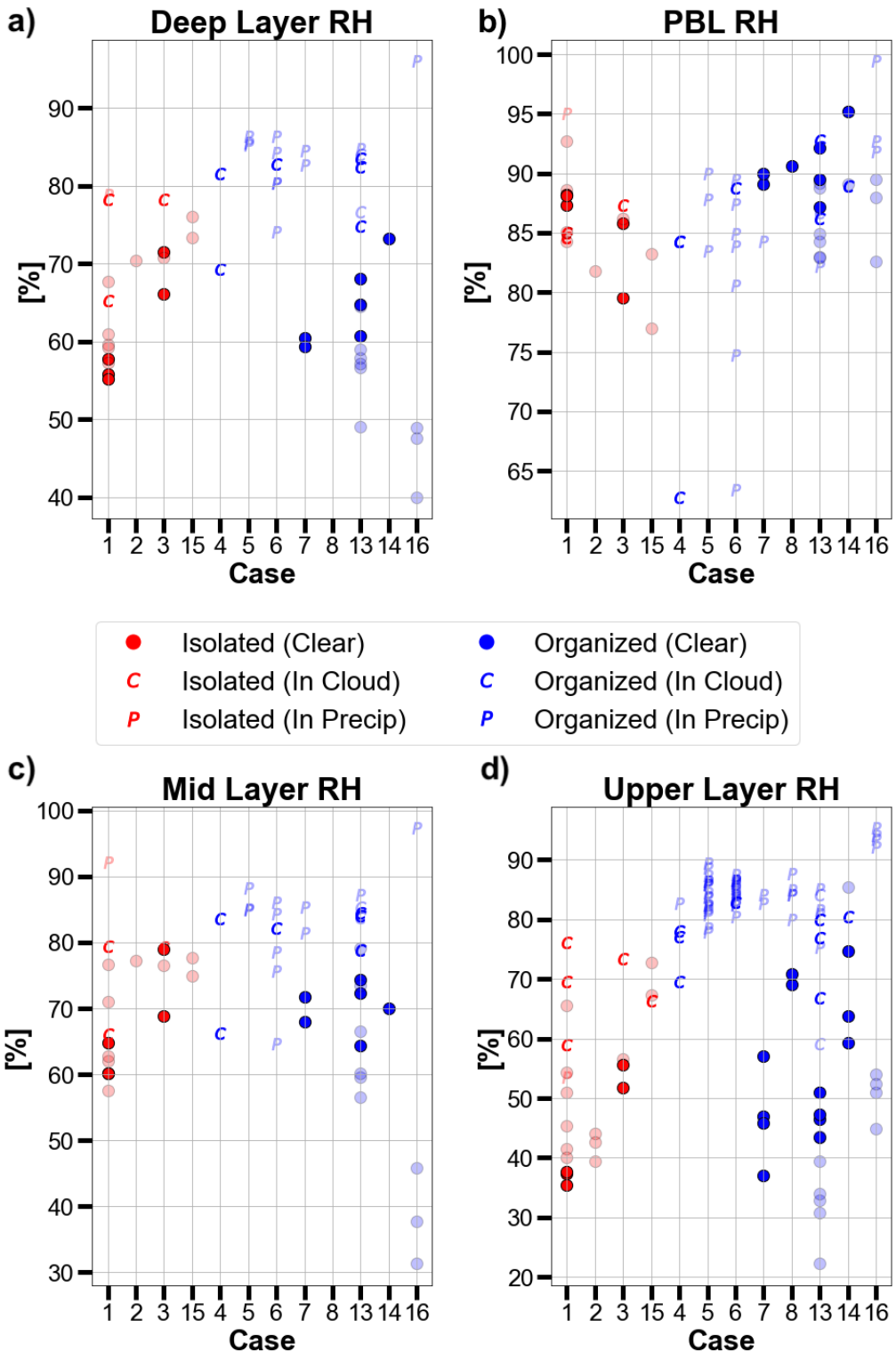

Figure 2.6: Same data as Figure 2.5, except dropsonde observations are further sorted by convective case (In Precip profiles included). Faded points denote observations not collected within convective inflow regions. Markers denote the convective-relative environment the dropsonde was deployed into.

Similar to RH, the PBL is a focal point for vertical wind speed shear distinctions between convective type. Organized convection has greater median PBL speed shear (5.6 kts vs. 3.5 kts, Figure 2.7b) compared to isolated convection, as well as greater mid (19.0 kts vs. 7.0 kts, Figure 2.7c) and deep layer (22.1 kts vs. 12.0 kts, Figure 2.7a) speed shears. In particular, the greater median mid layer speed shear of organized convection is statistically significant. As with prior metrics, a large degree of mean-layer speed shear variability also exists within each convective type (especially for organized convection). When grouped by case (Figure 2.8), large speed shear spreads within cases are evident and are notably unrelated to the environment the dropsondes were deployed into (i.e., Clear, In Cloud, or In Precip). However, similar to CAPE and RH, distinct mean-layer speed shear differences do exist amongst cases of similar convective type, which further warrants comparing individual cases in Section 2.4.2 and Section 2.4.3. Ultimately though, organized convection is associated with generally greater PBL, mid, and deep layer near-storm speed shear than isolated convection (Figure 2.8a,b,c). The PBL speed shear findings in particular are consistent with prior studies (e.g., Chen et al., 2017 and Chudler and Rutledge, 2021) and prevailing RKW theory concerning cold pool convective initiation (Yuter and Houze, 1995; Houze, 2018), though recent literature (e.g., Grant et al., 2018) suggests alternate explanations for the PBL shear relationship, with RKW theory not necessarily being applicable to the tropics.

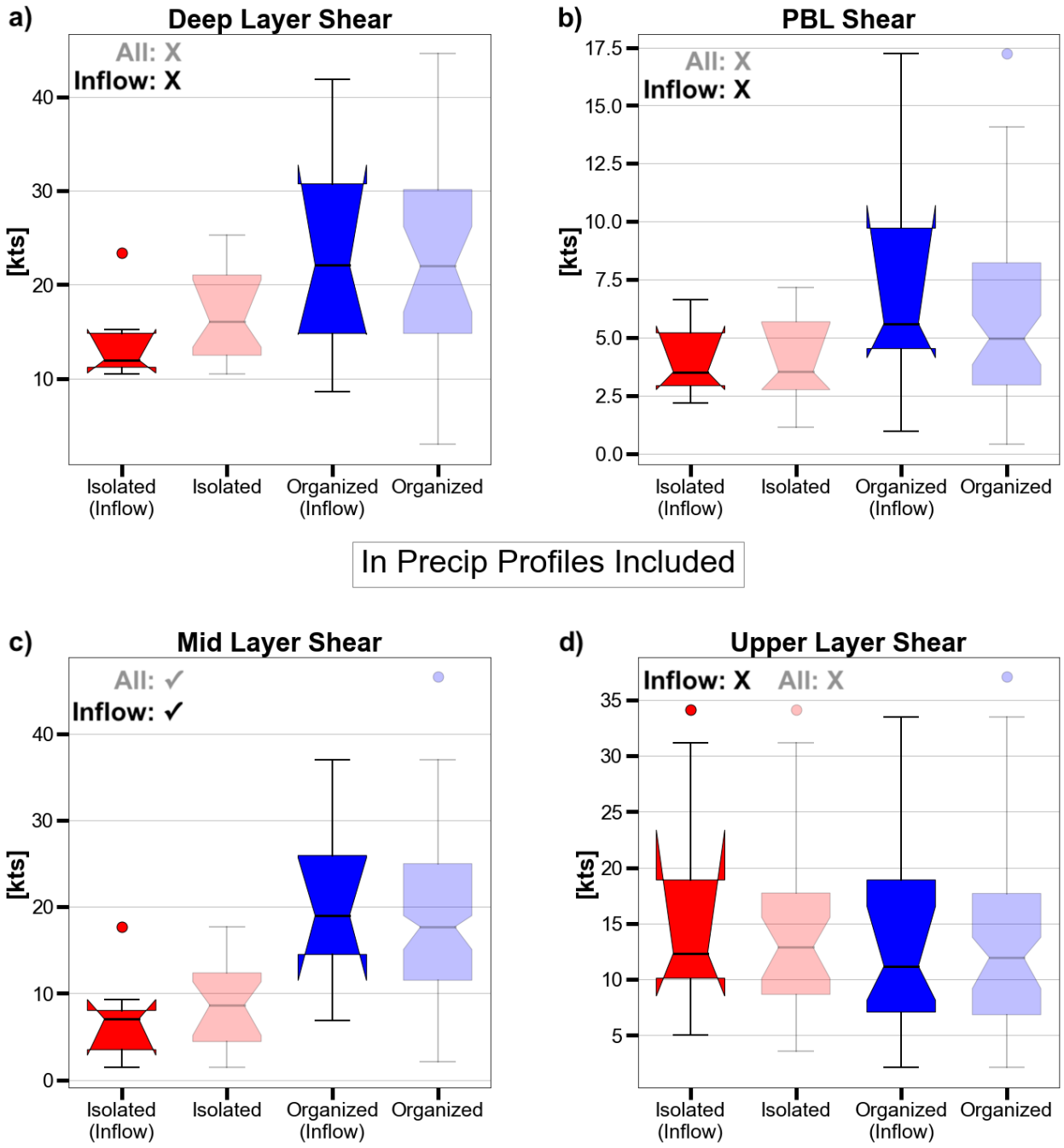

Figure 2.7: Same as Figure 2.3, except showing (a) deep layer speed shear, (b) PBL speed shear, (c) mid layer speed shear, and (d) upper layer speed shear. In Precip profiles are now included.

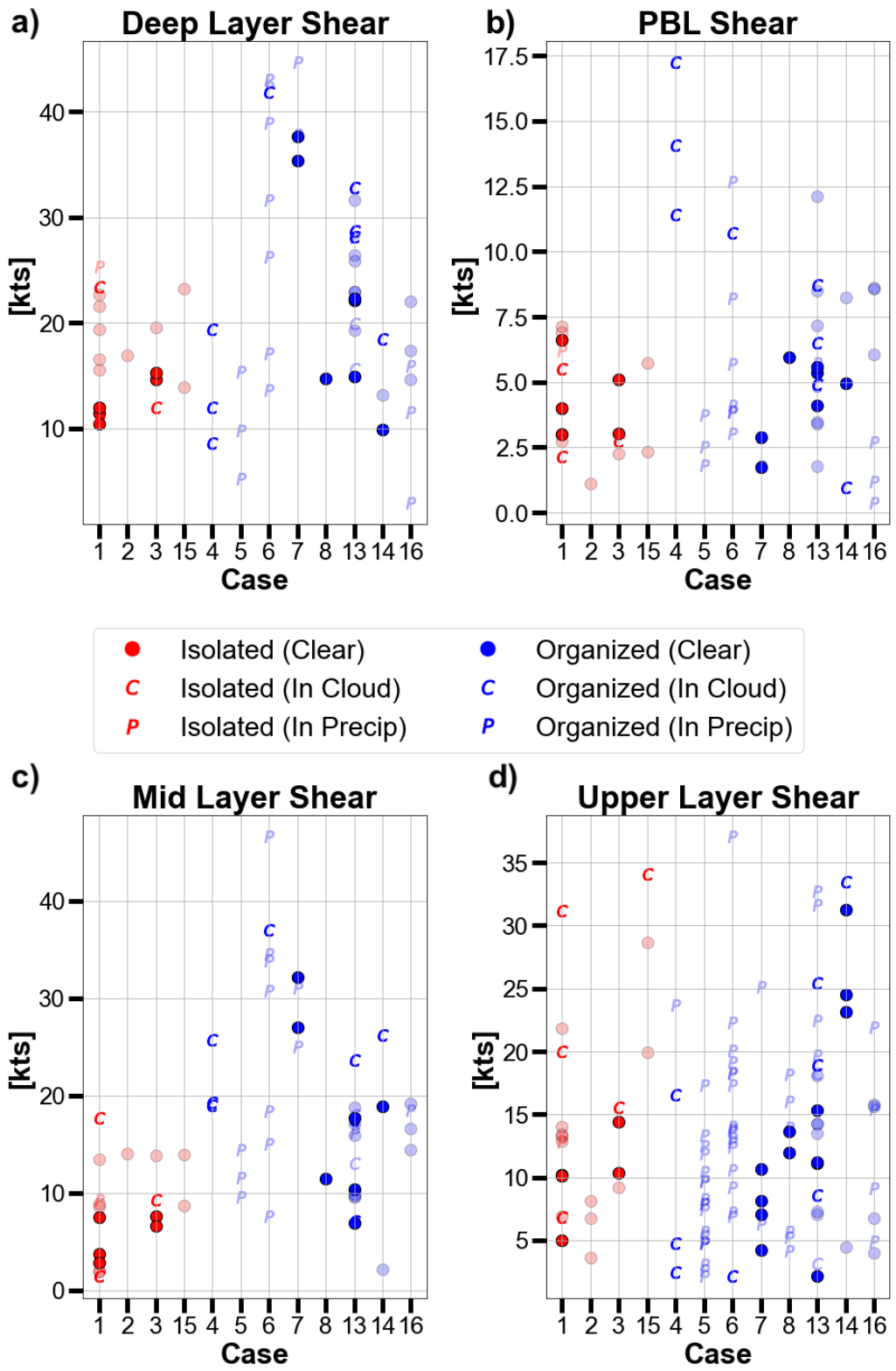

Figure 2.8: Same data as Figure 2.7, except dropsonde observations are further sorted by convective case. Faded points denote observations not collected within convective inflow regions. Markers denote the convective-relative environment the dropsonde was deployed into.

Incorporating the spatially and temporally denser DAWN observations provides an enhanced look into deep layer speed shear trends compared to dropsondes alone (Figure 2.9). The addition of the DAWN observations reveals even larger deep layer speed shear variability within each convective type (Figure 2.9a) and each convective case (Figure 2.9b) than the dropsonde observations previously showed. Notably, median deep layer speed shear is actually greater for isolated convection compared to organized convection (25.2 kts vs. 21.2 kts, Figure 2.9a), which the less frequent dropsonde data did not capture, and the results are statistically significant. When comparing all isolated case speed shear observations with the organized cases, however, the relationship between deep layer speed shear and convective type is unclear (Figure 2.9b).

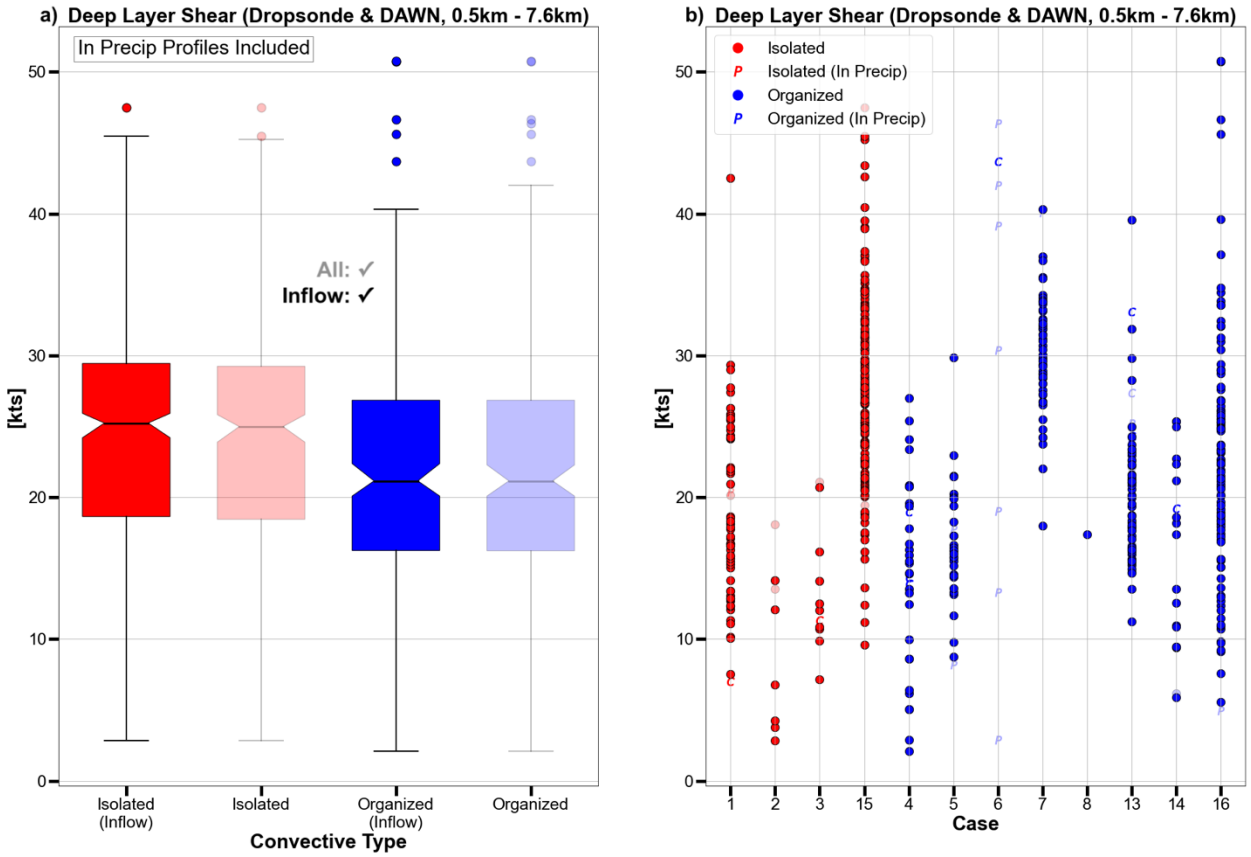

Figure 2.9: (a) Same as Figure 2.7a, except showing dropsonde- and DAWN-derived 0.5-km – 7.6-km deep layer speed shear. (b) Same as (a), except observations are further sorted by convective case. Markers denote if an observation was collected within an actively precipitating environment, and faded markers denote dropsonde observations not collected within convective inflow regions.

Overall, the composite analysis of near-storm environmental relationships with convective type reveals broad near-storm environmental metric variability within each convective type. However, general mean-layer CAPE, RH, and speed shear trends do exist with regards to horizontal TOC structure. Coupled with distinct metric variability between cases of similar convective type, it raises the question whether similar (or perhaps even more pronounced) near-storm environmental trends apply to vertical convective structure (i.e., convective intensity) for each convective type.

2.4.2 Near-storm Environmental Relationships with Convective Intensity (Isolated)

To analyze near-storm environmental relationships with isolated TOC intensity, CFADs (see Section 2.3.4) were created for each isolated case (except Case 15, which had limited APR-3 reflectivity data). The CFADs are 2-D histograms of reflectivity and height normalized by the maximum bin count in *each* height interval. Similar analysis was performed with the 2-D histograms normalized by maximum bin count in *any* height interval (i.e., joint PDFs), and each method produced the same conclusions. Cases with distinctly different mean-layer metric values (Section 2.4.1) had their CFADs differenced to evaluate differences in relative Ku-band reflectivity frequency at each height bin, thereby allowing assessment of which case was more intense. Median, first quartile, and third quartile Ku-band reflectivity profiles were created for cases in the difference CFADs as well for reference, providing alternate comparisons of convective intensity. The peak differences between cases in these reference reflectivity profiles collocate height-wise with the peak relative frequency differences of the difference CFADs, thereby supporting the difference CFAD interpretations. Subsequent comparison of convective intensities and their associated dropsonde mean-layer environmental metrics was performed.

Together, the isolated case comparisons show the more intense isolated case (an example shown in Figure 2.10a comparing Cases 1 and 2) to consistently possess greater deep and upper layer MUCAPE and MLCAPE (as determined in Figure 2.4), especially when comparing just the dropsondes deployed within convective inflow regions. This general relationship could result from greater CAPE environments promoting hydrometeor growth through enhanced thermodynamic instability (i.e., buoyancy) and consequently stronger updrafts that loft hydrometeors higher and for longer periods of time. No other environmental metrics showed as clear of a distinction in isolated convective intensity and thus are not shown.

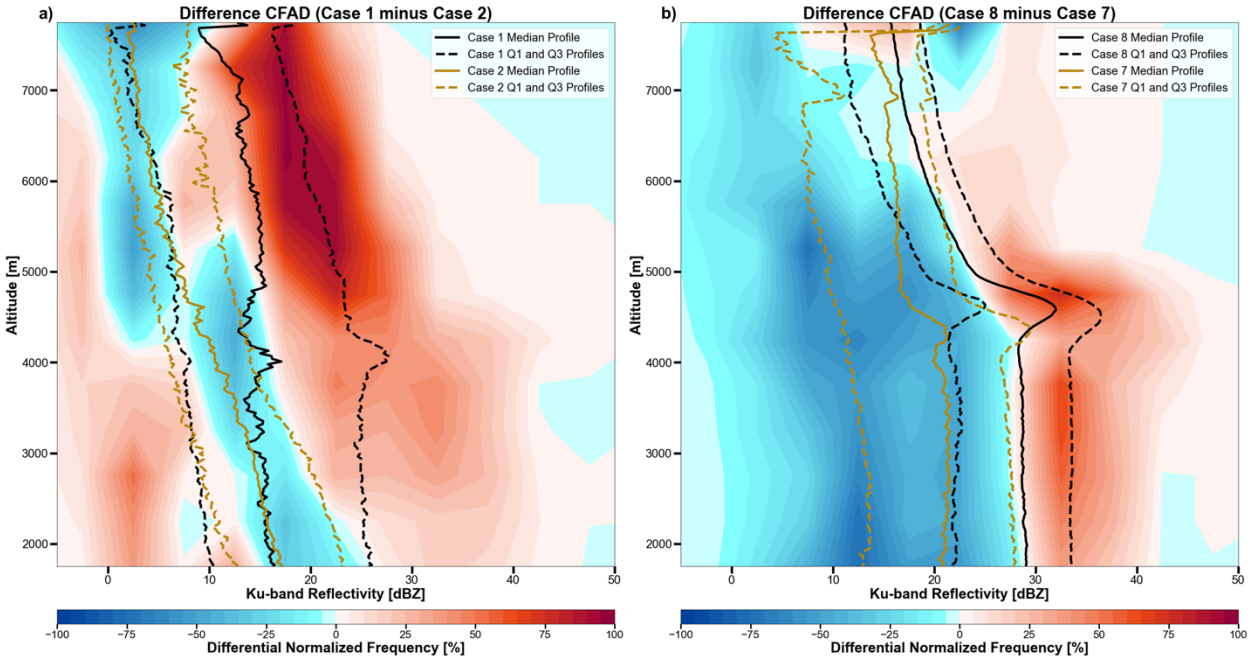

Figure 2.10: (a) Case 2 CFAD subtracted from the Case 1 CFAD. APR-3 Ku-band reflectivity data is binned into 5-dBZ and 0.5-km intervals and normalized by the maximum bin count in each height interval. Solid black and dark orange lines denote the median Ku-band reflectivity profiles for Case 1 and Case 2, respectively. Dashed black and dark orange lines denote the first and third quartile Ku-band reflectivity profiles for Case 1 and Case 2, respectively. The median and quartile reflectivity profiles are not binned at the 0.5-km CFAD resolution, but rather are at the original, higher resolution of the APR-3 instrument. (b) Same as (a), but for Case 7 and Case 8.

2.4.3 Near-storm Environmental Relationships with Convective Intensity (Organized)

Similar to the isolated case comparisons, organized TOC intensity was explored via CFADs with supporting median, first quartile, and third quartile Ku-band reflectivity profiles in the context of distinct mean-layer differences between cases (Section 2.4.1). When comparing all CPEX(-AW) organized convective cases with distinct mean-layer environmental metric differences, no consistent mean-layer MUCAPE nor MLCAPE relationships with convective intensity were found. However, when a notable difference in upper layer RH existed between two organized cases, the more intense convection (e.g., Figure 2.10b comparing Cases 7 and 8) was consistently associated with greater upper layer RH (Figure 2.6d). This relationship could be explained by less dry air entrainment above the melting level promoting enhanced hydrometeor growth and limiting negative buoyancy introduction. Additionally, when notable differences in mid layer and upper layer speed shears amongst inflow dropsondes existed between two organized cases, the more intense convection (e.g., Figure 2.10b comparing Cases 7 and 8) was consistently associated with greater upper layer shear (Figure 2.8d), yet lesser mid layer shear (Figure 2.8c).

When intercomparing the isolated case comparison results with those from organized cases, it is noteworthy that there are no similar, consistent near-storm mean-layer metric trends with convective intensity. This lack of similarity between convective types may reflect a greater and more variable impact of multi-core systems on their near-storm environments than single-core systems. An additional lack of consistent near-storm environmental relationships with organized TOC intensity may similarly reflect the variable impact of differently structured and aged multi-core systems on their near-storm environments. Indeed, diverse vertical organizational structures

of multi-core TOC (e.g., linear vs. non-linear MCSs) were observed during CPEX(-AW) and will be explored further in the following section.

2.4.4 Case 13 vs. Case 16 Organized Convection Comparison

As highlighted in Section 2.4.1, large mean-layer RH variability existed for organized convective systems (Figure 2.5). Upon further examination, Cases 13 and 16 contained many of the lowest mean-layer RH values of any sampled CPEX(-AW) convective system when considering all dropsondes (Figure 2.6), and thus were responsible for the particularly large mean-layer RH spreads of organized TOC. The relatively dry near-storm observations, coupled with the especially large RH variability, motivated further investigation into the convective environments of Case 13 and Case 16.

The convective flight legs and observations of Cases 13 and 16 each encompassed a synoptic-scale horizontal total precipitable water (TPW) gradient (Figure 2.11; Hristova-Veleva et al., 2020; Cooperative Institute for Meteorological Satellite Studies, 2023), providing a reason for large intra-case RH spreads and notably dry near-storm observations that were particularly influential on the RH results of Section 2.4.1. No other observed convective systems during CPEX(-AW) were located near synoptic-scale TPW gradients, making Cases 13 and 16 unique in that aspect. From a satellite-based perspective, both convective systems had similar areal coverage (Figure 2.11) with an intensifying sector and a matured sector identified by decreasing and increasing infrared brightness temperatures with time, respectively (not shown). Both cases' deep precipitating regions were located on the moist side of their respective synoptic-scale TPW gradient, with each TPW gradient collocated with a similar strength (~30 kts), along-gradient 800

– 650 hPa mid-level jet (not shown but observed by the dropsondes). However, despite these similarities, the vertical structures of the organized Case 13 and Case 16 convective systems were markedly different, with Case 13 mainly composed of leading line convective elements with trailing stratiform (Figure 2.12a), while Case 16 was characterized by numerous embedded convective elements within predominant widespread stratiform (Figure 2.12b). Cases 13 and 16 therefore provided a unique opportunity to investigate how differing organized vertical convective structures and their convective intensities relate to near-storm environmental parameters in the CPEX(-AW) region.

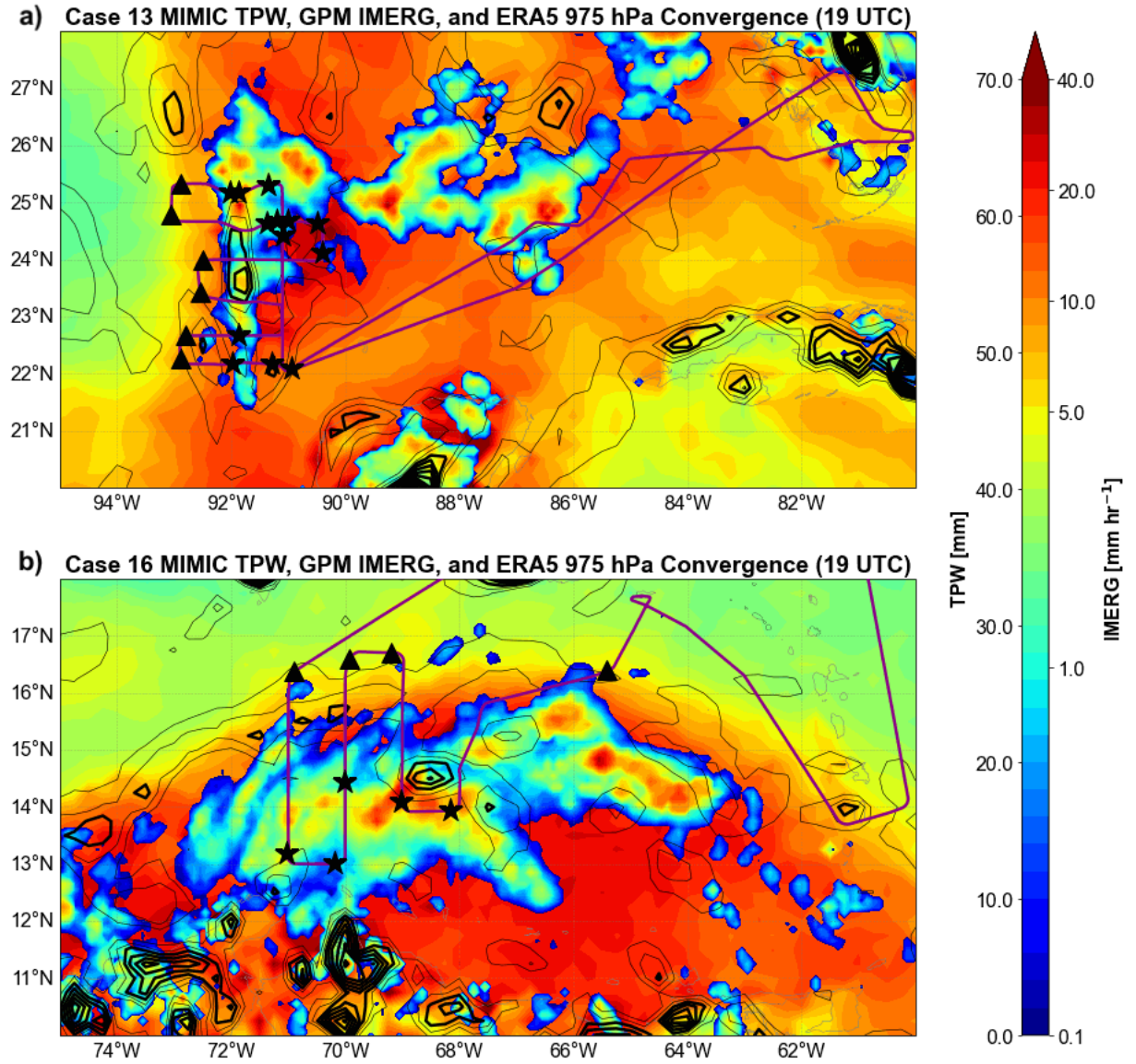

Figure 2.11: (a) Case 13 hourly MIMIC TPW (bottom layer fill), half-hourly averaged GPM IMERG surface precipitation estimation (top layer fill, averaged from the half hour preceding the listed time), ECMWF ERA5 hourly 975 hPa convergence (black contours, contoured every 2 x 10^{-5} s^{-1} and bolded ≥ *5 x 10^{-5} s^{-1}), and DC-8 science flight track (purple line, full flight). Black stars and triangles denote dropsondes deployed (during the full flight) on the moist and dry side, respectively, of the synoptic-scale TPW gradient. Thin gray outlines denote land. (b) Same as (a), but for Case 16.*

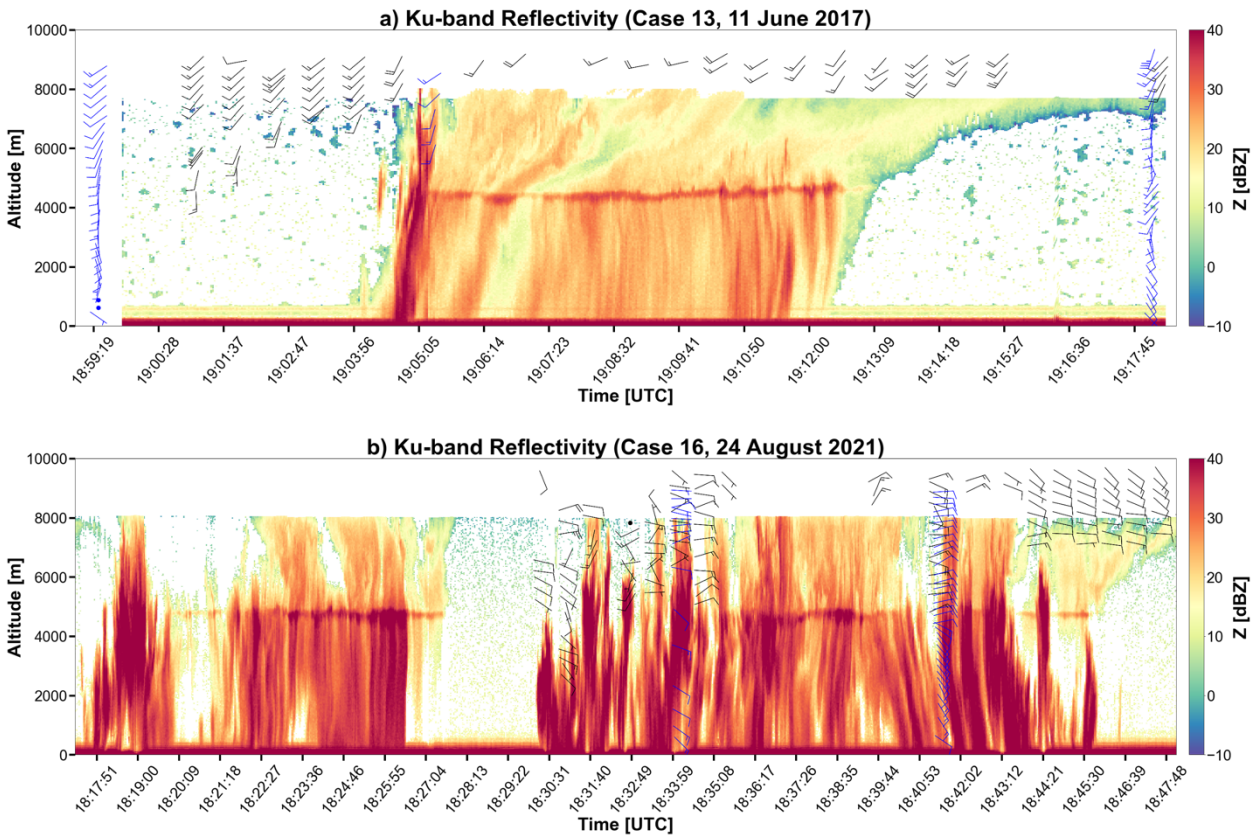

Figure 2.12: APR-3 Ku-band reflectivity profiles (fill), dropsonde wind profiles (blue barbs), and DAWN wind profiles (black barbs) for (a) Case 13 and (b) Case 16 organized cases. Case 13 has a leading line, trailing stratiform structure, while Case 16 has many embedded convective elements amongst prevailing stratiform.

For this case comparison, all dropsonde and DAWN observations for the Case 13 and Case 16 analysis were further contextualized as being collected on the moister side (i.e., within) or the drier side of (i.e., beyond) each case's synoptic-scale TPW gradient in Figure 2.11 (Figure 2.13, Figure 2.14). With Case 16 only having RH observations beyond the TPW gradient (Figure 2.13) and thus outside of the active convective environment, near-storm mean-layer RH comparisons could not be adequately performed between Case 13 and Case 16. However, vertical speed shear could still be investigated. A large spread in deep layer shear exists with considerable overlap between cases (Figure 2.14a), which results from the inclusion of DAWN measurements as in Section 2.4.1. Similarly, no clear mean-layer speed shear distinctions between cases were found for dropsondes

on the moist side of their respective TPW gradients (Figure 2.14). There is a hint of stronger PBL shear near the convection in Case 13, but Case 16 dropsondes within the TPW gradient were all in precipitating regions, thus highlighting inconsistencies in approaches to dropsonde targets across cases and campaigns. Therefore, no distinct differences in mean-layer shear with organized vertical convective structure is revealed from this case comparison, in part due to large variability in observational sampling methodology and large variability in the observations themselves.

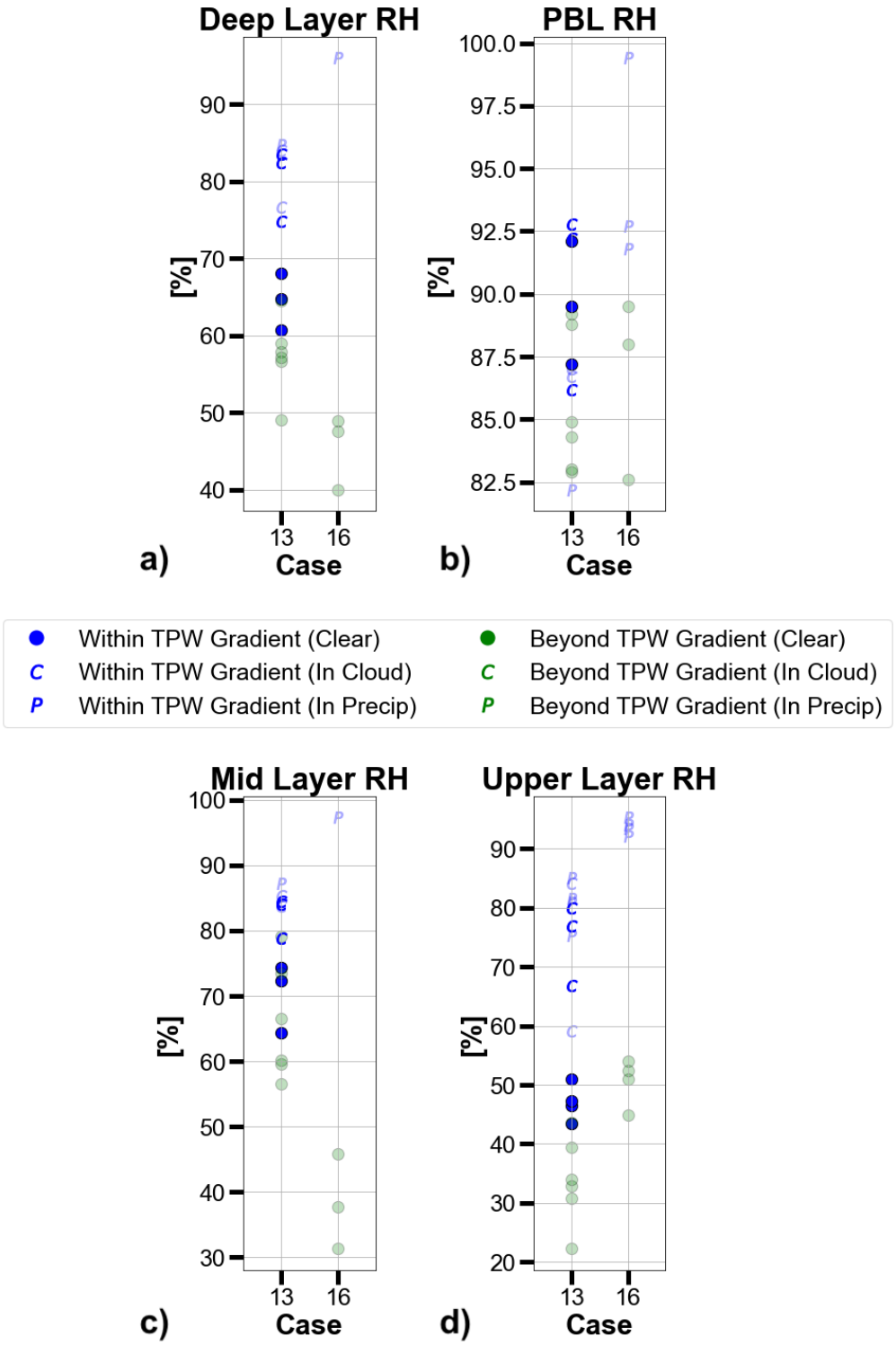

Figure 2.13: Dropsonde-derived (a) deep layer RH, (b) PBL RH, (c) mid layer RH, and (d) upper layer RH for Case 13 and Case 16. Observations are color-coded by the location of their dropsondes relative to the synoptic-scale TPW gradient, and faded points denote dropsonde observations not collected within convective inflow regions. Markers denote the convective-relative environment the dropsonde was deployed into.

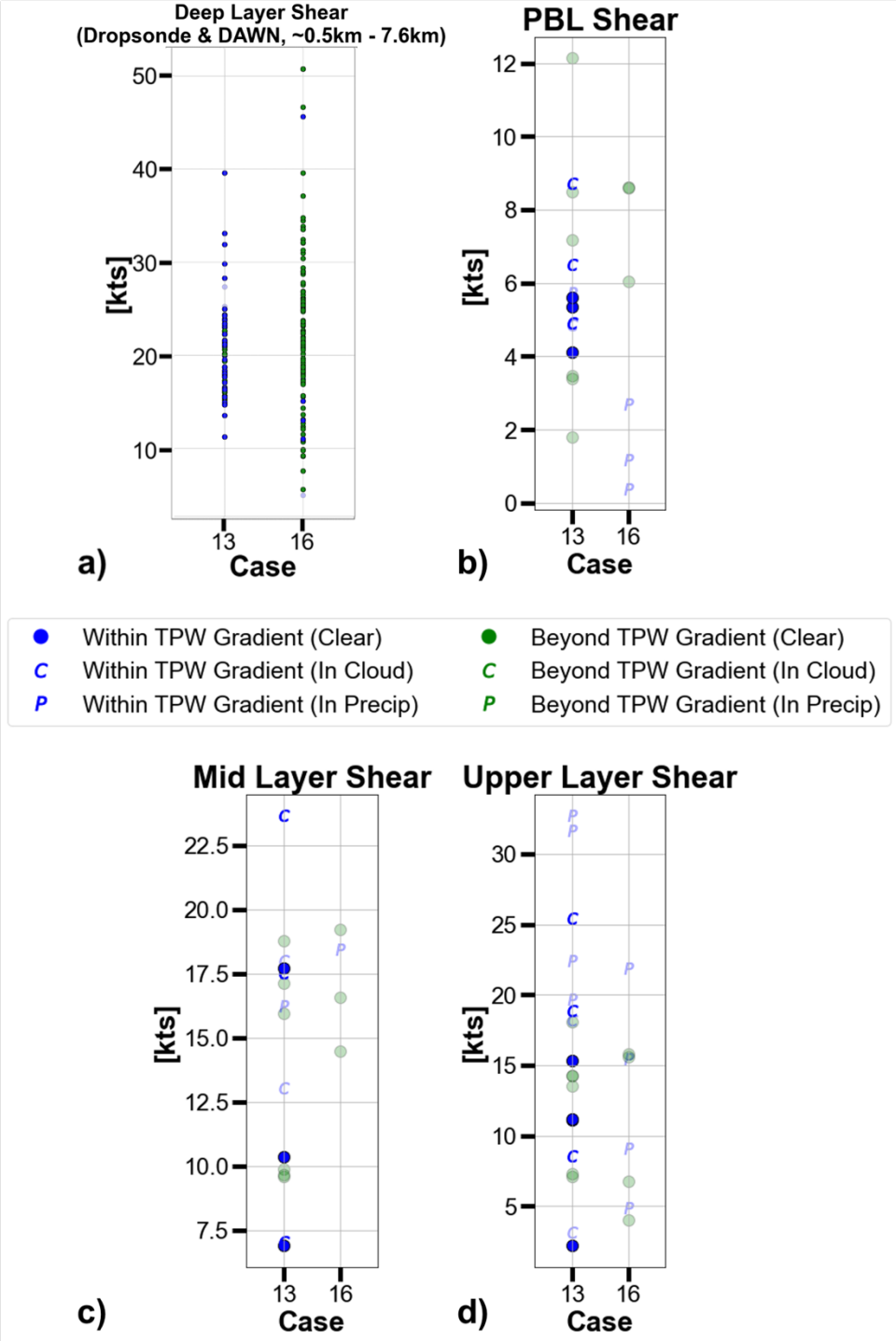

Figure 2.14: Same as Figure 2.13, except showing (a) 0.5-km – 7.6-km deep layer speed shear (DAWN observations included as well), (b) PBL speed shear, (c) mid layer speed shear, and (d) upper layer speed shear.

Without clear relationships between TOC structure and near-storm RH and wind shear from these two cases, there are additional environmental factors to consider in controlling convection formation, evolution, and intensity. Recent work (e.g., Inoue & Back, 2015; Galarneau et al., 2023) has highlighted not just the importance of moisture, but of low-level convergence in concentrating moisture and priming conditions for MCS development over tropical oceans. Incorporation of ECMWF ERA5 hourly wind convergence data (Hersbach et al., 2018) reveals the presence of mesoscale low-level (1000 hPa – 925 hPa) convergence during both Case 13 (Figure 2.15a,b) and Case 16 (Figure 2.15c,d). However, Case 16 has greater peak low-level convergence by as much as 2 x 10^{-5} s^{-1}, both at times preceding (Figure 2.15a,c) and during (Figure 2.15b,d) each case's respective peak IMERG precipitation rates. The differing near-storm peak low-level convergence magnitudes of Cases 13 and 16 motivated further analysis regarding a potential link between mesoscale low-level convergence and convective intensity.

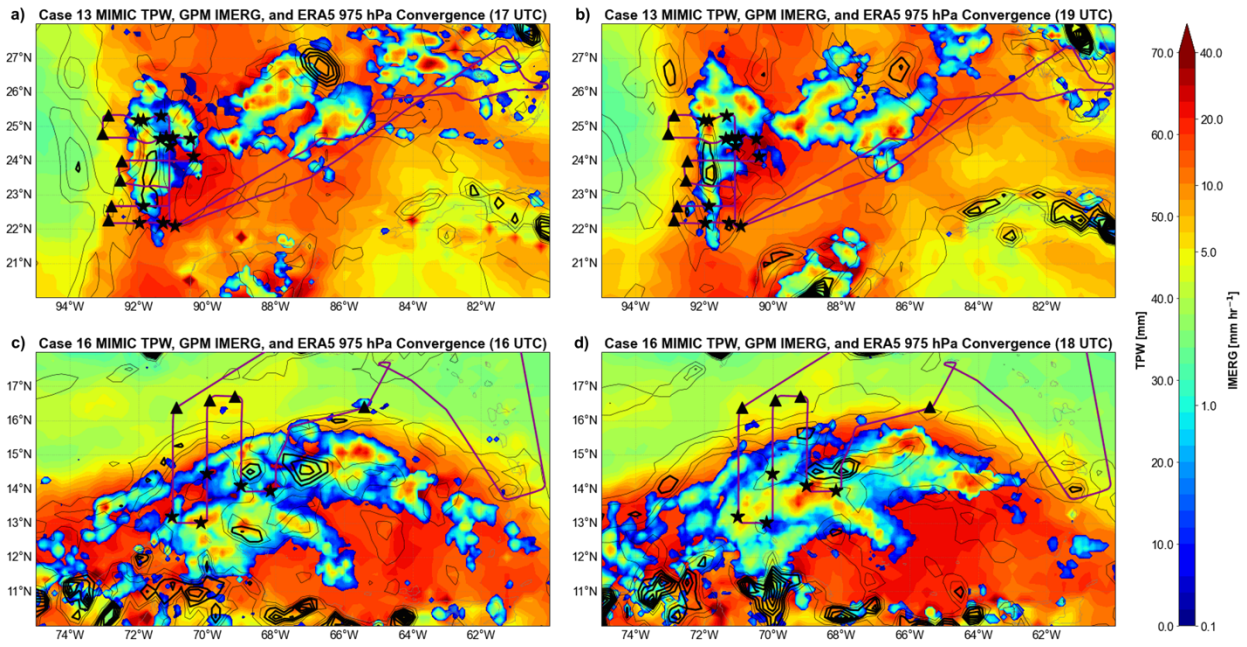

Figure 2.15: Same as Figure 2.11a, but for (a) Case 13 at 17 UTC, (b) Case 13 at 19 UTC, (c) Case 16 at 16 UTC, and (d) Case 16 at 18 UTC.

Ku-band reflectivity CFADs were again used to compare convective intensity between cases, with median, first quartile, and third quartile Ku-band reflectivity profiles providing an alternate, supporting convective intensity comparison (Figure 2.16), as in Sections 2.4.2 and 2.4.3. Case 16, with the greater peak mesoscale low-level convergence, was the more intense case, as reflected not only in the difference CFAD but by greater median and quartile Ku-band reflectivities throughout the vertical column (Figure 2.16). As such, this case comparison suggests a link between mesoscale low-level convergence magnitude and multi-core convective intensity.

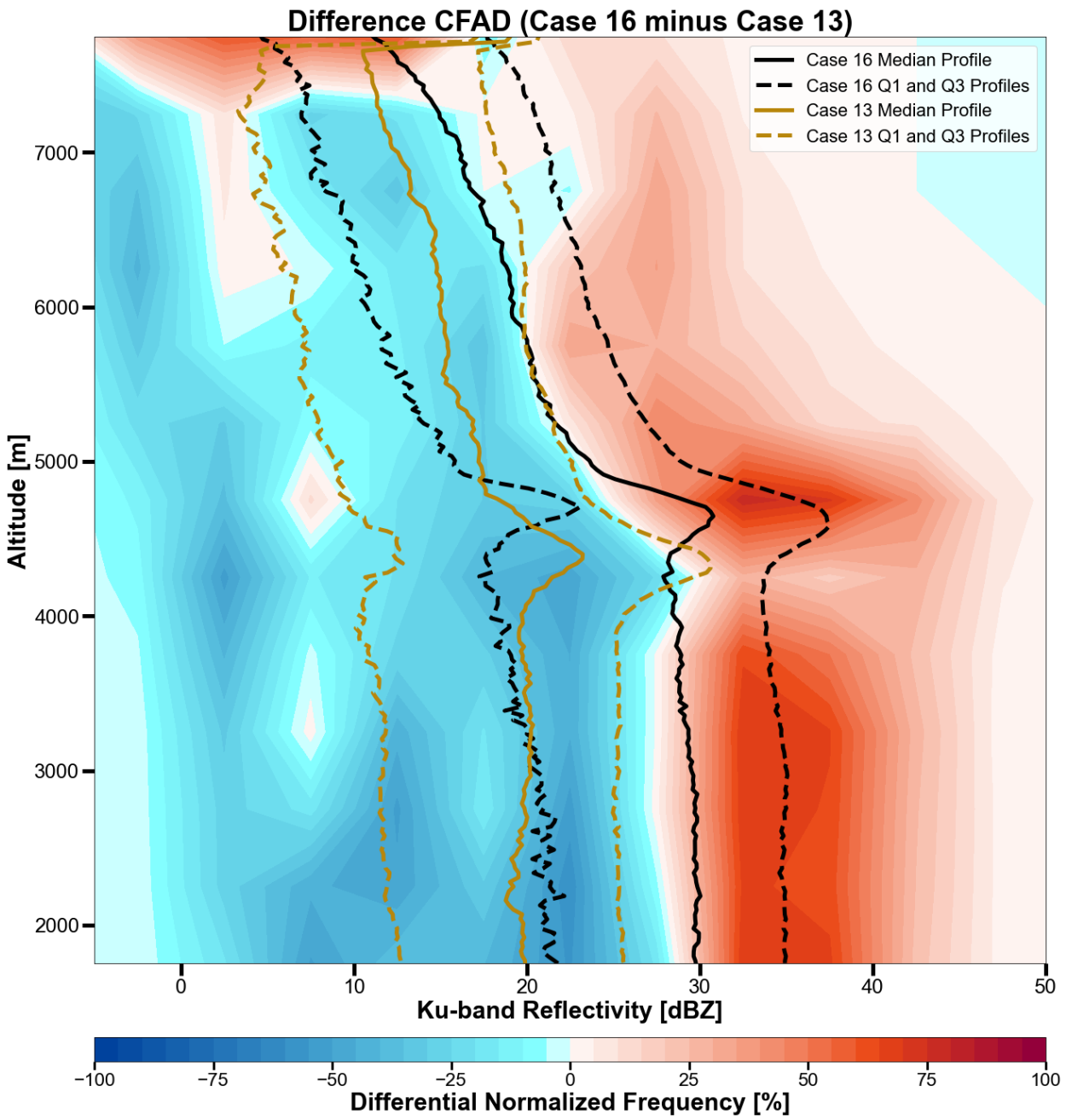

Figure 2.16: Same as Figure 2.10a, but for Case 13 and Case 16.

2.5 Discussion

The analysis presented in Section 2.4 showed that CPEX(-AW) near-storm, mean-layer environmental metrics varied widely within a given convective type and case, but notable environmental trends with convective type and intensity emerged amongst the variability. Mean-

layer RH was generally greater for organized TOC compared to isolated TOC (Section 2.4.1), which concurs with the prevailing idea that a drier tropical troposphere inhibits TOC development through enhanced dry air entrainment and negative buoyancy introduction. When evaluating convective intensity within the context of near-storm RH and CAPE, similar clear relationships were observed within the upper layers (i.e., above the melting level). More specifically, stronger organized TOC was associated with greater upper layer RH (Section 2.4.3), while stronger isolated TOC was linked to greater CAPE (Section 2.4.2). These results align with observations in the west Pacific (Cetrone & Houze, 2006 and Kingsmill & Houze, 1999, respectively) and are consistent with the concept of greater moisture and CAPE promoting hydrometeor growth through enhanced positive buoyancy. Performing a case comparison between two CPEX(-AW) MCSs forming on the moist side of strong synoptic-scale TPW gradients found greater peak mesoscale low-level wind convergence to be associated with greater convective intensity (Section 2.4.4). This finding is in line with recent literature (e.g., Inoue & Back, 2015; Galarneau et al., 2023) and the concept of low-level convergence concentrating moisture to produce more intense convection via the aforementioned mechanisms.

The result in Section 2.4.1 that PBL RH was generally greater for organized TOC compared to isolated TOC (Figure 2.5b, Figure 2.6b) is consistent with studies using CPM (Tompkins, 2001) and ERA-Interim reanalysis (Chen et al., 2017; Schiro et al., 2020) datasets, along with the prevailing idea that moister environments promote convective organization via reduced updraft dilution from dry air entrainment. Yet, the PBL RH finding differs from KWAJEX observations in the west Pacific (Cetrone & Houze, 2006), highlighting potential regional variability in these relationships. Mid and upper layer RH relationships with convective type were unclear (Figure

2.6c,d), which also differs from more conclusive observationally based studies in the west Pacific (e.g., Brown & Zhang, 1997; LeMone et al., 1998; Cetrone & Houze, 2006). The inconsistencies with other studies may be due to legitimate regional variation, but also from incorporation of observations from different convective regions and lifecycle stages (e.g., Mechem et al., 2002). Additionally, these RH trends may signify convective evolution in other ways, such as through relationships with other environmental metrics that impact convective lifecycle. For example, studies in the Indian Ocean (Savarin et al., 2014; Chen et al., 2016; Chandra et al., 2018) related drier mid-levels to greater PBL depth (via longer PBL recovery times) owing to enhanced dry air entrainment promoting stronger cold pools that can influence TOC evolution (e.g., Tompkins 2001; Feng et al., 2015; Rowe & Houze, 2015; Grant et al., 2018) and are known to vary globally over oceans (Garg et al. 2020). While the present study does not explicitly investigate cold pools, CPEX(-AW) observations do show a similar link between mid layer dryness and PBL depth ($R_{Pearson} \approx 0.537$, Figure 2.17), further highlighting the complexity in generalizing environmental moisture relationships with convective system structure.

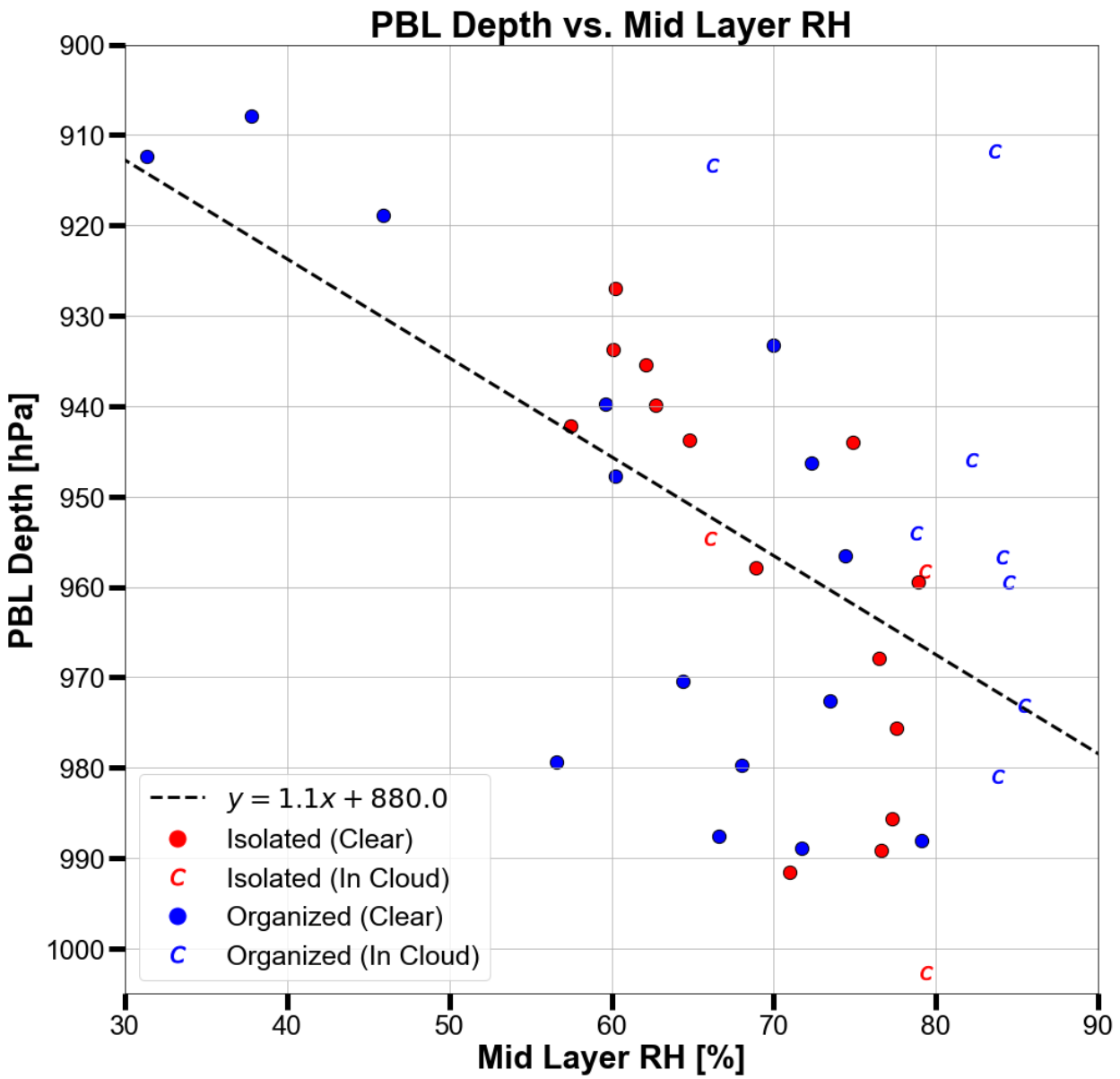

Figure 2.17: Dropsonde-derived PBL depth vs. mean mid layer RH (In Precip dropsondes excluded, dropsondes both within and outside of convective inflow regions included). Observations are color-coded by the convective type of the case they were associated with, and their markers denote the convective-relative environments their dropsondes were deployed into. A linear regression of the data is overlaid (black dashed line), with a corresponding regression coefficient of 1.1 hPa $\%^{-1}$ and a Pearson correlation coefficient of 0.537.

Consistent with previous research linking cold pools to convective lifecycle through relationships with wind shear via RKW theory (Yuter & Houze, 1995; Houze, 2018), vertical speed shear in the PBL and mid layer were generally greater for organized TOC compared to isolated TOC (Figure

2.8b,c). This finding is also consistent with prior ERA-Interim reanalysis and PISTON observational studies linking more organized convection to stronger low-level wind shear (e.g., Chen et al., 2017; Chudler & Rutledge, 2021). Differing from previous studies using CPM, reanalysis, and TOGA COARE data (Tompkins, 2001; Igel & van den Heever, 2015; Saxen & Rutledge, 2000), this CPEX(-AW) analysis did not find a clear link between deep layer shear and TOC horizontal structure (Figure 2.9b). However, previous studies, particularly those in the west Pacific, were predominately based on observations of quasi-linear TOC and thus may not be directly comparable to the CPEX(-AW) observations that sampled few quasi-linear convective systems. One example of a leading convection-trailing stratiform archetype was Case 13, which was compared with a non-linear MCS (Case 16) (Section 2.4.4). Owing to the inconsistency in reliable dropsonde observations on either side of the synoptic-scale TPW gradient, direct comparisons between the wind shear profiles between cases were inconclusive. However, a key result of this comparison was in highlighting the likely role of enhanced mesoscale low-level convergence in promoting more intense convection in the non-linear MCS (Case 16), pointing to a key component of future research.

2.6 Conclusions

Using a unique suite of collocated, high-resolution airborne observations of deep (non-tropical cyclone) TOC from the NASA 2017 CPEX and 2021 CPEX-AW field campaigns, this chapter presented an analysis of near-storm environmental relationships with 3-D TOC structure in the Gulf of Mexico, Caribbean Sea, and western Atlantic region. Large variability in near-storm mean-layer CAPE, RH, and vertical speed shear was observed amongst systems of similar convective type (isolated, organized) and also within individual convective systems. Despite this large

variability and the small sample size of 12 convective systems (4 isolated, 8 organized), notable links emerged between near-storm environmental metrics and 3-D convective structure:

- The PBL and mid layer were the layers most commonly related to horizontal TOC structure, with organized (i.e., multi-core) TOC being associated with generally greater RH and speed shear compared to isolated (i.e., single-core) TOC.
- The upper layer (i.e., above the melting level) was the layer most consistently related to vertical convective structure (i.e., TOC intensity), with more intense isolated TOC being associated with greater upper layer CAPE and more intense organized TOC being associated with greater upper layer RH.
- Greater peak mesoscale low-level convergence likely fostered more intense TOC in a comparison of two MCSs forming on the moist side of strong synoptic-scale TPW gradients.

While prior studies, combined with this chapter, find inconsistent relationships between near-storm PBL environments and TOC, this chapter and others denote the importance of PBL characteristics to the organization of TOC. A lack of similar environmental trends with TOC intensity across convective type may reflect a greater and more variable impact of multi-core TOC systems on their near-storm environments than single-core TOC systems, thereby necessitating distinguished process-level research on both types of TOC. Additionally, prior studies tend to not discuss upper layer environmental influences on TOC. The results of this chapter contend that relationships between TOC intensity and environments above the melting level should be given more attention.

With prior studies (e.g., Chen et al., 2017) showing TOC relationships with near-storm environments to vary regionally, this chapter helps address a notable regional gap in *in situ* analysis of relationships between TOC structure and near-storm environments. Consequently, the results of this chapter are specific to the Gulf of Mexico, Caribbean Sea, and western Atlantic region and cannot be confidently translated to other tropical oceanic regions. It is important to acknowledge the large variability and inconsistencies in CPEX(-AW) convection-relative spatial sampling as well, which are partly attributed to aforementioned limited sampling. The large variability and inconsistencies in spatial sampling, coupled with perhaps non-coincidental large variability in near-storm environmental metrics within both convective types and convective cases, prevent the results of this chapter from being a definitive evaluation of near-storm environmental relationships with TOC structure in the Gulf of Mexico, Caribbean Sea, and western Atlantic region.

Nevertheless, the unique capabilities of the CPEX(-AW) remote sensing instrumentation in their ability to capture essential small-scale (both spatially and temporally) near-storm environmental features and variability are highlighted in this chapter, and they serve as an important benchmark for future TOC studies. The CPEX(-AW) instrumentation, particularly DAWN, offer a glimpse into the potential of future spaceborne remote sensing, with higher resolution measurements capable of improving modeling efforts through improved process-level knowledge of tropical convection (e.g., Turk et al., 2020; Mazza & Chen, 2021), data assimilation (e.g., Cui et al., 2020; Hristova-Veleva et al., 2021; Minamide & Posselt, 2022), and model evaluation (e.g., Cui et al., 2020; Minamide & Posselt, 2022).

Future work will extend analysis of near-storm environmental relationships with 3-D TOC structure to the eastern Atlantic region using similar airborne observations from the recent 2022 NASA CPEX – Cabo Verde (CPEX-CV) field campaign. Unlike CPEX-AW, however, CPEX-CV science flights included a focus on repeated sampling of convective systems and similar storm-relative regions, providing the opportunity to better analyze and compare specific TOC regions that could not be adequately performed in this chapter.

Chapter 3

Linking In Situ Observations of Near-storm Environments to Tropical Oceanic Convective Structure from NASA CPEX-CV

3.1 Introduction

Deep convection is a prevailing feature of the atmosphere over tropical oceans and plays an important role in Earth's weather and climate on both regional and global scales (e.g., Zipser 1977; Gill, 1980; Houze, 1982; Houze, 1989; Young et al., 1995; Houze, 1997; Saxen & Rutledge, 1998; Hartmann et al., 2001; Mechem et al., 2006; Tobin et al., 2012; Del Genio & Chen, 2015; Grant et al., 2020; Bony et al., 2020; Chen et al., 2022). As such, global modeling efforts have long sought to parameterize deep tropical oceanic convection (TOC) by relating TOC structure and intensity to grid-scale environmental parameters, motivating the need to understand TOC-environment relationships. Previous studies attempting to generalize TOC-environment relationships across the tropics have noted the particular importance of tropospheric moisture and vertical wind shear (hereafter referred to as "wind shear") in influencing TOC structure and intensity. Regarding moisture, satellite (e.g., Bretherton et al., 2004), reanalysis (e.g., Chen et al., 2017; Schiro et al., 2020; Wolding et al., 2022; Chen et al., 2023; Muetzelfeldt et al., 2025), and

---

The following chapter is a reformatted preprint of Rodenkirch, B. D. & Rowe, A. K. (2025). *Journal of Geophysical Research: Atmospheres*. (In Review)

cloud-resolving model (CRM) (e.g., Tompkins, 2001) studies have linked greater mid-tropospheric moisture to larger and more intense precipitating areas, but with varying degrees of influence in context of other environmental parameters (e.g., wind shear). Meanwhile, low-tropospheric (e.g., planetary boundary layer (PBL)) moisture relationships with TOC vary in both strength and sign across studies (Tompkins, 2001; Chen et al., 2017; Schiro et al., 2020; Muetzelfeldt et al., 2025). The inconsistencies may in part be due to differing contributions of low- and mid-tropospheric inflow into TOC that vary with convective lifecycle stage (Mechem et al., 2002), necessitating contextualization of data by lifecycle stage. Similarly, wind shear relationships with TOC are inconclusive in satellite, reanalysis, and CRM studies. While some reanalysis (e.g., Igel & van den Heever, 2015; Chen et al., 2023; Roca et al., 2025) and CRM (e.g., Tompkins, 2001) studies find stronger deep layer shear to promote larger and more intense TOC systems, others suggest alternate relationships that are regionally dependent (e.g., Chen et al., 2017; Muetzelfeldt et al., 2025). Likewise, studies exist linking enhanced low-tropospheric shear to enhanced TOC intensity and structure (e.g., Anber et al., 2014; Mulholland et al., 2021) via mechanisms like RKW cold pool interactions (Rotunno et al., 1988) and increased horizontal convective mass flux from shear-induced enhanced convective inflow (e.g., Mulholland et al., 2021), while other studies contend less of an association of TOC structure with low-tropospheric shear (e.g., Grant et. al, 2018; Muetzelfeldt et al., 2025).

Inconsistencies in both wind shear and moisture relationships with TOC are likely a result of different types of datasets being used (i.e., satellite, reanalysis, CRM), varying and at times limited spatiotemporal data resolution, and regional variability (e.g., Chen et al., 2017; Muetzelfeldt et al., 2025). Field campaigns uniquely collect detailed environmental measurements near TOC systems

that can fill in spatiotemporal resolution gaps, including from reanalysis datasets that additionally rely on imperfect underlying models particularly in data-sparse regions like tropical oceans (Pincus et al., 2017; Chen et al., 2017; Wolding et al., 2022). Prior field campaigns in different tropical oceanic regions highlight regional dependencies in near-storm moisture and wind shear relationships with TOC that manifest as varying results across studies. An example is opposite relationships between PBL moisture and TOC size between the West Atlantic (Rodenkirch & Rowe, 2024) and the West Pacific (Cetrone & Houze, 2006). Additionally, some studies link enhanced low-tropospheric shear to enhanced TOC intensity and structure in the West Pacific (e.g., Alexander & Young, 1992; LeMone et al., 1998; Chudler & Rutledge, 2021) and West Atlantic (Rodenkirch & Rowe, 2024), while studies in the Indian Ocean (e.g., Guy & Jorgensen, 2014) show less of a relationship. Contributors to the regionally driven inconsistent results may be due to differing underlying organizational modes of analyzed TOC systems (e.g., quasi-linear in the West Pacific vs. non-linear in the West Atlantic), as well as large moisture and wind shear variabilities between and within individual convective environments, as observed during the NASA Convective Processes Experiment (CPEX; Chen & Zipser, 2017) and CPEX–Aerosols & Winds (CPEX-AW; Skofronick-Jackson et al., 2021) field campaigns in the West Atlantic (described in Rodenkirch & Rowe, 2024). Both factors are often linked via larger, more synoptic-scale components that vary regionally, further emphasizing the need to expand in situ studies to other tropical oceanic regions with different mesoscale and synoptic-scale characteristics.

In the tropical East Atlantic, regional modulation of environmental variables connected to African Easterly Waves (AEWs) is known to influence TOC prevalence, structure, and intensity (e.g., Cifelli et al., 2010; Guy et al., 2011; Wolding et al., 2020; Vargas Martes et al., 2023). Based on

wave interactions with coincident climatological features like the West African monsoon, trade winds, and African Easterly Jet, TOC has been shown to preferentially develop in certain sectors of AEWs. More specifically, studies have found locations along wave axes to be more favorable for development of more intense TOC due to the presence of moister air better protected from westerly low- and mid-tropospheric dry air intrusions (Janiga & Thorncroft, 2016; Brammer & Thorncroft, 2017; Núñez Ocasio et al., 2020). Additionally, regional modulation of dynamical convergence by AEWs has been attributed to TOC structure and intensity, with prior studies commonly linking enhanced lower tropospheric mesoscale convergence to increased convective updraft and precipitation intensity by way of enhanced column moisture flux and mass continuity (e.g., Lindzen & Nigam, 1987; Banacos & Schultz, 2005; Back & Bretherton, 2009; Inoue & Back, 2015; Raymond & Fuchs-Stone, 2021; Galarneau et al., 2023; Rodenkirch & Rowe, 2024; Feng et al., 2025; Muetzelfeldt et al., 2025). This relationship scales upwards to the synoptic scale, with more intense TOC having been located in regions ahead of the wave trough where lower tropospheric convergence was enhanced (e.g., Cifelli et al., 2010; Tomassini, 2018).

Despite the considerable impact of AEWs on TOC, high-resolution in situ TOC sampling is rare in the tropical East Atlantic. To address this observational need, the NASA CPEX—Cabo Verde (CPEX-CV; Zawislak et al., 2022; Nowottnick et al., 2024) field campaign operated for four weeks in September 2022 out of Sal Island using the DC-8 aircraft equipped with modern remote sensors and in situ data collection. Among this airborne instrumentation suite was a triple-wavelength airborne precipitation radar, a Doppler wind lidar, and dropsondes. Together, these instruments collected rare, coincident, high-resolution environmental data near convective systems suitable to study TOC across a range of local environmental conditions, including within influential AEWs.

Given the uniqueness of this suite of observations, the CPEX-CV field campaign presents an exceptional opportunity to analyze tropical East Atlantic near-storm environmental relationships with TOC. In this chapter, we aim to address: *how does TOC structure relate to the near-storm environment in different tropospheric layers in the tropical East Atlantic?*

To address this research question, the organization of the chapter is as follows. Section 3.2 offers a description of the CPEX-CV instrumentation, data, and methods used for the analysis. Section 3.3 presents the results of the CPEX-CV analysis, while Section 3.4 provides a discussion of the results in the context of regional variability, particularly with regard to an analysis using similar instrumentation data over the West Atlantic during the prior CPEX and CPEX-AW (hereafter referred to as CPEX(-AW)) field campaigns (Rodenkirch & Rowe, 2024). Section 3.5 concludes the chapter with main takeaways from the analysis and next steps for future research.

3.2 Data and Methods

3.2.1 CPEX-CV Overview

The CPEX-CV field campaign (Zawislak et al., 2022; Nowottnick et al., 2024) executed thirteen science flights during a 4-week span over the East Atlantic in September 2022 using the NASA DC-8 research aircraft. Three of six airborne science instruments aboard the DC-8 were used for this chapter: the Third-Generation Airborne Precipitation Radar (APR-3; Sadowy et al., 2003), the Doppler Aerosol WiNd Lidar (DAWN; Kavaya et al., 2014), and dropsondes. Combined, these three instruments provided rare, coincident measurements of 3-D convective structure, moisture, and winds (e.g., Figure 3.1) at vertical resolutions high enough to analyze near-storm characteristics within different layers of the troposphere. Within the thirteen science flights, 22

distinct deep precipitating TOC systems (or cases, as hereafter referred) were sampled within a variety of synoptic environments, including AEWs, the ITCZ, and just off the West African coast. Omitting one observed TOC system (Case 19) due to its association with Tropical Storm Hermine, as this chapter is focused on non-tropical cyclone-related TOC, subsequent analysis focuses on the remaining 21 TOC systems (Table 3.1). For more information about the CPEX-CV field campaign, especially regarding other instrument payloads and flights not discussed in this chapter, the authors refer readers to Nowottnick et al. (2024).

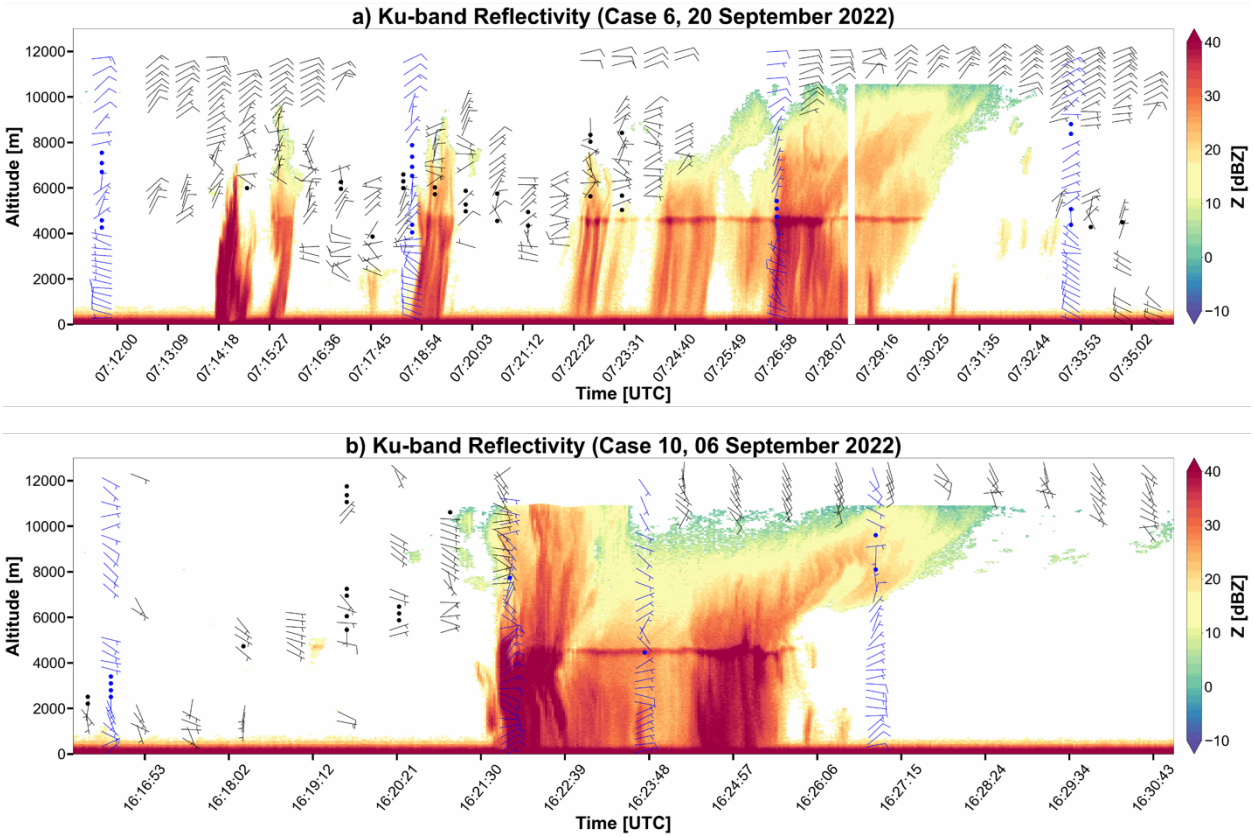

Figure 3.1: APR-3 Ku-band reflectivity profiles (fill), dropsonde wind profiles (blue barbs), and DAWN wind profiles (black barbs) for an (a) isolated and (b) organized TOC system observed during CPEX-CV.

Table 3.1: CPEX-CV convective cases used for analysis in this chapter, sorted by convective type. The time of day, lifecycle stage, and broader environment during convective sampling is denoted for each case. The number of associated near-storm dropsonde profiles (total, partial, inflow) for each case is provided with dropsonde deployment environment.

Case	Date	Convective Type	Time of Day	Broader Environment	Lifecycle Stage	Number of Dropsondes (Total/Partial/Inflow)	Clear	In Cloud	In Precip
1	20220909	Isolated	Afternoon	AEW	Growing	6/1/2	4	1	1
2	20220909	Isolated	Afternoon	AEW	Decaying	8/0/7	7	1	0
3	20220910	Isolated	Afternoon	ITCZ	Mature	2/0/0	2	0	0
4	20220910	Isolated	Afternoon	AEW	Decaying	2/0/0	2	0	0
5	20220916	Isolated	Afternoon	AEW	Decaying	3/0/3	3	0	0
6	20220920	Isolated	Morning	Coast	Decaying	4/0/1	1	2	1
7	20220920	Isolated	Morning	Coast	Growing	3/0/3	3	0	0
8	20220906	Organized	Morning/Afternoon	AEW	Mature	1/1/0	0	0	1
9	20220906	Organized	Afternoon	AEW/ITCZ	Growing/Mature/Decaying	9/0/6	7	1	1
10	20220906	Organized	Afternoon	AEW	Mature	10/3/2	1	2	7
11	20220907	Organized	Afternoon	AEW	Decaying	6/0/0	2	1	3
12	20220907	Organized	Afternoon	AEW	Mature	11/1/3	5	3	3
13	20220907	Organized	Afternoon	AEW	Mature	4/0/1	3	0	1
14	20220914	Organized	Morning/Afternoon	Coast	Decaying	10/2/3	4	5	1
15	20220914	Organized	Morning/Afternoon	Coast	Mature/Decaying	12/2/2	1	9	2
16	20220916	Organized	Afternoon	AEW	Mature/Decaying	6/0/4	3	2	1
17	20220916	Organized	Afternoon	AEW	Growing	8/1/2	1	6	1
18	20220922	Organized	Morning	AEW/Coast	Mature/Decaying	13/2/8	7	3	3
20	20220926	Organized	Morning	AEW	Growing/Mature/Decaying	21/6/8	6	6	9
21	20220929	Organized	Morning/Afternoon	AEW/Coast	Mature/Decaying	10/0/4	6	4	0
22	20220930	Organized	Afternoon	AEW	Mature/Decaying	6/0/3	3	2	1

3.2.2 CPEX-CV Datasets

CPEX-CV vertical profiles of temperature, humidity, and horizontal wind velocity were collected using the NSF National Center for Atmospheric Research (NCAR) RD41 dropsondes, which employed the Airborne Vertical Atmospheric Profiling System (AVAPS) developed by Vaisala Inc. (AVAPS Dropsondes, 2025). The dropsondes provided temperature accuracy of 0.2°C at 0.01°C resolution, RH accuracy of 3% at 0.1% resolution, and horizontal wind speed accuracy of 0.5 m s^{-1} at 0.1 m s^{-1} resolution, each at a vertical resolution of 0.01 hPa that is adequate for the purposes of this chapter (AVAPS Dropsondes, 2025). Dropsonde data were processed using the NCAR Atmospheric Sounding Processing ENvironments (ASPEN) software (Greco et al., 2018;

Vömel et al., 2021; Martin & Suhr, 2021), with additional processing details provided in CPEX-CV Dropsonde (2023).

High-resolution vertical profiles of near-storm horizontal wind were also collected by the airborne DAWN instrument during CPEX-CV. Equipped with a 2.053μm, 10-Hz laser, DAWN utilizes atmospheric aerosols to measure horizontal wind components (Kavaya et al., 2014; Turk et al., 2020; Greco et al., 2020). DAWN vertical profiles of horizontal winds were collected with an accuracy of < 0.10 kts with < ~2.92 kts precision at a horizontal resolution as fine as 4-5 km (Greco et al., 2020; CPEX-CV DAWN, 2023). Vertical resolution of DAWN wind profiles is 30 m using line-of-sight wind profiles (Greco et al., 2020; CPEX-CV DAWN, 2023), though severe attenuation from opaque clouds (e.g., anvil cirrus) and middle tropospheric retrieval gaps from low aerosol concentrations (e.g., Bedka et al., 2021) sometimes resulted in more limited vertical coverage. DAWN data were processed and quality controlled using methods described in Kavaya et al. (2014), Greco et al. (2020), Bedka et al. (2021), and CPEX-CV DAWN (2023).

CPEX-CV 3-D radar reflectivity profiles were collected by the APR-3 instrument (Sadowy et al., 2003). While APR-3 collects data at W- (94 GHz), Ku- (13.4-GHz), and Ka- (35.6 GHz) bands (Durden et al., 2012; Turk et al., 2020; Rodriguez-Monje, 2023), this chapter focuses on Ku-band, which more effectively samples intense precipitation structure. APR-3 Ku-band reflectivity has a vertical resolution (i.e., an along-beam gate spacing) of 60 m and a horizontal resolution of ~730 – 800 m at 10-km range with a 5-dBZ sensitivity (Sadowy et al., 2003; Durden et al., 2012; Durden et al., 2020). APR-3 Ku-band calibration uncertainty for CPEX-CV is estimated at 1 dB (Rodriguez-Monje, 2023).

3.2.3 Convective Case Characterization

Each of the 21 sampled TOC cases was categorized as either an isolated or organized convective system (Table 3.1). Using the Integrated Multi-satellitE Retrievals for GPM (IMERG) satellite surface precipitation estimation product (Huffman et al., 2019) in accordance with the methodology of Rodenkirch & Rowe (2024), isolated TOC was defined as horizontally small, single-core precipitating systems (e.g., Figure 3.2a) while organized TOC was defined as larger, multi-core precipitating systems (e.g., Figure 3.2b). Additionally, each case was characterized by convective lifecycle stage(s) (growing, mature, decaying) during the time of sampling using the Tracked IMERG Mesoscale Precipitation Systems (TIMPS) tracker (Russell, 2022; Rajagopal et al., 2023). Archived GOES-East IR COLOR imagery and APR-3 reflectivity scans through the convection aided in lifecycle characterization based on convective and stratiform components, as described in Rodenkirch & Rowe (2024). For example, the convection in Figure 3.1a was defined as decaying due to the predominant presence of weak stratiform, while the convection in Figure 3.1b was defined as mature due to presence of deep convective elements with strong stratiform. The broader environment for which each TOC case was associated with (i.e., within AEWs, the ITCZ, coastal) was also noted (Table 3.1). The time of day during sampling was denoted for each case as well (Table 3.1), though due to the focus of this chapter being on general relationships between the near-storm environment and TOC characteristics, diurnal variance is not expected to affect results of this chapter.

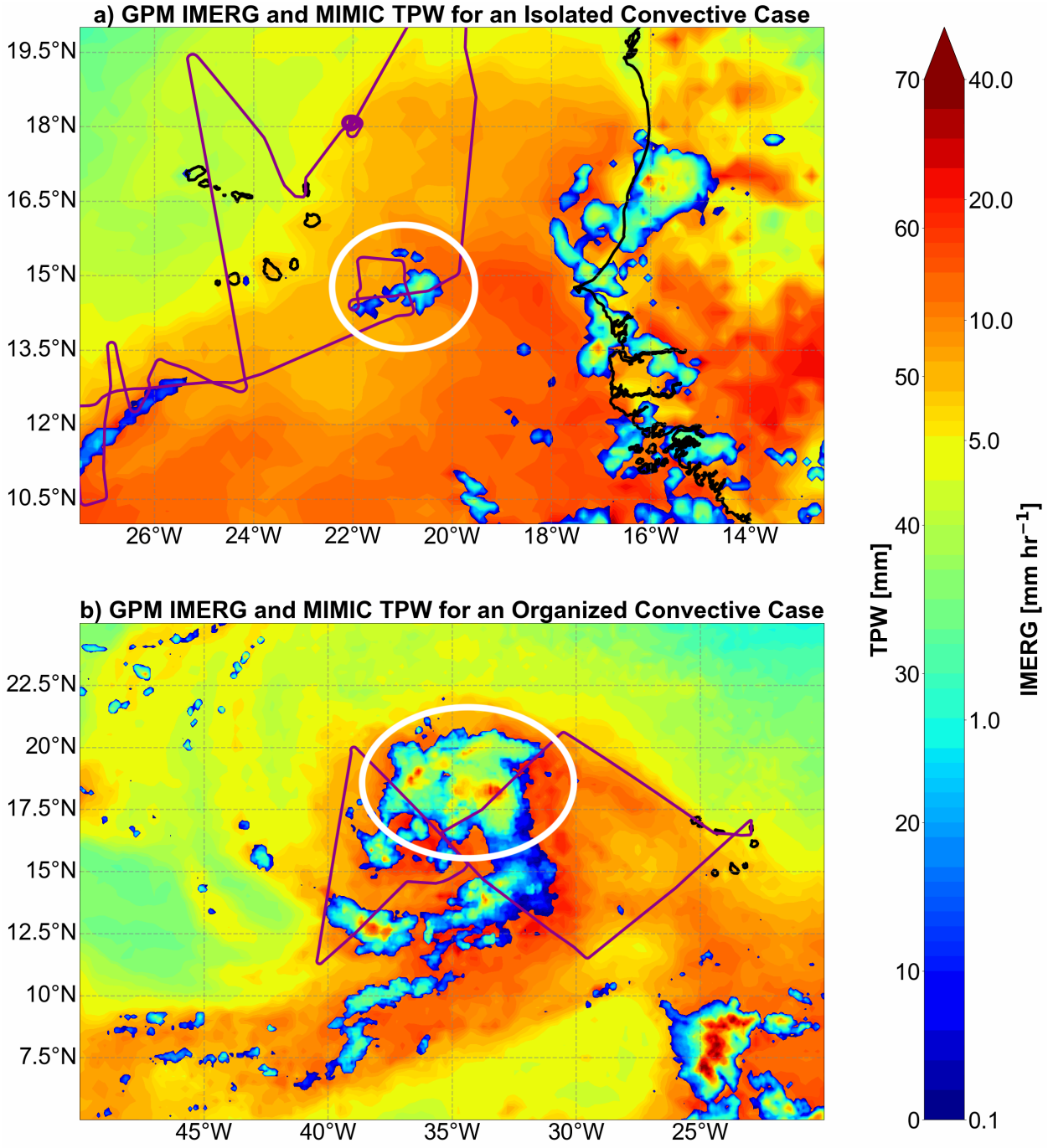

Figure 3.2: An example of (a) isolated and (b) organized TOC sampled during CPEX-CV (circled in white), as defined by GPM IMERG precipitation area and continuity. CPEX-CV science flight tracks are overlaid in purple. Black outlines denote land.

3.2.4 Dropsonde Characterization and Mean-layer, Near-storm Environmental Metrics

To relate TOC structure to near-storm environments, "near-storm" observations are defined in this chapter as in Rodenkirch & Rowe (2024) as being collected within ~10 minutes of flight time–or conservatively within ~150 km–of actively precipitating regions, which translates to closer distances to full convective cloud structures including anvil cirrus. Given this definition, 155 total dropsondes across the 21 CPEX-CV TOC cases (Table 3.1) qualified as near-storm observations, including 19 partial profile dropsondes with notable data gaps from GPS transmission issues. Each of these dropsondes was characterized by the convective type of its respective case, along with the convective lifecycle stage at the time of deployment as described in Section 3.2.3. While subsequent dropsonde analysis in Section 3.3 includes observations from all lifecycle stages, separate analysis was performed excluding the decaying stage, such to focus more on growing and mature stage environments that develop and sustain TOC. This complementary analysis produces similar results to that including all lifecycle stages, however, and is thus not shown.

In addition to convective type and lifecycle stage, the convective-relative environment each dropsonde was deployed into (i.e., Clear, In Cloud, In Precip) was recorded using similar methodology as Rodenkirch & Rowe (2024). The distribution of dropsondes across convective-relative environment for each case can be seen in Table 3.1. Examples of Clear (16:16:26 UTC), In Cloud (16:26:55 UTC), and In Precip (16:21:54 UTC, 16:23:45 UTC) dropsondes are shown in Figure 3.1b. Notably, 36 dropsondes deployed in regions actively precipitating at the surface (i.e., In Precip dropsondes) were excluded from moisture analysis, as their extensively saturated

moisture profiles were not representative of the surrounding environment influencing the convection.

Dropsondes deployed in convective inflow regions were also noted and chosen as the primary focus of observational analysis for this chapter owing to their sampled inflow environments likely influencing TOC more than non-inflow environments. To identify dropsondes in convective inflow regions, mean storm velocity of each convective case was first determined using the TIMPS tracker (Russell, 2022; Rajagopal et al., 2023). Given the potential of convective inflow to originate from both the low- and middle-troposphere (e.g., Mechem et al., 2002), both low- (975 hPa – 925 hPa) and mid- (900 hPa – 700 hPa) tropospheric mean wind velocities were then calculated for each dropsonde associated with a given convective case. At each dropsonde location, storm-relative motion vectors for the low- and middle-troposphere were subsequently calculated, and dropsondes that captured an inflow region in either layer were characterized as inflow dropsondes, of which there were 62 across the 21 convective cases.

Following dropsonde characterization, mean RH and wind shear were calculated for each dropsonde for four distinct tropospheric layers consistent with Rodenkirch & Rowe (2024): the PBL, mid layer (PBL top – melting level), upper layer (melting level – 7622.5 m, or ~400 hPa), and deep layer (near-surface – 7622.5 m). Notably, RH and wind shear were not calculated for partial profile dropsondes in layers with extensive data gaps. Dropsonde wind shear observations were supplemented with spatiotemporally denser near-storm DAWN wind shear, as described in Rodenkirch & Rowe (2024). Due to the absence of temperature and moisture measurements in DAWN necessary to define aforementioned layer thresholds, along with low signal-to-noise ratio

(i.e., noisy) near-surface data, 500 m - 7622.5 m deep layer shear was the only DAWN shear calculated. An alternate 500 m - 7622.5 m dropsonde deep layer shear was added in response for consistency with the DAWN deep layer shear definition.

3.2.5 Contoured Frequency by Altitude Diagrams

Analysis of convective intensity was executed using Contoured Frequency by Altitude Diagrams (CFADs; Yuter & Houze, 1995; Zagrodnik et al., 2019), following the methodology of Rodenkirch & Rowe (2024). 2-D histograms of APR-3 Ku-band reflectivity (5-dBZ bins) and altitude (0.5-km bins) for each convective case were normalized by the maximum bin count in *each* altitude interval to create the CFADs, with radar reflectivity intensity from hydrometeors serving as a proxy for convective updraft intensity (e.g., Zipser & Lutz, 1994; Zipser et al., 2006; Heymsfield et al., 2010; Ni et al., 2019). CFADs were generated separately for both convective and stratiform regions of storms, employing the objective Echo Classification from COnvectivity for Vertically pointing radars (ECCO-V) convective-stratiform partitioning algorithm (Dixon & Romatschke, 2022; Romatschke & Dixon, 2022).

Leveraging the reflectivity texture of a 2-D time-altitude radar scan, ECCO-V translates radar reflectivity into a metric called “convectivity” on a 0-1 scale (e.g., Figure 3.3a; Romatschke & Dixon, 2022). ECCO-V subsequently classifies the 2-D radar data into convective and stratiform echo types based on convectivity thresholds (e.g., Figure 3.3b). For this chapter, a convectivity threshold of 0.4 was used for basic convective-stratiform classification, with stratiform components identified as convectivity < 0.4 and convective components identified as convectivity ≥ 0.4. The maximum convectivity value for each Ku-band profile was used to produce a 1-D

convective-stratiform classification time series for each case (e.g., Figure 3.3c) for partitioning the Ku-band profiles (e.g., Figure 3.3d) in CFADs. Convective cases of similar convective type and lifecycle stage had their CFADs differenced from each other to create so-called “difference CFADs”, which provide insight into TOC structure and intensity differences between cases with distinctly different near-storm mean-layer environments (Yuter & Houze, 1995; Rodenkirch & Rowe, 2024).

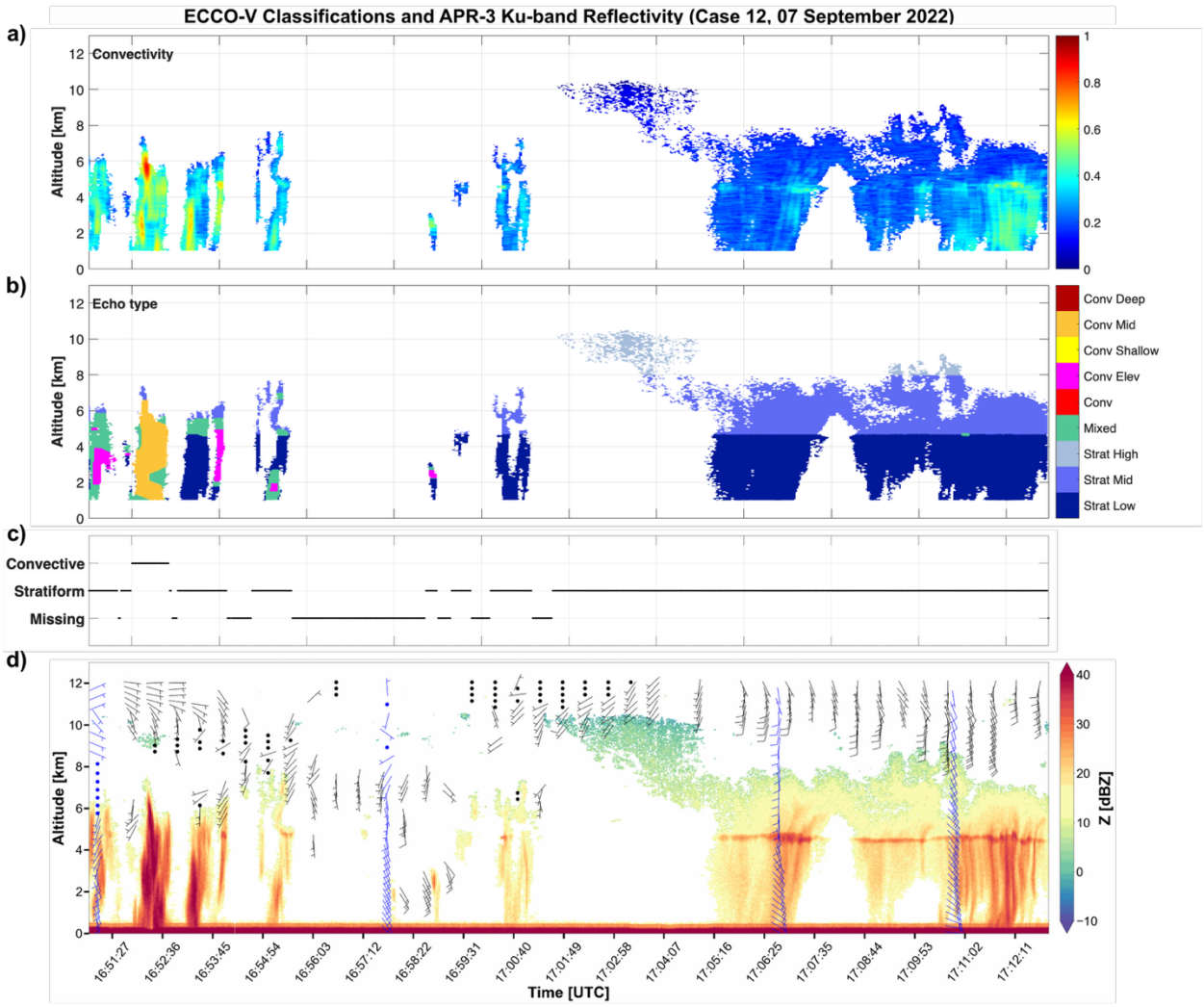

Figure 3.3: ECCO-V (a) convectivity, (b) 2-D convective echo classification, and (c) 1-D convective echo classification for (d) APR-3 Ku-band reflectivity (fill) of an organized TOC system observed during CPEX-CV. The "Missing" classification in (c) is assigned to times absent of sufficient 2-D APR-3 Ku-band reflectivity data for ECCO-V to determine a 1-D convective echo classification. Dropsonde wind profiles (blue barbs) and DAWN wind profiles (black barbs) collected during the sampling of the observed TOC system are overlaid in (d), as in Figure 3.1.

3.2.6 Convection- and AEW-relative Convergence

Convective intensity analysis from the perspective of dynamical convergence was integrated into this chapter to supplement the dropsonde and DAWN moisture and wind shear analysis. Using European Centre for Medium-Range Weather Forecasts (ECMWF) Reanalysis v5 (ERA5) (Hersbach et al., 2018) hourly wind data smoothed with a 5-point filter, low- (975 hPa) and mid-

(700 hPa) tropospheric convergence were manually calculated on a uniform 0.25° x 0.25° horizontal grid across the East Atlantic for the time periods of CPEX-CV convective science flight legs. For the duration of a given convective case's in situ sampling, probability density functions (PDFs) of low- and mid-tropospheric convergence were created within two distinct frameworks to evaluate dynamical convergence relationships with TOC intensity from the CFADs in Section 3.2.5.

Given the documented influence of mesoscale convergence on TOC (e.g., Banacos & Schultz, 2005; Inoue & Back, 2015; Galarneau et al., 2023; Rodenkirch & Rowe, 2024; Feng et al., 2025; Muetzelfeldt et al., 2025), the first framework is convection-relative, in which convergence values within a 5° x 5° box centered on the TIMPS rain rate-weighted centroid (Rajagopal et al., 2023) of a given moving TOC system were incorporated into the PDFs. The convection-relative framework provides insight into the influence of near-storm convergence on TOC intensity. However, near-storm convergence can be influenced considerably by the convection itself, particularly at later lifecycle stages when convectively coupled gravity waves (e.g., Raymond & Fuchs, 2007; Kiladis et al., 2009; Lane & Zhang, 2011; Adames et al., 2019) have had more time to propagate outwards from the convection to influence the greater local environment. To help mitigate this influence, near-storm convergence during the decaying lifecycle stage was omitted from the analysis. Ideally, convergence data during the mature phase of convection would be omitted as well, but limited CPEX-CV sampling during the growing stage made it unfeasible to filter out the mature stage. Furthermore, convection-relative box sizes of 3° x 3°, 4° x 4°, and 6° x 6° were also tested, producing similar outcomes that lend to the robustness of the results.

Acknowledging extended impacts of convergence on TOC up to the synoptic scale within AEWs (e.g., Cifelli et al., 2010; Tomassini, 2018), an AEW-relative convergence framework was employed in addition to the convection-relative framework. This framework not only provides insight into AEW synoptic-scale influence on embedded TOC, but its larger scale compared to individual convection reduces the relative influence of a given TOC system on convergence PDFs, thereby providing a better gauge of convergence influence on TOC. Within the AEW-relative framework, a CPEX-CV convective case embedded within an AEW had two separate convergence PDFs generated for it, both of which were composed of convergence data throughout the duration of in situ sampling. The first PDF contained all convergence values within a 10° x 10° box centered on the tracked AEW centroid (Lawton et al., 2022; Lawton, 2024). The second PDF contained convergence values within the half of the AEW (i.e., north, south, east, west sector) for which the TOC was embedded. This translated to roughly a 5° x 10° box, accounting for AEW horizontal asymmetry using inflection points of 5-point smoothed 700 hPa meridional wind to define the meridional wave axis (e.g., Cifelli et al., 2010) and the AEW centroid latitude (Lawton et al., 2022; Lawton, 2024) to define the zonal wave axis.

3.3 CPEX-CV Results

3.3.1 Near-storm Moisture and Wind Shear Relationships with Convective Type

To analyze how near-storm moisture and vertical wind shear relate to single- (i.e., isolated) versus multi-core (i.e., organized) TOC systems, a composite statistical approach is employed using box-and-whisker plots (e.g., Figure 3.4). As described in Section 3.2.4, near-storm dropsonde moisture and wind shear are evaluated within four distinct tropospheric layers, with particular focus given to dropsonde observations of convective inflow environments that are likely influencing TOC

more than non-inflow environments. That being said, similar trends emerge between convective type and near-storm environments when including observations from non-inflow regions. Dropsonde observations from all near-storm regions (i.e., both inflow and non-inflow) are thus additionally included in subsequent figures of this subsection.

Focusing first on moisture, organized TOC is observed to have generally greater RH in three of the four tropospheric layers of focus compared to isolated TOC. When comparing median values within inflow regions, organized TOC has slightly greater deep layer (80.8% vs. 78.1%, Figure 3.4a) and mid layer (81.2% vs. 79.9%, Figure 3.4c) RH than isolated TOC, but particularly greater upper layer (76.5% vs. 69.5%, Figure 3.4d) RH. These results concur with West Pacific (e.g., Brown & Zhang, 1997; LeMone et al., 1998; Tompkins, 2001; Bretherton et al., 2004; Cetrone & Houze, 2006; Holloway & Neelin, 2009; Chen et al., 2017; Schiro et al., 2020; Wolding et al., 2022; Chen et al., 2023) and West Atlantic (e.g., Rodenkirch & Rowe, 2024) studies of TOC, wherein greater tropospheric moisture is linked to more organized TOC. The deep layer and mid layer median RH differences between convective types do fall within the cited dropsonde moisture accuracy (3%; AVAPS Dropsondes, 2025), however, thereby translating to indistinct differences. Similarly, while isolated TOC is associated with slightly greater median RH in the PBL than organized TOC (89.1% vs. 88.1%, Figure 3.4b), the difference in median values is less than the dropsonde moisture accuracy. However, these dropsonde observations do notably convey smaller moisture variance in the PBL in near-storm environments compared to the other three layers, wherein large moisture variability exists for both isolated and organized TOC. The large moisture variability persists within each layer in individual convective cases as well (Figure 3.5), even after accounting for dropsonde deployment environment (i.e., Clear, In Cloud, In Precip). The largest

moisture variabilities notably are associated with organized TOC cases (e.g., Case 12; Figure 3.5), which given their larger sizes compared to isolated TOC, may be attributed to convective flight legs with larger spatial coverages that encompass more diverse mesoscale environments. That being said, less moisture variability exists amongst dropsondes within inflow environments (Figure 3.5), which lends further credence to focusing on inflow environments.

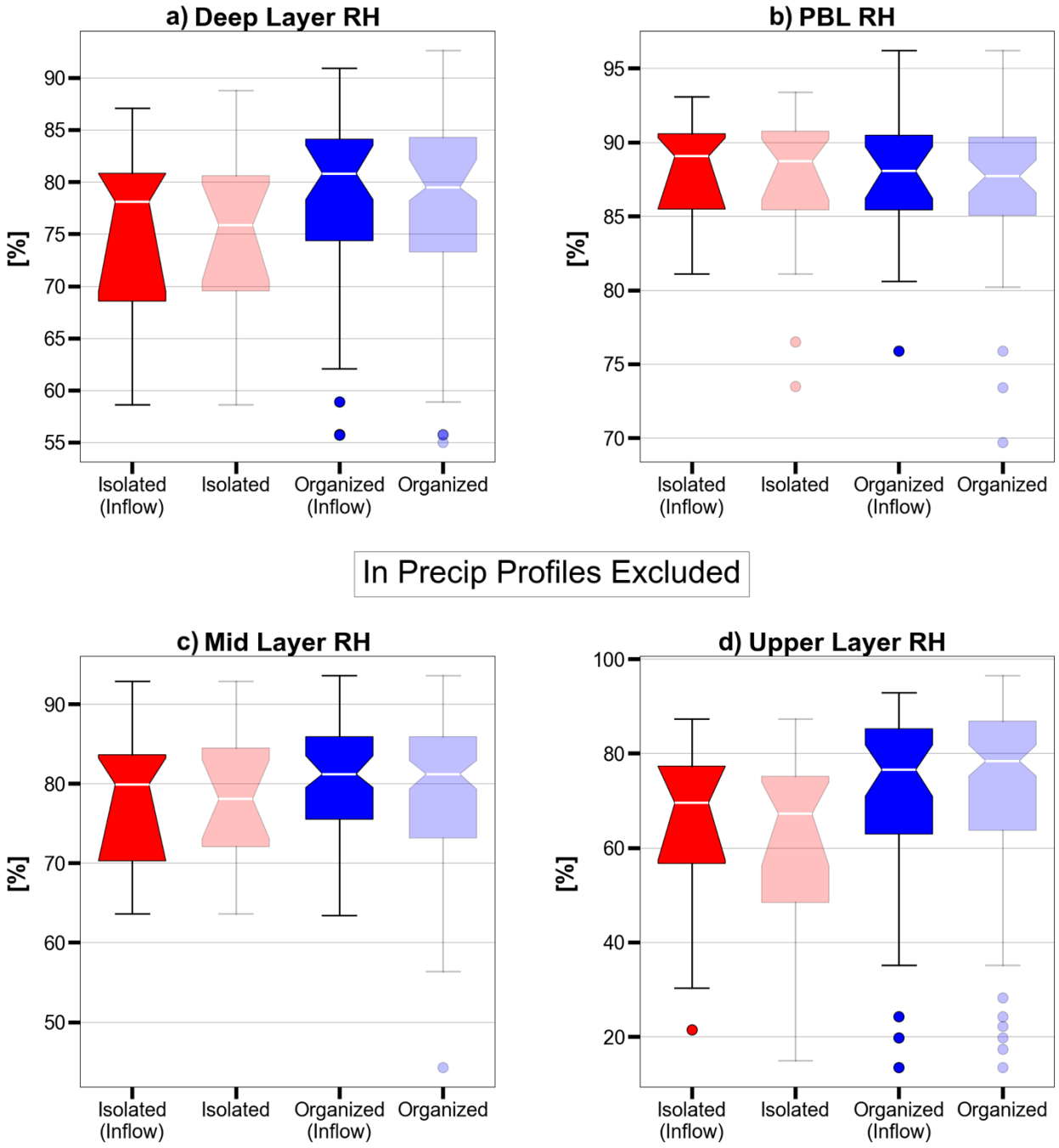

Figure 3.4: Dropsonde-derived near-storm (a) deep layer RH, (b) PBL RH, (c) mid layer RH, and (d) upper layer RH for isolated (red) and organized (blue) TOC systems sampled during CPEX-CV (In Precip profiles excluded). Faded boxes denote observations collected both within and outside of convective inflow (i.e., all near-storm) regions, while saturated boxes denote observations collected only within convective inflow regions. Each box extends from the first quartile to the third quartile of the data, with a white line at the median. Whiskers extend from the box by up to 1.5 times the inter-quartile range, and outlier points are points beyond the whiskers. Notches denote statistical significance with a 95% confidence level via bootstrapping the median 10,000 times and using a Gaussian-based asymptotic approximation.

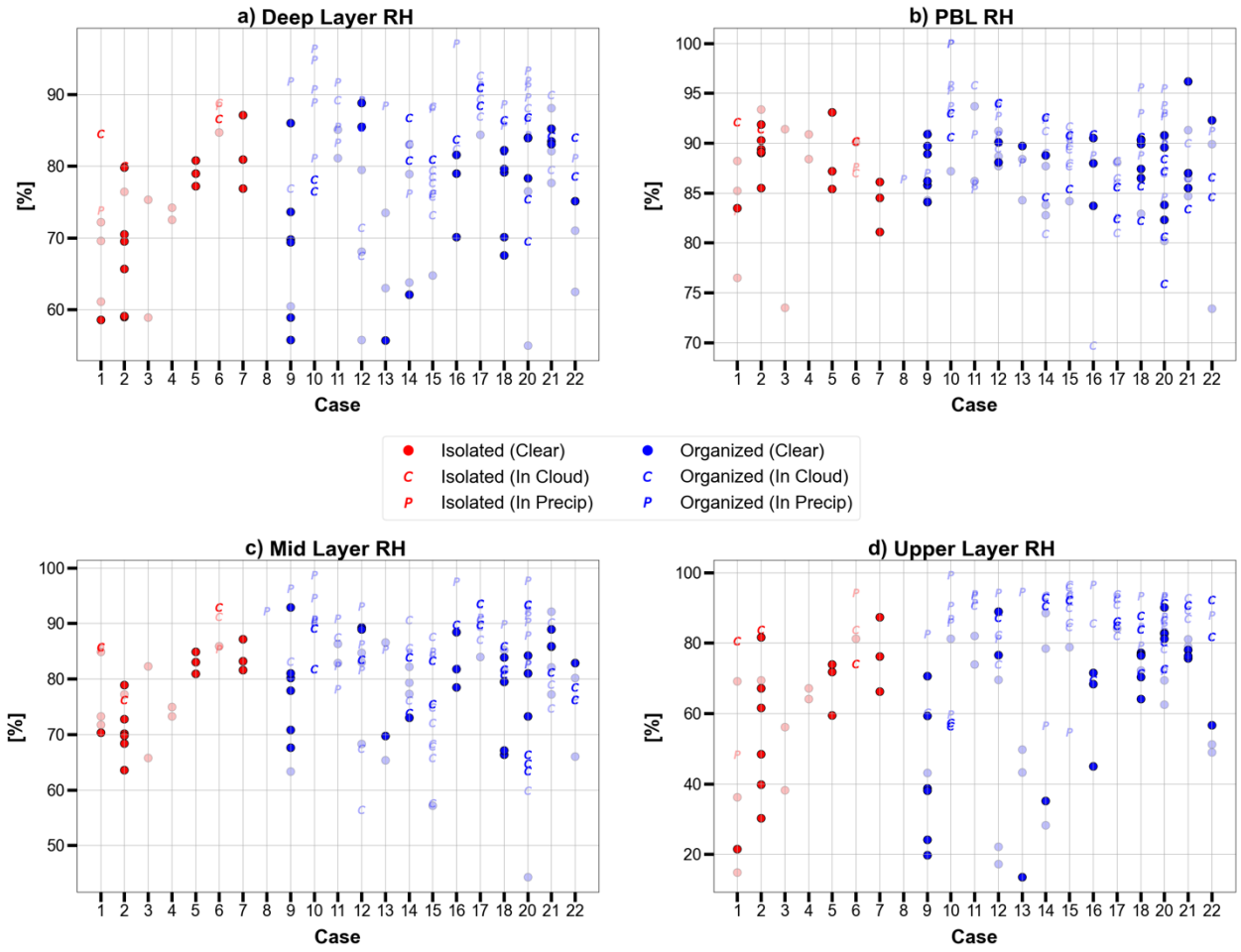

Figure 3.5: Same data as Figure 3.4, except near-storm dropsonde observations are further sorted by convective case (In Precip profiles included). Faded points denote observations not collected within convective inflow regions. Markers denote the convective-relative environment the dropsonde was deployed into.

Similar to RH, deep layer vertical wind shear is observed to be greater for organized TOC than isolated TOC, with a median value for inflow dropsondes of 16.6 kts versus 12.1 kts, respectively (Figure 3.6a). This relationship holds when integrating the spatiotemporally denser and more numerous DAWN observations (Figure 3.7a), with organized TOC having a median deep layer shear of 17.5 kts compared to 11.1 kts for isolated TOC. These results align with prior studies over the oceanic tropics (e.g., Saxen & Rutledge, 2000; Igel & van den Heever, 2015; Rodenkirch et al., 2025) that link larger and more organized TOC systems to greater deep layer shear. Meanwhile, wind shear in the PBL is greater for isolated TOC, with a median value of 6.3 kts compared to 4.7

kts for organized TOC inflow dropsondes (Figure 3.6b), which conflicts with prior studies in different tropical oceanic regions (e.g., Chen et al., 2017; Chudler and Rutledge, 2021; Rodenkirch & Rowe, 2024). Differences in mid and upper layer median shear are minimal (< 0.8 kts) between convective types (Figure 3.6c-d). However, the mid layer possesses the greatest median (12.8 kts for isolated TOC, 12.2 kts for organized TOC) and overall (36.8 kts for isolated TOC, 62.8 kts for organized TOC) shear values for each convective type within any layer. Notably, while the climatological African Easterly Jet was frequently observed within the mid layer (not shown), it is not expected to have had a notable influence on the observed large mid layer shear values, as it did not extend to the bottom nor top height thresholds used for mid layer wind shear calculation. Overall, large shear variability is found within each tropospheric layer for each convective type, though more so for organized TOC (Figure 3.6, Figure 3.7a). As with RH, the large shear variabilities in each layer extend to individual convective cases (Figure 3.7b, Figure 3.8), even when excluding In Cloud and In Precip observations that may locally enhance shear.

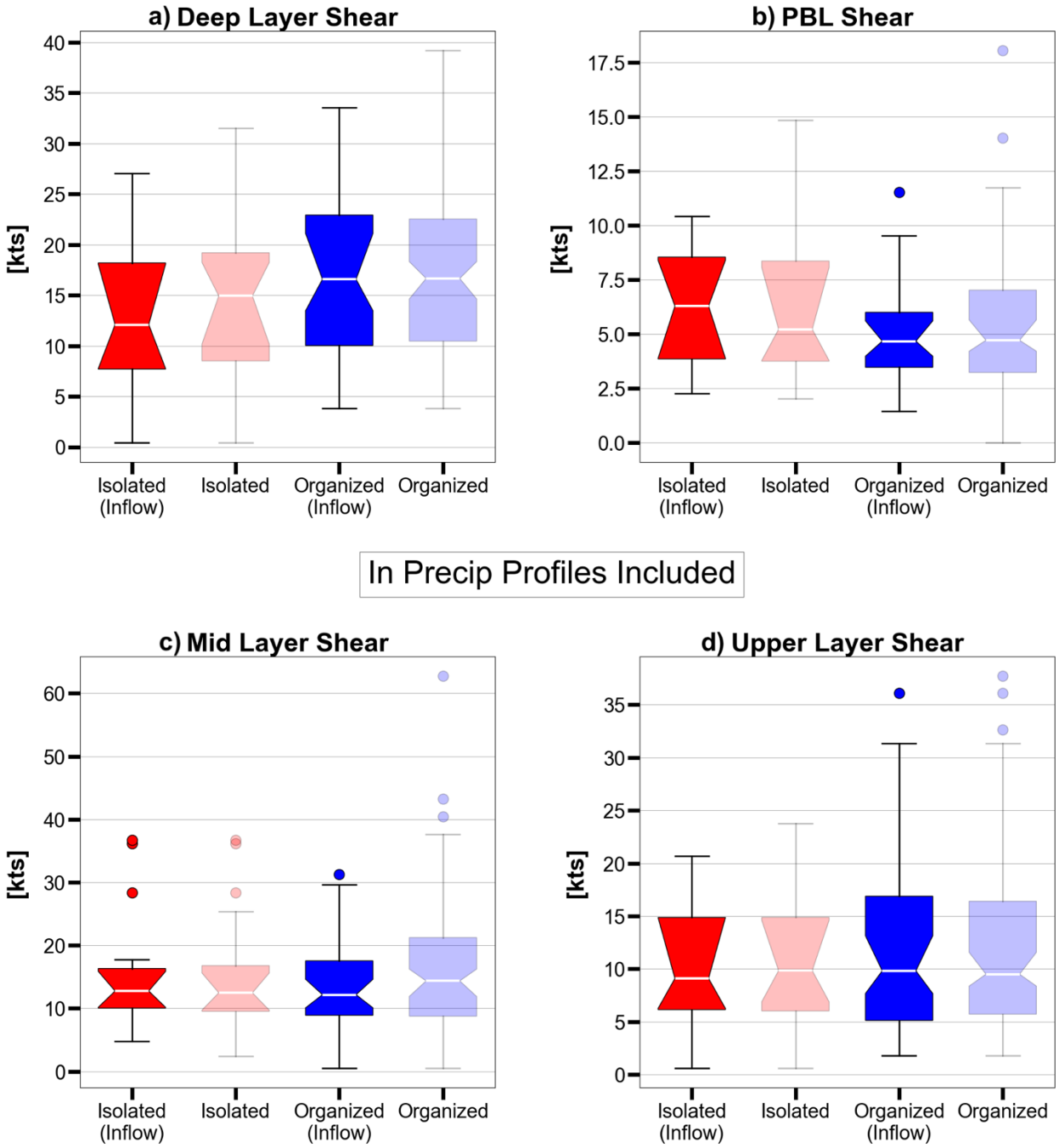

Figure 3.6: Same as Figure 3.4, except showing near-storm (a) deep layer speed shear, (b) PBL speed shear, (c) mid layer speed shear, and (d) upper layer speed shear. In Precip profiles are now included.

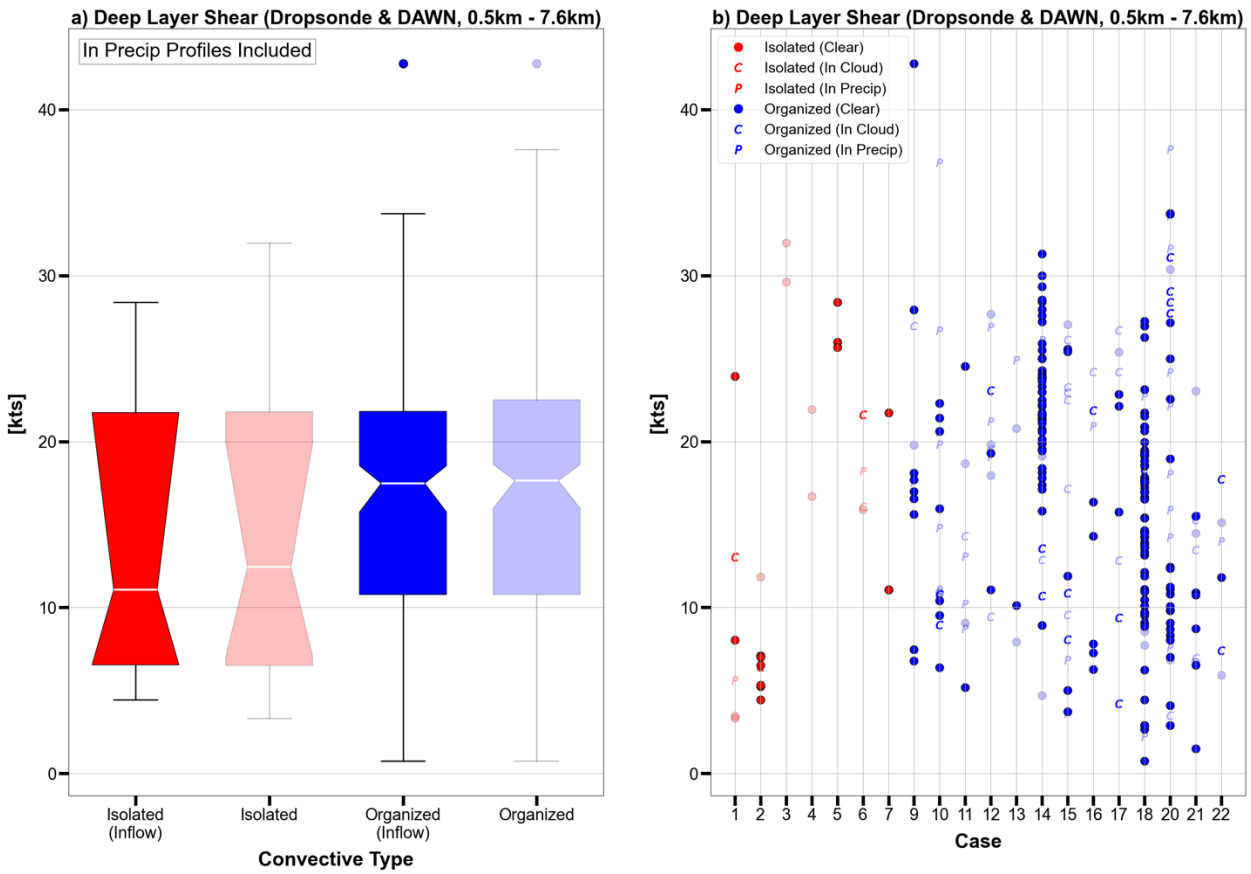

Figure 3.7: (a) Same as Figure 3.6a, except showing dropsonde- and DAWN-derived near-storm 0.5-km – 7.6-km deep layer speed shear. (b) Same as (a), except observations are further sorted by convective case. Markers denote the convective-relative environment the observation was collected in, and faded markers denote dropsonde observations not collected within convective inflow regions.

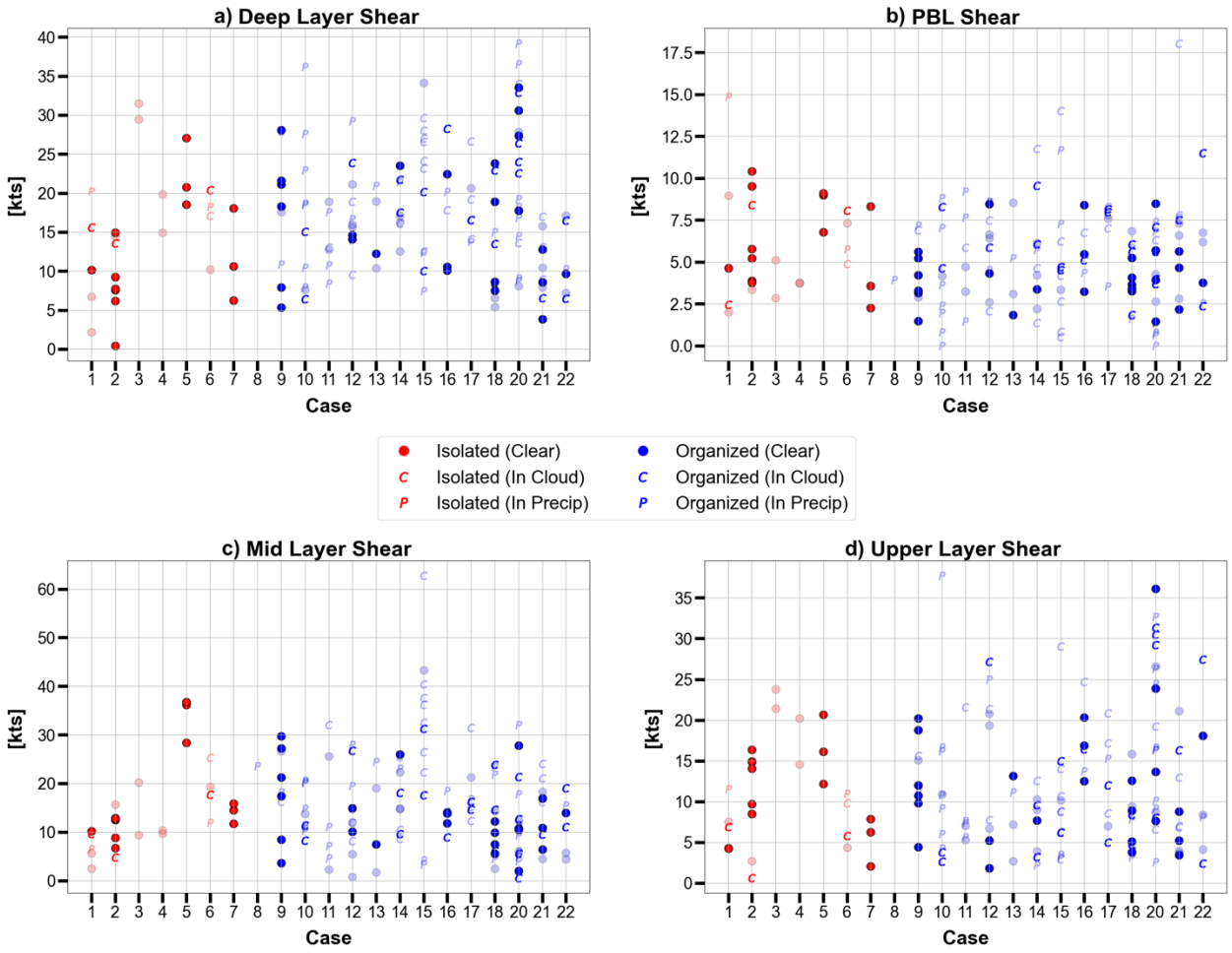

Figure 3.8: Same data as Figure 3.6, except near-storm dropsonde observations are further sorted by convective case. Faded points denote observations not collected within convective inflow regions. Markers denote the convective-relative environment the dropsonde was deployed into.

Though large near-storm moisture and wind shear variability prevail within each tropospheric layer across convective type and within individual cases, general mean-layer RH and shear trends with convective type do emerge amongst the variability. Notably, however, the results of the composite analysis are not statistically significant (as denoted by overlapping "notches" around the medians in the box-and-whisker plots), which may in part be due to the limited sample sizes of the CPEX-CV datasets. That being said, the results from this novel dataset provide insight into how near-storm moisture and wind shear relate to TOC structure in the East Atlantic. Notably, there are convective cases of similar convective type that have distinctly different near-storm

moisture and/or shear from each other (e.g., isolated Cases 2 and 7 with non-overlapping mid layer RH ranges in Figure 3.5c). As such, these cases offer the opportunity to expand the composite analysis of TOC structure to include individual case comparisons focusing on vertical convective structure, wherein TOC intensity of similar type cases can be evaluated against differing near-storm moisture and wind shear environments.

3.3.2 Near-storm Moisture and Wind Shear Relationships with Convective Intensity

For analysis of TOC intensity, CFADs of APR-3 Ku-band reflectivity were generated for each convective case implementing ECCO-V convective-stratiform partitioning (Dixon & Romatschke, 2022; Romatschke & Dixon, 2022), as described in Section 3.2.5. Subsequent difference CFADs were created between cases, allowing for evaluation of relative Ku-band reflectivity frequency differences by altitude that are a proxy for TOC intensity differences (Section 3.2.5). Difference CFADs were only produced between cases that had similar convective type, lifecycle stage, and presence of convective and/or stratiform elements in their APR-3 data, but had distinct differences in at least one mean-layer environmental metric for convective inflow regions (using Figures 3.6-3.8), with In Precip dropsondes excluded for RH. Implementing these qualifications resulted in 9 case comparisons of convective regions and 15 case comparisons of stratiform regions for near-storm RH, as well as 19 convective region case comparisons and 26 stratiform region case comparisons for near-storm wind shear.

Together, the convective and stratiform region case comparisons reflect similar TOC intensity relationships between cases, though the magnitudes and altitudes of the most pronounced intensity differences can vary (e.g., Figure 3.9, where more negative differential frequencies of high Ku-

band reflectivity across heights are found in (b) stratiform compared to (a) convective region difference CFADs between Cases 10 and 12). The case comparisons reveal no definitive links between TOC intensity and near-storm RH in the PBL and above the melting level (i.e., the upper layer). However, when distinct differences in mid layer RH exist between two cases (9 out of 24 convective and stratiform region case comparisons combined), the more intense case has a distinctly drier mid layer 8 out of 9 times. Notably, these 8 instances of drier mid layers being associated with more intense TOC are not paired with definitively greater mixed-layer nor most-unstable CAPE environments (not shown), supporting the concept of CAPE being a poor proxy for convective intensity in the tropics (e.g., Sherwood, 1999; Sobel et al. 2004; Yano et al. 2005; Elsaesser and Kummerow 2013; Schiro et al., 2020).

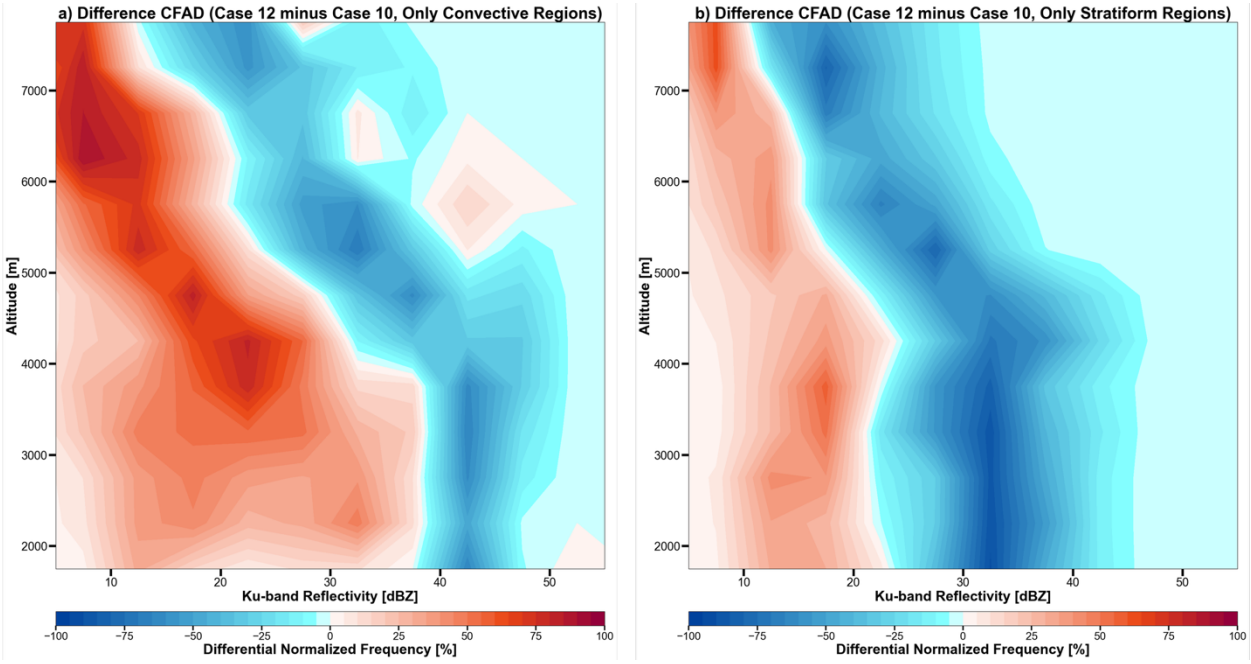

Figure 3.9: Case 10 CFAD subtracted from the Case 12 CFAD using APR-3 Ku-band reflectivity data from only (a) convective regions and (b) stratiform regions, as determined by the ECCO-V convective-stratiform partitioning algorithm. Reflectivity data is binned into 5-dBZ and 0.5-km intervals and normalized by the maximum bin count in each height interval.

Regarding wind shear, no definitive links with TOC intensity exist in the mid layer and deep layer. However, when distinct differences in PBL shear exist, albeit for only 9 out of 45 convective and stratiform region case comparisons combined, the more intense TOC system is associated with greater PBL shear 7 out of 9 times. Meanwhile, when distinct differences in upper layer shear exist (8 out of 45 convective and stratiform region case comparisons combined), the less intense TOC system is associated with greater upper layer shear 7 out of 8 times.

Overall though, the aforementioned results convey a lack of consistent moisture and shear links with TOC intensity within each tropospheric layer. As such, these findings likely reflect the presence of additional environmental influences on TOC intensity that up to this point have not been considered. Namely, the association of 16 of the 21 convective cases with AEWs behooves a supplemental investigation into how AEW dynamics, such as lower tropospheric dynamical convergence on the meso- and synoptic-scale, can influence the intensity and development of TOC in addition to near-storm moisture and wind shear.

3.3.3 Dynamical Convergence Relationships with AEW-embedded Convection from Consecutive Flights

Lower tropospheric dynamical convergence impacts on TOC intensity in the context of AEWs was investigated via an analysis of two CPEX-CV convective cases embedded within an AEW, namely Case 10 and Case 12. Cases 10 and 12 were both organized systems of roughly similar size sampled during their mature lifecycle stage on consecutive days (Figure 3.10a,b). Both cases were also embedded within the same AEW and located in the northern sector of the wave's moisture trough, seemingly shielded from intruding dry air into the southwestern sector of the wave (Figure 3.10).

These AEW dry air intrusions were common during CPEX-CV (Nowottnick et al., 2024), and along with the general moisture gradients surrounding AEWs (e.g., Figure 3.10), are likely responsible for the large near-storm moisture variabilities observed within each convective type and case (particularly organized TOC) in Section 3.3.1. In addition to their similar AEW-relative locations and sizes, both Case 10 and Case 12 have similar mean-layer wind shear distributions (Figure 3.7b, Figure 3.8), as well as similar lower tropospheric moisture distributions in inflow environments (i.e., PBL RH of 88-94% in Figure 3.5b and mid layer RH of 81-90% in Figure 3.5c) that are moister on average than most other organized cases. However, Case 10 is notably more intense than Case 12, as represented by negative differential frequencies of Ku-band reflectivity across the majority of altitudes in Figure 3.9. All of the aforementioned similarities between the two cases with still markedly different intensities provide a particularly unique opportunity to investigate potential influences of lower tropospheric dynamical convergence on TOC intensity under the umbrella of AEW dynamics.

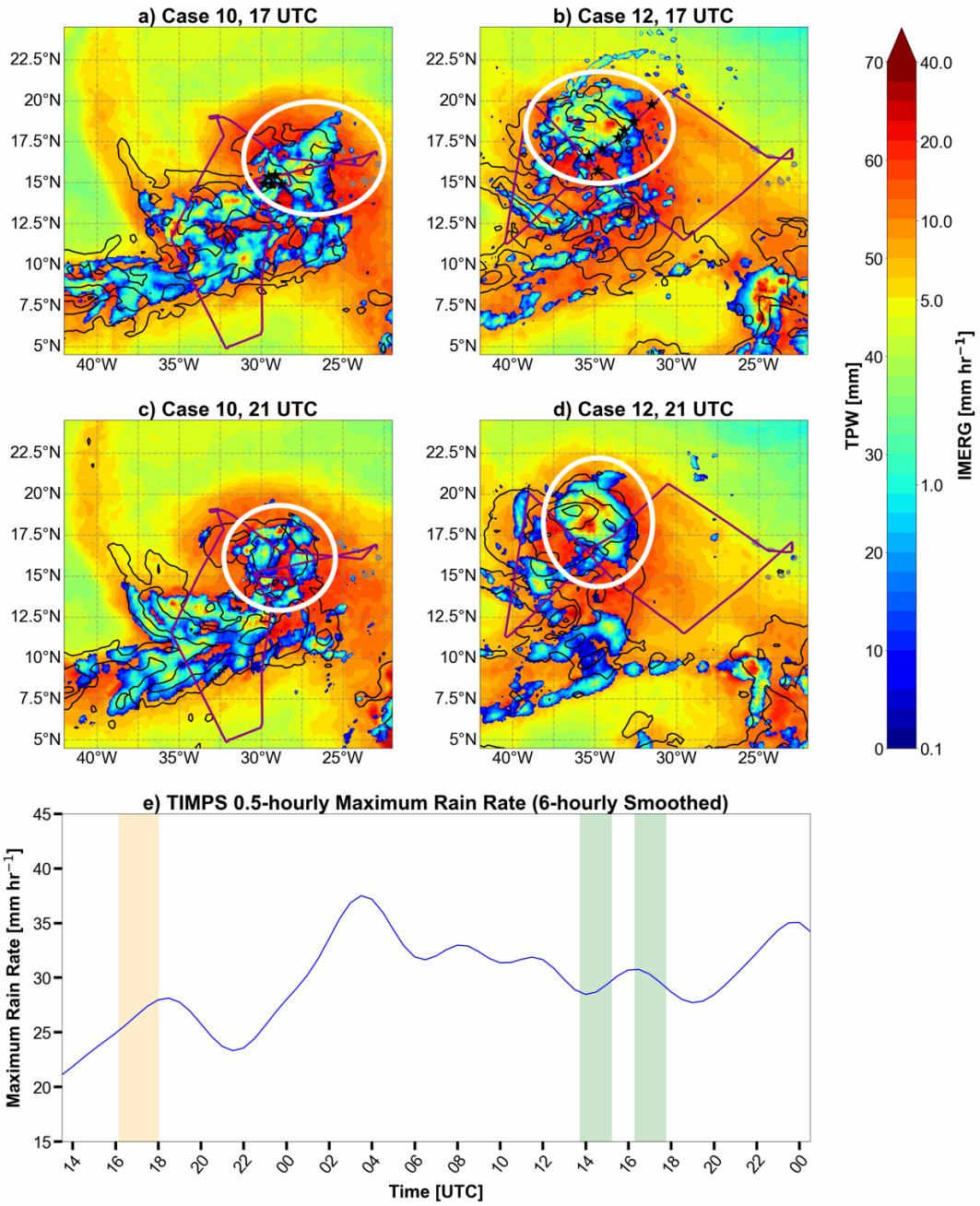

Figure 3.10: Hourly MIMIC total precipitable water (bottom layer fill), half-hourly averaged GPM IMERG surface precipitation estimation (top layer fill, averaged from the half hour preceding the listed time), ECMWF ERA5 hourly surface precipitation rate (black contours, contoured at 0.1, 1.0, 5.0, 10.0, 20.0, and 40.0 mm hr^{-1}), and DC-8 science flight track (purple line, full flight) for (a) Case 10 at 17 UTC, (b) Case 12 at 17 UTC, (c) Case 10 at 21 UTC, and (d) Case 12 at 21 UTC. Each convective case is circled in white in its respective panels, and black stars denote dropsondes deployed within the given hour. Thin gray outlines denote land. (e) TIMPS-derived maximum rain rate time series for Cases 10 and 12, which were tracked by TIMPS as the same convective system. Half-hourly values are smoothed using a 6-hourly Gaussian-based filter. Orange and green shading denote the time ranges of CPEX-CV in situ sampling for Case 10 and Case 12, respectively.

Lower tropospheric dynamical convergence is first examined using a convection-relative framework (Section 3.2.6), wherein the mesoscale impacts of convergence on TOC intensity are inferred. PDFs of manually calculated convergence from ERA5 wind data are created using a 5° x 5° box centered on, encompassing the majority of (Figure 3.10), and following each TIMPS-tracked TOC system during their growing and mature lifecycle stages (Figure 3.11). Collocation of ERA5 and TIMPS-utilized IMERG surface rain rate locations was confirmed for each TOC system (e.g., Figure 3.10), giving confidence that utilized ERA5 convergence values were representative of reality. Through this framework, the more intense Case 10 is associated with weaker near-surface (975 hPa) convergence (0.83×10^{-5} s^{-1} vs. 1.20×10^{-5} s^{-1} means) and lower free tropospheric (700 hPa) convergence (0.14×10^{-5} s^{-1} vs. 0.53×10^{-5} s^{-1} means) than the less intense Case 12. There is likely a non-negligible influence of the convection on the convergence incorporated into the PDFs at this scale, so a synoptic-scale AEW-relative framework is also applied given that both Case 10 and 12 are located in roughly the same sector relative to the wave trough.

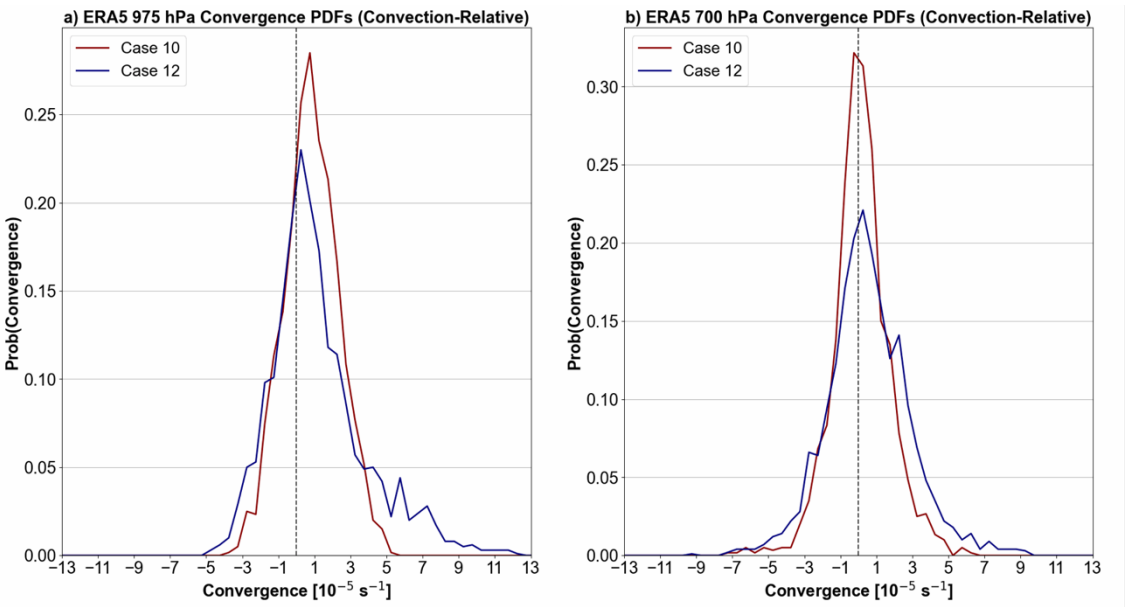

Figure 3.11: Convection-relative probability distribution functions of ERA5 convergence at (a) 975 hPa and (b) 700 hPa for Case 10 (red) and Case 12 (blue). Convergence is binned every 0.5 x 10^{-5} s^{-1} using only data within a 5° x 5° box centered around each propagating convective case's TIMPS-identified rain rate-weighted centroid during TIMPS-identified growing and mature convective lifecycle stages.

Using the AEW-relative framework (Section 3.2.6), convergence boxes encompassing the full wave trough (i.e., a 10° x 10° box) and the northern sector of the wave trough (i.e., a 5° x 10° box where Cases 10 and 12 predominantly reside) are the focus of analysis. Resulting convergence PDFs for each case (Figure 3.12) communicate similar takeaways to that of the mesoscale convection-relative framework, with the more intense Case 10 located in a region of weaker near-surface and lower free tropospheric convergence than Case 12. Specifically, PDFs using data within the full AEW (Figure 3.11a,c) reveal Case 10 to have a 975 hPa convergence mean of 0.57 x 10^{-5} s^{-1} versus 0.67 x 10^{-5} s^{-1} for Case 12, with a 700 hPa convergence mean of 0.18 x 10^{-5} s^{-1} compared to 0.23 x 10^{-5} s^{-1} for Case 12. Meanwhile, PDFs using data within just the northern sector of the wave (Figure 3.11b,d) show a Case 10 975 hPa convergence mean of 0.43 x 10^{-5} s^{-1} versus 1.01 x 10^{-5} s^{-1} for Case 12 and a Case 10 700 hPa convergence mean of 0.00 x 10^{-5} s^{-1} compared to 0.03 x 10^{-5} s^{-1} for Case 12.

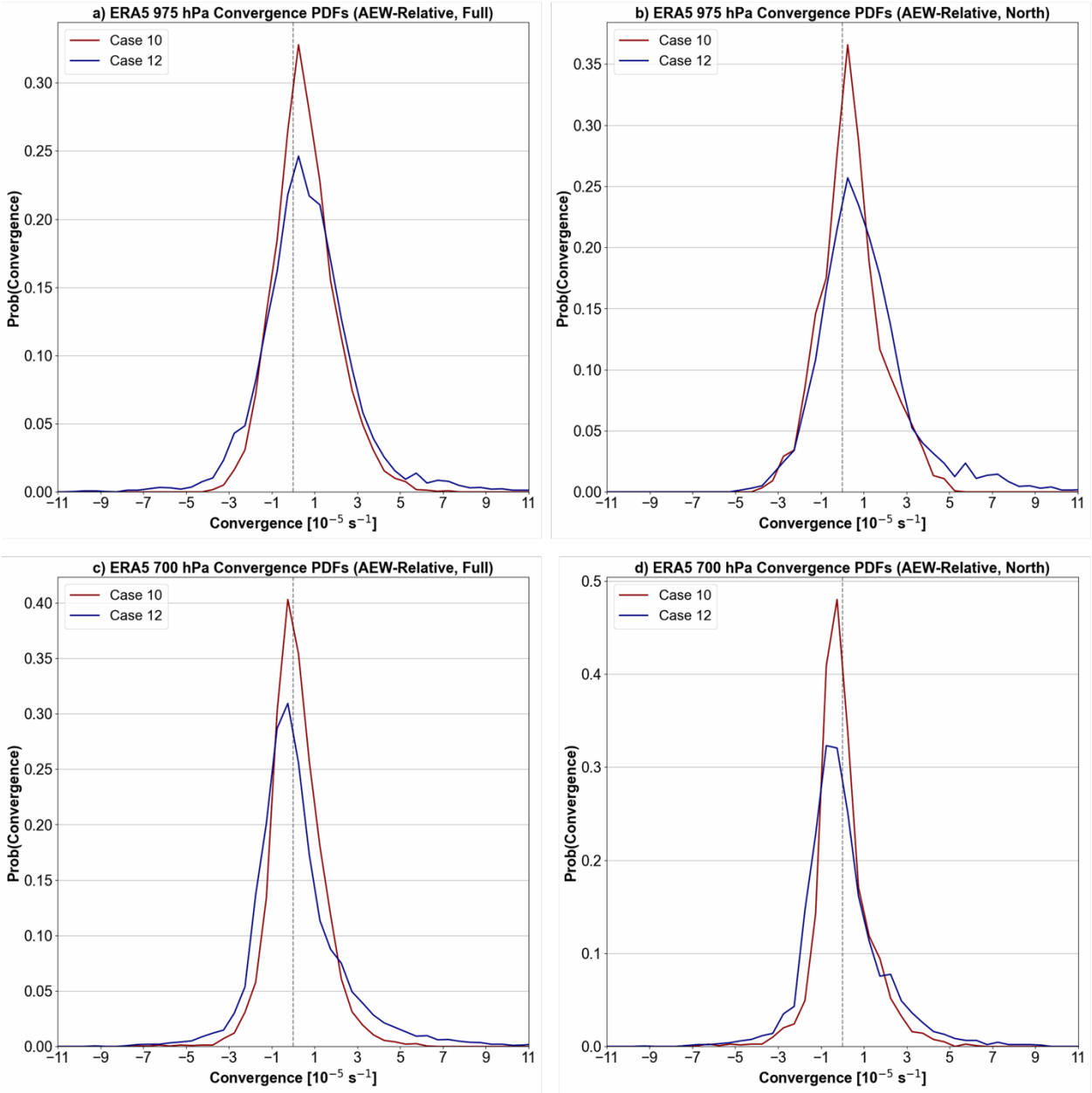

Figure 3.12: (a) AEW-relative probability distribution functions of ERA5 975 hPa convergence for Case 10 (red) and Case 12 (blue). Convergence is binned every 0.5 x 10^{-5} s^{-1} using only data within a 10° x 10° box centered on the tracked centroid of the propagating AEW within which each convective case is embedded. (b) Same as (a) except using only convergence data within the northern sector of the AEW (a 5° x 10° box). (c) Same as (a) except for 700 hPa convergence. (d) Same as (b) except for 700 hPa convergence.

Given the similar mean-layer wind shear and lower tropospheric RH distributions of the two cases, weaker lower tropospheric convergence being associated with the more intense TOC system is inconsistent with expectations based on prior studies (e.g., Banacos & Schultz, 2005; Cifelli et al., 2010; Inoue & Back, 2015; Tomassini, 2018; Galarneau et al., 2023; Rodenkirch & Rowe, 2024; Feng et al., 2025; Muetzelfeldt et al., 2025). In theory, all else being equal, weaker convergence in the lower troposphere would result in decreased lofting of larger hydrometeors, translating to less intense TOC. While Case 10 is located slightly closer to the center of the AEW moisture trough than Case 12, which may slightly favor convective development (e.g., Mayta & Adames Corraliza, 2024), the convection- and wave-relative convergence results in relation to TOC intensity merit further exploration of the cases beyond their sampling time periods.

Investigation into the lifecycle of each TOC system after sampling reveals the more intense Case 10 decayed for nearly four hours after in situ sampling (Figure 3.10a,c) while the less intense Case 12 maintained for over four hours following sampling (Figure 3.10b,d), as supported by both IMERG surface rain rate estimation (Figure 3.10a-d) and TIMPS-derived system maximum rain rates (Figure 3.10e). Given the otherwise similar environments, the post-sampling decay of Case 10 and maintenance of Case 12 coupled with weaker and stronger lower tropospheric convergence during sampling, respectively, suggests lag-lead relationships between lower tropospheric convergence and TOC intensity. These inferred lag-lead intensity-convergence relationships are consistent with prior studies pertaining to dynamical convergence influence on TOC directly (e.g., Kiladis et al., 2006; Mayta & Adames Corraliza, 2024) and indirectly as a means for column moisture convergence (e.g., Holloway & Neelin, 2009; Mayta & Adames Corraliza, 2024).

3.4 Regional Comparisons

3.4.1 CPEX-CV in Context of CPEX(-AW)

Composite analysis presented in Section 3.3.1 using CPEX-CV data showed relationships between mean-layer, near-storm moisture and wind shear relationships with convective type amongst large variabilities within both convective type and case. Comparison of these results in the East Atlantic with the West Atlantic where CPEX(-AW) collected similar data is warranted to diagnose potential regional variabilities of near-storm environmental relationships using similar methodologies (Rodenkirch & Rowe, 2024). Concentrating first on moisture, organized TOC was shown in Section 3.3.1 to have generally greater free-tropospheric RH compared to isolated TOC in the East Atlantic, despite large spreads in each layer (Figure 3.4). Evaluation against similar analysis from CPEX(-AW) in the West Atlantic (Figure 3.13) reveals East Atlantic near-storm environments in the free troposphere (Figure 3.13c,d) to be moister yet more variable than those in the West Atlantic, though the differences are not statistically significant for inflow observations. However, the generally greater near-storm moisture variabilities, which are present for both isolated and organized TOC, may be an artifact of larger sample sizes, more diverse synoptic-scale environments, and different TOC sampling strategies during CPEX-CV (Nowottnick et al., 2024) compared to CPEX(-AW) (Rodenkirch & Rowe, 2024). More notable is that similar near-storm moisture relationships with convective type in the free troposphere exist across the tropical Atlantic, in that organized TOC is associated with moister free-tropospheric environments than isolated TOC (Figure 3.13).

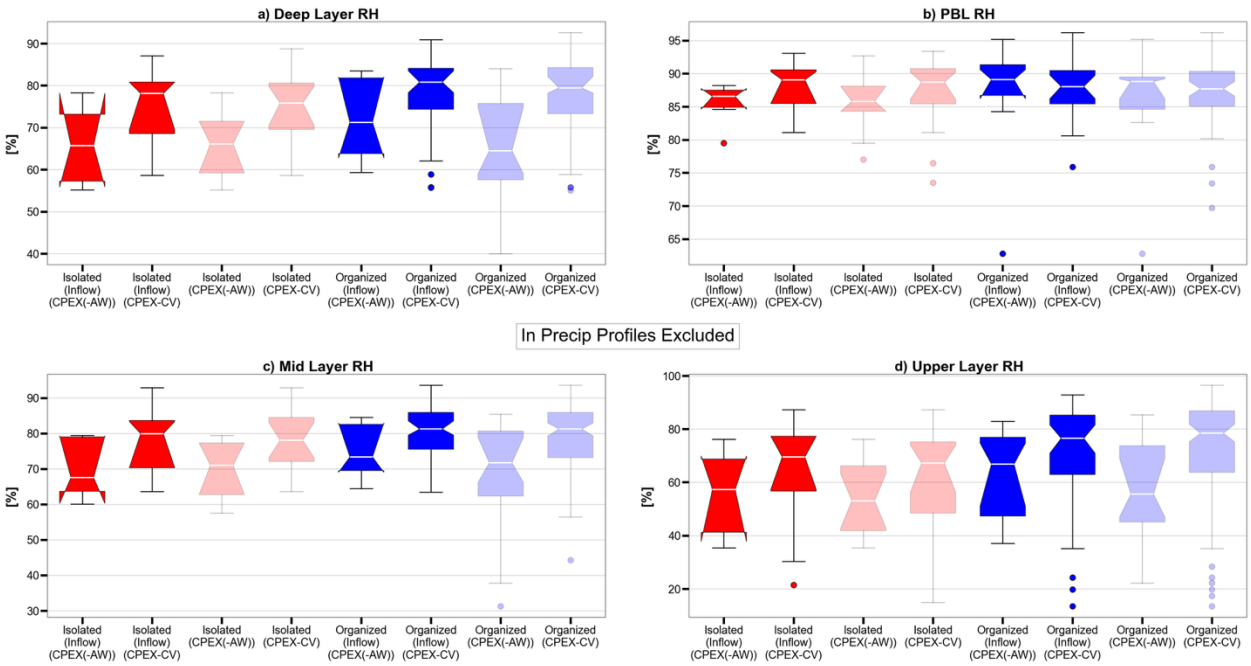

Figure 3.13: Same as Figure 3.4, except now including CPEX and CPEX-AW near-storm dropsonde observations over the West Atlantic basin.

Regional comparisons of near-storm wind shear between the East and West Atlantic tell a different story, however. While CPEX-CV data from the East Atlantic conveyed larger near-storm moisture spreads, mean-layer near-storm shear spreads between the two regions are not consistently greater or lesser than the other for both convective types (Figure 3.14). Similarly, near-storm shear magnitudes are not consistently greater across most tropospheric layers in the East Atlantic compared to the West Atlantic, unlike moisture. Rather, East Atlantic environments near organized TOC sampled by CPEX-CV had generally lesser shear in each layer than those of the West Atlantic sampled by CPEX(-AW) (Figure 3.14), with lesser deep (Figure 3.14a) and upper (Figure 3.14d) layer shear also applying to isolated TOC in the East Atlantic. The deep layer shear differences, in particular, are statistically significant both when including and excluding non-inflow dropsonde observations (Figure 3.14a). Concurrently, near-storm shear relationships with convective type differ between the East and West Atlantic for each tropospheric layer. As discussed in Section

3.3.1, deep and upper layer shear are generally greater for organized TOC in the East Atlantic, while PBL and mid layer shear medians are slightly greater for isolated TOC (Figure 3.6; Figure 3.7a; Figure 3.14). Meanwhile, deep and upper layer shear are generally lesser for organized TOC in the West Atlantic, while PBL and mid layer shear medians are lesser for isolated TOC (Figure 3.14). As such, the CPEX field campaign series observations reveal the presence of regional variability in near-storm environmental relationships that extends suggested regional variability in local TOC-environment relationships from prior reanalysis studies (e.g., Chen et al., 2017; Muetzelfeldt et al., 2025) to the tropical Atlantic and down to convective process-level scales.

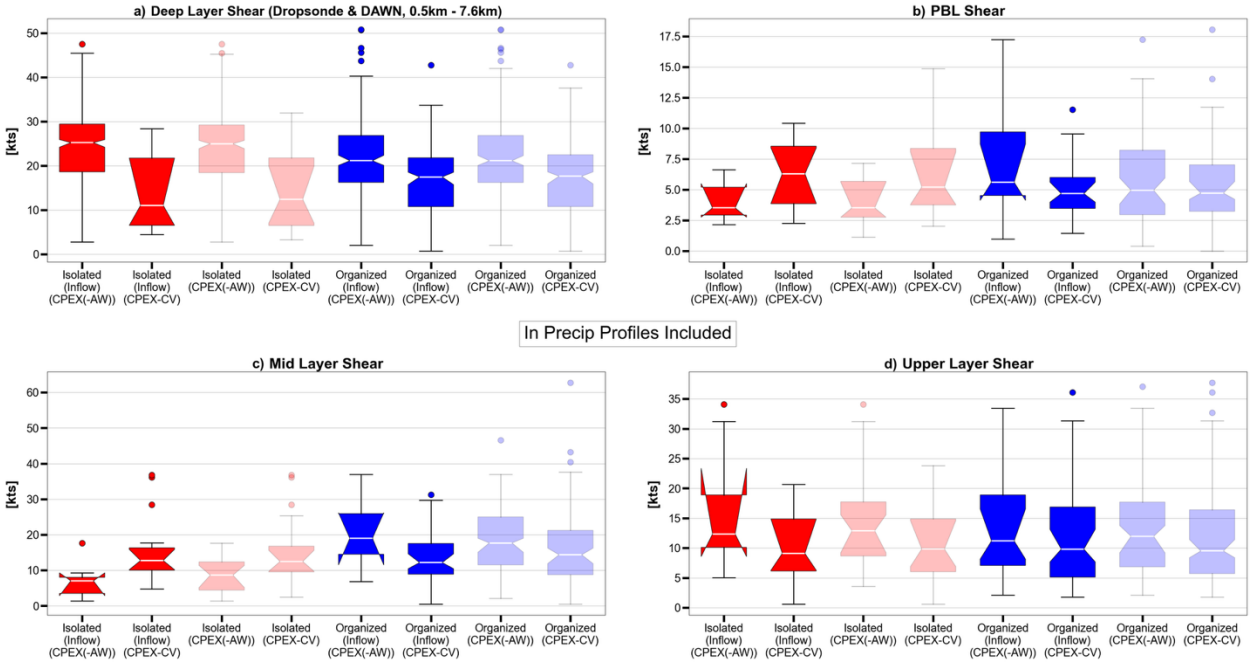

Figure 3.14: Same as Figure 3.6, except now including CPEX and CPEX-AW near-storm dropsonde observations over the West Atlantic basin. Near-storm DAWN observations from each field campaign are also included in (a), similar to Figure 3.7a.

3.4.2 Joint Near-storm Moisture and Wind Shear Relationships with Convective Type

Combination of high-resolution in situ observations across the tropical Atlantic from the 3-part

CPEX field campaign series not only allows for regional comparison of near-storm environmental relationships with TOC shown in Section 3.4.1, but the diverse array of sampled near-storm moisture and wind shear environments also provides the opportunity to assess how these variables may influence TOC structure together. To accomplish this, CPEX series dropsonde observations of moisture and shear in each of the four tropospheric layers (Section 3.2.4) were paired with one another, and their paired values were evaluated in the context of convective type (e.g., Figure 3.15). Amongst the 16 total combinations of mean-layer moisture and shear, 3 combinations relay notable trends: mid layer RH with deep layer shear (Figure 3.15a), mid layer RH with PBL shear (Figure 3.15b), and upper layer RH with upper layer shear (Figure 3.15c). Together, the trio of combinations show organized TOC to dominate at particularly large (i.e., > 80%) free-tropospheric (i.e., mid and upper layer) RH values, regardless of shear magnitude in any layer (Figure 3.15). Similarly, organized TOC dominates in particularly strong shear environments, both in the PBL (> 10 kts, Figure 3.15b) and in the other layers (> 20 kts, Figure 3.15a,c). Therefore, when either mean-layer shear or mid layer RH values are large, the other is less of a determining factor of convective type. Likewise, when both mean-layer shear and mid layer RH values are large, dropsonde observations are predominately associated with organized TOC (Figure 3.15). Meanwhile, deep layer shear is linked to convective type when mid layer RH is more moderate (e.g., 60-75%), with more organized TOC sampled with increasing deep layer shear (Figure 3.15a). Altogether, these findings concur with prior field campaign studies isolating free-tropospheric moisture (e.g., Brown & Zhang, 1997; LeMone et al., 1998; Cetrone & Houze, 2006; Holloway & Neelin, 2009; Wolding et al., 2022; Rodenkirch & Rowe, 2024), deep layer shear (e.g., Saxen & Rutledge, 2000; Rodenkirch & Rowe, 2024), and low-tropospheric shear (e.g., Alexander & Young, 1992; LeMone et al., 1998; Chudler & Rutledge, 2021; Rodenkirch & Rowe, 2024)

impacts on TOC structure, but with valuable added contextualization of the degree of influence of moisture and shear relative to the magnitude of the other that is consistent with prior CRM studies (e.g., Tompkins, 2001; Rodenkirch et al., 2025).

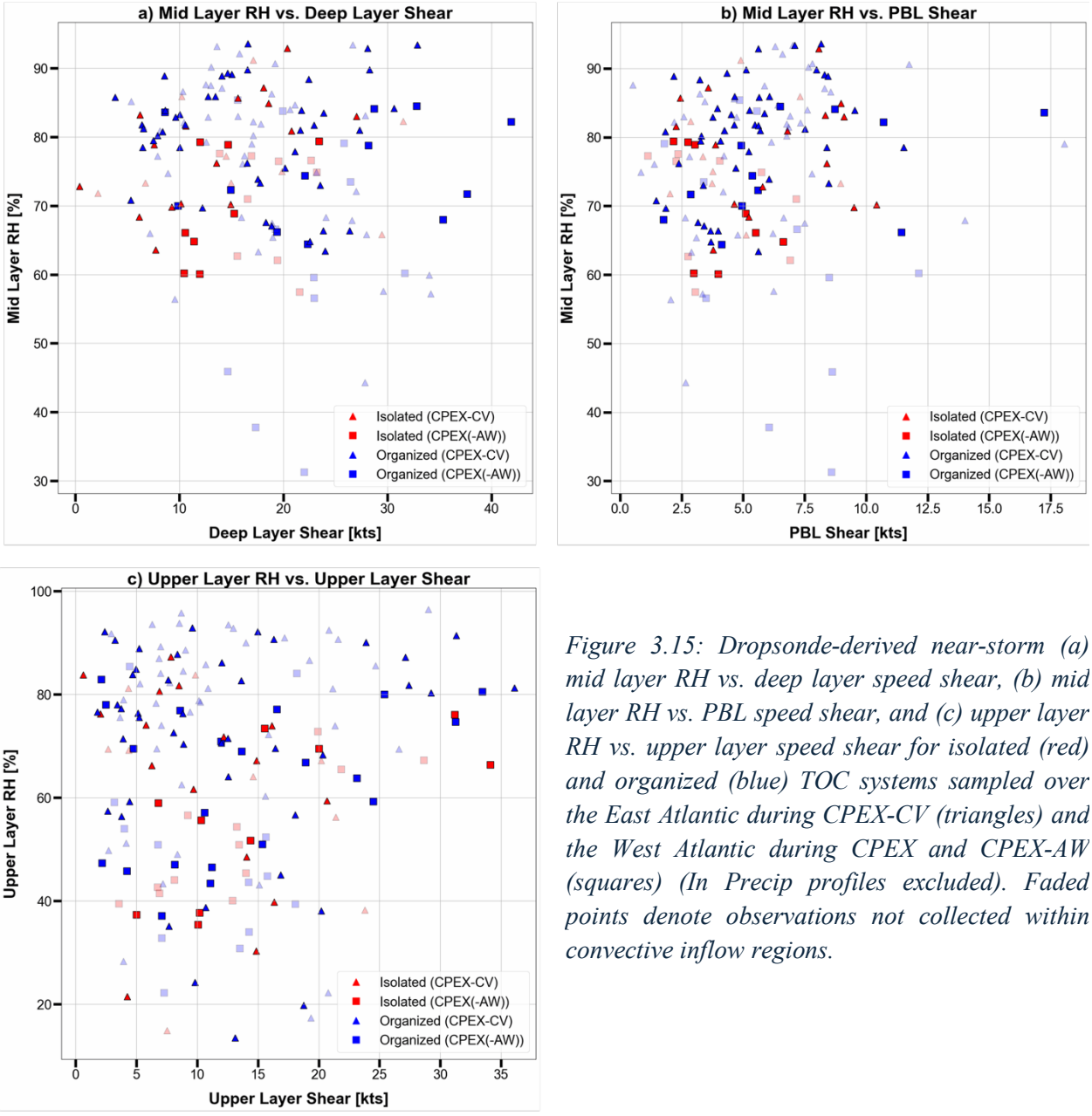

Figure 3.15: Dropsonde-derived near-storm (a) mid layer RH vs. deep layer speed shear, (b) mid layer RH vs. PBL speed shear, and (c) upper layer RH vs. upper layer speed shear for isolated (red) and organized (blue) TOC systems sampled over the East Atlantic during CPEX-CV (triangles) and the West Atlantic during CPEX and CPEX-AW (squares) (In Precip profiles excluded). Faded points denote observations not collected within convective inflow regions.

3.5 Conclusions

This chapter presents an investigation into near-storm environmental relationships with TOC structure in the tropical East Atlantic using a unique modern suite of coincident, high-resolution airborne observations from the NASA 2022 CPEX-CV field campaign. Analysis of dropsonde, APR-3 radar, and DAWN wind lidar data, focused on convective inflow regions, revealed large spreads in RH and vertical wind shear both within and across isolated (i.e., single-core) and organized (i.e., multi-core) TOC systems. Notable links with TOC structure emerged amongst the variability and were subsequently evaluated against similar analysis using NASA 2017 CPEX and 2021 CPEX-AW data in the tropical West Atlantic (Rodenkirch & Rowe, 2024) to assess regional variability in near-storm environmental relationships across the tropical Atlantic basin. In total, the CPEX-CV near-storm analysis and subsequent regional comparison with CPEX(-AW) convey the following key insights:

- In the East Atlantic, more intense CPEX-CV TOC was weakly linked to greater PBL wind shear, as well as a drier middle troposphere and lesser wind shear above the melting level.
- CPEX-CV organized TOC was associated with generally greater deep layer wind shear and free-tropospheric RH than isolated TOC.
- Similar free-tropospheric RH relationships with convective type (i.e., isolated vs. organized TOC) exist between the West (CPEX(-AW)) and East (CPEX-CV) Atlantic, though wind shear relationships differ between the two regions for each of the four tropospheric vertical layers analyzed.
- Combining near-storm observations from the entire 3-part CPEX field campaign series across the tropical Atlantic, analysis of joint effects of near-storm moisture and wind shear on TOC found free-tropospheric RH to be more of a determining factor on convective type

than wind shear when it was high (i.e., > 80%), and vice versa for wind shear when it was strong (i.e., > 10 kts for the PBL, > 20 kts for the deep layer and above the melting level).

The results of this chapter help address a notable regional gap in the literature regarding TOC relationships with near-storm environments in the East Atlantic using modern, high-resolution in situ observations. Expansion of analysis to joint effects of moisture and wind shear on TOC structure denote the contextual influence of one with respect to the other. Regional variabilities in near-storm environmental relationships between the East and West Atlantic extend local environmental variability between other tropical oceanic regions, as suggested by prior studies using lower spatiotemporal resolution reanalysis data (e.g., Chen et al., 2017; Muetzelfeldt et al., 2025), to the tropical Atlantic and down to finer, convective process-level scales. The CPEX field campaign series also highlights the value of high-resolution in situ measurements as an essential supplement to satellite remote sensing and reanalysis, in that large near-storm environmental variabilities both within and across TOC systems are observed that are otherwise difficult to capture by lower spatiotemporal resolutions.

The large near-storm environmental variabilities observed during CPEX-CV, in particular, may provide insight into why there were no definitive moisture and wind shear relationships with TOC intensity for most tropospheric layers (Section 3.3.2). An additional factor, however, was likely the presence of additional environmental influences, namely dynamical convergence that itself is regularly modulated by AEWs in the East Atlantic. With a majority of TOC systems sampled by CPEX-CV embedded within an AEW, a case comparison between two systems with otherwise similar environmental conditions and wave-relative locations was undertaken to discern the

potential role of dynamical convergence on TOC intensity. Lag-lead relationships between TOC intensity and ERA5 lower tropospheric convergence on both convective (meso-) and AEW (synoptic-) scales were inferred, wherein stronger and weaker convergence preceded TOC maintenance and decay, respectively, on timescales of a few hours. Complementing a case comparison between two TOC systems from the prior CPEX(-AW) campaigns that linked greater peak lower tropospheric convergence to greater TOC intensity (Rodenkirch & Rowe, 2024), this result of delayed impact additionally suggests that dynamical convergence may be a key, though somewhat complex, factor in influencing TOC structure. As such, the role of dynamical convergence may explain the lack of statistically significant near-storm moisture and shear relationships with convective type and TOC intensity in Sections 3.3.1 and 3.3.2, respectively, though a more detailed investigation is left for future work.

Future studies should therefore aim to conduct additional TOC case comparisons to test the robustness of the lag-lead lower tropospheric dynamical convergence relationships inferred in this chapter. Toward this effort, high-resolution modeling constrained by CPEX field campaign series observations could quantify near-storm environmental relationships and the individual roles of environmental components (e.g., Rodenkirch et al., 2025), including uncovering mechanisms pertaining to TOC-environment relationships in the context of AEWs. The noted regional variability in TOC-environment relationships within the tropical Atlantic elucidated by the CPEX field campaign series also discourages application of results to other tropical oceanic regions and consequently encourages extension of near-storm environmental analysis to the tropical Pacific and Indian basins, ideally with identical tropospheric vertical layer definitions for more equitable subsequent regional comparisons.

Chapter 4

Interregional Evaluation of Near-storm Convective Environments in the Tropical Northwest Pacific from NASA CAMP^{2}Ex

4.1 Introduction

Precipitating convection is a prevalent feature over tropical oceans and plays an important role in driving both regional and global weather and climate (e.g., Zipser 1977; Gill, 1980; Houze, 1982; Houze, 1989; Young et al., 1995; Houze, 1997; Saxen & Rutledge, 1998; Hartmann et al., 2001; Mechem et al., 2006; Tobin et al., 2012; Del Genio & Chen, 2015; Feng et al., 2015; Grant et al., 2020; Bony et al., 2020; Chen et al., 2022; Pilewskie & L'Ecuyer, 2026). Given its influence, global modeling efforts have long focused on parameterizing precipitating tropical oceanic convection (TOC) by relating TOC structure and intensity to grid-scale environmental parameters, motivating the need to understand TOC relationships with its local environment. Prior studies have attempted to develop generalized TOC-environment relationships across the tropics and have noted the particular importance of low- and mid-tropospheric moisture and vertical wind shear (hereafter referred to as "wind shear") in impacting TOC structure and intensity.

The following chapter is in preparation for submission with authors Rodenkirch, B. D. & Rowe, A. K. to *Journal of Geophysical Research: Atmospheres*.

Regarding moisture, reanalysis (e.g., Chen et al., 2017; Schiro et al., 2020; Adames et al., 2021; Wolding et al., 2022; Chen et al., 2023; Muetzelfeldt et al., 2025), cloud-resolving model (CRM) (e.g., Tompkins, 2001), and satellite observational studies (e.g., Bretherton et al., 2004) have found larger and more intense precipitating areas to be associated with greater mid-tropospheric moisture, but with varying degrees of influence in context of other environmental parameters like wind shear. Meanwhile, TOC relationships with low-tropospheric moisture vary in both strength and sign across studies, including within the planetary boundary layer (PBL) (e.g., Tompkins, 2001; Chen et al., 2017; Schiro et al., 2020; Muetzelfeldt et al., 2025). Inconsistencies may potentially be from differing contributions of low- and mid-tropospheric inflow into TOC that vary with convective lifecycle stage (Mechem et al., 2002), thereby necessitating contextualization of local environmental data by TOC lifecycle.

Similar to moisture, wind shear relationships with TOC are inconclusive across studies. While some CRM studies (e.g., Anber et al., 2014; Mulholland et al., 2021) find stronger low-tropospheric shear to promote greater TOC intensity and size via mechanisms like RKW cold pool dynamics (Rotunno et al., 1988) and enhanced horizontal convective mass flux (e.g., Mulholland et al., 2021), other CRM (e.g., Grant et al., 2018) and reanalysis (e.g., Muetzelfeldt et al., 2025) studies contend less of an association of TOC structure with low-tropospheric shear. Likewise, CRM (e.g., Tompkins, 2001) and reanalysis (e.g., Igel & van den Heever, 2015; Chen et al., 2023; Roca et al., 2025) studies exist linking enhanced wind shear in deeper tropospheric layers to larger and more intense TOC systems, while other studies suggest alternate relationships that are regionally dependent (e.g., Chen et al., 2017; Galarneau et al., 2023; Muetzelfeldt et al., 2025).

Inconsistencies in both moisture and wind shear relationships with TOC across studies are likely the result of many factors, including differing dataset types (i.e., satellite, reanalysis, CRM), limited spatiotemporal data resolution, and aforementioned regional variability (e.g., Chen et al., 2017; Galarneau et al., 2023; Muetzelfeldt et al., 2025) stemming from differing regional climatologies and associated prevailing types of TOC (Houze et al., 2015). Motivated by these issues, field campaigns have been employed within a diverse set of tropical oceanic regions. Field campaigns uniquely sample detailed in situ environmental measurements near TOC systems that can fill in spatiotemporal resolution gaps, including from reanalysis datasets that rely on imperfect underlying model parameterizations, particularly in data-sparse regions like tropical oceans (Randall et al., 2003; Arakawa, 2004; Pincus et al., 2017; Chen et al., 2017; Satoh et al., 2019; Rio et al., 2019; Wolding et al., 2022).

Field campaigns within different tropical oceanic regions highlight regional dependencies in TOC relationships with near-storm moisture and wind shear that manifest as inconsistent results across studies. An example is opposing relationships between PBL moisture and TOC size between the tropical West Pacific (Cetrone & Houze, 2006) and tropical East Atlantic (Rodenkirch & Rowe, 2025) compared to the tropical West Atlantic (Rodenkirch & Rowe, 2024). Additionally, some field studies link stronger low-tropospheric shear, including within the PBL, to enhanced TOC intensity and size in the West Atlantic (Rodenkirch & Rowe, 2024) and West Pacific (e.g., Alexander & Young, 1992; LeMone et al., 1998; Chudler & Rutledge, 2021), while studies in the Indian Ocean (e.g., Guy & Jorgensen, 2014) and East Atlantic (Rodenkirch & Rowe, 2025) show less of a relationship or even an opposing one.

Contributors to the inconsistent results between regions may be due to differing underlying organizational modes of analyzed TOC systems (e.g., predominantly quasi-linear in tropical West Pacific studies vs. non-linear in tropical Atlantic studies) and large variabilities in moisture and wind shear both within and between individual convective environments, as observed during the National Aeronautics and Space Administration Convective Processes Experiment (NASA CPEX; Chen & Zipser, 2017), CPEX–Aerosols & Winds (CPEX-AW; Skofronick-Jackson et al., 2021), and CPEX–Cabo Verde (CPEX-CV; Zawislak et al., 2022; Nowottnick et al., 2024) field campaigns across the tropical North Atlantic (Rodenkirch & Rowe, 2024; Rodenkirch & Rowe, 2025). Both factors are often linked via larger, more synoptic-scale features that vary regionally and contribute to regionally different climatological environments. In turn, this can result in differing frequencies of TOC morphologies (e.g., Chen et al., 2017) and altered degrees of moisture and shear influence on TOC (e.g., Sakaeda & Torri, 2022), further emphasizing the continued need to expand in situ studies of TOC to tropical oceanic regions with different climatological mesoscale and synoptic-scale characteristics.

In the tropical West Pacific, regional modulation of low- and mid-tropospheric moisture—and consequently TOC frequency, morphology, and intensity—is connected to large-scale features like the Madden-Julian Oscillation (MJO; e.g., Madden & Julian, 1971; Madden & Julian, 1972; Zhang, 2005), the El Niño Southern Oscillation (ENSO; e.g., Sullivan et al., 2019), and the Asian monsoon (e.g., Chang et al. 2005). While the tropical West Pacific is already one of the moister tropical oceanic basins climatologically (e.g., Chen et al., 2017), moister conditions supporting larger and more intense TOC prevail during active phases of the MJO, La Niña phases of ENSO, and the wet monsoon season, while drier conditions supporting weaker and more isolated TOC

prevail during inactive MJO phases, El Niño, and the dry monsoon season (e.g., Guy & Jorgensen, 2014; Qian et al., 2010; Chen et al., 2016; Dias et al., 2017; Chandra et al, 2018; Sullivan et al., 2019; Reid et al., 2023). In general, low- and mid-tropospheric wind shear are also known to vary by MJO phase, further impacting regional TOC frequency and structure (e.g., LeMone et al., 1998; Guy & Jorgensen, 2014; Rowe & Houze, 2014; Rowe & Houze, 2015; Chen et al., 2016).

Despite the considerable influences of large-scale features like the MJO, ENSO, and Asian monsoon on TOC, modern-day coordinated field campaign efforts geared towards high-resolution TOC sampling are rare in the West Pacific, particularly in the tropical Northwest Pacific that even went unsampled by older West Pacific field campaigns like the Tropical Ocean – Global Atmosphere Coupled Ocean Atmosphere Response Experiment (TOGA COARE; e.g., Brown & Zhang, 1997), Kwajalein Experiment (KWAJEX; e.g., Cetrone & Houze, 2006), and Equatorial Mesoscale Experiment (EMEX; e.g., Alexander & Young, 1992) to the south and east. To address this observational need, the NASA Cloud, Aerosol, and Monsoon Processes Philippines Experiment (CAMP^{2}Ex; Reid et al., 2023) field campaign operated for six weeks from late August to early October 2019 out of Luzon Island in the Philippines using the P-3 aircraft equipped with modern remote sensors and in situ data collection. Among this airborne instrumentation suite was a triple-wavelength airborne precipitation radar and dropsondes. These instruments collected rare, coincident, high-resolution near-storm environmental data suitable to study TOC across a range of local environmental conditions, including within a prevailing weak El Niño, the Asian monsoon, and different MJO phases (Reid et al., 2023).

While CAMP^{2}Ex was primarily focused on studying aerosol interactions with small and congestus TOC, De Vera et al. (2024) noted relationships between CAMP^{2}Ex shallow cumuli and non-aerosol environmental conditions. Given that CAMP^{2}Ex also sampled deeper precipitating TOC systems (Reid et al., 2023), the CAMP^{2}Ex field campaign presents an opportunity to expand upon the work of De Vera et al. (2024) to analyze tropical Northwest Pacific near-storm moisture and wind shear relationships with precipitating TOC. Additionally, the similar modern-day, high-resolution TOC and near-storm environmental datasets of CAMP^{2}Ex to that of the three-part tropical North Atlantic NASA CPEX field campaign series offers a unique opportunity to investigate potential variabilities in TOC-environment relationships between tropical oceanic regions with different climatological features using the same methodology (Rodenkirch & Rowe, 2024; Rodenkirch & Rowe, 2025). As such, all together this chapter aims to address: *how does TOC structure relate to near-storm moisture and wind shear in the tropical Northwest Pacific, and how do these relationships compare to those of similarly analyzed tropical North Atlantic regions?*

To address this research question, the chapter is organized as follows. Section 4.2 offers a description of the CAMP^{2}Ex instrumentation, data, and methods used for the analysis. Section 4.3 presents the results of the CAMP^{2}Ex analysis, while Section 4.4 provides a discussion of the results in the context of regional comparison, particularly with regard to similar analyses using similar airborne instrumentation data over the tropical North Atlantic from the NASA CPEX series (Rodenkirch & Rowe, 2024; Rodenkirch & Rowe, 2025). Section 4.5 concludes the chapter with main takeaways from the analysis and next steps for future research.

4.2 Data and Methods

4.2.1 CAMP^{2}Ex Overview

The CAMP^{2}Ex field campaign (van den Heever et al., 2019; Reid et al., 2023) executed 19 science flights during a six-week period over the Maritime Continent region of the tropical Northwest Pacific from late August to early October 2019 using the NASA P-3 research aircraft. Aboard the P-3 aircraft, the Third-Generation Airborne Precipitation Radar (APR-3; Sadowy et al., 2003) and dropsondes together provided coincident measurements of 3-D convective structure, moisture, and winds (e.g., Figure 4.1) at vertical resolutions high enough to analyze near-storm characteristics within different layers of the troposphere. As such, these two instruments were the primary sources of data used for this chapter. Additionally, four radiosondes launched from the Research Vessel *Sally Ride* in coordination with the Office of Naval Research Propagation of Intraseasonal Tropical Oscillations (ONR PISTON) experiment (Sobel et al., 2021; NASA/LARC/SD/ASDC, 2023) supplemented the dropsonde observations near a P-3-sampled TOC system on 17 September 2019 (Table 4.1). Within the 19 science flights, 19 distinct non-tropical cyclone (TC)-related precipitating TOC systems (or cases, as hereafter referred) were sampled within a variety of synoptic environments, including prevailing weak El Niño conditions, the southwesterly and northeasterly Asian monsoons, and convectively active and suppressed periods of the MJO (Table 4.1). For more information about the CAMP^{2}Ex field campaign, especially regarding other project objectives, instrument payloads, flights, and environmental sampling not discussed in this chapter, please refer to Reid et al. (2023).

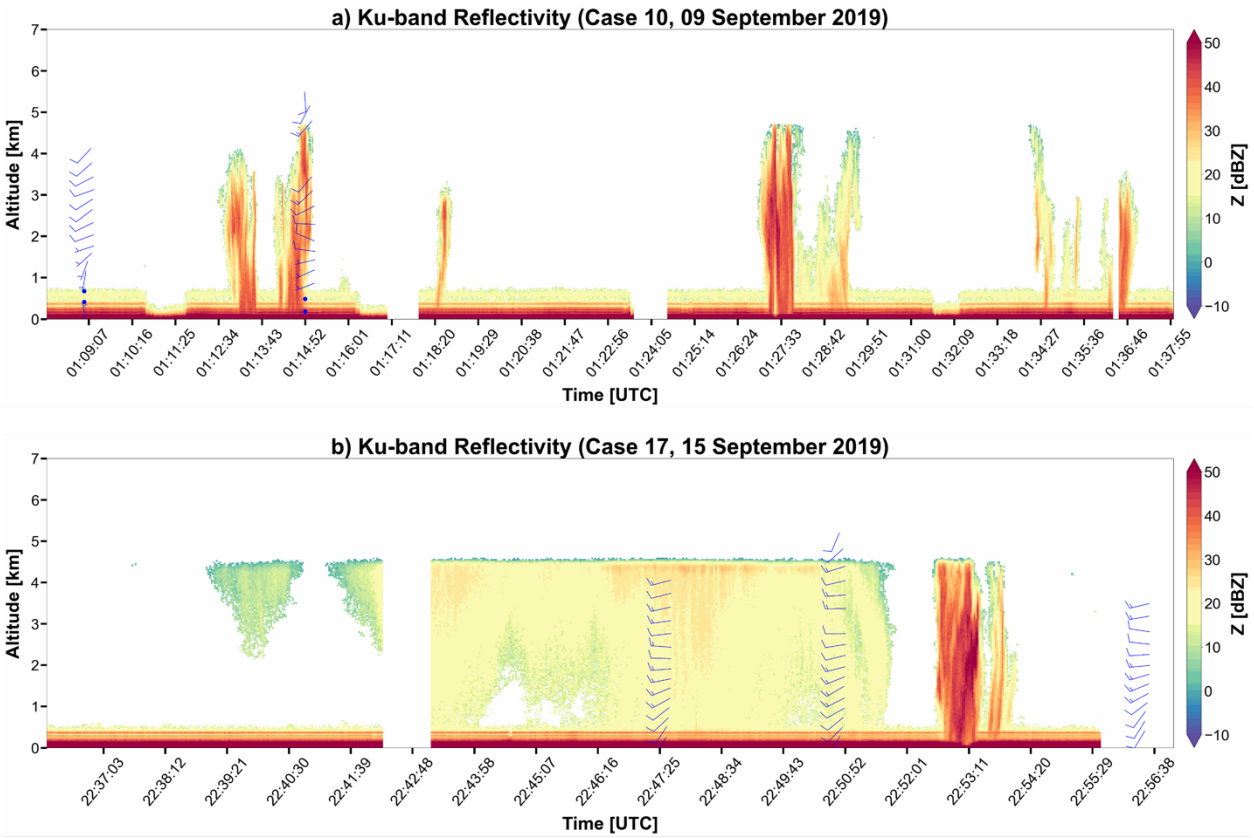

Figure 4.1: APR-3 Ku-band reflectivity profiles (fill) and sonde wind profiles (blue barbs) for an (a) isolated and (b) organized TOC system observed during CAMP²Ex.

Table 4.1: CAMP²Ex convective cases used for analysis in this chapter, sorted by convective type. The time of day, lifecycle stage, and MJO phase during convective sampling is denoted for each case. The number of associated near-storm sonde profiles (total, inflow) for each case is provided with sonde deployment environment.

Case	Date	Convective Type	Time of Day	MJO Phase	Lifecycle Stage	Number of Sondes (Total/Inflow)	Clear	In Cloud	In Precip
1	20190829	Isolated	Morning	Active	Growing/Mature/Decaying	7/3	6	0	1
2	20190830	Isolated	Afternoon	Active	Decaying	2/2	2	0	0
3	20190831	Isolated	Morning	Active	Decaying	1/1	1	0	0
4	20190831	Isolated	Afternoon	Active	Growing	1/1	1	0	0
5	20190904	Isolated	Morning/Afternoon	Active	Mature/Decaying	2/1	2	0	0
6	20190904	Isolated	Afternoon	Active	Mature	1/1	1	0	0
7	20190904	Isolated	Afternoon	Active	Mature	1/1	1	0	0
8	20190907	Isolated	Afternoon	Active	Decaying	1/0	0	1	0
9	20190909	Isolated	Morning	Active	Growing/Decaying	3/0	2	1	0
10	20190909	Isolated	Morning	Active	Growing/Decaying	5/1	3	1	1
11	20191001	Isolated	Morning	Suppressed	Growing	1/0	1	0	0
12	20191002	Isolated	Afternoon	Suppressed	Mature	1/1	1	0	0
13	20191003	Isolated	Morning	Suppressed	Growing	3/0	3	0	0
14	20191004	Isolated	Morning	Suppressed	Decaying	4/1	4	0	0
15	20190907	Organized	Morning	Active	Growing	3/1	1	1	1
16	20190907	Organized	Morning/Afternoon	Active	Growing/Decaying	3/2	3	0	0
17	20190915	Organized	Morning/Afternoon	Suppressed	Decaying	6/6	4	2	0
18	20190917	Organized	Morning/Afternoon	Suppressed	Mature/Decaying	15/0	6	5	4
19	20191005	Organized	Morning/Afternoon	Suppressed	Growing/Mature	9/3	7	2	0

4.2.2 CAMP²Ex Datasets

CAMP²Ex vertical profiles of temperature, humidity, and horizontal wind velocity were collected using the NSF National Center for Atmospheric Research (NCAR) RD41 dropsondes, which employed the Airborne Vertical Atmospheric Profiling System (AVAPS) developed by Vaisala Inc. (NSF NCAR Earth Observing Laboratory, 1993; Hock & Franklin, 1999; Vaisala, 2018; Vömel et al., 2020). The dropsondes provided temperature accuracy of 0.2°C at 0.01°C resolution, RH accuracy of 3% at 0.1% resolution, and horizontal wind speed accuracy of 0.5 m s^{-1} at 0.1 m s^{-1} resolution, each at a vertical resolution of 0.01 hPa that is adequate for the purposes of this chapter (Vaisala, 2018; CAMP²Ex Dropsonde, 2020). Dropsonde data were processed using the NCAR Atmospheric Sounding Processing ENvironments (ASPEN) software (Vömel et al., 2020;

Martin & Suhr, 2021), with additional processing details provided in Vömel et al. (2020) and CAMP^{2}Ex Dropsonde (2020). Supplemental PISTON Vaisala RS41-SGP radiosondes, of which only four qualified for use in this chapter as being launched near P-3-sampled TOC systems, provided similar vertical profiling at similar resolutions and accuracies as the CAMP^{2}Ex RD41 dropsondes, with quality control procedures consistent with Ciesielski et al. (2014).

CAMP^{2}Ex 3-D radar reflectivity profiles were collected by the APR-3 instrument (Sadowy et al., 2003). While APR-3 collects data at W- (94 GHz), Ka- (35.6 GHz), and Ku- (13.4-GHz) bands (Durden et al., 2012; CAMP^{2}Ex APR-3, 2023), this chapter focuses on Ku-band, which more effectively samples intense precipitation structure. APR-3 Ku-band reflectivity has a vertical resolution (i.e., an along-beam gate spacing) of 60 m and a horizontal resolution of ~730 – 800 m at 10-km range with a 5-dBZ sensitivity (Sadowy et al., 2003; Durden et al., 2012; Durden et al., 2020). APR-3 Ku-band calibration uncertainty for CAMP^{2}Ex is estimated at 1 dB (Tanelli et al., 2006; CAMP^{2}Ex APR-3, 2023).

4.2.3 Convective Case Characterization

Each of the 19 sampled TOC cases was categorized as either an isolated or organized convective type (Table 4.1). Using archived Advanced Himawari-8 Imager (AHI; Da, 2015) IR imagery and the Integrated Multi-satellitE Retrievals for GPM (IMERG) satellite surface precipitation estimation product (Huffman et al., 2019) in accordance with the methodology of Rodenkirch & Rowe (2024) and Rodenkirch & Rowe (2025), isolated TOC was defined manually as horizontally small, single-core (from AHI IR) precipitating (from IMERG) systems (e.g., Figure 4.2a) while organized TOC was defined as larger, multi-core precipitating systems (e.g., Figure 4.2b). With

some cases lacking prolonged sampling and multiple flight legs through the TOC system (e.g., Figure 4.2b), each case was contextualized by convective lifecycle stage(s) (growing, mature, decaying) during the time of sampling using the Tracked IMERG Mesoscale Precipitation Systems (TIMPS) tracker (Russell, 2022; Rajagopal et al., 2023) and archived AHI IR imagery (Da, 2015). The MJO phase during sampling was denoted for each case as well, with isolated and organized TOC notably each sampled during convectively active and suppressed MJO phases (Table 4.1; Reid et al., 2023) that mitigate MJO phase sampling bias in the results. Additionally, the time of day during sampling was recorded for each case (Table 4.1), though due to the focus of this chapter being on general relationships between the near-storm environment and TOC characteristics, diurnal variance is not expected to affect results of this chapter.

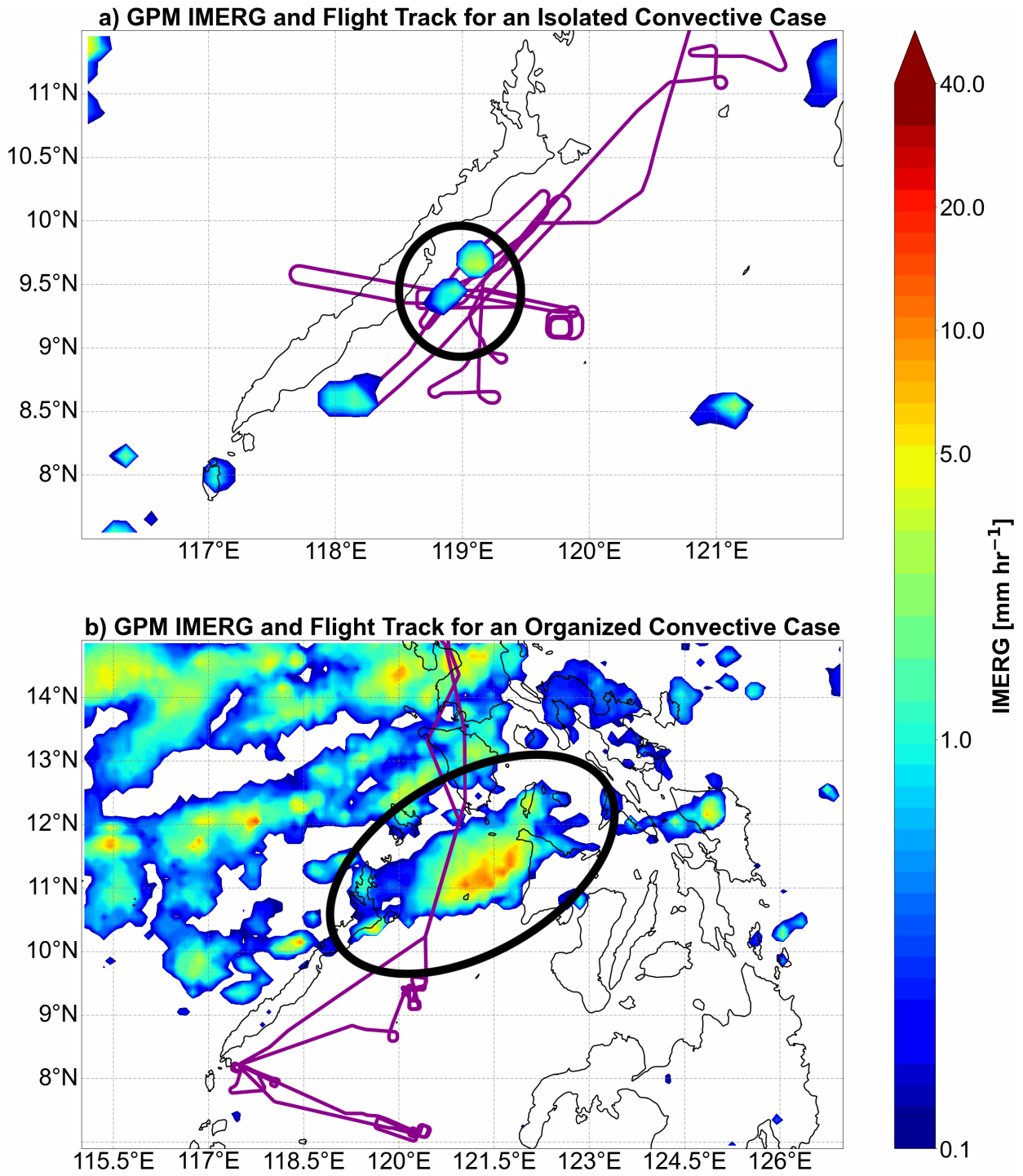

Figure 4.2: Example of an (a) isolated TOC system (Case 1) and (b) organized TOC system (Case 17) sampled during CAMP^{2}Ex (circled in bold black), as defined by GPM IMERG precipitation area and continuity. CAMP^{2}Ex science flight tracks are overlaid in purple. Thin black outlines denote land.

4.2.4 Sonde Characterization and Mean-layer, Near-storm Environmental Metrics

To relate TOC structure to near-storm environments, "near-storm" observations are defined in this chapter as in Rodenkirch & Rowe (2024) and Rodenkirch & Rowe (2025) as being collected within ~10 minutes–or conservatively within ~150 km–of actively precipitating regions, which translates to closer distances to full convective cloud structures including anvil cirrus. Given this definition, 69 total sondes (65 dropsondes, 4 radiosondes) across the 19 CAMP^{2}Ex TOC cases (Table 4.1) qualified as near-storm observations. Each of these sondes was characterized by the convective type of its respective case, along with the convective lifecycle stage at the time of deployment as described in Section 4.2.3. While subsequent sonde analysis in Section 4.3 includes observations from all lifecycle stages, separate analysis was performed excluding the decaying stage to focus more on growing and mature stage environments that develop and sustain TOC. Both sets of analyses produce similar results, and thus the analysis including observations from all lifecycle stages is subsequently shown to highlight the full scope of the sonde observations.

In addition to convective type and lifecycle stage, the convective-relative environment each sonde was deployed into (i.e., Clear, In Cloud, In Precip) was recorded using similar methodology as Rodenkirch & Rowe (2024) and Rodenkirch & Rowe (2025) based on sonde and APR-3 data. The distribution of sondes across convective-relative environment for each case can be seen in Table 4.1. Examples of Clear (01:09:00 UTC) and In Precip (01:14:53 UTC) sondes are shown in Figure 4.1a. Notably, 7 sondes deployed in regions actively precipitating at the surface (i.e., In Precip sondes) were excluded from moisture analysis, as their extensively saturated moisture profiles were not representative of the surrounding environment influencing the convection.

Sondes deployed in convective inflow regions were also noted and chosen as the primary focus of observational analysis for this chapter due to their sampled inflow environments likely influencing TOC more than non-inflow environments. To identify sondes in convective inflow regions, mean storm velocity of each convective case was determined using the TIMPS tracker (Russell, 2022; Rajagopal et al., 2023) with complementary manual estimations using archived AHI IR imagery (Da, 2015) coordinates at the start and end times of the case sampling period. Given the potential of convective inflow to originate from both the lower and middle troposphere (e.g., Mechem et al., 2002), both low- (975 hPa – 925 hPa) and mid- (900 hPa – 700 hPa) tropospheric mean wind velocities were then calculated for each sonde associated with a given convective case. At each sonde location, storm-relative motion vectors for the lower and middle troposphere were subsequently calculated, and sondes deployed in an inflow region in either layer were characterized as inflow sondes, of which there were 25 across the 19 convective cases.

Following sonde characterization, mean RH and wind shear were calculated for each sonde for four distinct tropospheric layers consistent with Rodenkirch & Rowe (2024) and Rodenkirch & Rowe (2025): the PBL, mid layer (PBL top – melting level), upper layer (melting level – 7622.5 m, or ~400 hPa), and deep layer (near-surface – 7622.5 m). However, CAMP^{2}Ex dropsondes rarely captured the full extent of the upper layer (and thus the deep layer) due to typical P-3 flight levels of 6-8 km (Reid et al., 2023) and time delays in dropsonde GPS availability post-launch (Vömel et al., 2020). As such, this chapter will focus on analysis of TOC relationships with near-storm RH and wind shear in the PBL and mid layer exclusively, where sonde observations were more plentiful.

4.2.5 Contoured Frequency by Altitude Diagrams

Analysis of convective intensity was executed using Contoured Frequency by Altitude Diagrams (CFADs; Yuter & Houze, 1995; Zagrodnik et al., 2019), in accordance with the methodology of Rodenkirch & Rowe (2024) and Rodenkirch & Rowe (2025). To create the CFADs, two-dimensional (2-D) histograms of APR-3 Ku-band reflectivity (5-dBZ bins) and altitude (0.5-km bins) for each convective case were normalized by the maximum bin count in *each* altitude interval, with radar reflectivity intensity from hydrometeors serving as a proxy for convective updraft intensity (e.g., Zipser & Lutz, 1994; Zipser et al., 2006; Heymsfield et al., 2010; Ni et al., 2019). CFADs were generated for the convective regions of storms only using the objective Echo Classification from COnvectivity for Vertically pointing radars (ECCO-V) convective-stratiform partitioning algorithm (Dixon & Romatschke, 2022; Romatschke & Dixon, 2022).

Leveraging the reflectivity texture of a 2-D time-altitude radar scan, ECCO-V translates radar reflectivity into a metric called "convectivity" on a 0-1 scale (e.g., Figure 4.3a; Romatschke & Dixon, 2022). ECCO-V subsequently classifies the 2-D radar data into convective, stratiform, and mixed echo types based on convectivity thresholds (e.g., Figure 4.3b). A convectivity threshold of 0.4 was used for basic convective-stratiform classification in this chapter, with convective components identified as convectivity ≥ 0.4. The maximum convectivity value for each Ku-band profile was used to produce a 1-D convective-stratiform classification time series for each case (e.g., Figure 4.3c) for partitioning the Ku-band profiles (e.g., Figure 4.3d) in CFADs. Convective cases of similar convective type and lifecycle stage had their CFADs differenced from each other to create "difference CFADs", which provide insight into TOC structure and intensity differences

between cases with distinctly different near-storm mean-layer environments (Yuter & Houze, 1995; Rodenkirch & Rowe, 2024; Rodenkirch & Rowe, 2025).

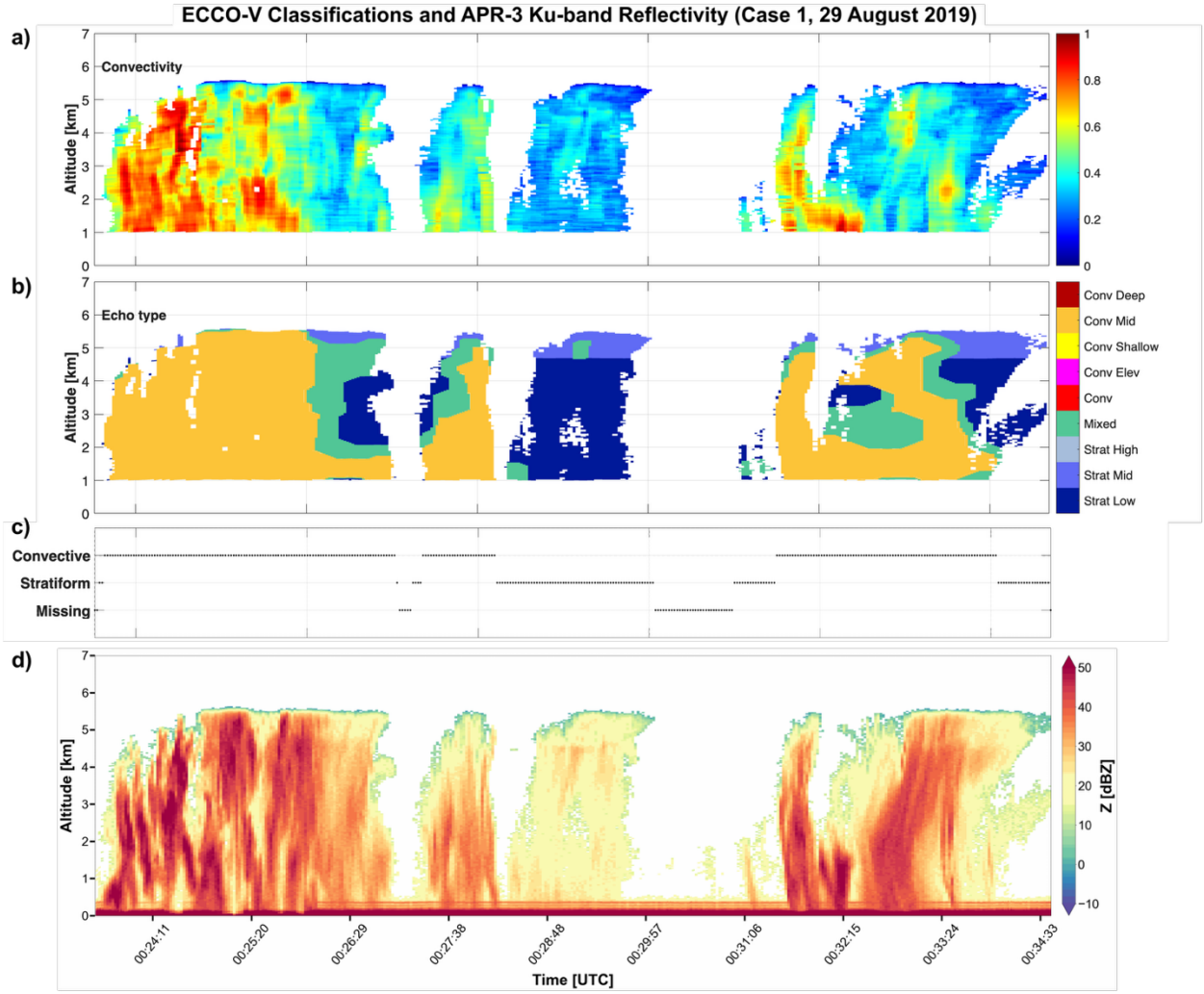

Figure 4.3: ECCO-V (a) convectivity, (b) 2-D convective echo classification, and (c) 1-D convective echo classification for (d) APR-3 Ku-band reflectivity (fill) of a TOC system observed during CAMP²Ex. The "Missing" classification in (c) is assigned to times absent of sufficient 2-D APR-3 Ku-band reflectivity data for ECCO-V to determine a 1-D convective echo classification.

4.3 CAMP^{2}Ex Results

4.3.1 Near-storm Moisture and Wind Shear Relationships with Convective Type

To assess near-storm moisture and vertical wind shear relationships with single- (i.e., isolated) and multi-core (i.e., organized) TOC systems, mean-layer sonde metrics are analyzed using a composite statistical approach with box-and-whisker plots (e.g., Figure 4.4). As described in Section 4.2.4, near-storm sonde moisture and wind shear are evaluated below the melting level within and above the PBL (i.e., the so-called "mid layer"), where observations are much more numerous than in higher parts of the troposphere. Particular focus is paid towards sonde observations of convective inflow environments that likely influence TOC more than non-inflow environments, though similar trends exist between convective type and near-storm environments when including observations outside of inflow regions. As such, sonde observations from all near-storm regions (i.e., both inflow and non-inflow environments) are included in subsequent figures, in addition to observations exclusively from inflow environments as separate sets.

Focusing first on moisture, isolated and organized TOC are observed to have similar spreads in PBL and mid layer RH (Figure 4.3). Though isolated TOC first and third quartiles of mid layer RH within inflow regions each exceed that of organized TOC, their median values of 77.6% and 77.0%, respectively, are close enough such that the differences are not statistically significant, as denoted by overlapping "notches" around the medians in the box-and-whisker plots in Figure 4.3. The lack of statistically significant moisture differences applies to the PBL as well, with inflow sonde median PBL RH of 88.1% for isolated TOC and 88.2% for organized TOC. A culprit of the indistinct moisture relationships may be the large observed moisture variability both within isolated and organized TOC as a whole (Figure 4.4) and in between and within individual

convective cases (Figure 4.5), even after accounting for sonde deployment environment (i.e., Clear, In Cloud, In Precip). Filtering out observations from non-inflow regions does decrease some of the moisture variability, however, lending further credence to analysis focus on sonde observations from inflow environments.

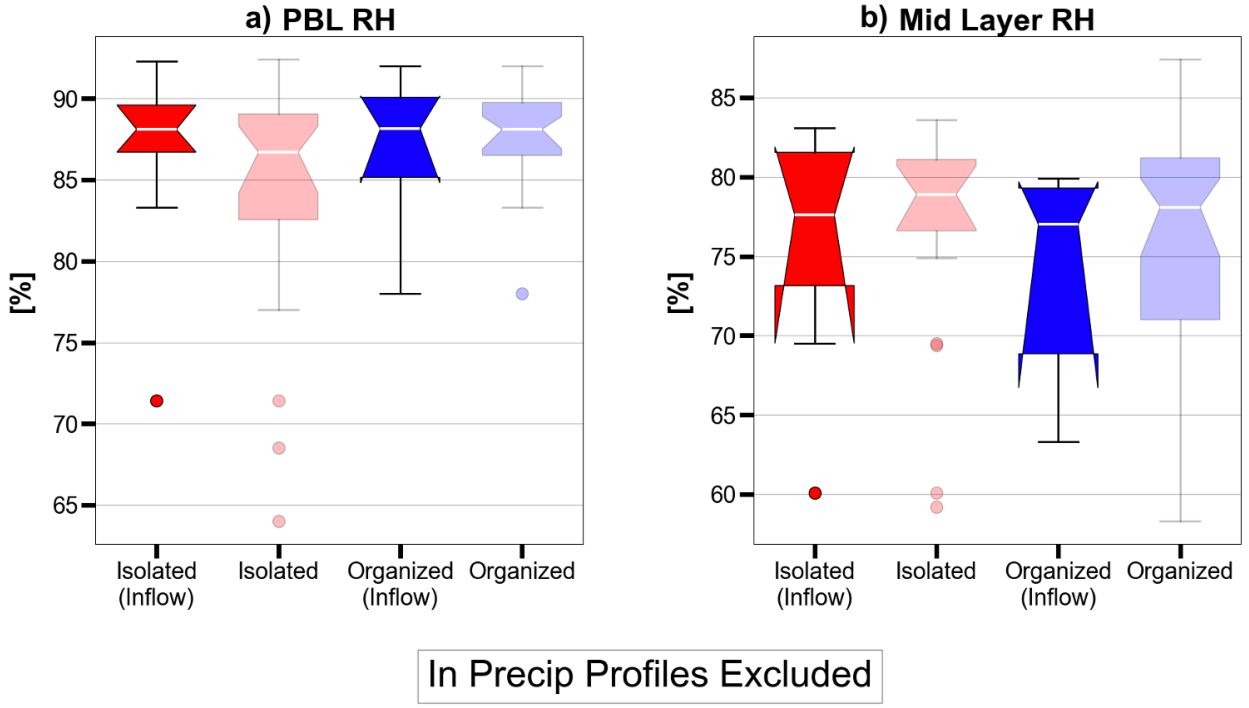

Figure 4.4: Sonde-derived near-storm (a) PBL RH and (b) mid layer RH for isolated (red) and organized (blue) TOC systems sampled during CAMP²Ex (In Precip profiles excluded). Faded boxes denote observations collected both within and outside of convective inflow (i.e., all near-storm) regions, while saturated boxes denote observations collected only within convective inflow regions. Each box extends from the first quartile to the third quartile of the data, with a white line at the median. Whiskers extend from the box by up to 1.5 times the interquartile range, and outlier points are points beyond the whiskers. Notches denote statistical significance with a 95% confidence level via bootstrapping the median 10,000 times and using a Gaussian-based asymptotic approximation. Extended notches are the result of the confidence interval bounds extending beyond the first or third quartile.

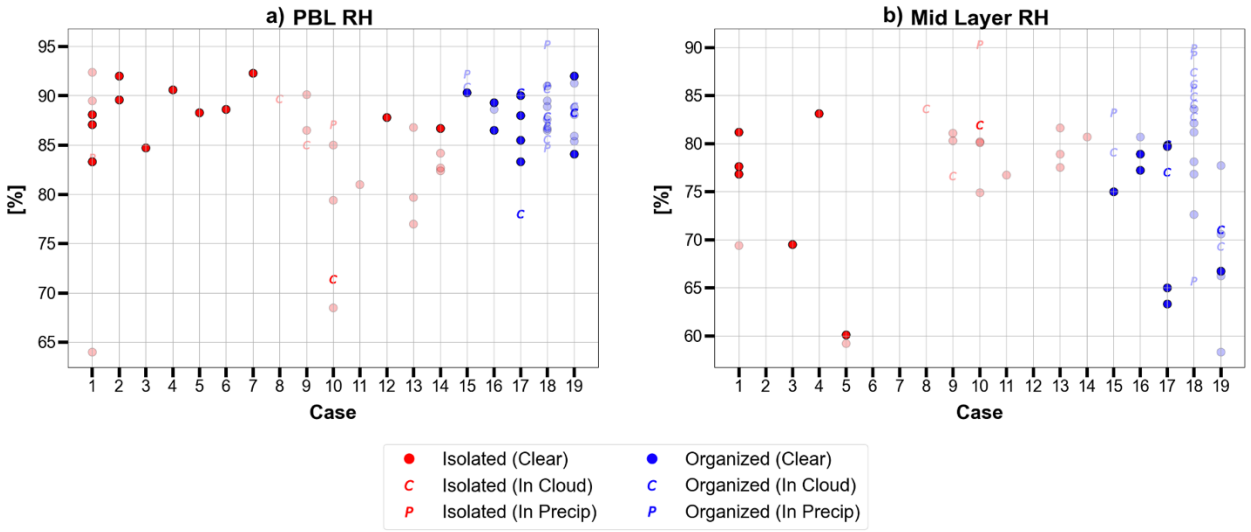

Figure 4.5: Same data as Figure 4.4, except near-storm sonde observations are further sorted by convective case (In Precip profiles included). Faded points denote observations not collected within convective inflow regions. Markers denote the convective-relative environment the sonde was deployed into.

Similar to moisture, notable PBL and mid layer vertical wind shear variabilities exist both within each convective type (Figure 4.6) and within convective systems (Figure 4.7), particularly for organized TOC. While no statistically significant differences in wind shear are present in the mid layer between isolated (median of 13.1 kts) and organized (median of 12.2 kts) TOC (Figure 4.6b), the PBL exhibits a clearer distinction. PBL shear is observed to be greater for organized TOC than isolated TOC at a statistically significant level, with inflow sonde median values of 9.9 kts versus 3.2 kts, respectively (Figure 4.6a). Notably, high near-storm PBL shear values near organized TOC exceeding the median value of 9.9 kts are observed even when excluding In Cloud and In Precip observations that may locally enhance shear (Figure 4.7a).

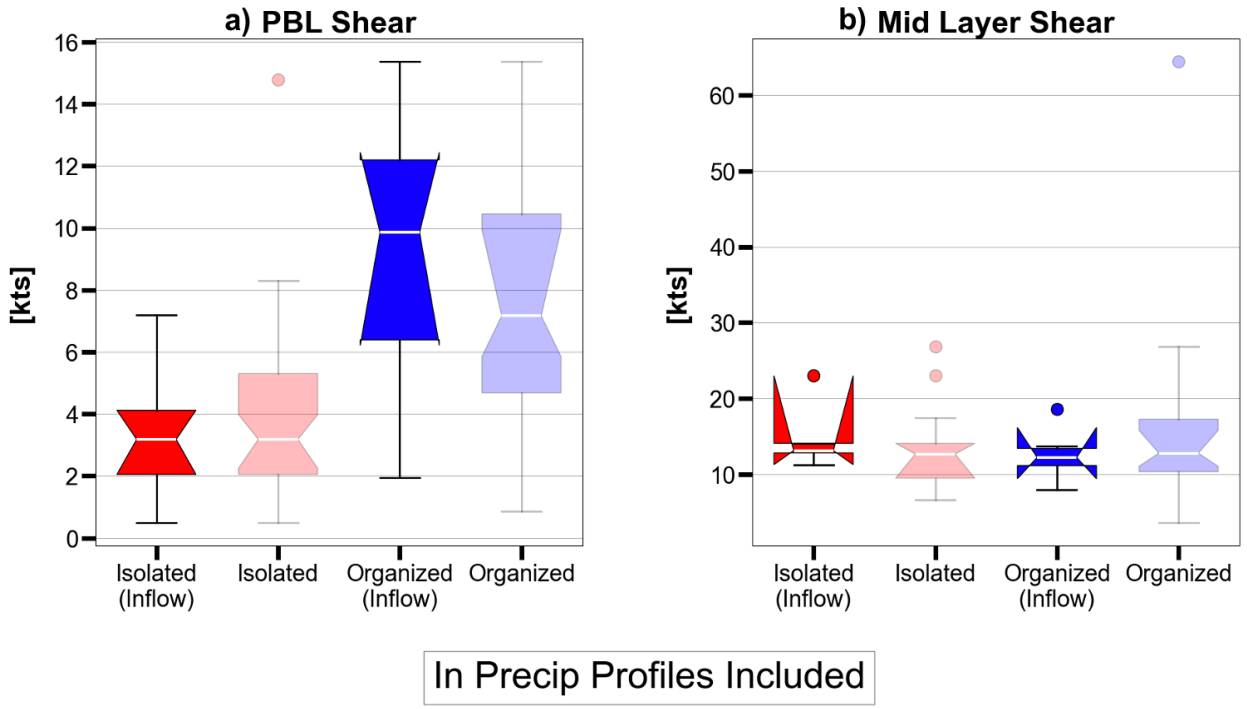

Figure 4.6: Same as Figure 4.4, except showing near-storm (a) PBL speed shear and (b) mid layer speed shear. In Precip profiles are now included.

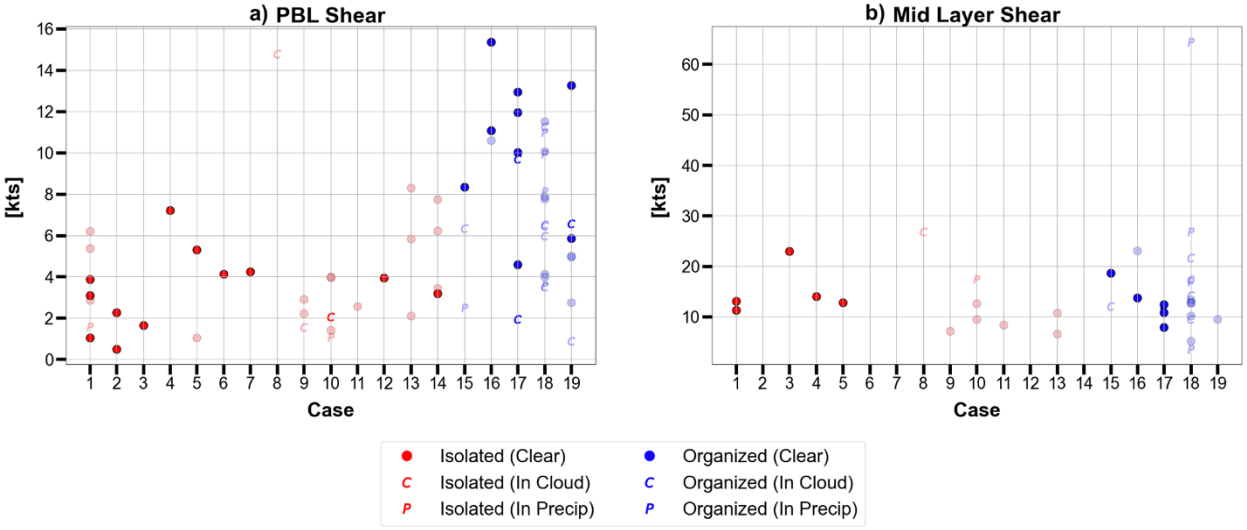

Figure 4.7: Same data as Figure 4.6, except near-storm sonde observations are further sorted by convective case. Faded points denote observations not collected within convective inflow regions. Markers denote the convective-relative environment the sonde was deployed into.

Apart from the distinct PBL shear relationship with convective type, the composite TOC-environment statistical analysis overall conveys statistically insignificant relationships between convective type and near-storm moisture and shear below the melting level. A limited sample size of near-storm sonde observations during CAMP^{2}Ex may contribute to these weak relationships, including large observed moisture and shear variabilities both within isolated and organized TOC types (Figures 4.4, 4.6) and in between and within individual convective cases (Figures 4.5, 4.7). These large near-storm environmental variabilities, particularly regarding distinct differences between cases of similar convective type (e.g., organized Cases 15 and 17 with only marginally overlapping mid layer shear ranges in Figure 4.7b), motivate expansion of the composite analysis to individual case comparisons, wherein TOC vertical structure and intensity of similar type cases can be evaluated against differing near-storm moisture and wind shear environments.

4.3.2 Near-storm Moisture and Wind Shear Relationships with Convective Intensity

To analyze TOC vertical structure, CFADs of APR-3 Ku-band reflectivity were created for the convective regions of each convective case utilizing the ECCO-V convective-stratiform partitioning algorithm (Dixon & Romatschke, 2022; Romatschke & Dixon, 2022), as described in Section 4.2.5. Subsequent difference CFADs were constructed between cases, allowing for evaluation of relative Ku-band reflectivity frequency differences by altitude that serve as a proxy for TOC intensity differences (Section 4.2.5). Difference CFADs were notably only produced between cases that had distinct differences in at least one tropospheric layer's moisture or wind shear metric (using Figures 4.5 and 4.7), yet had similar convective type and presence of mature convective elements in their APR-3 data. Consistent with the composite statistical analysis of Section 4.3.1, this analysis also only used sonde observations from convective inflow regions and

excluded In Precip sondes for moisture. Implementing each of these qualifications, further restricted by CAMP^{2}Ex science flights rarely sampling convective structure close to the centers of TOC systems that adequately represent their intensity (e.g., Figure 4.2b), resulted in two valid convective case comparisons with distinctly different near-storm moisture (one isolated case comparison) or wind shear (one organized case comparison).

The isolated TOC case comparison evaluated intensity differences between Case 1 (Figure 4.2a) and Case 10. Between the two cases, Case 1 was the more intense convection, as shown in Figure 4.8a by negative differential frequencies of greater Ku-band reflectivity values throughout the vertical column. Case 1 also had distinctly greater PBL RH than Case 10 (Figure 4.5a) with no other distinct moisture nor wind shear differences below the melting level, thereby suggesting (albeit limited) a positive link between PBL RH and TOC intensity. Meanwhile, the organized TOC case comparison focused on intensity differences between Case 17 (Figure 4.2b) and Case 15, with Case 15 having distinctly greater mid layer shear than Case 17 (Figure 4.7b). The difference CFAD between the two cases (Figure 4.8b) reveals Case 15 to be less intense than Case 17, as reflected in the positive differential frequencies of greater Ku-band reflectivity values throughout the majority of the vertical column. Without any other distinct wind shear nor moisture differences below the melting level between Case 15 and Case 17, this case comparison (albeit limited) would suggest enhanced mid layer shear to negatively impact TOC intensity.

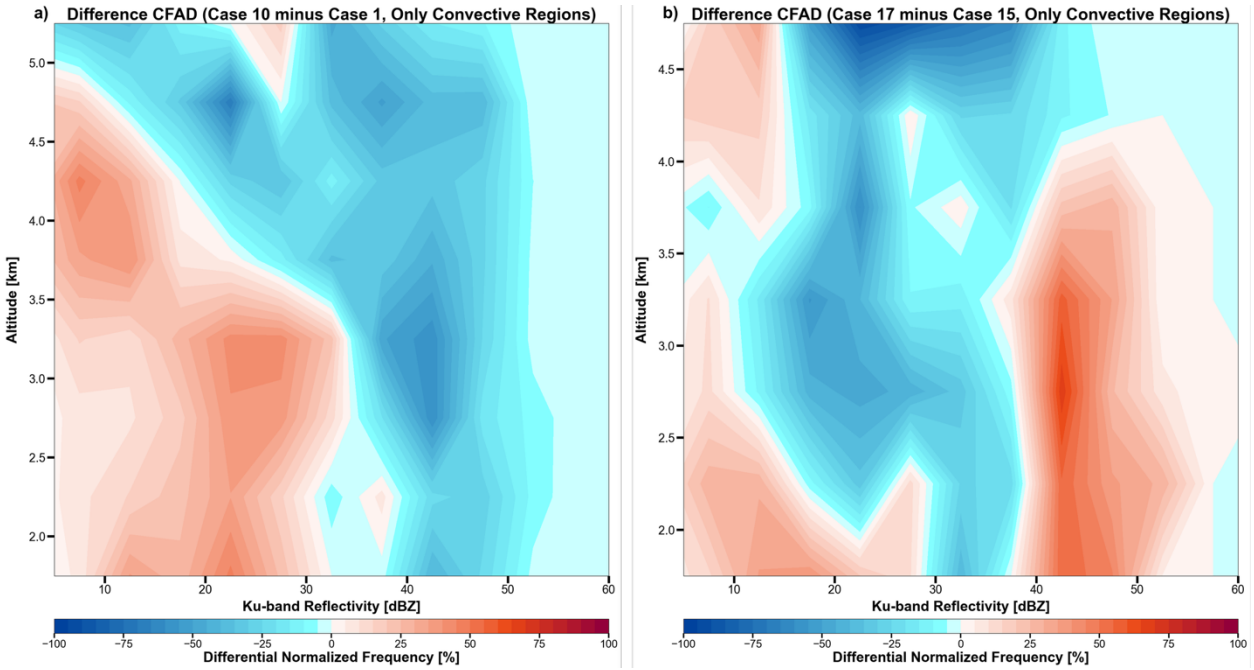

Figure 4.8: (a) Case 1 CFAD subtracted from the Case 10 CFAD and (b) Case 15 CFAD subtracted from the Case 17 CFAD using APR-3 Ku-band reflectivity data from only convective regions, as determined by the ECCO-V convective-stratiform partitioning algorithm. Reflectivity data is binned into 5-dBZ and 0.5-km intervals and normalized by the maximum bin count in each height interval.

4.4 CAMP^{2}Ex Regional Comparisons with Other In Situ TOC Studies

Composite statistical analysis presented in Section 4.3 using CAMP^{2}Ex data revealed large PBL and mid-tropospheric near-storm environmental variabilities within both convective type and case. Notably, the large near-storm variabilities were present even across convective cases sampled during similar MJO phase (Table 4.1; Figures 4.5 and 4.7), thereby exonerating the MJO as the root cause of the variabilities. Resulting from the large variabilities, relationships between convective type and near-storm moisture and wind shear in the PBL and mid layer were mostly weak and statistically insignificant.

Concentrating first on moisture, the lack of statistically significant differences in PBL and mid layer RH between CAMP^{2}Ex convective types (Figure 4.4; Section 4.3.1) is inconsistent with prior tropical West Pacific reanalysis (e.g., Chen et al., 2017) and in situ (e.g., from TOGA COARE, KWAJEX) studies of TOC south and east of the CAMP^{2}Ex domain (e.g., Brown & Zhang, 1997; LeMone et al., 1998; Cetrone & Houze, 2006; Holloway & Neelin, 2009) that attribute enhanced tropospheric moisture to larger, more organized TOC. These differing results may reflect regional variability within the broader tropical West Pacific, though different in situ sampling targets (e.g., linear TOC targeted during TOGA COARE vs. non-linear TOC sampled during CAMP^{2}Ex) and different background synoptic moisture conditions (e.g., MJO, ENSO, and Asian monsoon phases) during sampling periods are also likely culprits. Additionally, inconsistent tropospheric vertical layer definitions over which moisture is calculated across studies may contribute to the differences. To more equitably diagnose potential regional variabilities in near-storm environmental relationships, a more focused comparison of the tropical Northwest Pacific with the tropical West and East Atlantic, where similar instrumentation data from the CPEX series was analyzed using consistent methodologies and layer definitions (Rodenkirch & Rowe, 2024; Rodenkirch & Rowe, 2025), is warranted.

The statistically insignificant CAMP^{2}Ex moisture relationships with convective type align with those found from the CPEX series in the tropical West and East Atlantic (Figure 4.9; Rodenkirch & Rowe, 2024; Rodenkirch & Rowe, 2025), albeit with smaller differences between inflow sonde median RH values in the PBL (0.1%, compared to 2.5% from CPEX(-AW) and 1.0% from CPEX-CV) and mid layer (0.6%, compared to 5.9% from CPEX(-AW) and 1.3% from CPEX-CV).

CAMP^{2}Ex PBL and mid layer moisture are also found to be less variable near organized TOC compared to airborne observations from the CPEX series (Figure 4.9), both when including and excluding sonde observations outside of inflow regions. However, the lesser near-storm moisture variabilities may be an artifact of less expansive flight tracks and sampling around organized TOC during CAMP^{2}Ex (e.g., Figure 4.2b) compared to the CPEX series (Rodenkirch & Rowe, 2024; Rodenkirch & Rowe, 2025). A more notable comparison is how CAMP^{2}Ex median PBL and mid layer RH near both isolated and organized TOC are all (apart from mid layer RH when including non-inflow sondes) in between the medians from the tropical West and East Atlantic (Figure 4.9). Given that the tropical West Pacific is a generally moister basin than across the tropical North Atlantic (e.g., Chen et al., 2017), this result may point to tropical oceanic basin moisture climatologies not necessarily translating to basin near-storm moisture environments. That being said, the CAMP^{2}Ex sampling period coincided with a prevailing weak El Niño that may have contributed to drier near-storm conditions than normal (e.g., Qian et al., 2010; Sullivan et al., 2019; Reid et al., 2023).

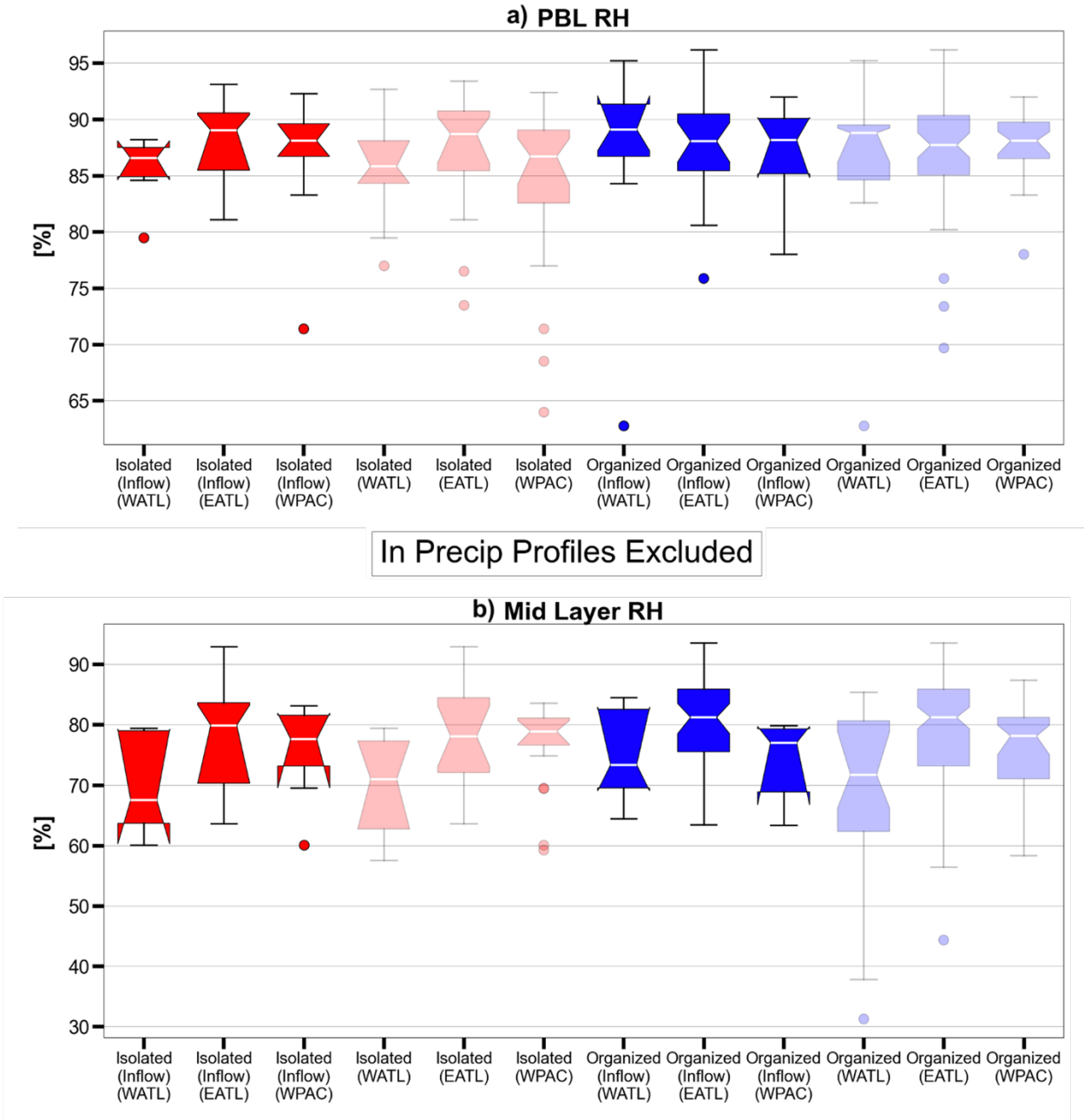

Figure 4.9: Same as Figure 4.4 for CAMP^{2}Ex near-storm sonde observations over the West Pacific (WPAC) basin, except now including CPEX and CPEX-AW near-storm dropsonde observations over the West Atlantic (WATL) basin and CPEX-CV near-storm dropsonde observations over the East Atlantic (EATL) basin.

Regardless, the drier near-storm environments observed during CAMP^{2}Ex likely contributed to a greater role than normal of near-storm wind shear in influencing whether non-linear TOC was isolated or organized, consistent with suggestions of prior studies (e.g., Sakaeda & Torri, 2022;

Chen et al., 2023) and supported by less definitive CAMP^{2}Ex moisture relationships between isolated and organized TOC compared to those of the CPEX series (Figure 4.9). More specifically, PBL shear was statistically significantly greater for organized TOC than isolated TOC both when including and excluding sonde observations outside of inflow regions (Figure 4.6a; Section 4.3.2). Compared to CPEX series observations across the tropical North Atlantic, the PBL shear differences between isolated and organized TOC during CAMP^{2}Ex were much more pronounced, with inflow sonde median PBL shear differences between convective type of 6.7 kts compared to 2.1 kts from CPEX(-AW) and 1.6 kts from CPEX-CV (Figure 4.10a). Outside of the more pronounced differences between convective type, the general relationship of greater near-storm PBL shear with more organized TOC from CAMP^{2}Ex concurs with prior regional studies of the tropical West Pacific, Indian Ocean, and tropical West Atlantic (e.g., Chen et al., 2017; Chudler & Rutledge, 2021; Rodenkirch & Rowe, 2024). However, the CAMP^{2}Ex PBL shear results differ from CPEX-CV results in the tropical East Atlantic (Figure 4.10a; Rodenkirch & Rowe, 2025) that similarly sampled and analyzed non-linear (albeit deeper) TOC, further pointing to regional variability in near-storm environmental relationships with TOC that has been suggested by studies at both the meso-beta scale (e.g., Chen et al., 2017; Galarneau et al., 2023; Muetzelfeldt et al., 2025) and down to smaller, convective process-level scales (e.g., Rodenkirch & Rowe, 2025).

Notably, CAMP^{2}Ex median PBL shear near organized TOC was greater than that for CPEX(-AW) and—at a statistically significant level—CPEX-CV, both when including and excluding sonde observations outside of inflow regions (Figure 4.10a). High PBL shear is historically linked to more organized convection via RKW cold pool interactions (e.g., Rotunno et al., 1988; LeMone et al., 1998). However, RKW theory is primarily related to linear convective organization, and

each of the five sampled CAMP^{2}Ex organized TOC systems were non-linear. Coupled with a lack of cold pool signatures present in the organized TOC sondes with high PBL shear (i.e., > 10 kts; Figure 4.7a), the relationship of CAMP^{2}Ex organized TOC to greater PBL shear is likely attributed to mechanisms unrelated to traditional RKW dynamics, which have been argued to not be as applicable to TOC (e.g., Grant et al., 2018). The CAMP^{2}Ex TOC-PBL shear relationship is also likely not strongly tied to MJO influence, given isolated and organized TOC data being collected during both active and suppressed MJO phases (Table 4.1; Reid et al., 2023). One factor at play may be the proximity of TOC systems to nearby islands, which could introduce sea-land breeze circulations that both enhance local PBL wind shear and invigorate TOC via enhanced near-surface convergence (e.g., Qian, 2008; Jury et al., 2009; Qian et al., 2010, Rios-Berrios et al., 2023). Another alternate mechanism may be countergradient transport of momentum downward into the PBL by the organized TOC systems (e.g., LeMone et al., 1984) that acts to enhance shear in the PBL. Investigation into this mechanism, as well as the effects of sea-land breezes, within CAMP^{2}Ex TOC observations is left for future work.

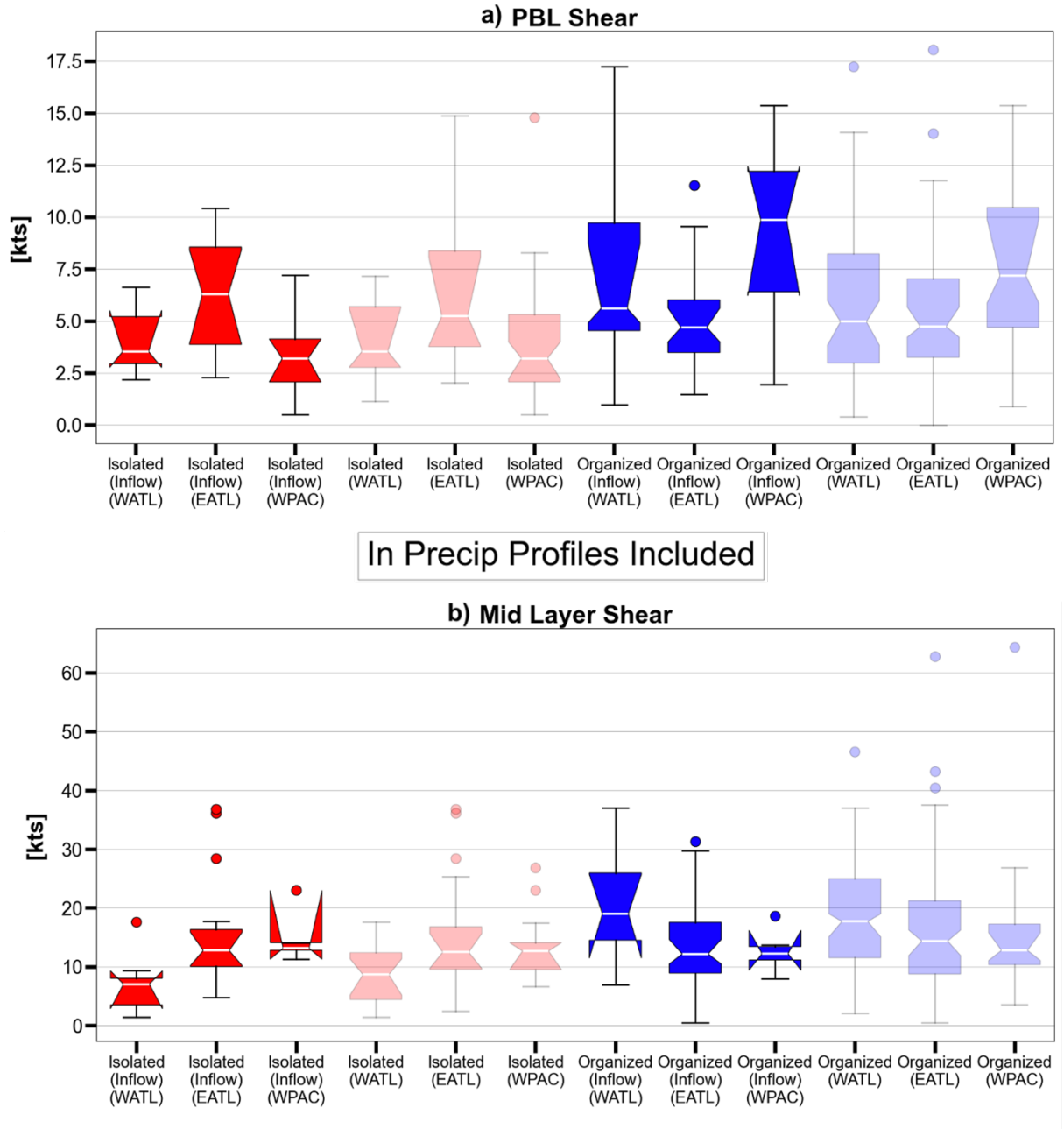

Figure 4.10: Same as Figure 4.6 for CAMP²Ex near-storm sonde observations over the West Pacific (WPAC) basin, except now including CPEX and CPEX-AW near-storm dropsonde observations over the West Atlantic (WATL) basin and CPEX-CV near-storm dropsonde observations over the East Atlantic (EATL) basin.

4.5 Conclusions

This chapter presents an investigation into near-storm moisture and vertical wind shear relationships with TOC structure below the melting level in the tropical Northwest Pacific using a unique suite of coincident, high-resolution airborne observations from the NASA 2019 CAMP^{2}Ex field campaign. Analysis of CAMP^{2}Ex dropsondes, APR-3 radar, and supplemental ONR PISTON experiment radiosondes focusing on convective inflow regions revealed large spreads in RH and wind shear both within and across isolated (i.e., single-core) and organized (i.e., multi-core) TOC systems. Notable trends with TOC structure emerged amongst the variability and were subsequently evaluated against similar analyses using NASA 2017 CPEX and CPEX-AW data in the tropical West Atlantic (Rodenkirch & Rowe, 2024) and NASA 2022 CPEX-CV data in the tropical East Atlantic (Rodenkirch & Rowe, 2025) to assess regional variability in TOC-environment relationships. Collectively, the CAMP^{2}Ex near-storm analysis and subsequent regional comparisons with CPEX series analyses convey the following key insights:

- In the tropical Northwest Pacific, near-storm wind shear in the PBL was stronger for organized TOC at a statistically significant level compared to isolated TOC. This TOC-PBL shear relationship was notably stronger than in the West Atlantic (CPEX(-AW)) and East Atlantic (CPEX-CV) using similar observations and analyses.
- RH in the PBL and between the top of the PBL and the melting level (i.e., mid layer) were statistically similar for CAMP^{2}Ex isolated and organized TOC.
- Different strengths and signs of relationships between convective type (i.e., isolated vs. organized TOC) and near-storm RH and wind shear below the melting level exist between the tropical Northwest Pacific (CAMP^{2}Ex), West Atlantic (CPEX(-AW)), and East

Atlantic (CPEX-CV), signaling potential regional variability in TOC-environment relationships.

The results of this chapter help address a notable regional gap in the literature pertaining to TOC relationships with near-storm environments in the tropical Northwest Pacific using modern, high-resolution in situ observations. Observed differences in near-storm moisture and shear relationships between the tropical Northwest Pacific, West Atlantic, and East Atlantic support prior studies suggesting regional variabilities in TOC-environment relationships using lower spatiotemporal resolution reanalysis data (e.g., Chen et al., 2017; Galarneau et al., 2023; Muetzelfeldt et al., 2025) and extend these studies' findings down to finer, convective process-level scales. The CAMP^{2}Ex field campaign, coupled with the CPEX field campaign series, also highlights the value of high-resolution in situ measurements as essential supplements to satellite, reanalysis, and CRM datasets, in that large near-storm environmental variabilities both within and across TOC systems are observed that are otherwise difficult to capture by lower spatiotemporal resolutions and imperfect model parameterizations.

The large near-storm environmental variabilities observed during CAMP^{2}Ex may help explain the observed lack of definitive moisture relationships with convective type. Contributions to the variability likely stem from compounding influences of different MJO, ENSO, and Asian monsoon phases present during the six-week CAMP^{2}Ex sampling period (Section 4.2.1), along with TOC sampling in diverse aerosol environments known to influence TOC (e.g., Rosenfeld, 1999; Yuan et al., 2011; Storer et al., 2014) that was a primary focus of CAMP^{2}Ex (Reid et al., 2023). In particular, a prevailing El Niño throughout the duration of the campaign resulted in drier and more

drought-like conditions in the Northwest Pacific compared to climatology (Reid et al., 2023). The drier conditions may have suppressed typically more robust moisture relationships with TOC structure that have been observed in other subregions of the tropical West Pacific to the south and east of the CAMP^{2}Ex domain (e.g., Brown & Zhang, 1997; LeMone et al., 1998; Cetrone & Houze, 2006; Holloway & Neelin, 2009), while simultaneously enhancing the wind shear influence (Section 4.3.1) in the drier environments as suggested by prior studies (e.g., Sakaeda & Torri, 2022; Chen et al., 2023; Rodenkirch et al., 2025).

Extension of near-storm moisture and wind shear analysis to TOC intensity via CFAD comparisons of APR-3 Ku-band reflectivity (Section 4.3.2) found more intense CAMP^{2}Ex TOC to be associated with a moister PBL and weaker mid layer wind shear. However, APR-3 sampling close to the centers of TOC systems that most adequately represent intensity was rare—particularly amongst organized TOC—resulting in the TOC intensity CFAD analysis only being comprised of two TOC case comparisons that discourage generalized conclusions. Given this analysis limitation, more case comparisons are clearly needed to claim definitive links between TOC intensity and near-storm moisture and wind shear in the tropical Northwest Pacific.

Future studies should expand the analysis of this chapter using observational data from other regions with similar methodologies that promote easier interstudy comparisons. Future research should also consider other mesoscale environmental influencers like aerosols, dynamical convergence, and gravity waves. While each of these variables can notably impact TOC by themselves, the degree to which each matter relative to the magnitudes of the others needs to be elucidated for more holistic understanding and prediction of TOC. Toward this effort, high-

resolution idealized numerical modeling constrained by field campaign observations like CAMP^{2}Ex could help quantify near-storm environmental relationships and the individual roles of environmental components (e.g., Rodenkirch et al., 2025). Regional variabilities in TOC-environment relationships between the tropical Northwest Pacific, West Atlantic, and East Atlantic illuminated by the CAMP^{2}Ex and CPEX field campaigns also discourages application of the CAMP^{2}Ex results to other tropical oceanic regions. Consequently, extension of similar near-storm environmental analysis to other tropical oceanic basins like the Indian Ocean and other Pacific basins, preferably with identical tropospheric vertical layer definitions for more equitable subsequent regional comparisons, is strongly encouraged.

Chapter 5

Vertical Wind Shear and Moisture Influences on Tropical Oceanic Convection in Idealized Numerical Model Simulations

5.1 Introduction

Deep tropical oceanic convection (TOC) is a prevalent feature of the tropical atmosphere. It plays key roles in driving both regional and global weather and climate, including influences on the large-scale tropical atmospheric circulation through three-dimensional (3-D) redistribution of mass, heat, moisture, and momentum (e.g., Zipser 1977; Alexander & Young, 1992; Young et al., 1995; Brown & Zhang, 1997; LeMone et al., 1998; Saxen & Rutledge, 1998; Saxen & Rutledge, 2000; Tompkins, 2001; Cetrone & Houze, 2006; Mechem et al., 2006; Liu & Liang, 2010; Grant et al., 2020; Mulholland et al., 2021; Chen et al., 2023; Maybee et al., 2024). Their 3-D convective cloud structures also significantly impact radiative fluxes, particularly near cloud-top levels (e.g., Hartmann et al., 2001; Tobin et al., 2012; Del Genio & Chen, 2015; Hartmann, 2016; Grant et al., 2020; Bony et al., 2020; Pilewskie & L'Ecuyer, 2022; Pilewskie & L'Ecuyer, 2026). TOC frequently produces thermodynamically driven cold pools, which can, amongst many impacts, initiate new deep convection and alter planetary boundary layer (PBL) characteristics (e.g.,

---

The following chapter is a reformatted preprint of Rodenkirch, B. D., Rowe, A. K., & Rios-Berrios, R. (2025). *Journal of Geophysical Research: Atmospheres*. (In Review)

Esbensen & McPhaden, 1996; Saxen & Rutledge, 1998; Feng et al., 2015; Rowe & Houze, 2015; Chandra et al., 2018; Houze, 2018; Touzé-Peiffer et al., 2021; Sakaeda & Torri, 2023). Accurate TOC representation and parameterization is therefore critical for the success of weather and climate modeling efforts. However, challenges persist in predicting and modeling TOC and their influences. A notable shortcoming of many weather and climate modeling efforts is accurate 3-D TOC spatial organization representation (e.g., Randall et al., 2003; Arakawa, 2004; Rio et al., 2019), ranging from horizontal structure (e.g., extent) and vertical structure (e.g., bottom- vs. top-heavy, intensity) of individual TOC systems to collective spatial organization (e.g., clustered vs. random) of numerous TOC systems across a broad region.

Challenges in understanding and modeling TOC spatial organization can be partly attributed to well-recognized, yet inconclusive, influences of local tropospheric moisture and vertical wind shear (hereafter referred to as "wind shear") conditions on how TOC organizes. Wind shear influences on TOC spatial organization arguably remain less understood than moisture influences, with wind observations largely relying on in situ data collection, while moisture observations benefit from longer records of satellite remote sensing profiling (e.g., Kummerow et al., 1998; Chahine et al., 2006). Reanalyses can supplement limited wind observations but are inherently limited in spatiotemporal resolution and reliance on imperfect underlying models in data-sparse regions like tropical oceans (Chen et al., 2017).

Field campaigns collecting in situ wind shear observations, with a historic focus on the western Pacific (e.g., TOGA-COARE, EMEX, PISTON), have linked greater low-tropospheric wind shear to greater linearity of individual mesoscale convective systems (MCSs) (Alexander & Young,

1992; LeMone et al., 1998; Chudler & Rutledge, 2021), in agreement with traditional RKW theory relating low-tropospheric wind shear to linear convective organization via cold pool interactions (Rotunno et al., 1988). However, RKW theory has been shown in cloud-resolving models (CRMs) to not be as applicable to oceanic convective system evolution as to land-based linear MCSs. More specifically, cold pools over tropical oceans tend to be much weaker than over land due to typically moister prevailing environmental conditions (e.g., Lane & Moncrieff, 2015), and TOC updrafts have been shown to experience enhanced entrainment of cold pool air that instead inhibits convective development and sustainment rather than promoting it (Grant et al. 2018).

Deep tropospheric (hereafter referred to as "deep layer") wind shear has garnered attention in numerous studies using in situ observational (e.g., Saxen & Rutledge, 2000) and reanalysis (e.g., Igel & van den Heever, 2015; Chen et al., 2017) datasets to better understand tropical oceanic MCS characteristics and lifecycle. Together, these observational studies link greater deep layer wind shear to more intense and horizontally larger individual TOC systems. Studies using CRMs also find that enhanced low-tropospheric and deep layer wind shear both favor greater TOC spatial organization (Tompkins, 2001; Robe & Emanuel, 2001; Anber et al., 2014; Cheng et al., 2020; Grant et al., 2020; Mulholland et al., 2021). However, most of these studies focus on individual storms and not collective populations of storms. Studies that do focus on collective TOC spatial organization tend to focus more on its relationships with moisture, notably finding a consistent positive correlation with moisture in the lower free troposphere (LFT) (e.g., Brown & Zhang, 1997; LeMone et al., 1998; Tompkins, 2001; Bretherton et al., 2004; Cetrone & Houze, 2006; Holloway & Neelin, 2009; Chen et al., 2017; Schiro et al., 2020; Wolding et al., 2022; Chen et al., 2023). CRM studies investigating collective TOC organization seldom include background winds,

let alone wind shear, and observational studies tend to analyze moisture and wind shear without consideration of how the two may act in tandem with one another. A few notable studies that do assess the joint effects of moisture and wind shear, however, have suggested that the role of each in influencing TOC can be dependent on the magnitude of the other, with wind shear effects on TOC development and organization particularly enhanced in drier environments that would otherwise be detrimental to TOC (and vice versa) (Sakaeda & Torri, 2022; Peters et al., 2022). These studies support continued investigation into the coupled role of wind shear and moisture in together influencing TOC.

Overall, despite progress from previous studies linking TOC spatial organization to wind shear, sample sizes of TOC systems remain limited, especially outside of quasi-linear TOC. Regional dependencies of wind shear relationships with TOC spatial organization (e.g., Chen et al., 2017) also behoove collection and study of observations from a diverse array of tropical oceanic regions. Toward addressing these limitations, the National Aeronautics and Space Administration (NASA) executed a three-part field campaign series across the tropical North Atlantic: the Convective Processes Experiment (CPEX, 2017; Chen & Zipser, 2017), CPEX—Aerosols & Winds (CPEX-AW, 2021; Skofronick-Jackson et al., 2021), and CPEX—Cabo Verde (CPEX-CV, 2022; Zawislak et al., 2022). The NASA CPEX series collected near-storm data suitable to study the structure and spatial organization of a variety of TOC types across a wide range of local environmental conditions, including deep layer wind shear imposed by prevailing boreal summer climatological features like the subtropical jet in the West Atlantic and West African Monsoon (WAM) flow and the African Easterly Jet in the East Atlantic. Rare, coincident, and high-resolution airborne profiling of 3-D TOC structure and near-storm environments from the CPEX

series revealed larger and more intense TOC systems to generally be associated with both greater deep layer wind shear and greater LFT moisture (Rodenkirch & Rowe, 2024; Martinez et al., 2025). However, the inability to separate individual deep layer wind shear and LFT moisture influences on TOC spatial organization limits the ability to evaluate the relative influence of either. This constraint is an inherent, prevailing limitation of observational studies and thus motivates the use of an idealized CRM to isolate the impacts of shear from that of moisture on the spatial organization of a population of TOC.

With the benefit of NASA CPEX series observations to inform realistic model wind shear and moisture values (Rodenkirch & Rowe, 2024), this chapter will aim to address the question *how do local environmental wind shear and LFT moisture together influence collective TOC spatial organization?*

To address this research question, the format of the chapter is as follows. Section 5.2 offers a description of the idealized model setup, sensitivity test designs, and metrics used for analysis. Section 5.3 presents the results of analysis with regard to how local environmental deep layer wind shear in varying LFT moisture environments influences collective TOC spatial organization and intensity. Section 5.4 provides a discussion of the results in the context of prior studies, while Section 5.5 concludes the chapter with main takeaways from the analysis and proposed steps for future research.

5.2 Experimental Design

5.2.1 Numerical Model

Idealized numerical model simulations of TOC with varying environmental deep layer wind shear and LFT moisture were executed using Cloud Model 1 (CM1; Bryan & Fritsch, 2002), Release 21.1 (R21.1). CM1 is a 3-D, non-hydrostatic, and non-linear CRM designed to study atmospheric phenomena, such as TOC, in an idealized framework. For the purposes of this chapter, CM1 is configured to produce convection permitting model (CPM) simulations similar to the framework of Bretherton et al. (2005). The Rapid Radiative Transfer Model for general circulation models (RRTMG) (Iacono et al., 2008) is utilized for the radiation scheme, and surface fluxes for heat and moisture are turned on. Incoming top-of-atmosphere solar radiation is a constant 650.83 W m^{-2}, and thus there is no diurnal cycle. Implementation of a diurnal cycle was tested separately and did not notably affect the results of this chapter. PBL turbulence is parameterized using a Louis-type scheme (Bryan & Rotunno, 2009), and model microphysics are represented by the Morrison double-moment bulk scheme (Morrison et al., 2009). The Thompson double-moment bulk microphysics scheme (Thompson et al., 2008) was separately tested and did not affect the main results of this chapter. CM1 is configured with a fully compressible dynamical core (Klemp & Wilhelmson, 1978) and no Coriolis acceleration. The cutoff diameter for drop breakup is set at 200 x 10^{-6} m, and convection is set to freely initiate without any forced initial perturbation technique.

CM1 is spatially set to a 576 x 576 km square domain to allow for the coexistence of numerous convective systems within the model domain (Bretherton et al., 2005). A uniform horizontal grid spacing of 1-km and periodic lateral boundary conditions are implemented with the goal of

resolving individual convective systems without domain-imposed limited lifetimes. Model depth extends to 25 km with a vertically stretched grid (Wilhelmson & Chen, 1982) with 0.1-km spacing below 2.5 km expanding to 0.5-km spacing above 7 km. Vertical boundary conditions are semi-slip at the bottom and free-slip at the top. CM1 runtime is set to 25 days to allow for model spin up of persistent spatial clustering of a population of convective systems (Grant et al., 2020). Sea surface temperatures (SSTs) are uniformly fixed at 302.15 K, consistent with typical tropical North Atlantic values observed during the CPEX field campaign series, though increased 1-2 K to create more robust TOC systems via enhanced surface fluxes. A summary of all the CM1 configurations can be found in Table 5.1.

Table 5.1: Summary of the CM1 R21.1 configuration.

Attribute	**Value/Setting**
Runtime	25 days
Horizontal grid spacing type	Uniform
Horizontal grid spacing	1000 m
Vertical grid spacing type	Stretched; Wilhelmson & Chen (1982)
Vertical grid spacing (below 2500 m)	100 m
Vertical grid spacing (above 7000 m)	500 m
Vertical grid top	25000 m
Vertical coordinate	Height (m)
Number of x, y, z grid points	577 x 577 x 77
Bottom boundary condition	Semi-slip
Top boundary condition	Free-slip
Lateral boundary conditions	Periodic
Simplified physics scheme	CPM; Bretherton et al. (2005)
Microphysics scheme	Morrison double-moment; Morrison et al. (2009)
Boundary layer physics scheme	Louis-type; Bryan & Rotunno (2009)
Subgrid turbulence scheme	Mesoscale modeling with Louis-type PBL parameterization; Bryan & Rotunno (2009)
Radiation scheme	RRTMG; Iacono et al. (2008)
Diurnal cycle	None
Surface fluxes of heat & moisture	Yes
Sea surface temperature	302.15 K
Diffusion	Sixth order
Second- & sixth-order difference coefficient	75-0.04
Rayleigh dampening	Yes; above 20000 m AGL
Dissipative heating	Yes
Fully compressible	Yes; Klemp & Wilhelmson (1978)
Coriolis acceleration	No
Specified balance assumption for initial 3-D pressure field	Non-hydrostatic
Convection initiation technique	No perturbations
Cutoff diameter for drop breakup	200×10^{-6} m

5.2.2 BASE Simulation

In order to address the proposed science question, a baseline (BASE) simulation is first executed as a control for which subsequent sensitivity simulations using differing environmental deep layer wind shear and LFT moisture are evaluated against. Building upon the model configurations described in Section 5.2.1, CM1 domain-mean temperature, moisture, and wind profiles are initialized by and continuously nudged towards an inputted atmospheric sounding. Nudging is implemented to prevent the environment from changing during integration time, which would obscure the effects of the imposed vertical wind shear and LFT moisture on TOC spatial organization. Nudging commences after an initial 24 hour period that allows for faster initial spontaneous convective generation. Uniform 5 m s^{-1} easterly winds at all heights are set as the initialized atmospheric wind profile (Figure 5.1b). As such, the BASE simulation has no domain-mean vertical wind shear. The initialized thermodynamic sounding is predominantly the mean sounding of non-precipitating inflow environments of multi-core TOC sampled by CPEX series dropsondes (Figure 5.1a; Rodenkirch & Rowe, 2024), in order that the simulation environment is immediately favorable for convective development. This mean sounding is interpolated to 10-hPa vertical spacing, extending from 1000 hPa to 300 hPa. Above 300 hPa and at the surface, for which the CPEX dropsondes did not sample, thermodynamic values representing typical moist tropical climatology are used (Dunion, 2011). Consequent domain-mean LFT relative humidity (RH) of the BASE simulation is 76%, with the LFT being defined onward as extending from the top of the PBL (defined as 900 mb) up to the freezing level (~570 mb). Hereafter, this BASE LFT RH will be denoted as RH-B.

Resulting domain-wide horizontal distribution of TOC after the 25-day BASE simulation runtime is depicted in Figure 5.2a. TOC systems in BASE exhibit realistic convective cores, stratiform (e.g., brightband) regions, and anvils (Figures 5.2c, 5.2d), thereby providing confidence in model and simulation setups toward addressing the science objectives of this chapter. Additionally, domain averages in rain rate (~4.6 mm day^{-1}), total precipitable water (TPW, ~58.5 mm), and domain-wide maximum updraft velocity (~26.3 m s^{-1}) are all consistent with realistic tropical oceanic environments (Stephens, 1990; Heymsfield et al., 2010; Adler et al., 2012).

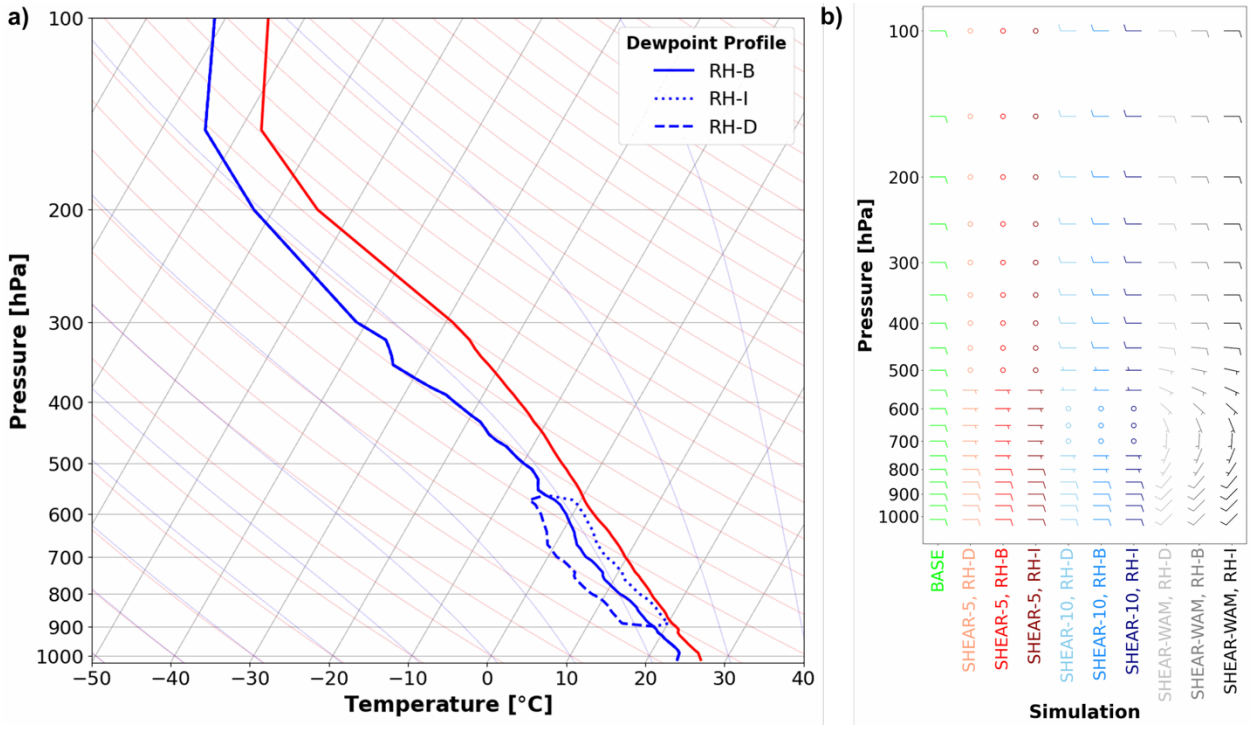

Figure 5.1: (a) Thermodynamic skew-T diagrams of temperature (red) and dewpoint (blue), and (b) wind profiles (full barb = 5 m s^{-1}, half barb = 2.5 m s^{-1}) for each CM1 simulation.

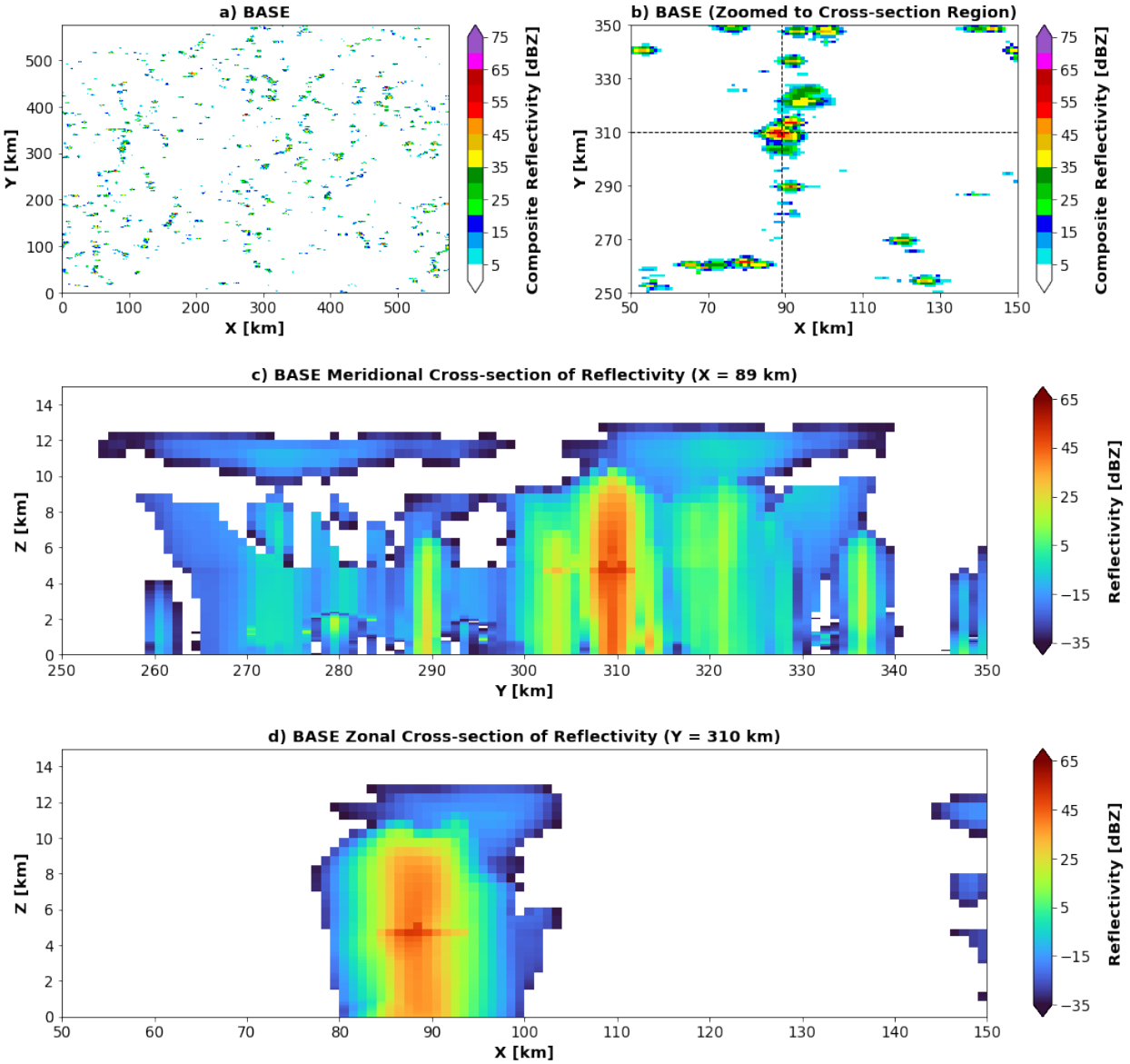

Figure 5.2: BASE (a) plan view simulated composite reflectivity, (b) zoomed-in view of a convective system from (a), (c) meridional cross-section of simulated reflectivity through the convective system in (b), and (d) zonal cross-section of simulated reflectivity through the convective system in (b) during the last hour of the simulation. Vertical and horizontal dashed black lines in (b) denote meridional and zonal cross-section locations for (c) and (d), respectively.

5.2.3 Sensitivity Simulations

To investigate local environmental wind shear influences on collective TOC spatial organization in the context of LFT moisture variability, nine sensitivity simulations using a variety of deep layer wind shear and LFT moisture combinations are executed. As with BASE, all sensitivity

simulations abide by the model configurations described in Section 5.2.1. Additionally, each sensitivity simulation is initialized with the same atmospheric sounding as BASE. However, after 24 hours, each sensitivity simulation domain-mean environment is continuously nudged towards one of three deep layer wind shear profiles and one of three LFT moisture profiles (note: each sensitivity simulation is still nudged toward the initialized temperature profile identical to BASE).

The three deep layer shear profiles are as follows, with the deep layer being defined as extending from 900 mb (i.e., PBL top) to 400 mb: SHEAR-5 (5.0 m s^{-1} unidirectional westerly shear), SHEAR-10 (10.0 m s^{-1} westerly shear), and SHEAR-WAM (9.2 m s^{-1} northeasterly shear) (Figure 5.1b). Chosen wind shear magnitudes and ranges are informed by the high-resolution near-storm wind observations collected by dropsondes and the Doppler Aerosol WiNd Lidar (Kavaya et al., 2014; Greco et al., 2020) over a variety of atmospheric conditions during the CPEX campaign series (Rodenkirch & Rowe, 2024). Wind speeds and directions are linearly adjusted from 900 mb to 400 mb to create each deep layer wind shear profile, with winds below 900 mb and above 400 mb equal to the 900 mb and 400 mb winds, respectively. Sensitivities to other shapes of vertical profiles of horizontal winds are left for future studies. SHEAR-WAM refers to deep layer wind shear associated with typical WAM flow of a backing wind profile with height with low-tropospheric southwesterly winds. In addition to supplying a wind profile that includes both zonal and meridional directional shear to sensitivity simulations, the WAM is a prevalent feature of East Atlantic boreal summer climatology and a key driver of boreal summer TOC in the East Atlantic (Parker et al., 2005; Bickle et al., 2022), thus justifying the inclusion of its characteristic wind shear in this chapter.

The three distinct LFT moisture profiles of the sensitivity simulations are as follows: RH-D (LFT RH = 60%), RH-I (LFT RH = 90%), and the aforementioned RH-B (LFT RH = 76%) (Figure 5.1a). Similar to wind shear, chosen LFT RH magnitudes and ranges are informed by the high-resolution near-storm moisture observations collected by CPEX series dropsondes (Rodenkirch & Rowe, 2024). To create the RH-D and RH-I LFT moisture profiles, respectively, an amount of water vapor equivalent to the difference between the desired RH and RH-B is subtracted or added to each vertical level within the LFT, such that each vertical level's respective RH decreases or increases uniformly. Coupling each of the three distinct LFT moisture profiles with each of the three distinct deep layer wind shear profiles produces nine sensitivity simulations to evaluate against one another and BASE: "SHEAR-5, RH-D", "SHEAR-5, RH-B", "SHEAR-5, RH-I", "SHEAR-10, RH-D", "SHEAR-10, RH-B", "SHEAR-10, RH-I", "SHEAR-WAM, RH-D", "SHEAR-WAM, RH-B", and "SHEAR-WAM, RH-I". Thermodynamic profiles and vertical profiles of horizontal winds for each of these unique sensitivity simulations are illustrated in Figure 5.1.

5.2.4 TOC System Identification, Organization, and Intensity

Quantitative spatial analysis of TOC precipitating systems and their updrafts in the CM1 simulations is executed with the help of the Tracking and Object-Based Analysis of Clouds (TOBAC) feature detection algorithm (Heikenfeld et al., 2019; Sokolowsky et al., 2024). Domain-wide TOC spatial organization is quantified using TOBAC-identified TOC systems and the I_{org} non-randomness convective organizational index (Tompkins & Semie, 2017; Wing et al., 2018). Utilizing nearest-neighbor distances between convective systems to characterize domain-wide convective organization on a scale of 0 to 1 (with larger I_{org} values equating to a greater degree of

collective spatial clustering, or spatial organization, as hereafter referred), I_{org} is adept at assessing domain-wide spatial organization of convection. For both TOBAC and I_{org}, individual TOC systems are identified using a 30-dBZ composite reflectivity threshold across 1 km^2 area (i.e., at least one grid point), while TOC updraft areas are identified with TOBAC using a 1 m s^{-1} vertical velocity threshold anywhere in the vertical column of grid points contained within a 30-dBZ TOC system. Given that the 1 m s^{-1} vertical velocity threshold can be met at any height level, an identified updraft area composed of multiple grid points may not necessarily serve as a proxy for updraft width at any individual height level, but rather the collective horizontal extent of an updraft throughout the vertical.

Five distinct metrics are used to evaluate TOC intensity. Maximum 30-dBZ reflectivity height (e.g., DeMott & Rutledge, 1998), a common proxy for updraft strength through inferred lofted hydrometeor height (e.g., Balogun et al., 2020), is compiled for each vertical column within individual TOC systems and averaged to assess convective intensity of TOC systems within each simulation. Maximum updraft velocity within individual TOC systems is similarly compiled and averaged as a metric of convective intensity. Mean convective updraft mass flux is calculated for each height level in each simulation using 30-dBZ composite reflectivity and 1 m s^{-1} vertical velocity thresholds, with the 0-2.5 km layer of particular focus as a characteristic convective inflow layer (Mulholland et al., 2021). Domain-wide surface rain rate (excluding non-raining grid points) and maximum convergence are also included as measures of convective intensity, as they do not necessarily correlate with maximum 30-dBZ height, updraft velocity, nor updraft mass flux as much as the latter three correlate with each other, and therefore offer more independent alternate proxies for intensity. Each aforementioned intensity and spatial metric for each simulation's

population of individual TOC systems is averaged and analyzed over the last five days of each simulation to allow for model spin up time and stabilization denoted by persistent collective spatial organization. Statistical significance for each metric mean is assessed via a 95% confidence interval calculated by bootstrapping each mean 10,000 times.

For analysis of collective TOC vertical structure, vertical velocity profiles located within each 30-dBZ TOC system occurring over the last five days of each simulation are binned into two-dimensional (2-D) histograms with 1-m s^{-1} and 0.5-km intervals. Vertical velocity is binned from -10 m s^{-1} to 30 m s^{-1}, and height bins extend from 0 km to 20 km. The logarithm of each 2-D histogram is taken to better distinguish infrequent, but important, large vertical velocities. The subsequent logarithmic 2-D histogram is normalized by the maximum bin count in each height interval to create logarithmic Contoured Frequency by Altitude Diagrams (CFADs) (Yuter & Houze, 1995), allowing for frequency comparisons across a given height level. Subsequent so-called "logarithmic difference CFADs" are produced by subtracting one simulation's logarithmic CFAD from another. These logarithmic difference CFADs allow for investigation of collective vertical structure and intensity differences between TOC systems produced by different simulations of varying deep layer wind shear and LFT moisture (see Section 5.3.2, Yuter & Houze, 1995).

5.3 Results

5.3.1 Collective Horizontal TOC Organization: Spatial Organization and Area

To assess collective horizontal TOC organization in the context of varying deep layer wind shear and LFT moisture, domain-wide spatial organization and mean convective area for the population

of individual TOC systems is intercompared across each simulation. Compared to BASE (Figure 5.2a), the sensitivity simulations each begin to produce notable TOC spatial organization patterns after 15 days, similar to those that can be seen in Figure 5.3 during the last hour of each simulation. Wind shear simulations with LFT RH equal to (RH-B) or less than (RH-D) BASE produce broad bands of clustered convection oriented and propagating parallel to the deep layer shear vector. Simulations with reduced LFT moisture notably contain fewer of these broad bands of clustered TOC. The result is RH-D simulations having the greatest degrees of I_{org} spatial organization both within each unique shear trio and relative to BASE that are statistically significant using the 95% confidence interval (Table 5.2). Meanwhile, wind shear simulations with increased LFT RH (RH-I) produce markedly different TOC spatial organization, with more numerous and narrower streets of clustered TOC (compared to the RH-B and RH-D shear simulations) that are oriented perpendicular, yet still propagating parallel, to the deep layer shear vector. Of note is the apparent lack of spatially organized TOC in the SHEAR-WAM, RH-I simulation (Figure 5.3i). However, an hourly animation of SHEAR-WAM, RH-I composite reflectivity (not shown) reveals a combination of aforementioned spatial organization patterns. Broad bands of clustered TOC oriented and propagating parallel to the deep layer shear vector–consistent with RH-B and RH-D simulations–coexist with narrow TOC streets oriented perpendicular, yet still propagating parallel, to the deep layer shear vector–consistent with other RH-I simulations. Proposed mechanisms for the formation of markedly different spatially organized TOC clusters for the RH-I simulations compared to the RH-B and RH-D simulations will be discussed in Section 5.4.1.

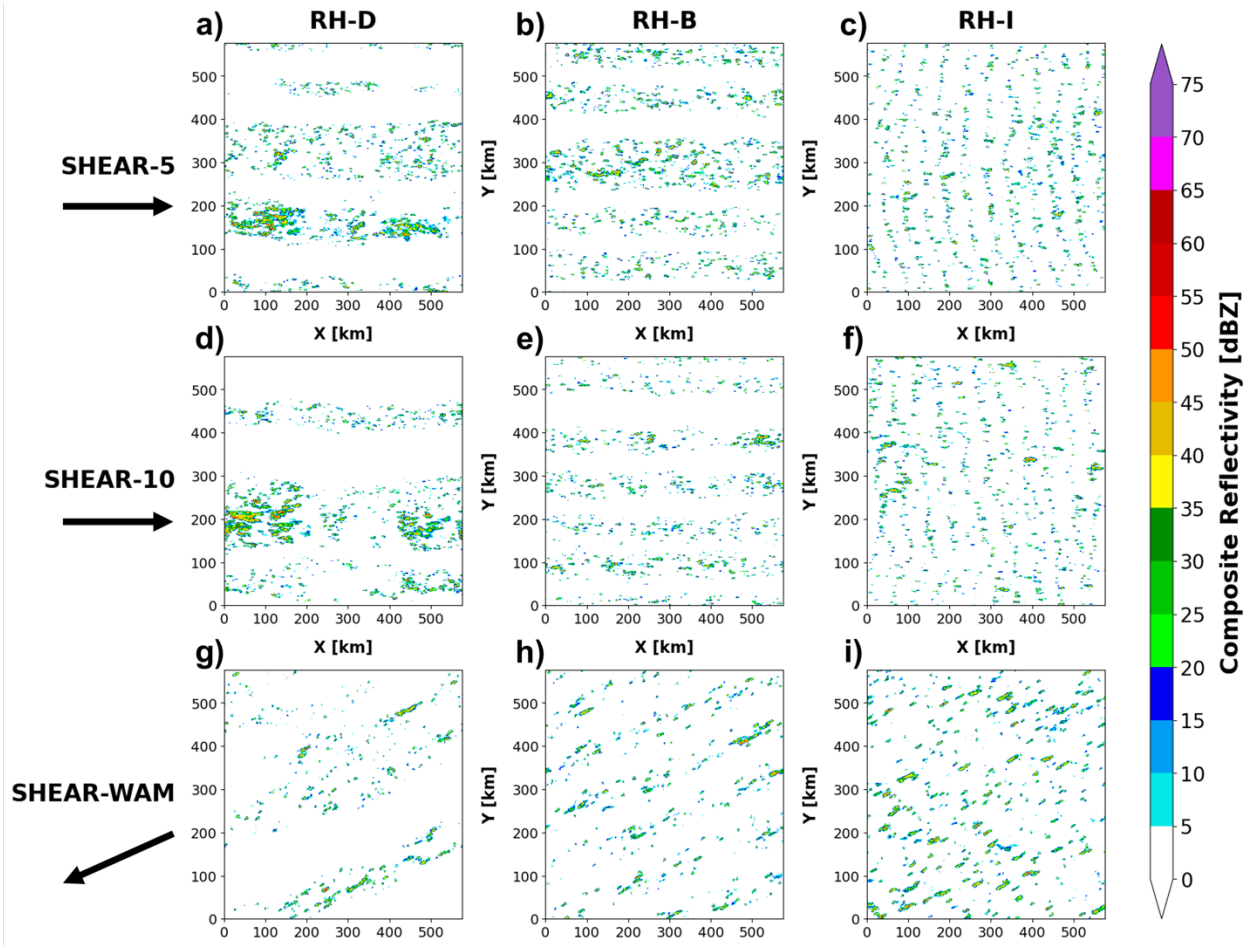

Figure 5.3: Same as Figure 5.2a, except for (a) SHEAR-5, RH-D, (b) SHEAR-5, RH-B, (c) SHEAR-5, RH-I, (d) SHEAR-10, RH-D, (e) SHEAR-10, RH-B, (f) SHEAR-10, RH-I, (g) SHEAR-WAM, RH-D, (h) SHEAR-WAM, RH-B, (i) SHEAR-WAM, RH-I during the last hour of the simulation. Each arrow below the deep layer shear labels denotes the direction of the deep layer shear vector for each simulation in the given row.

Table 5.2: Mean statistics (bolded and underlined) for each CM1 simulation. Means are calculated for data across the last 5 days of each simulation using hourly data outputs. Values above and below each mean indicate the 95% confidence interval for statistical significance, calculated via bootstrapping the mean 10,000 times.

Statistic	BASE	SHEAR-5, RH-D	SHEAR-5, RH-B	SHEAR-5, RH-I	SHEAR-10, RH-D	SHEAR-10, RH-B	SHEAR-10, RH-I	SHEAR-WAM, RH-D	SHEAR-WAM, RH-B	SHEAR-WAM, RH-I
I_{org} mean	0.656 **0.653** 0.650	0.742 **0.739** 0.737	0.634 **0.632** 0.630	0.657 **0.655** 0.652	0.727 **0.724** 0.722	0.649 **0.647** 0.644	0.630 **0.628** 0.626	0.754 **0.751** 0.748	0.684 **0.681** 0.677	0.641 **0.637** 0.634
TOC system area mean [km^2]	6.96 **6.88** 6.81	18.26 **17.41** 16.60	9.07 **8.97** 8.87	7.49 **7.41** 7.34	10.86 **10.61** 10.38	7.53 **7.42** 7.32	7.57 **7.46** 7.36	12.59 **12.30** 12.02	17.01 **16.70** 16.38	22.38 **22.02** 21.67
TOC system updraft area mean [km^2]	2.42 **2.40** 2.38	5.45 **5.29** 5.14	3.29 **3.27** 3.24	3.34 **3.32** 3.29	4.17 **4.11** 4.05	3.27 **3.23** 3.20	3.77 **3.73** 3.70	5.88 **5.77** 5.67	7.00 **6.88** 6.76	9.37 **9.23** 9.09
Number of TOC systems mean	392.00 **388.33** 384.66	525.67 **517.28** 509.16	621.04 **613.01** 604.73	546.88 **543.63** 540.48	525.39 **519.81** 514.10	506.88 **502.15** 497.40	519.87 **516.60** 513.23	216.54 **213.08** 209.63	243.24 **239.71** 236.26	286.90 **284.42** 281.92
TOC system max 30-dBZ height mean [km]	4.00 **3.99** 3.98	4.51 **4.50** 4.49	3.93 **3.92** 3.91	3.60 **3.59** 3.58	3.40 **3.39** 3.38	2.99 **2.98** 2.97	2.86 **2.85** 2.84	2.96 **2.95** 2.94	3.34 **3.33** 3.32	3.45 **3.44** 3.43
TOC system mean max updraft velocity [m s^{-1}]	3.63 **3.62** 3.60	3.48 **3.47** 3.46	3.58 **3.57** 3.56	3.61 **3.60** 3.59	3.37 **3.36** 3.35	3.27 **3.25** 3.24	3.09 **3.08** 3.07	3.20 **3.18** 3.17	3.07 **3.06** 3.05	3.16 **3.15** 3.14
Rain rate domain mean [mm hr^{-1}]	0.193 **0.192** 0.190	0.378 **0.376** 0.375	0.241 **0.240** 0.239	0.252 **0.251** 0.250	0.307 **0.306** 0.304	0.212 **0.211** 0.210	0.217 **0.216** 0.215	0.220 **0.219** 0.218	0.221 **0.220** 0.219	0.294 **0.293** 0.292
Domain max convergence mean [10^5 s^{-1}]	20.27 **19.29** 18.39	33.45 **30.14** 27.23	17.87 **17.12** 16.41	15.97 **15.25** 14.59	32.57 **29.66** 27.08	17.98 **17.20** 16.48	14.36 **13.78** 13.23	40.06 **36.33** 32.78	23.56 **21.84** 20.35	17.72 **16.90** 16.20
Convective updraft mass flux mean (0-2.5 km) [kg m^{-2} s^{-1}]	50.24 **50.18** 50.13	55.97 **55.92** 55.88	50.89 **50.86** 50.81	47.16 **47.13** 47.09	56.03 **55.97** 55.92	50.53 **50.48** 50.44	46.44 **46.40** 46.36	55.48 **55.40** 55.32	50.81 **50.76** 50.71	46.90 **46.86** 46.82
TPW domain mean variability (raining – non-raining grid points) [mm]	3.48 **3.47** 3.46	12.42 **12.41** 12.40	6.87 **6.86** 6.85	1.10 **1.09** 1.08	10.72 **10.71** 10.70	5.05 **5.04** 5.03	0.96 **0.95** 0.94	6.28 **6.27** 6.26	4.39 **4.38** 4.37	0.93 **0.92** 0.91

While notable spatial organization patterns prevail within each sensitivity simulation, individual storms within the clustered bands exist in a variety of sizes and intensities, with simulations periodically fostering larger and more intense systems that may not necessarily be depicted in Figure 5.3. To represent these variations collectively, subsequent statistics are calculated over the final five days of each simulation, notably coinciding with the timing of persistent spatial organization patterns.

Focusing first on spatial statistics across individual storms (defined using the 30-dBZ composite reflectivity threshold in Section 5.2.4), notably no consistent relationships between LFT moisture and TOC system area nor TOC updraft area are evident across the trio of differing deep layer shear profiles (Table 5.2). For example, with SHEAR-WAM, mean TOC system area monotonically increases from 12.30 km^2 with RH-D to 22.02 km^2 with RH-I. Meanwhile, mean TOC system area monotonically decreases from 17.41 km^2 with RH-D to 7.41 km^2 with RH-I under SHEAR-5. This result is inconsistent with prior studies linking increased LFT moisture to larger TOC systems (e.g., Cetrone & Houze, 2006; Chen et al., 2017; Schiro et al., 2020; Chen et al., 2023; Rodenkirch & Rowe, 2024) and consequently, like other studies (e.g., Mulholland et al., 2021; Sakaeda & Torri, 2022; Peters et al., 2022), suggests more complex conditional dependence of moisture and wind shear relationships with TOC on each other's magnitude.

Deep layer wind shear itself, however, does consistently coincide with greater mean TOC system areas (Table 5.2) and higher frequencies of large (i.e., > 40 km^2) systems (Figure 5.4a). The statistically significant relationship for mean TOC system area translates to convective updraft area as well, with TOC updrafts covering broader horizontal areas on average with imposed

SHEAR-5 (3.27 km^2), SHEAR-10 (3.23 km^2), and SHEAR-WAM (6.88 km^2) deep layer shear compared to BASE (2.40 km^2) with no deep layer shear (Table 5.2). Mean convective system and updraft areas, along with frequency of large systems (Figure 5.4a), are particularly high for the SHEAR-WAM simulations, though simulations with this shear profile also produce a lesser number of storms on average, even relative to BASE (Table 5.2). Larger convective systems with imposed deep layer shear are hypothesized to occur via convective system tilting downshear and concomitant hydrometeor advection, which will be explored more in Section 5.4.1.

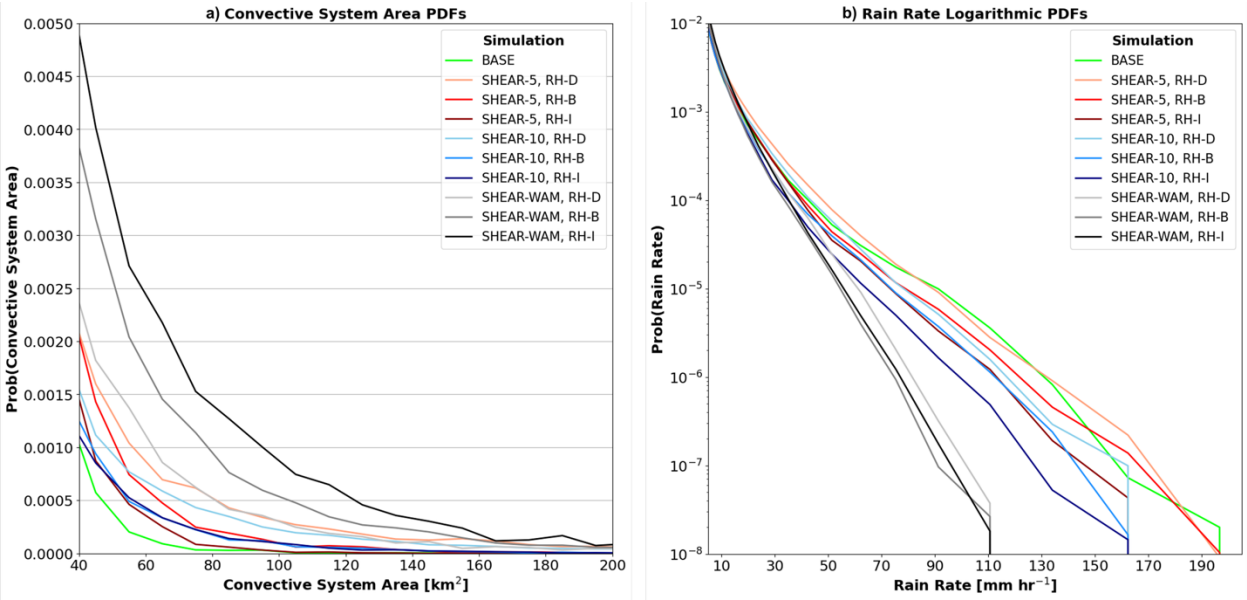

Figure 5.4: Probability distribution functions of (a) convective system area (binned every 10 km^2) and (b) surface rain rate (logarithmically binned) for each CM1 simulation. Each probability distribution function is calculated for data across the last 5 days of each simulation using hourly data outputs.

5.3.2 Collective TOC Intensity and Vertical Structure

Implementation of deep layer wind shear has been shown to influence horizontal TOC organization by way of increased spatial organization and system area (Section 5.3.1). These notable results motivate investigation as to whether deep layer shear influences on TOC organization translate to the vertical as well, manifested via convective intensity and vertical structure. To evaluate deep

layer wind shear impacts on TOC intensity, first the maximum height of 30-dBZ reflectivity is analyzed for the last five days of each simulation. Compared to BASE, the mean maximum 30-dBZ height within TOC systems over the last five days is lower on a statistically significant level for all but one sensitivity simulation (Table 5.2), signaling less intense convective regions when deep layer shear is implemented. The only exception is SHEAR-5, RH-D, whose TOC systems have a statistically significant mean maximum 30-dBZ height of 4.50 km compared to 3.99 km in BASE. However, isolating comparisons of simulations to just those with identical moisture profiles more clearly supports less intense convective regions with greater deep layer shear magnitudes. For example, for simulations with RH-B, mean maximum 30-dBZ height of TOC systems monotonically decreases from 3.99 km in BASE to 3.92 km in SHEAR-5 to 3.33 km in SHEAR-WAM to 2.98 km in SHEAR-10. A similar monotonic trend is found amongst the RH-I simulations, and while the trend is non-monotonic for the RH-D simulations, the weakest deep layer shear magnitude (i.e., SHEAR-5, RH-D) still similarly has the highest mean maximum 30-dBZ height at a statistically significant level.

Consistent with lower maximum 30-dBZ heights, each sensitivity simulation is associated with lower mean maximum convective updraft velocities relative to BASE (Table 5.2), with each comparison to BASE being statistically significant except for the SHEAR-5, RH-I simulation. Additionally, in spite of statistically significant higher domain mean surface rain rates in each deep layer shear simulation compared to BASE (Table 5.2), strong deep layer shear (i.e., SHEAR-10 and SHEAR-WAM) is associated with less frequent intense (i.e., > 10 mm hr^{-1}) surface rain rates (Figure 5.4b). Altogether, the maximum 30-dBZ height, convective updraft velocity, and intense surface rain rate convective intensity proxies concur in support of imposed deep layer shear

promoting weaker convective intensities. Less intense TOC with imposed deep layer shear is hypothesized to occur via convective updraft and system tilting by the shear (Robe & Emanuel, 2001; Igel & van den Heever, 2015), which will be examined in greater detail in Section 5.4.2.

Notably, the trio of SHEAR-5 simulations tends to contain TOC systems with the highest mean surface rain rates compared to simulations with stronger deep layer shear (Table 5.2), which is also supported by higher frequencies of particularly high (i.e., > 70 mm hr^{-1}) surface rain rates in weak shear environments (Figure 5.4b). Similarly, the trio of SHEAR-5 simulations also tends to have the greatest mean convective updraft velocities (Table 5.2). Coupled with SHEAR-5 TOC systems having the greatest mean maximum 30-dBZ heights of all the shear simulations at a statistically significant level (Table 5.2), these results continue to convey weaker deep layer shear environments favoring more intense TOC than stronger deep layer shear environments.

Of note is a lack of consistent relationships between LFT moisture and TOC intensity across the trio of differing deep layer shear profiles. Coupled with the lack of consistent relationships between LFT moisture and TOC system and updraft areas described in Section 5.3.1, these results continue to suggest conditional dependence of moisture and wind shear relationships with 3-D TOC structure on each other's magnitude. The suggested prevailing conditional dependence in relation to TOC intensity may stem from deep layer wind shear and LFT moisture uniquely impacting the vertical dynamical flow within TOC systems, warranting further investigation. Logarithmic difference CFADs of TOC vertical velocity between each sensitivity simulation and BASE (see Section 5.2.4) are consequently evaluated to assess differences in collective vertical structure of TOC in varying deep layer shear and LFT moisture environments. Across a range of LFT moisture

environments, environments with weak deep layer shear (i.e., SHEAR-5) consistently promote more top-heavy TOC systems relative to an environment with no shear (i.e., BASE), as represented by more positive differential frequencies of high vertical velocity above 5 km than below 5 km in Figure 5.5a-c. Conversely, represented by more positive differential frequencies of high vertical velocity below 5 km than above 5 km, environments with strong deep layer shear (i.e., SHEAR-10 and SHEAR-WAM) tend to promote more bottom-heavy TOC systems (Figure 5.5d-h). Meanwhile, across varying deep layer shear environments, TOC is found to transition from more bottom-heavy to more top-heavy with increasing LFT moisture (Figure 5.5a-c, Figure 5.5d-f, Figure 5.5g-i). The proclivity of TOC being more top-heavy with weaker deep layer shear and moister LFTs will be discussed more in Section 5.4.3.

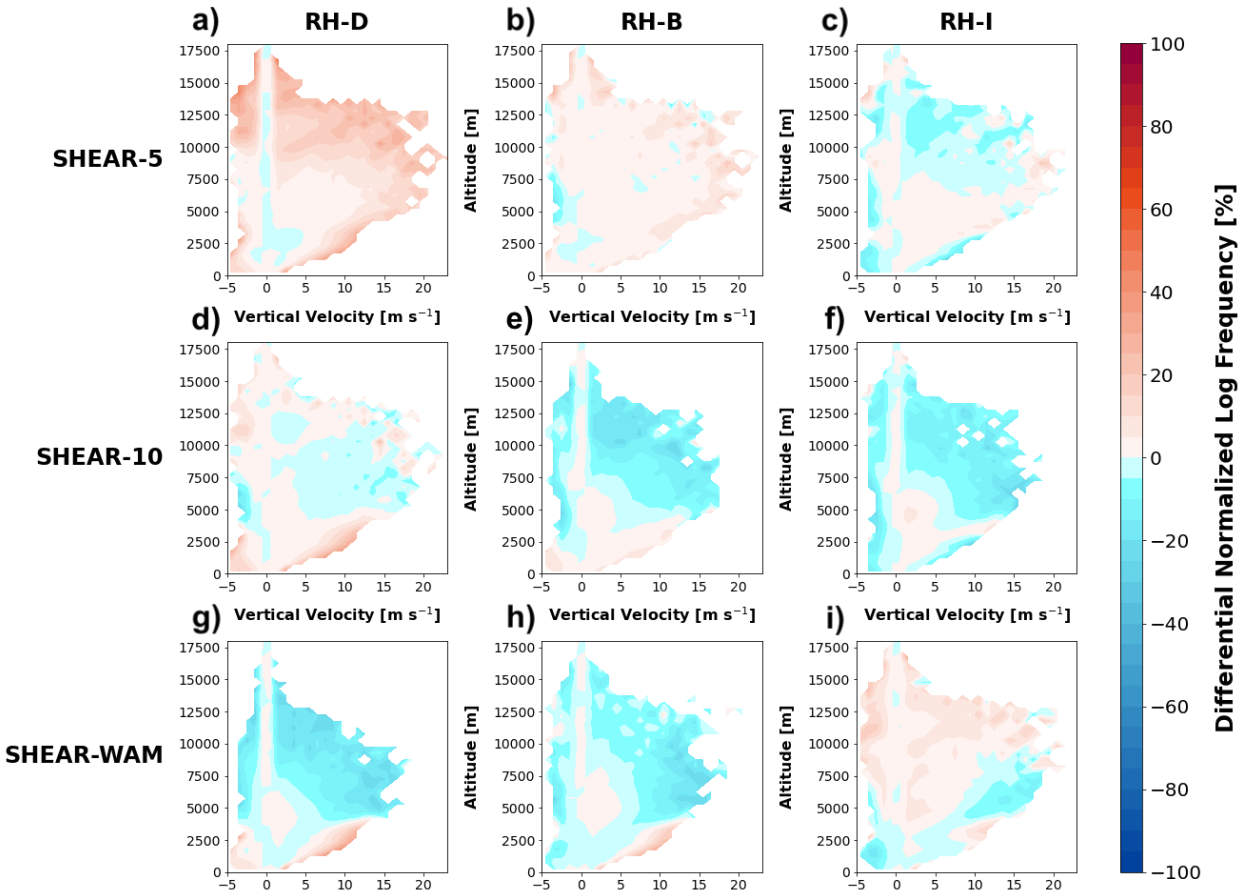

Figure 5.5: Logarithmic difference CFADs of vertical velocity between BASE and (a) SHEAR-5, RH-D, (b) SHEAR-5, RH-B, (c) SHEAR-5, RH-I, (d) SHEAR-10, RH-D, (e) SHEAR-10, RH-B, (f) SHEAR-10, RH-I, (g) SHEAR-WAM, RH-D, (h) SHEAR-WAM, RH-B, (i) SHEAR-WAM, RH-I. Vertical velocity data is binned into 1-m s^{-1} and 0.5-km intervals and normalized by the maximum bin count in each height interval. Each logarithmic difference CFAD is calculated for data across the last 5 days of each simulation using hourly data outputs.

5.4 Discussion

5.4.1 Collective Horizontal TOC Organization: Spatial Organization and Self-Aggregation

The notable clustering of TOC seen in each deep layer wind shear sensitivity simulation (Section 5.3.1) motivates further investigation into the reasoning behind the observed TOC spatial organization. Examination of domain-wide zonally averaged Hovmöller diagrams of TPW (Figure 5.6a), near-surface temperature (Figure 5.6b), and composite reflectivity (Figure 5.6c) for the RH-

B and RH-D deep layer wind shear simulations reveal trends with time characteristic of convective self-aggregation (Bretherton et al., 2005; Wing et al., 2017; Holloway et al., 2017). Accordingly, anomalously moist, cool, and rainy bands generally get moister, cooler, and more rainy with time. Simultaneously, anomalously dry, warm, and less rainy bands generally get drier, warmer, and even less rainy with time. Additionally supported by statistically significant larger TPW variability between raining and non-raining grid points (Table 5.2), these observed trends are much stronger compared to BASE. As such, deep layer shear fosters enhanced convective self-aggregation perpendicular to the shear vector in the RH-B and RH-D sensitivity simulations.

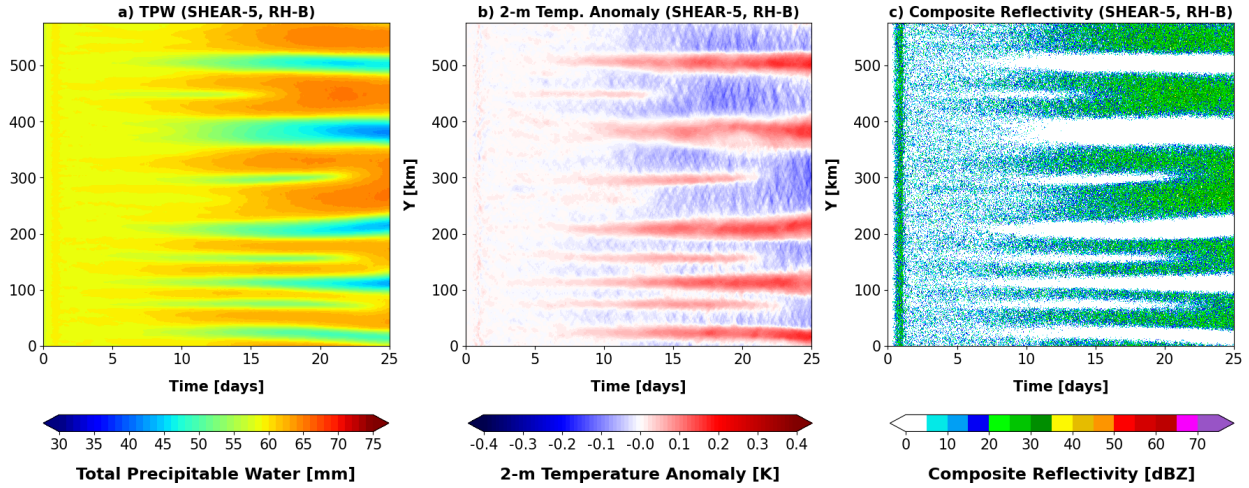

Figure 5.6: Hovmöller diagrams of zonally averaged hourly (a) TPW, (b) 2-meter temperature anomalies, and (c) composite reflectivity for the SHEAR-5, RH-B simulation.

Convective self-aggregation perpendicular to the deep layer shear vector aligns with similar CRM studies of TOC with imposed deep layer shear (e.g., Bretherton et al., 2005). Under an imposed uniform domain-wide deep layer shear profile, moisture anomalies collocated with convection via detrainment and precipitation are predominantly advected parallel to the shear. This translates to moisture anomalies being sheared out in the direction parallel, but not perpendicular to, the shear vector (Figure 5.7b). In simulations with periodic lateral boundary conditions (i.e., those of this chapter), the preferential shear-parallel moisture advection by the deep layer shear results in

persistent, shear-parallel bands of positive and negative moisture anomalies that respectively continue to support and suppress convection (Figure 5.7). The shear-parallel bands of moisture anomalies further support the described convective self-aggregation through weak temperature gradient (WTG) balance characteristic of the tropics (e.g., Sobel & Bretherton, 2000; Sobel et al., 2001). In WTG balance, enhanced diabatic latent heating within convective bands collocated with increased moisture is balanced by adiabatic cooling via ascent that further promotes convective development. Meanwhile, enhanced diabatic radiative cooling within non-convective bands collocated with decreased moisture is balanced by adiabatic warming via descent that further inhibits convective development. These characteristic WTG features of collocated enhanced moisture, ascent, and convection and separately collocated decreased moisture, descent, and lack of convection are indeed present in the RH-B and RH-D deep layer shear simulations. These characteristic WTG features are exemplified in Figure 5.8 with a domain-wide cross-section of 5-day zonally averaged flow and moisture through the broad bands of clustered TOC in the SHEAR-5, RH-B simulation (e.g., Figure 5.7a).

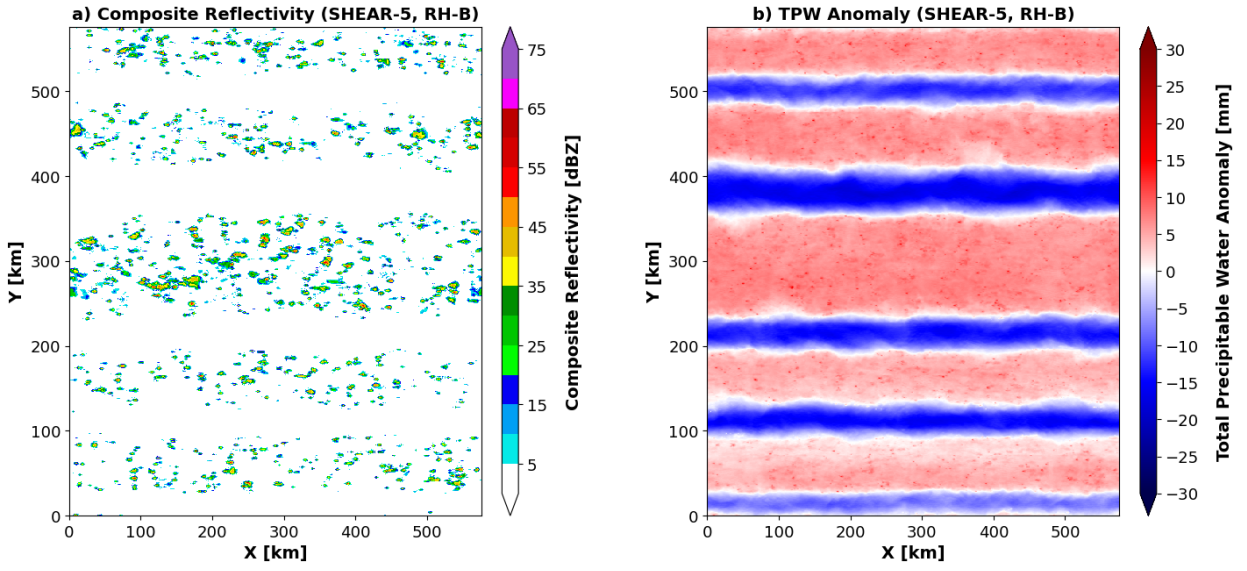

Figure 5.7: SHEAR-5, RH-B plan view (a) composite reflectivity and (b) TPW anomalies during the last hour of the simulation.

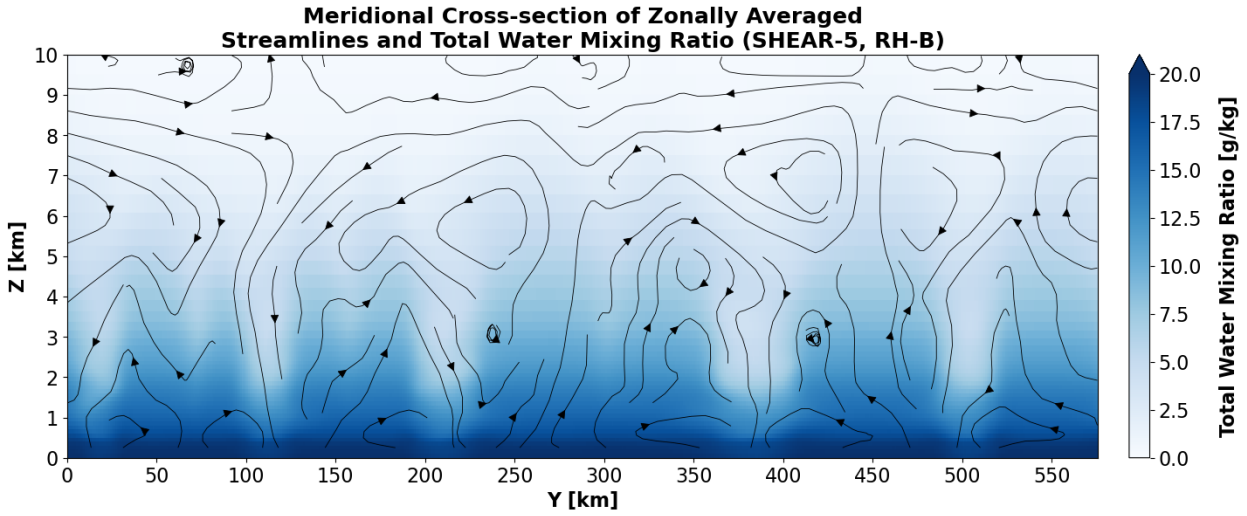

Figure 5.8: Meridional cross-section of streamlines (arrows) and total water mixing ratio (fill) for SHEAR-5, RH-B, averaged zonally and across the last 5 days of the simulation. A 9-point smoothing filter is applied once to the streamlines.

While bands of intensifying moisture, temperature, and precipitation anomalies characteristic of convective self-aggregation are observed in the RH-B and RH-D deep layer wind shear simulations, similar trends are not observed in the RH-I deep layer shear simulations. With the RH-I simulations producing narrow streets of organized TOC oriented perpendicular, yet still propagating parallel, to the deep layer shear vector (Figure 5.3c,f,i), collocated anomalies in moisture, temperature, and precipitation are continually propagating into regions that previously had anomalies of opposite sign. Therefore, every region of the domain experiences periodic fluctuations in moisture, temperature, and precipitation, manifesting as narrow streaks in Hovmöller diagrams (e.g., Figure 5.9). Moist, cool, and rainy regions do not get moister, cooler, and rainier with time (and vice versa) as a result, indicating a different mechanism for TOC spatial organization in the RH-I deep layer shear simulations. Supplementing domain-wide moisture and temperature evolution (Figure 5.9) with instantaneous hourly domain-wide moisture, temperature, and convective inhibition (CIN; e.g., Figure 5.10) reveals spatial patterns consistent with the presence of convectively coupled gravity waves (CCGWs; e.g., Raymond & Fuchs, 2007; Kiladis

et al., 2009; Adames et al., 2019). Narrow streets of alternating moisture, temperature, and CIN anomalies complement the narrow streets of organized TOC (Figure 5.10). These patterns are characteristic signatures of CCGWs through forced adiabatic fluctuation of temperature and stability via wave propagation (e.g., Lane & Zhang, 2011). Though further investigation into CCGWs as a mechanism for TOC spatial organization is left for future work, the more distinctive fingerprint of CCGWs in the RH-I simulations, which are associated with more top-heavy TOC (Section 5.3.2), aligns with prior studies linking convective top-heaviness to stronger CCGWs (Fuchs et al., 2012; Yamazaki & Miura, 2024). As such, the apparent increased influence of CCGWs in moister LFT environments may also play a role in the increased top-heaviness of TOC in moister LFTs seen in the sensitivity simulations (Figure 5.5).

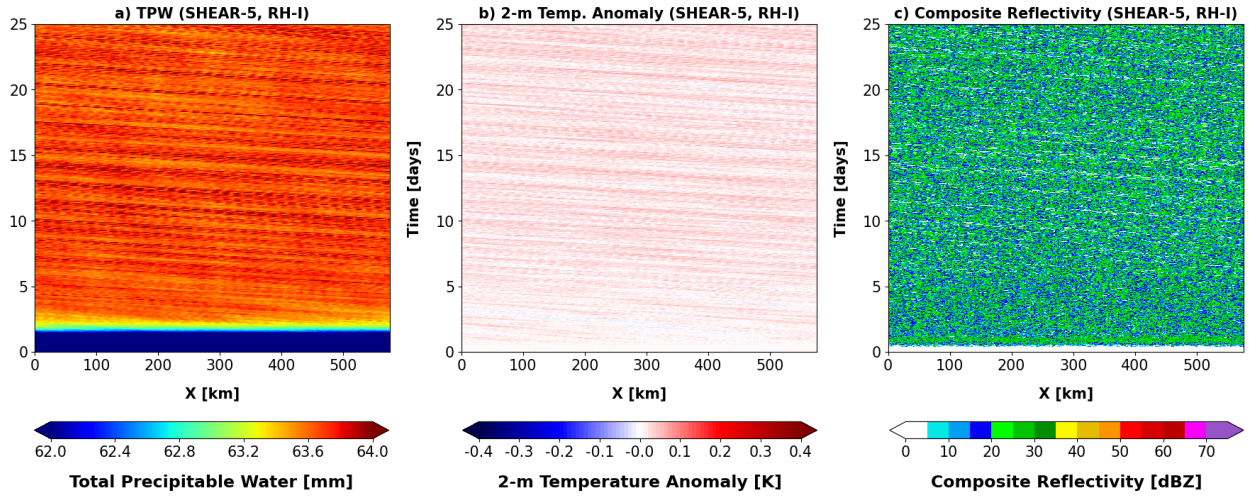

Figure 5.9: Hovmöller diagrams of meridionally averaged hourly (a) TPW, (b) 2-meter temperature anomalies, and (c) composite reflectivity for the SHEAR-5, RH-I simulation.

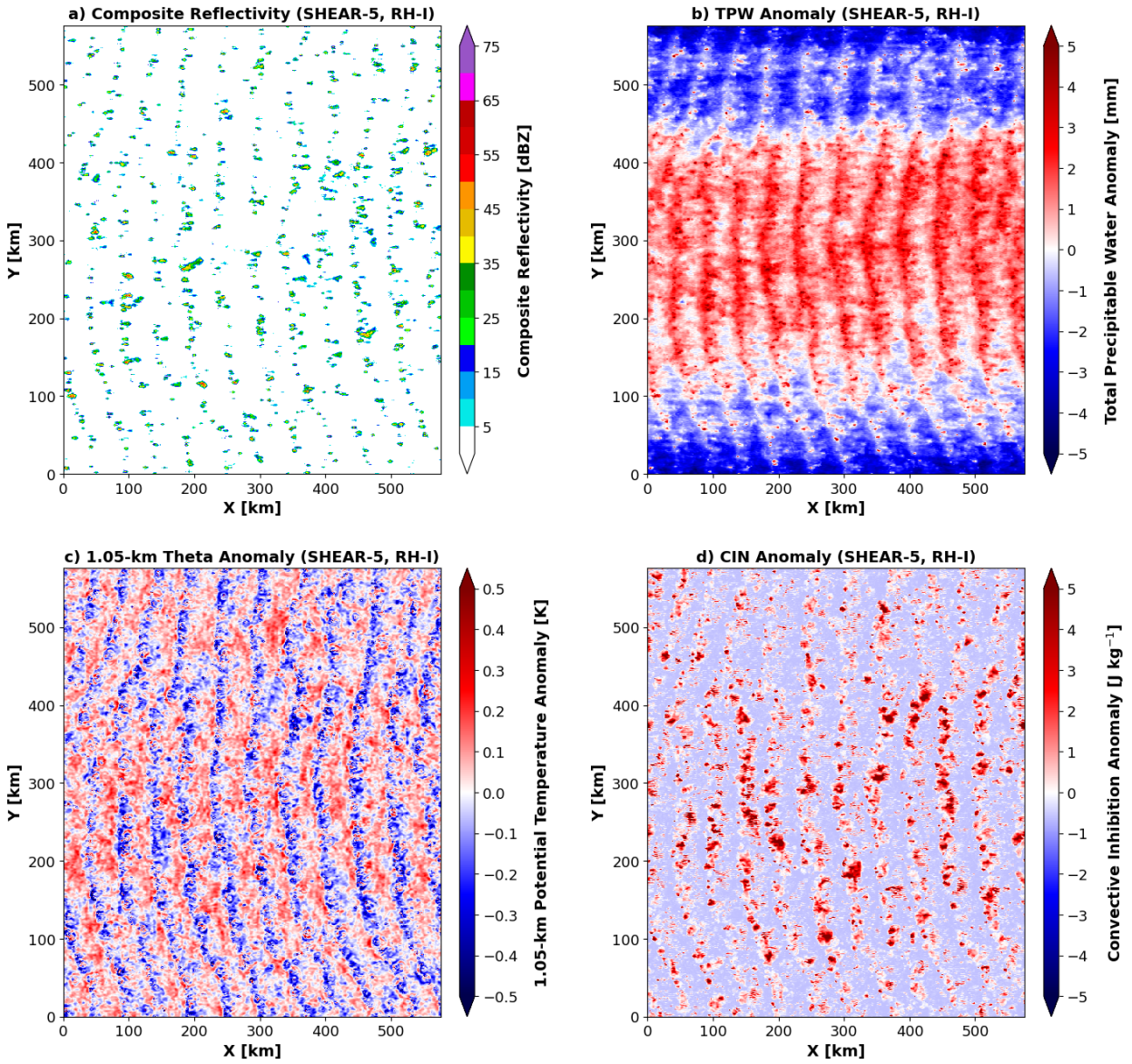

Figure 5.10: SHEAR-5, RH-I plan view (a) composite reflectivity, (b) TPW anomalies, (c) 1.05-km (~900 mb) potential temperature anomalies, and (d) CIN anomalies during the last hour of the simulation.

In addition to fostering distinctively different spatial organization than the RH-B and RH-D deep layer wind shear simulations, it is noteworthy that the RH-I deep layer wind shear simulations produce similar TOC spatial organization patterns to that of an RH-I simulation with no imposed deep layer shear (i.e., NO SHEAR, RH-I; Figure 5.11). Combined, these results suggest that when LFT moisture is high (e.g., 90% RH, as in this chapter), LFT moisture exerts a dominant control

of convective spatial organization over deep layer wind shear. Conversely, prevailing broad-banded convective spatial organization in the RH-B and RH-D deep layer shear simulations (Figure 5.3) suggest deep layer shear to play a more influential role in convective spatial organization in moderate LFT moisture environments (e.g., 60% and 76% RH, as in this chapter). These results are consistent with the observational findings of Sakaeda & Torri (2022), which found enhanced sensitivity of TOC spatial organization to vertical wind shear in drier environments over the Indian Ocean.

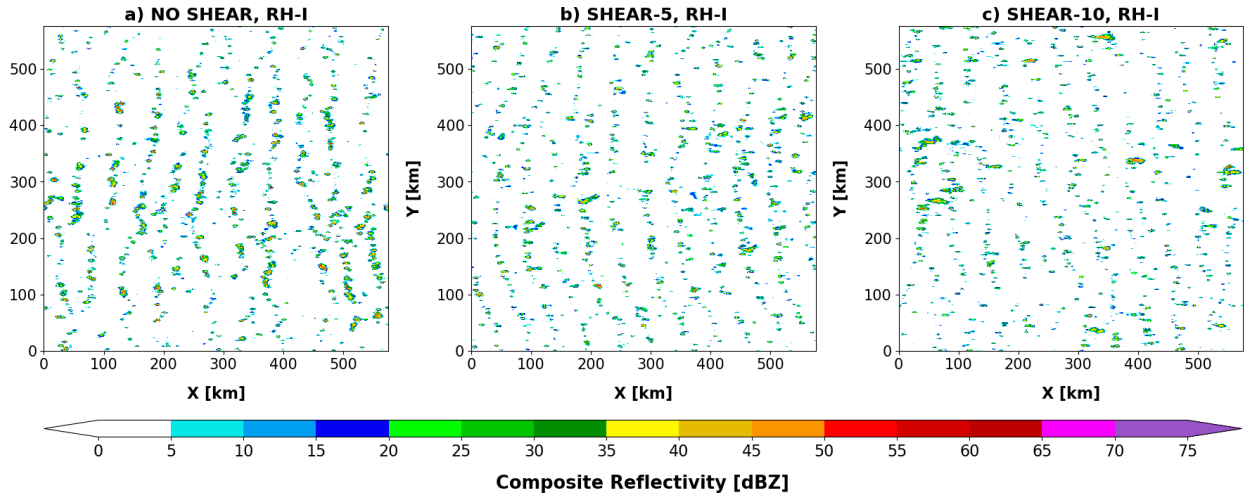

Figure 5.11: Same as Figure 5.2a, except for (a) NO SHEAR, RH-I, (b) SHEAR-5, RH-I, and (c) SHEAR-10, RH-I.

While results support that deep layer shear and higher LFT moisture promote TOC spatial organization through self-aggregation and CCGWs, respectively, the RH-D deep layer shear simulations in particular are linked to the greatest TOC spatial organization at a statistically significant level (Section 5.3.1, Table 5.2). In addition to the aforementioned shearing out of moisture anomalies by deep layer shear, the particularly high degree of TOC self-aggregation in the RH-D simulations is likely also related to collective ancillary impacts of deep layer shear and a drier LFT on convective cold pools. Environments with deep layer shear act to tilt convective systems downshear more than environments without shear (Lasher-Trapp et al., 2021). Evidence

of this shear-induced convective tilting is present in cross-sections through individual TOC systems in the deep layer shear simulations (e.g., Figure 5.12b) vs. BASE (e.g., Figure 5.12a), wherein both the convective updrafts and systems themselves are tilted downshear in sheared environments. While this convective tilting, accompanied by downshear hydrometeor advection, increases convective system area (Table 5.2; Igel & van den Heever, 2015; Chen et al., 2023), it can simultaneously increase entrainment-driven dilution into convective systems by increasing the perimeters of the convective systems (Cheng et al., 2020; Lasher-Trapp et al., 2021; Jo & Lasher-Trapp, 2022). The resultant negative buoyancy introduction, particularly with a drier LFT, ultimately suppresses deep convection in regions isolated from pre-existing convection, where detrained moisture and hydrometeor ingestion would otherwise aid developing systems (Schlemmer & Hohenegger, 2014; Feng et al., 2015; Moser & Lasher-Trapp, 2018; Becker et al., 2018; Cheng et al., 2020; Becker & Hohenegger, 2021). The result is convective spatial organization and consequent decreased distance between convective systems in the presence of deep layer shear and a drier LFT, which is indeed observed in the sensitivity simulations (Figure 5.3).

The accommodating drier LFT also leads to drier air being ingested into the convective systems that can help produce more intense cold pools through enhanced hydrometeor evaporation. The sensitivity simulations support this claim, with the RH-D simulations producing more frequent strong (i.e., > 1 K) cold pools (defined by negative 2-m temperature anomalies) than all but one of the RH-B and RH-I simulations (Figure 5.13). Coupled with the aforementioned increased proximity of convective systems with deep layer shear, the more frequent strong cold pools from drier LFTs can produce more frequent, more extensive, and stronger near-surface cold pool

interactions (Schlemmer & Hohenegger, 2014; Feng et al., 2015; Rowe & Houze, 2015; Moser & Lasher-Trapp, 2018; Cheng et al., 2020). Stronger low-tropospheric convergence in the RH-D deep layer shear simulations can occur as a result of the stronger near-surface cold pool interactions, which is indeed seen at a statistically significant level relative to both BASE and all other deep layer shear simulations (Table 5.2). Consequently, the stronger and closer proximity cold pools can act to maintain and initiate larger and stronger TOC systems with time (Schlemmer & Hohenegger, 2014; Sakaeda & Torri, 2022) along their more extensive and stronger intersecting near-surface boundaries, as supported by higher composite reflectivities along stronger simulated cold pool boundary arcs (e.g., Figure 5.14). The larger TOC systems produced by the more frequent, more extensive, and stronger near-surface cold pool interactions can thereby lead to enhanced TOC clustering with time that likely yields the particularly high degree of I_{org} TOC spatial organization seen in the RH-D deep layer shear simulations (Table 5.2; Feng et al., 2015; Rowe & Houze, 2015; Cheng et al., 2020; Moser & Lasher-Trapp, 2018).

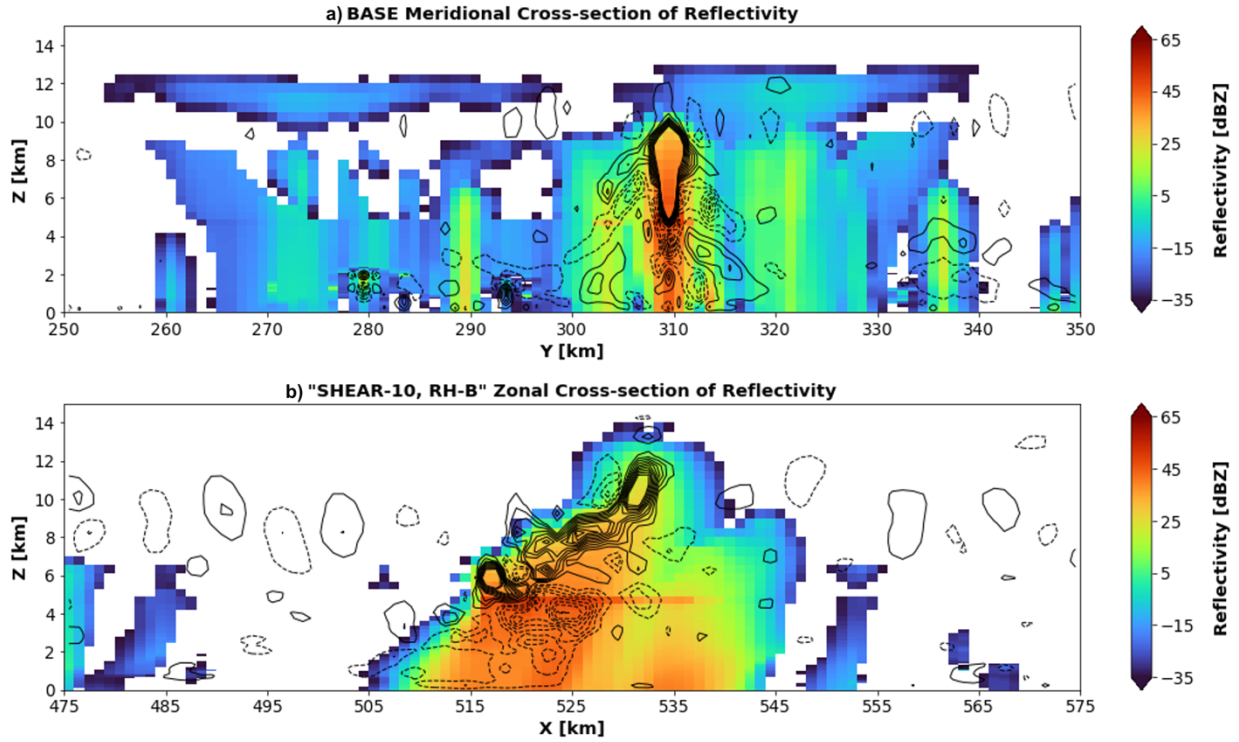

Figure 5.12: Cross-section of simulated reflectivity (fill) and vertical velocity (contours) through a convective system in (a) BASE and (b) SHEAR-10, RH-B taken during the last hour of each simulation. Vertical velocity is contoured every 0.15 m s^{-1} for both negative (dashed) and positive (solid) values ranging from -1.5 m s^{-1} to 1.5 m s^{-1}.

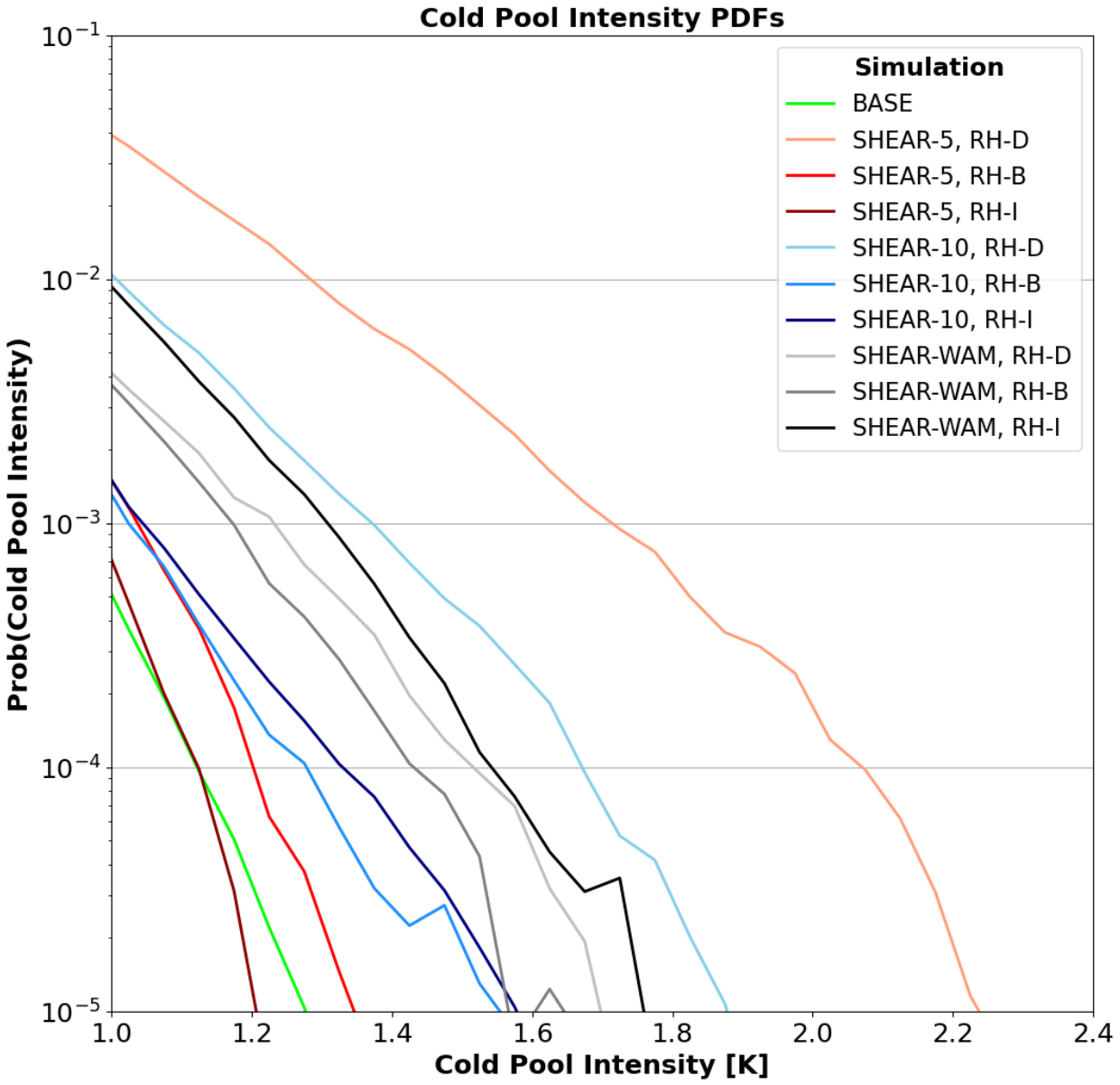

Figure 5.13: Same as Figure 5.4a, except for cold pool intensity (binned every 0.05 K), defined as the magnitude of a negative anomaly in 2-meter temperature relative to the domain-wide average.

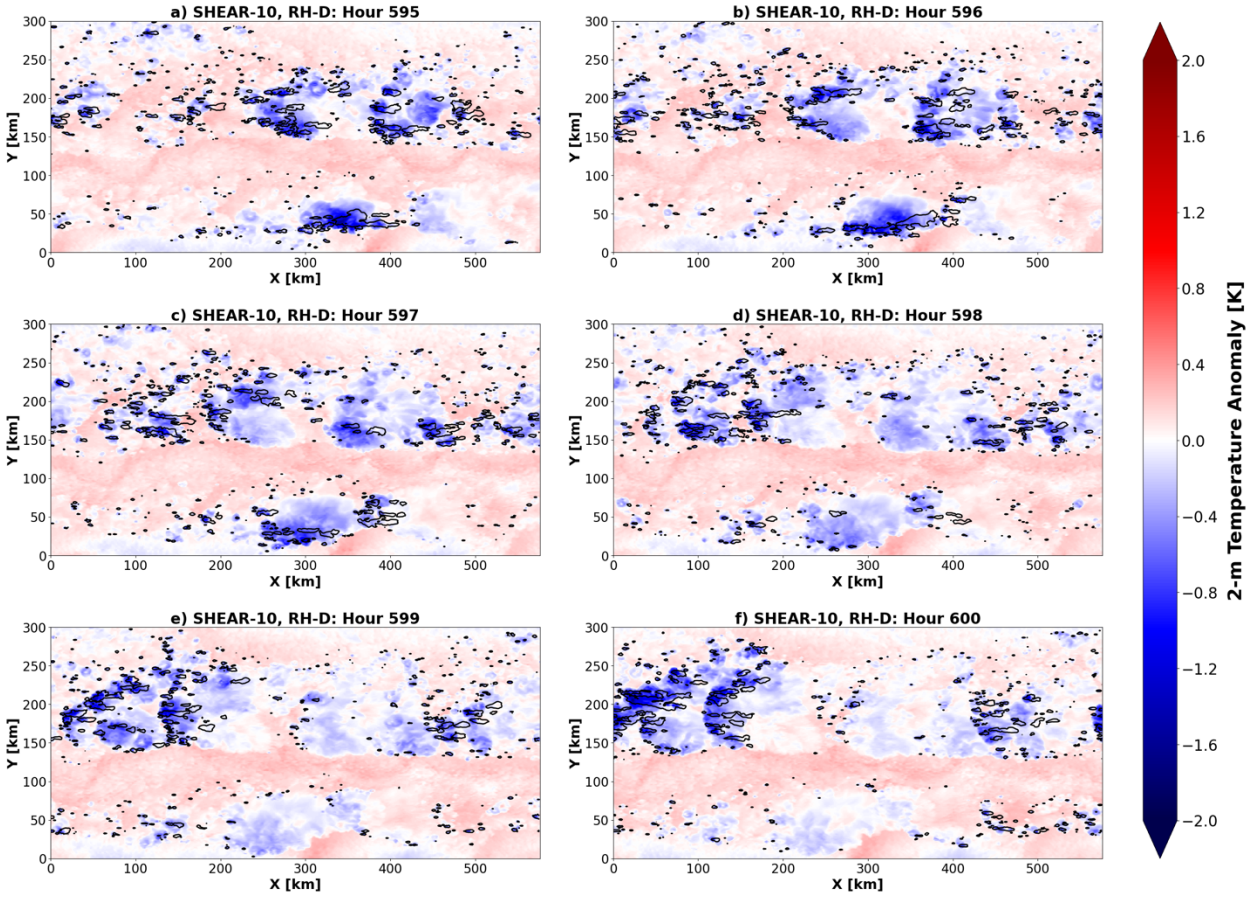

Figure 5.14: SHEAR-10, RH-D plan view 2-meter temperature anomalies (fill) and 30-dBZ composite reflectivity (contours) during the last 6 hours of the simulation.

5.4.2 Collective TOC Intensity: System Tilting vs. Updraft Mass Flux

Notable impacts of deep layer wind shear were found to extend from collective horizontal TOC organization (e.g., enhanced spatial organization and larger TOC systems [Section 5.3.1]) to collective TOC intensity in the vertical as well, with less intense TOC systems observed in each sensitivity simulation (Section 5.3.2). Examination of vertical cross-sections through individual storms in each simulation reveals tilted systems and updrafts in the deep layer shear simulations (e.g., Figure 5.12b) compared to more upright systems and updrafts in BASE (e.g., Figure 5.12a). This result is consistent with other simulated (e.g., Robe & Emanuel, 2001; Peters et al., 2019) and observed (e.g., Igel & van den Heever, 2015) convective systems in sheared environments, and

may explain the weaker convective intensities seen in the deep layer shear simulations. While system tilting by shear can provide more effective updraft and downdraft separation to help maintain TOC systems, the tilting also acts to deflect updrafts towards the horizontal plane and thus reduce vertical velocities. These proposed reduced vertical velocities from shear tilting are indeed seen in the mean column-maximum convective updraft vertical velocities at a statistically significant level for all but the SHEAR-5, RH-I simulation (Table 5.2). Reduced maximum vertical velocities from shear tilting within individual TOC systems are also noted, with a SHEAR-10, RH-B system in Figure 5.12b having a maximum vertical velocity of 3.35 m s^{-1} compared to 14.51 m s^{-1} of a BASE system in Figure 5.12a, for example. Compounding the reduced vertical velocities through updraft deflection, system tilting by deep layer shear can also be detrimental to TOC intensity through respondent enhanced downward dynamic pressure perturbations from consequent larger updraft areas (Parker 2010; Peters 2016; Peters et al., 2019; Peters et al., 2022) and enhanced entrainment-driven dilution from consequent larger TOC systems (Table 5.2) via increased convective cloud perimeters (Markowski & Richardson, 2011; Cheng et al., 2020; Lasher-Trapp et al., 2021; Jo & Lasher-Trapp, 2022). However, neither dynamic pressure perturbations nor entrainment are explicitly resolved in the 1-km horizontal grid spacing sensitivity simulation. Therefore, evaluating the impacts of each on TOC intensity in the context of deep layer shear is left for future work.

It is notable that the described negative effects of deep layer wind shear on TOC intensity through system tilting appear to outweigh the positive effects that deep layer shear has on TOC intensity. Complementing more effective updraft and downdraft separation within individual storms (e.g., Figure 5.12b), greater 0 – 2.5 km updraft mass fluxes are also seen at a statistically significant

level relative to BASE for simulations lacking a particularly moist, and thus convectively more favorable, LFT (i.e., RH-B and RH-D shear simulations; Table 5.2). The enhanced 0 – 2.5 km updraft mass fluxes, paired with aforementioned statistically significant larger updraft areas, have together been shown in prior studies to stem from shear-induced enhanced convective inflow through mass continuity (e.g., Mulholland et al., 2021). With wider updrafts being less susceptible to detrimental entrainment-driven dilution (e.g., Mulholland et al., 2021), the imposed deep layer shear in the sensitivity simulations could thus provide dynamical support for TOC systems through enhanced convective inflow that manifests via larger updraft areas and mass fluxes (Peters et al., 2019; Peters et al., 2022). In the simulations of this chapter, however, the consequent enhanced vertical mass fluxes with enhanced convective inflow appear to manifest more through updraft area expansion rather than updraft intensification, as updraft velocities are collectively weaker relative to BASE (Table 5.2). As such, the benefits of imposed deep layer shear on TOC intensity through enhanced updraft mass fluxes and areas are either not present or, more likely, outweighed by the negative effects of tilting by the shear described above. Given the updraft area definition of this chapter (Section 5.2.4), it is also possible that the larger updraft areas do not actually translate to wider updrafts that would reduce entrainment-driven dilution, thereby omitting a benefactor of TOC intensity.

5.4.3 Deep Layer Shear and LFT Moisture Effects on TOC Vertical Structure

In addition to reducing collective TOC intensity, tilting of individual convective systems by the imposed deep layer wind shear is likely a key influence on collective vertical TOC structure as well. As deep layer shear increases, updrafts become more deflected into the horizontal (e.g., Figure 5.12b). As such, tilted convective systems with vertical velocity profiles weighted more

towards the surface become more prevalent with strong deep layer shear compared to weak deep layer shear, resulting in the more bottom-heavy TOC seen in Section 5.3.2 (Figure 5.5d-I vs. Figure 5.5a-c). Systems becoming more bottom-heavy with stronger deep layer shear do not necessarily reduce higher frequencies of greater vertical velocities at higher altitudes relative to an environment with no shear, however. Benefits of imposed deep layer shear to vertical velocities, such as more effective convective updraft and downdraft separation (e.g., Figure 5.12b), can aid vertical velocities in updrafts at higher levels while simultaneously still weighting vertical velocity profiles more towards the surface (e.g., Figure 5.5d).

Drier LFTs appear to complement stronger deep layer shear in producing more bottom-heavy TOC (Section 5.3.2). As seen in Figure 5.5, vertical velocities within convective systems become more weighted towards the surface with decreasing LFT moisture, while increasing LFT moisture weights convective vertical velocities more towards higher altitudes. These effects of LFT moisture on convective bottom- and top-heaviness are likely related to the detrimental effects of entrainment-driven dilution, which increasingly act to reduce updraft buoyancy in the free troposphere with decreasing LFT moisture. The 1-km horizontal grid spacing of the simulations of this chapter does not explicitly resolve entrainment, however, and therefore investigations into the role of entrainment on TOC vertical structure are left for future studies.

5.5 Conclusions

This chapter presents an investigation into how local environmental deep layer wind shear influences collective TOC spatial organization in the context of LFT moisture variability in an idealized model framework. Using the CM1 idealized numerical model with a 576 x 576 km square

domain, 1-km horizontal grid spacing, and periodic boundary conditions, a set of nine sensitivity simulations with varying deep layer shear and LFT moisture profiles informed by NASA CPEX airborne field campaign series observations in the tropical North Atlantic revealed the following key insights:

- Deep layer wind shear promotes convective spatial organization. LFT moisture appears to be the dominant control of convective spatial organization over deep layer wind shear when it is high, while convective spatial organization in moderate LFT moisture environments is more dependent on deep layer wind shear.
- In moderate LFT moisture environments, deep layer shear promotes convective self-aggregation perpendicular to the shear vector due to shearing out of moisture anomalies in the direction parallel to the shear vector. In high LFT moisture environments, CCGWs are likely a main driver of convective spatial organization. Stronger cold pools resulting from lower LFT moisture environments may provide an additional means of convective spatial organization through stronger and more extensive near-surface cold pool interactions.
- Deep layer shear likely promotes less intense TOC through updraft deflection from convective tilting.
- Strong deep layer shear and a drier LFT both promote more bottom-heavy TOC, while weak deep layer shear and a moister LFT both promote more top-heavy TOC.

The results of this chapter help address a notable gap in literature pertaining to how deep layer shear and LFT moisture can impact the collective spatial organization of a population of TOC. The usage of an idealized CRM provides the advantage of being able to separate the relative influences of deep layer shear and LFT moisture from one another, while also allowing their influences to be

investigated in tandem with one another. The CM1 model setup utilized in this chapter initializes sensitivity simulations with realistic environmental conditions as well, with CPEX series observations informing and constraining the tested deep layer shear and LFT moisture ranges to realistic near-storm values across a variety of TOC organizational modes over the tropical North Atlantic (Rodenkirch & Rowe, 2024).

That being said, idealized modeling is inherently not completely representative of the real world. This unavoidable quality manifests in the simulations most notably via alternating bands of clustered TOC that were not observed during the CPEX series nor are observed over the oceanic tropics in general. These bands of clustered TOC are likely artifacts of unrealistic periodic boundary conditions imposed on a regional domain, model nudging to specified shear and moisture profiles, and long simulation timescales (i.e., 25 days) wherein radiative influences are likely to be overemphasized. Nevertheless, the structures of individual convective systems within these clustered bands are consistent with convection sampled during CPEX (Rodenkirch & Rowe, 2024; Martinez et al., 2025), thereby providing confidence in the key takeaways.

Additional limitations of the CM1 idealized modeling setup do exist, however. It is important to note that the damping timescale used for model nudging affects the spatial organization patterns seen in this chapter. Longer nudging damping timescales (e.g., 48 hours vs. the utilized 12 hours) are associated with decreased TOC organization, though this is not unexpected due to longer damping timescales translating to greater deviation from the desired initialized environmental conditions. The 1-km horizontal grid spacing used in the CM1 simulations also notably does not truly resolve individual convective cells, particularly updrafts, and it also does not explicitly

resolve entrainment. Shallow clouds also have been shown in prior studies to play an important role in convective spatial organization (e.g., Muller & Held, 2012; Muller & Bony, 2015; Wing et al., 2017; Muller et al., 2022) and were not investigated in this chapter, primarily due to the focus of this chapter on deep convective systems.

Future work should aim to address the limitations of the current study described above through extended analysis of additional sensitivity simulations, including investigating the role of shallow clouds, as well as resolving the influence of entrainment using higher resolution model domains. A more in-depth assessment of the role of CCGWs in spatial organization is also recommended, as is further quantifying draft tilt, separation, and strength within individual convective systems to further elucidate deep layer shear influences on TOC intensity and vertical structure. Observational analysis of diverse TOC environments, including differing deep layer wind shear and LFT moisture, is additionally encouraged, so that the applicability of idealized modeling studies of TOC spatial organization, such as this chapter, to reality can be effectively evaluated.

Chapter 6

Syntheses, Conclusions, and Future Work

Deep convection is a prevalent feature of the atmosphere over tropical oceans and plays key roles in modulating Earth's weather and climate on both regional and global scales (e.g., Zipser 1977; Gill, 1980; Houze, 1982; Houze, 1989; Young et al., 1995; Houze, 1997; Saxen & Rutledge, 1998; Hartmann et al., 2001; Mechem et al., 2006; Tobin et al., 2012; Del Genio & Chen, 2015; Grant et al., 2020; Bony et al., 2020; Chen et al., 2022). As such, global modeling efforts have long sought to parameterize and predict TOC by relating TOC structure and intensity to grid-scale environmental parameters (e.g., Arakawa, 1969; Arakawa & Schubert, 1974; Tiedtke, 1993; Randall & Fowler, 1999; Grabowski & Smolarkiewicz, 1999; Grabowski, 2001; Randall et al., 2003; Arakawa, 2004; Rio et al., 2019; Satoh et al., 2019), motivating the need to understand TOC-environment relationships. Prior literature attempting to generalize TOC-environment relationships across the tropics have noted the particular importance of tropospheric moisture (e.g., Brown & Zhang, 1997; LeMone et al., 1998; Saxen & Rutledge, 2000; Tompkins, 2001; Bretherton et al., 2004; Cetrone & Houze, 2006; Holloway & Neelin, 2009; Chen et al., 2017; Hannah, 2017; Ahmed & Neelin, 2018; Schiro et al., 2020; Wolding et al., 2020; Adames et al., 2021; Padullés et al., 2022; Wolding et al., 2022; Chen et al., 2023; Wolding et al., 2024; Muetzelfeldt et al., 2025) and vertical wind shear (e.g., Rotunno et al., 1988; Alexander & Young, 1992; LeMone et al., 1998; Tompkins, 2001; Bretherton et al., 2005; Anber et al., 2014; Guy & Jorgensen, 2014; Igel & van den Heever, 2015; Peters 2016; Chen et al., 2017; Morrison & Peters

2018; Peters et al. 2019; Chudler & Rutledge, 2021; Mulholland et al., 2021; Baidu et al. 2022; Peters et al. 2022; Chen et al., 2023; Maybee et al. 2024; Roca et al., 2025) as primary influences of TOC structure and intensity. However, these prior studies often come to differing conclusions on the degree of influence of each, with both moisture and wind shear relationships with TOC being inconsistent in both strength and sign across studies.

These inconsistencies in the literature are likely the result of limited spatiotemporal data resolutions of satellite and reanalysis data, imperfect convective-scale parameterizations in CRMs (e.g., Randall et al., 2003; Arakawa, 2004; Satoh et al., 2019; Rio et al., 2019), and regional variability (e.g., Chen et al., 2017; Galarneau et al., 2023; Muetzelfeldt et al., 2025). Motivated by these issues, field campaigns within specific tropical oceanic regions have been executed that uniquely collect frequent, high-resolution measurements in a variety of environments near a variety of TOC system morphologies that cannot be replicated by satellite remote sensing, reanalysis, nor CRMs. Historical field campaigns like TOGA COARE and KWAJEX in the tropical West Pacific and GATE and NAMMA in the tropical East Atlantic have made great strides in advancing TOC-environment knowledge, but inconsistent findings prevail. These inconsistent findings may be attributed to factors like differing tropospheric layer definitions over which local environmental moisture and wind shear are calculated, intercomparison of results from different TOC morphologies (i.e. quasi-linear vs. non-linear), and cross-comparison of results from regionally different climatologies that may lead to altered degrees of influence of moisture and wind shear on TOC (e.g., Chen et al, 2017; Sakaeda & Torri, 2022; Peters et al., 2022; Chen et al., 2023). Targeted in situ regional studies of TOC, particularly with modern-day, high-resolution field campaign measurements of and near historically understudied non-linear TOC, are thus

needed with successive interregional comparisons with consistent layer definitions for moisture and wind shear to provide a more holistic evaluation of TOC-environment relationships. Such is the motivation and goal of this dissertation, which is accomplished through analysis of modern-day, high-resolution field campaign measurements from the NASA CPEX, CPEX-AW, CPEX-CV, and CAMP^{2}Ex field campaigns across the tropical North Atlantic and Northwest Pacific, further supplemented by idealized CRM simulations to better elucidate the individual and combined effects of local moisture and wind shear on collective TOC structure and intensity.

6.1 Chapter 2 Summary (CPEX(-AW))

Using coincident, high-resolution airborne radar, lidar, and dropsonde profiling of 3-D convective structure and near-storm environments from the NASA 2017 CPEX (Chen & Zipser, 2017) and 2021 CPEX-AW (Skofronick-Jackson et al., 2021) field campaigns, Chapter 2 aimed to evaluate how TOC structure related to near-storm environmental RH and wind shear in four defined tropospheric vertical layers in the tropical West Atlantic. Amongst large near-storm moisture and wind shear variabilities within and across TOC systems, organized (i.e., multi-core) TOC was found be associated with generally greater RH and wind shear below the melting level compared to isolated (i.e., single-core) TOC, though the results were only statistically significant for mid-tropospheric shear. Additionally, more intense organized TOC was weakly linked to greater moisture above the melting level. A case comparison between two organized TOC systems with different spatial orientations (i.e., one non-linear and one quasi-linear) in otherwise similar synoptic environments also suggested greater low-level convergence to likely promote more intense TOC.

6.2 Chapter 3 Summary (CPEX-CV)

A similar approach using similar instrumentation as in Chapter 2 was applied to the NASA 2022 CPEX-CV (Zawislak et al., 2022; Nowottnick et al., 2024) field campaign in Chapter 3 to evaluate how TOC structure related to near-storm environmental RH and wind shear in the tropical East Atlantic. Amongst large near-storm moisture and wind shear variabilities within and across TOC systems, organized TOC was linked to generally greater free-tropospheric RH and deep layer wind shear than isolated TOC, though the results were not statistically significant. More intense TOC was also weakly linked to greater PBL wind shear, but lesser shear above the melting level and a drier mid-troposphere. Additionally, analysis of the joint effects of near-storm moisture and wind shear from all CPEX series dropsonde observations found PBL, deep layer, and above melting level wind shear to be linked more to convective type than free-tropospheric moisture when it was strong, and vice versa for high free-tropospheric moisture.

6.3 Chapter 4 Summary (CAMP^{2}Ex)

Using coincident, high-resolution airborne radar and sonde profiling of 3-D convective structure and near-storm environments from the NASA 2019 CAMP^{2}Ex (Reid et al., 2023) field campaign (similar in instrumentation and methodology to Chapters 2 and 3), Chapter 4 aimed to evaluate how TOC structure related to near-storm environmental RH and wind shear below the melting level in the tropical Northwest Pacific. Amongst large near-storm moisture and wind shear variabilities within and across TOC systems, organized TOC was linked to generally stronger PBL wind shear at a statistically significant level compared to isolated TOC. Meanwhile, moisture below the melting level was statistically similar for isolated and organized TOC.

6.4 Interregional Comparison Synthesis

While regional variations in TOC relationships with local environments have been previously explored, this dissertation is the first time field campaign studies have been compared with similar methodologies. The chosen projects reflect similar modern instrumentation with remote sensing and in situ capabilities to provide high-resolution near-storm environmental data for a variety of types of convective systems (i.e., isolated and non-linear organized systems) in different climatological regimes. This interregional comparison afforded by analysis provided in Chapters 2-4 is paramount to provide a more holistic evaluation of TOC-environment relationships and to diagnose potential regional variabilities, including highlighting the value and challenges inherent to using airborne field data.

Comparison of results between the tropical West Atlantic (Chapter 2), East Atlantic (Chapter 3), and Northwest Pacific (Chapter 4) reveal only one consistency across the three regions: statistically similar PBL and mid-tropospheric moisture between isolated and organized TOC. This trend is particularly unexpected for the mid-troposphere, given the large body of literature linking larger, more organized TOC systems to greater mid-tropospheric moisture (e.g., Brown & Zhang, 1997; LeMone et al., 1998; Tompkins, 2001; Bretherton et al., 2004; Cetrone & Houze, 2006; Holloway & Neelin, 2009; Chen et al., 2017; Hannah, 2017; Schiro et al., 2020; Wolding et al., 2022; Chen et al., 2023; Wolding et al., 2024; Muetzelfeldt et al., 2025). The lack of definitive composite mid-tropospheric moisture differences between convective types does not necessarily imply application to individual TOC system evolution and intensity, however. Studies like Martinez et al. (2025) show enhanced mid-tropospheric moisture to support maintenance and growth of individual TOC systems from CPEX-CV, while drier mid-tropospheric conditions promoted TOC dissipation.

Likewise, large intracase near-storm environmental variabilities and individual case comparisons from Chapters 2 and 3 support the existence of temporally sensitive local environmental relationships with individual TOC evolution and intensity that can cloud composite TOC-environment relationships, even when implementing lifecycle contextualization to try and filter out influences of TOC itself on the local environment. The inherently limited field campaign sample sizes may also play a role, as well as the influence of wind shear that has been suggested by prior studies (e.g., Sakaeda & Torri, 2022; Peters et al., 2022; Chen et al., 2023) to complicate the degree of buoyancy and entrainment-related moisture influences on TOC structure.

Regional variabilities existed for wind shear relationships with TOC, unlike for moisture. The tropical Northwest Pacific had the strongest PBL shear relationship with convective type amongst the three basins and was statistically significant both when including and excluding sonde observations outside of inflow regions. The tropical Northwest Pacific general PBL shear relationship of stronger PBL wind shear for organized TOC was consistent with the West Atlantic and inconsistent with the East Atlantic. However, the West and East Atlantic TOC-PBL shear relationships were each statistically insignificant. Similar to the tropical Northwest Pacific with PBL shear, the tropical West Atlantic had the strongest and only statistically significant mid-tropospheric shear relationship with convective type amongst the three basins, both when including and excluding sonde observations outside of inflow regions. While all but the West Atlantic TOC-mid-tropospheric shear relationships were statistically similar, it is notable that the general TOC-wind shear relationships in each of the four analyzed tropospheric layers were different between the West and East Atlantic.

Combined with the aforementioned differences in TOC-shear relationships with the tropical Northwest Pacific, the tropical Atlantic interregional comparisons reveal the presence of regional variability in local TOC-environment relationships that extends suggestions from prior studies (e.g., Chen et al., 2017; Galarneau et al., 2023; Muetzelfeldt et al., 2025) to the tropical Atlantic, tropical Northwest Pacific, and down to convective process-level scales. That being said, these regional variabilities may be an artifact of differing TOC sampling strategies across regionally diverse non-linear TOC morphologies (e.g., shallower isolated TOC sampled in the tropical Northwest Pacific compared to the tropical Atlantic) that could also explain observed moisture and wind shear variability differences within convective type between regions. Moisture and wind shear relationships with TOC are also difficult to isolate from each other using in situ observations, which together with prior studies suggesting variable moisture and wind shear influences on TOC dependent on the magnitude of the other (e.g., Sakaeda & Torri, 2022; Peters et al., 2022; Chen et al., 2023), motivates additional analysis approaches. Given these field campaign data limitations, supplementing the field campaign analysis with idealized CRM sensitivity simulations is warranted, wherein environments constrained by field campaign observations can be better controlled to analyze how local moisture and wind shear impact TOC both individually and in tandem with each other.

6.5 Chapter 5 Summary (Idealized Numerical Modeling)

Chapter 5 aimed to evaluate how local moisture and wind shear separately and together influence collective TOC spatial organization using CM1 idealized numerical modeling (Bryan & Fritsch, 2002). Informed by NASA CPEX series near-storm dropsonde observations (Chen & Zipser, 2017; Skofronick-Jackson et al., 2021; Zawislak et al., 2022), nine sensitivity simulations with different

combinations of deep layer wind shear and mid-tropospheric moisture revealed deep layer shear to promote TOC spatial organization and larger but less intense TOC systems. Meanwhile, mid-tropospheric moisture had no consistent relationships with TOC area nor intensity across a trio differing deep layer shear profiles, though a drier mid-troposphere was linked to enhanced TOC spatial organization. Additionally, mid-tropospheric moisture appeared to be the dominant control of TOC spatial organization when it was high, while TOC spatial organization was more dependent on deep layer wind shear in more moderate mid-tropospheric moisture environments. Sensitivity simulations with high mid-tropospheric moisture also displayed moisture, temperature, precipitation, and convective inhibition spatial patterns consistent with the presence of convectively coupled gravity waves (e.g., Raymond & Fuchs, 2007; Kiladis et al., 2009; Lane & Zhang, 2011; Adames et al., 2019) that were postulated to act as an additional influence on TOC structure and spatial organization.

6.6 Overall Conclusions Regarding Tropical Oceanic Convection Relationships with Local Environments

Overall, coincident, high-resolution observations from modern-day field campaign observations collected during the NASA CPEX, CPEX-AW, CPEX-CV, and CAMP^{2}Ex field campaigns across the tropical North Atlantic and Northwest Pacific convey large near-storm moisture and wind shear variabilities throughout the troposphere, both within individual TOC system lifecycles and collectively within convective types. The large environmental variabilities are ubiquitous across different tropical oceanic regions, even with exclusive selection of observations from inflow regions of storms. The similar near-storm airborne datasets and methodologies used in the analysis across field campaigns and regions lends credence to the robustness of the results, and they provide

a unique look into the incredibly variable nature of local TOC environments that is difficult to capture using spatiotemporally limited satellites, reanalysis, and CRMs.

While generalized relationships between convective type and near-storm moisture and wind shear do emerge amongst the variability within each field campaign, statistically significant results are limited, and there are not any consistent environmental relationships with convective type nor intensity across the three regions of focus. The latter particularly conflicts with broad agreement amongst prior theoretical, observational, reanalysis, and CRM studies that greater mid-tropospheric moisture promotes larger and more intense TOC (e.g., Brown & Zhang, 1997; LeMone et al., 1998; Tompkins, 2001; Bretherton et al., 2004; Cetrone & Houze, 2006; Holloway & Neelin, 2009; Chen et al., 2017; Hannah, 2017; Ahmed & Neelin, 2018; Schiro et al., 2020; Adames et al., 2021; Wolding et al., 2022; Chen et al., 2023; Wolding et al., 2024; Muetzelfeldt et al., 2025). The statistical insignificance and inconsistencies of this relationship across campaigns suggests that this relationship may not be as straightforward as prior studies contend. Rather, this and other tropospheric moisture and wind shear relationships appear more nuanced. Coupled with aforementioned robust large near-storm moisture and wind shear variabilities, these results likely reflect a conditional dependence of moisture and wind shear relationships with TOC structure on each other that is supported by the supplemental CM1 idealized numerical modeling sensitivity simulation results of Chapter 5.

In turn, the prevailing magnitudes of moisture and wind shear are tied to characteristic regional and (sub)seasonal larger scale features, such as the SAL and AEJ in the tropical East Atlantic (e.g., Cook, 1999; Wong & Dessler, 2005; Kaufman et al., 2005; Engelstaedter et al., 2006; Nicholls &

Mohr, 2010), AEWs across the tropical Atlantic (e.g., Kaufman et al., 2005; Engelstaedter et al., 2006; Nicholls & Mohr, 2010; Guy et al., 2011; Wolding et al., 2020; Vargas Martes et al., 2023; Mayta & Adames Corraliza, 2024), and the MJO, ENSO, and Asian monsoon in the tropical Northwest Pacific (e.g., Madden & Julian, 1971; Madden & Julian, 1972; LeMone et al., 1998; Zhang, 2005; Chang et al. 2005; Qian et al., 2010; Guy & Jorgensen, 2014; Rowe & Houze, 2014; Rowe & Houze, 2015; Chen et al., 2016; Dias et al., 2017; Chandra et al, 2018; Sullivan et al., 2019; Reid et al., 2023). Through modulation of prevailing moisture and wind shear, these larger scale features consequently favor certain TOC morphologies with different levels of theoretical dependencies on moisture [i.e., isolated TOC with plume buoyancy and entrainment-driven dilution (e.g., Hannah, 2017; Ahmed & Neelin, 2018; Adames et al., 2021; Wolding et al., 2022; Wolding et al., 2024)] and wind shear [i.e., organized quasi-linear TOC with horizontal convective mass flux (e.g., Mulholland et al., 2021) and sometimes RKW theory (Rotunno et al., 1988)]. As such, altogether the conditional dependence of moisture and wind shear relationships with TOC is likely intrinsically related to the region and time of year of the observational sampling that ultimately can manifest as both interregional variabilities and inconsistent intraregional results regarding local TOC-environment relationships that are indeed seen across studies.

On top of larger scale feature influences, individual case comparisons from Chapters 2 and 3 highlight the impacts of dynamical convergence on TOC structure and intensity that is supported by prior studies (e.g., Banacos & Schultz, 2005; Cifelli et al., 2010; Inoue & Back, 2015; Tomassini, 2018; et al., 2023; Feng et al., 2025; Muetzelfeldt et al., 2025). Meanwhile, Chapter 5 and past literature (e.g., Raymond & Fuchs, 2007; Kiladis et al., 2009; Lane & Zhang, 2011; Fuchs et al., 2012; Adames et al., 2019; Yamazaki & Miura, 2024) denote the role of convectively

coupled gravity waves in influencing TOC, while aerosols are also known to impact TOC (e.g., Rosenfeld, 1999; Yuan et al., 2011; Storer et al., 2014) and thus were a major focus of CPEX series (Chen & Zipser, 2017; Skofronick-Jackson et al., 2021; Zawislak et al., 2022; Nowottnick et al., 2024) and CAMP^{2}Ex (Reid et al., 2023) sampling. As such, each of these environmental variables, which are also modulated by aforementioned regional and (sub)seasonal larger scale features, provide further conditionality to TOC relationships with moisture and wind shear that likely contribute to the documented interregional variabilities and inconsistent intraregional results.

6.7 Limitations Motivating Future Work

The primary focus of this dissertation is centered around an interregional evaluation of local tropospheric moisture and wind shear relationships with 3-D TOC structure. While the impacts of local dynamical convergence and gravity waves are briefly explored in Chapters 2-3 and Chapter 5, respectively, their scope is limited to a few individual case comparisons and simulations. Given the notable influences of local dynamical convergence, gravity waves, and unexplored aerosols on TOC, as well as suggested conditional impacts of environmental influences on TOC structure outlined in Section 6.6, future studies should expand the interregional field campaign analysis to investigate these additional relationships with 3-D TOC structure. Evaluation of these local TOC-environment relationships should be conducted not only in the three regions highlighted in this dissertation, but in other tropical oceanic regions as well that have sufficient in situ observations. Local dynamical convergence, gravity waves, and aerosols can be difficult to retrieve from observational data, however, and reanalysis data (like that incorporated in Chapters 2-3) is limited by factors like spatiotemporal resolution and imperfect precipitation representation (e.g., Gelaro et al., 2017; Chen et al., 2017). As such, high-resolution idealized numerical modeling sensitivity

simulations constrained by field campaign observations should supplement the field campaign analysis, such that the individual roles of dynamical convergence, gravity waves, and aerosols, as well as moisture and wind shear, in influencing TOC structure can be better understood and contextualized with respect to the magnitudes of the others.

While this dissertation uniquely analyzes modern-day coincident, high-resolution airborne observations near historically understudied non-linear TOC that is a novel contribution to the literature, each of the NASA CPEX, CPEX-AW, CPEX-CV, and CAMP^{2}Ex field campaigns employed different TOC flight track sampling strategies (Chen & Zipser, 2017; Skofronick-Jackson et al., 2021; Zawislak et al., 2022; Reid et al., 2023; Nowottnick et al., 2024). Coupled with already restrictive sample sizes that are obstacles to statistical significance, observations from different regions and lifecycle stages of storms were additionally frequently analyzed together, as was shallower CAMP^{2}Ex isolated TOC with deeper CPEX series isolated TOC that altogether is suboptimal. Future work should thus aim to plan future TOC airborne field campaigns with improved and consistent environmental sampling strategies that minimize storm influence, particularly in tropical oceanic regions with prevalent convection like the East, Central, and Southwest Pacific (Figure 1.7) that lack modern-day, high-resolution airborne TOC measurements. The airborne field campaign planning should include intentional coordination with modeling operations, wherein models (e.g., large eddy simulations) are leveraged to strategically design optimized TOC flight track sampling strategies that will acquire better targeted field campaign observations to more effectively initialize and constrain model runs when assimilated. Field campaign observations should also be improved via upgrades to the in situ and remote sensing technology themselves, with higher instrument accuracies needed to adequately capture

and quantify what are at times small but important convective process-level relationships between TOC and its local environment.

Bibliography

Adames, Á. F., Kim, D., Clark, S. K., Ming, Y., & Inoue, K. (2019). Scale analysis of moist thermodynamics in a simple model and the relationship between moisture modes and gravity waves. *Journal of the Atmospheric Sciences*, **76**, 3863–3881. https://doi.org/10.1175/jas-d-19-0121.1

Adames, Á. F., Powell, S. W., Ahmed, F., Mayta, V. C., & Neelin, J. D. (2021). Tropical precipitation evolution in a buoyancy-budget framework. *Journal of the Atmospheric Sciences*, **78**, 509–528. https://doi.org/10.1175/jas-d-20-0074.1

Adhikari, A., Liu, C., & Hayden, L. (2019). Uncertainties of GPM microwave imager precipitation estimates related to precipitation system size and intensity. *Journal of Hydrometeorology*, **20**, 1907–1923. https://doi.org/10.1175/jhm-d-19-0038.1

Adler, R. F., Gu, G., & Huffman, G. J. (2012). Estimating climatological bias errors for the Global Precipitation Climatology Project (GPCP). *Journal of Applied Meteorology and Climatology*, **51**, 84–99. https://doi.org/10.1175/jamc-d-11-052.1

Ahmed, F., & Neelin, J. D. (2018). Reverse engineering the tropical precipitation–buoyancy relationship. *Journal of the Atmospheric Sciences*, **75**, 1587–1608. https://doi.org/10.1175/jas-d-17-0333.1

Alexander, G. D., & Young, G. S. (1992). The relationship between EMEX mesoscale precipitation feature properties and their environmental characteristics. *Monthly Weather Review*, **120**, 554–564. https://doi.org/10.1175/1520-0493(1992)120<0554:trbemp>2.0.co;2

Alfaro, D. A. (2017). Low-tropospheric shear in the structure of squall lines: Impacts on latent heating under layer-lifting ascent. *Journal of the Atmospheric Sciences*, **74**, 229–248. https://doi.org/10.1175/jas-d-16-0168.1

Anber, U., Wang, S., & Sobel, A. (2014). Response of atmospheric convection to vertical wind shear: sloud-system-resolving simulations with parameterized large-scale circulation. Part I: specified radiative cooling. *Journal of the Atmospheric Sciences*, **71**, 2976–2993. https://doi.org/10.1175/jas-d-13-0320.1

Arakawa, A. (1969). Parameterization of cumulus clouds. *Proc. Symp. on Numerical Weather Prediction*, Tokyo, Japan, WMO/International Union of Geodesy and Geophysics, 1–6.

Arakawa, A. (2004). The cumulus parameterization problem: past, present, and future. *Journal of Climate*, **17**, 2493–2525. https://doi.org/10.1175/1520-0442(2004)017<2493:ratcpp>2.0.co;2

Arakawa, A., & Schubert, W. H. (1974). Interaction of a cumulus cloud ensemble with the large-scale environment, part I. *Journal of the Atmospheric Sciences*, 31, 674–701. https://doi.org/10.1175/1520-0469(1974)031<0674:ioacce>2.0.co;2

AVAPS Dropsondes. *AVAPS Dropsondes | Earth Observing Laboratory*. https://www.eol.ucar.edu/content/avaps-dropsondes. (Accessed May 8, 2023)

Back, L. E., & Bretherton, C. S. (2009). On the relationship between SST gradients, boundary layer winds, and convergence over the tropical oceans. *Journal of Climate*, **22**, 4182–4196. https://doi.org/10.1175/2009jcli2392.1

Baidu, M., Schwendike, J., Marsham, J. H., & Bain, C. (2022). Effects of vertical wind shear on intensities of mesoscale convective systems over West and Central Africa. *Atmospheric Science Letters*, **23**. https://doi.org/10.1002/asl.1094

Balogun, R. A., Adeyewa, Z. D., Adefisan, E. A., & Okogbue, E. C. (2020). Vertical structure and frequencies of deep convection during active periods of the West and Central African monsoon season. *Theoretical and Applied Climatology*, **141**, 615–626. https://doi.org/10.1007/s00704-020-03203-6

Banacos, P. C., & Schultz, D. M. (2005). The use of moisture flux convergence in forecasting convective initiation: historical and operational perspectives. *Weather and Forecasting*, **20**, 351–366. https://doi.org/10.1175/waf858.1

Barthe, C., Asencio, N., Lafore, J., Chong, M., Campistron, B., & Cazenave, F. (2010). Multi-scale analysis of the 25–27 July 2006 convective period over Niamey: Comparison between Doppler radar observations and simulations. *Quarterly Journal of the Royal Meteorological Society*, **136**, 190–208. https://doi.org/10.1002/qj.539

Becker, T., & Hohenegger, C. (2021). Entrainment and its dependency on environmental conditions and convective organization in convection-permitting simulations. *Monthly Weather Review*, **149**, 537–550. https://doi.org/10.1175/mwr-d-20-0229.1

Becker, T., Bretherton, C. S., Hohenegger, C., & Stevens, B. (2018). Estimating bulk entrainment with unaggregated and aggregated convection. *Geophysical Research Letters*, **45**, 455–462. https://doi.org/10.1002/2017gl076640

Bedka, K. M., Nehrir, A. R., Kavaya, M., Barton-Grimley, R., Beaubien, M., Carroll, B., et al. (2021). Airborne lidar observations of wind, water vapor, and aerosol profiles during the NASA Aeolus calibration and validation (Cal/Val) test flight campaign. *Atmospheric Measurement Techniques*, **14**, 4305–4334. https://doi.org/10.5194/amt-14-4305-2021

Bickle, M., Marsham, J. H., Griffiths, S. D., Ross, A. N., & Crook, J. (2022). The influence of the diurnal cycle in wind shear and thermodynamics on squall lines in the West African monsoon. *Journal of the Atmospheric Sciences*, **79**, 2125–2143. https://doi.org/10.1175/jas-d-21-0025.1

Black, P., Harrison, L., Beaubien, M., Bluth, R., Woods, R., Penny, A., et al. (2017). High-definition sounding system (HDSS) for atmospheric profiling. *Journal of Atmospheric and Oceanic Technology*, **34**, 777–796. https://doi.org/10.1175/jtech-d-14-00210.1

Blumberg, W. G., Halbert, K. T., Supinie, T. A., Marsh, P. T., Thompson, R. L., & Hart, J. A. (2017). SHARPpy: An open-source sounding analysis toolkit for the atmospheric sciences [Software]. *Bulletin of the American Meteorological Society*, **98**, 1625–1636. https://doi.org/10.1175/bams-d-15-00309.1

Bony, S., Semie, A., Kramer, R. J., Soden, B., Tompkins, A. M., & Emanuel, K. A. (2020). Observed modulation of the tropical radiation budget by deep convective organization and lower-tropospheric stability. *AGU Advances*, **1**, https://doi.org/10.1029/2019av000155

Bretherton, C. S., Blossey, P. N., & Khairoutdinov, M. (2005). An energy-balance analysis of deep convective self-aggregation above uniform SST. *Journal of the Atmospheric Sciences*, **62**, 4273–4292. https://doi.org/10.1175/jas3614.1

Bretherton, C. S., Peters, M. E., & Back, L. E. (2004). Relationships between water vapor path and precipitation over the tropical oceans. *Journal of Climate*, **17**, 1517–1528. https://doi.org/10.1175/1520-0442(2004)017,1517:RBWVPA.2.0.CO;2

Brown, R. G., & Zhang, C. (1997). Variability of midtropospheric moisture and its effect on cloud-top height distribution during TOGA COARE*. Journal of the Atmospheric Sciences, 54, 2760–2774. https://doi.org/10.1175/1520-0469(1997)054<2760:vommai>2.0.co;2

Brammer, A., & Thorncroft, C. D. (2017). Spatial and temporal variability of the three-dimensional flow around African easterly waves. *Monthly Weather Review*, **145**, 2879–2895. https://doi.org/10.1175/mwr-d-16-0454.1

Bryan, G. H., & Fritsch, J. M. (2002). A benchmark simulation for moist nonhydrostatic numerical models. *Monthly Weather Review*, **130**, 2917–2928. https://doi.org/10.1175/1520-0493(2002)130<2917:absfmn>2.0.co;2

Bryan, G. H., & Rotunno, R. (2009). The maximum intensity of tropical cyclones in axisymmetric numerical model simulations. *Monthly Weather Review*, **137**, 1770–1789. https://doi.org/10.1175/2008mwr2709.1

CAMP^{2}Ex APR-3 (2023). Product handbook for the Airborne Cloud and Precipitation Radar of Third Generation (APR3): CAMP^{2}Ex 2019 (release 2.3) [Readme]. *National Aeronautics and Space Administration Doc*., 18 pp. [Available online at https://www-air.larc.nasa.gov/cgi-bin/enzFile?d27141B08DF7F1ACFBAD5C83F9313E20C792f7075622d6169722f5846532f43414d503245582f323031392f5033425f41495243524146542f54414e454c4c492e53494d4f4e452f43414d503245782d415052332d4c325a565f5033425f526561646d655f3234303332392e706466]

CAMP^{2}Ex Dropsonde (2020). CAMP^{2}Ex AVAPS ReadMe/Quick Start Guide [Readme]. *National Center for Atmospheric Research Earth Observing Laboratory Doc.*, 6 pp. [Available online at https://www-air.larc.nasa.gov/cgi-bin/enzFile?d27141B08DF7F1ACFBAD5C83F9313E20C792f7075622d6169722f5846532f43414d503245582f323031392f5033425f41495243524146542f56414e44454e4845455645522e535553414e2f43414d503245582d64726f70736f6e6465735f5033425f52315f524541444d452e706466]

Caswell, T., Droettboom, M., Lee, A., Hunter, J., Firing, E., Hoffmann T., et al. (2021). Matplotlib v3.4.2 [Software]. Zenodo. https://doi.org/10.5281/zenodo.4743323

Cetrone, J., & Houze, R.A., Jr. (2006). Characteristics of tropical convection over the ocean near Kwajalein. *Monthly Weather Review*, **134**, 834–853. https://doi.org/10.1175/mwr3075.1

Chahine, M. T., Pagano, T. S., Aumann, H. H., Atlas, R., Barnet, C., Blaisdell, J., et al. (2006). AIRS improving weather forecasting and providing new data on greenhouse gases. *Bulletin of the American Meteorological Society*, **87**, 911–926. https://doi.org/10.1175/bams-87-7-911

Chandra, A. S., Zuidema, P., Krueger, S., Kochanski, A., Szoeke, S. P., & Zhang J. (2018). Moisture distributions in tropical cold pools from equatorial Indian Ocean observations and cloud-resolving simulations. *Journal of Geophysical Research: Atmospheres*, **123**. https://doi.org/10.1029/2018jd028634

Chang, C.-P., Wang, Z., McBride, J., & Liu, C.-H. (2005). Annual cycle of Southeast Asia—maritime continent rainfall and the asymmetric monsoon transition. *Journal of Climate*, **18**, 287–301. https://doi.org/10.1175/jcli-3257.1

Chen, B., Liu, C., & Mapes, B. E. (2017). Relationships between large precipitating systems and atmospheric factors at a grid scale. *Journal of the Atmospheric Sciences*, **74**, 531–552. https://doi.org/10.1175/jas-d-16-0049

Chen, S. S., & Zipser, E. J. (2017). Convective Process Experiment (CPEX) field campaign collection [Dataset]. NASA EOSDIS Global Hydrometeorology Resource Center Distributed Active Archive Center. https://doi.org/10.5067/CPEX/DATA101

Chen, S. S., Kerns, B. W., Guy, N., Jorgensen, D. P., Delanoë, J., Viltard, N., et al. (2016). Aircraft observations of dry air, the ITCZ, convective cloud systems, and cold pools in MJO during DYNAMO. *Bulletin of the American Meteorological Society*, **97**, 405–423. https://doi.org/10.1175/bams-d-13-00196.1

Chen, X., Leung, L. R., Feng, Z., & Song, F. (2022). Crucial role of mesoscale convective systems in the vertical mass, water, and energy transports of the South Asian summer monsoon. *Journal of Climate*, **35**, 91–108. https://doi.org/10.1175/jcli-d-21-0124.1

Chen, X., Leung, L. R., Feng, Z., & Yang, Q. (2023). Environmental controls on MCS lifetime rainfall over tropical oceans. *Geophysical Research Letters*, **50**. https://doi.org/10.1029/2023GL103267

Cheng, W., Kim, D., Rowe, A., Moon, Y., & Wang, S. (2020). Mechanisms of convective clustering during a 2-day rain event in AMIE/DYNAMO. *Journal of Advances in Modeling Earth Systems*, **12**. https://doi.org/10.1029/2019ms001907

Chudler, K., & Rutledge, S. A. (2021). The coupling between convective variability and large-scale flow patterns observed during PISTON 2018-19. *Journal of Climate*, **34**, 7199-7218. https://doi.org/10.1175/jcli-d-20-0785.1

Ciesielski, P. E., Yu, H., Johnson, R. H., Yoneyama, K., Katsumata, M., Long, C. N., et al. (2014). Quality-controlled upper-air sounding dataset for DYNAMO/CINDY/AMIE: development and corrections. *Journal of Atmospheric and Oceanic Technology*, **31**, 741–764. https://doi.org/10.1175/jtech-d-13-00165.1

Cifelli, R., Lang, T., Rutledge, S. A., Guy, N., Zipser, E. J., Zawislak, J., & Holzworth, R. (2010). Characteristics of an African easterly wave observed during NAMMA. *Journal of the Atmospheric Sciences*, **67**, 3–25. https://doi.org/10.1175/2009jas3141.1

Computational and Information Systems Laboratory (2023). Derecho: HPE Cray EX System (University Community Computing) [Software]. NSF National Center for Atmospheric Research, Boulder, CO. https://doi.org/10.5065/qx9a-pg09

Cook, K. H. (1999). Generation of the African Easterly Jet and its role in determining West African precipitation. *Journal of Climate*, **12**, 1165–1184. https://doi.org/10.1175/1520-0442(1999)012<1165:gotaej>2.0.co;2

Cooperative Institute for Meteorological Satellite Studies (2023). SSMI/SSMIS/AMSR2-derived MIMIC-TPW (Morphed Integrated Microwave Imagery at CIMSS - Total Precipitable Water) Global Satellite Imagery Version 2 [Dataset]. Cooperative Institute for Meteorological Satellite Studies (CIMSS). (Accessed on 20-Dec-2023). https://bin.ssec.wisc.edu/pub/mtpw2/data/

Cooperative Institute for Meteorological Satellite Studies (2025). SSMI/SSMIS/AMSR2-derived MIMIC-TPW (Morphed Integrated Microwave Imagery at CIMSS - Total Precipitable Water) Global Satellite Imagery Version 2 [Dataset]. Cooperative Institute for Meteorological Satellite Studies (CIMSS). https://bin.ssec.wisc.edu/pub/mtpw2/data/

CPEX APR-3 (2018). Product handbook for Airborne Precipitation Radar Third Generation (APR3) CPEX Data [Readme]. *National Aeronautics and Space Administration Doc*., 18 pp. [Available online at https://tcis.jpl.nasa.gov/data/cpex/apr3/APR3_CPEX_Format_R2_180425.pdf]

CPEX DAWN (2019). Readme file for CPEX DAWN data [Readme]. *National Aeronautics and Space Administration Doc.*, 5 pp. [Available online at https://tcis.jpl.nasa.gov/data/cpex/dawn/v5/CPEX_DAWN_README.txt]

CPEX-CV DAWN (2023). README for Doppler Aerosol WiNd Lidar (DAWN) CPEX-CV and CPEX-AW Data Version 1 Data Release [Readme]. *National Aeronautics and Space Administration Langley Research Center Doc.*, 9 pp. [Available online at https://www-air.larc.nasa.gov/cgi-bin/enzFile?c1684C5749C53F525A470B4E964F4D05ABA2f7075622d6169722f5846532f435045582f323032322f4443385f41495243524146542f4245444b412e4b524953544f504845522f6370657863762d4441574e5f4443385f32303232303930365f52305f524541444d452e706466]

CPEX Dropsonde (2019). Readme file for CPEX dropsonde data [Readme]. *National Aeronautics and Space Administration Doc.*, 2 pp. [Available online at https://tcis.jpl.nasa.gov/data/cpex/dropsonde/v2_2019-03/CPEX_DROPSONDE_README.txt03/CPEX_DROPSONDE_README.txt]

CPEX-CV Dropsonde (2023). Dropsonde data report Convective Processes Experiment – Cabo Verde CPEX-CV (2022) [Readme]. *National Center for Atmospheric Research Earth Observing Laboratory Doc.*, 27 pp. [Available online at https://www-air.larc.nasa.gov/cgi-bin/enzFile?c1684C5749C53F525A470B4E964F4D05ABA2f7075622d6169722f5846532f435045582f323032322f4443385f41495243524146542f54484f524e48494c4c2e4c45452f4350455843562d64726f70736f6e64655f4443385f32303232303631365f52305f7468727532303232313030325f524541444d452e706466]

Cui, Z., Pu, Z., Emmitt, G. D., & Greco, S. (2020). The impact of airborne Doppler Aerosol Wind (DAWN) lidar wind profiles on numerical simulations of tropical convective systems during the NASA Convective Processes Experiment (CPEX). *Journal of Atmospheric and Oceanic Technology*, **37**, 705–722. https://doi.org/10.1175/jtech-d-19-0123.1

Da, C. (2015) Preliminary assessment of the Advanced Himawari Imager (AHI) measurement onboard Himawari-8 geostationary satellite. *Remote Sensing Letters*, **6**, 637–646. https://doi.org/10.1080/2150704x.2015.1066522

De Vera, M. V., Di Girolamo, L., Zhao, G., Rauber, R. M., Nesbitt, S. W., & McFarquhar, G. M. (2024). Observations of the macrophysical properties of cumulus cloud fields over the tropical western Pacific and their connection to meteorological variables. *Atmospheric Chemistry and Physics*, **24**, 5603–5623. https://doi.org/10.5194/acp-24-5603-2024

Del Genio, A. D., & Chen, Y. (2015). Cloud-radiative driving of the Madden-Julian Oscillation as seen by the A-train. *Journal of Geophysical Research: Atmospheres*, **120**, 5344–5356. https://doi.org/10.1002/2015jd023278

DeMott, C. A., & Rutledge, S. A. (1998). The vertical structure of TOGAR COARE convection. Part I: radar echo distributions. *Journal of the Atmospheric Sciences*, **55**, 2730–2747. https://doi.org/10.1175/1520-0469(1998)055<2730:tvsotc>2.0.co;2

Dias, J., Sakaeda, N., Kiladis, G. N., & Kikuchi, K. (2017). Influences of the MJO on the space-time organization of tropical convection. *Journal of Geophysical Research: Atmospheres*, **122**, 8012–8032. https://doi.org/10.1002/2017JD026526

Dixon, M., & Romatschke, U. (2022). Three-dimensional convective–stratiform echo-type classification and convectivity retrieval from radar reflectivity. *Journal of Atmospheric and Oceanic Technology*, **39**, 1685–1704. https://doi.org/10.1175/jtech-d-22-0018.1

Dixon, M., & Romatschke, U. (2022). Three-dimensional convective–stratiform echo-type classification and convectivity retrieval from radar reflectivity. *Journal of Atmospheric and Oceanic Technology*, **39**, 1685–1704. https://doi.org/10.1175/jtech-d-22-0018.1

Dunion, J. P. (2011). Rewriting the climatology of the tropical North Atlantic and Caribbean Sea atmosphere. *Journal of Climate*, **24**, 893–908. https://doi.org/10.1175/2010jcli3496.1

Durden, S. L., Li, L., Im, E., & Yueh, S. H. (2003). A surface reference technique for airborne Doppler radar measurements in hurricanes. *Journal of Atmospheric and Oceanic Technology*, **20**, 269–275. https://doi.org/10.1175/1520-0426(2003)020<0269:asrtfa>2.0.co;2

Durden, S. L., Tanelli, S., & Im, E. (2012). Recent observations of clouds and precipitation by the Airborne Precipitation Radar 2nd generation in support of the GPM and ACE Missions. *SPIE Proceedings*. https://doi.org/10.1117/12.977574

Durden, S. L., Tanelli, S., & Sy, O. O. (2020). Comparison of GPM DPR and airborne radar observations in OLYMPEX. *IEEE Geoscience and Remote Sensing Letters*, **17**, 1707–1711. https://doi.org/10.1109/lgrs.2019.2952287

Elsaesser, G. S., & Kummerow, C. D. (2013). A multisensor observational depiction of the transition from light to heavy rainfall on subdaily time scales. *Journal of the Atmospheric Sciences*, **70**, 2309–2324. https://doi.org/10.1175/jas-d-12-0210.1

Engelstaedter, S., Tegen, I., & Washington, R. (2006). North African dust emissions and transport. *Earth-Science Reviews*, **79**, 73–100. https://doi.org/10.1016/j.earscirev.2006.06.004

Esbensen, S. K., & McPhaden, M. J. (1996). Enhancement of tropical ocean evaporation and sensible heat flux by atmospheric mesoscale systems. *Journal of Climate*, **9**, 2307–2325. https://doi.org/10.1175/1520-0442(1996)009<2307:eotoea>2.0.co;2

Feng, C., Pu, Z., Nehrir, A. R., Bedka, K. M. & Doyle, J. (2025). Benefits of assimilating DAWN and HALO observations for numerical simulations of tropical convective systems associated with African easterly waves during NASA's CPEX-AW and CPEX-CV. *Journal of Atmospheric and Oceanic Technology*, **42**, 1419–1444. https://doi.org/10.1175/jtech-d-24-0138.1

Feng, Z., Hagos, S., Rowe, A. K., Burleyson, C. D., Martini, M. N., & Szoeke, S. P. (2015). Mechanisms of convective cloud organization by cold pools over tropical warm ocean during the AMIE/DYNAMO field campaign. *Journal of Advances in Modeling Earth Systems*, **7**, 357–381. https://doi.org/10.1002/2014ms000384

Feng, Z., Ruby Leung, L., Liu, N., Wang, J., Houze Jr., R. A., Li, J., et al. (2021). A global high-resolution mesoscale convective system database using satellite-derived cloud tops, surface precipitation, and tracking. *Journal of Geophysical Research: Atmospheres*, **126**. https://doi.org/10.1029/2020jd034202

Fierro, A. O., Simpson, J., LeMone, M. A., Straka, J. M., & Smull, B. F. (2009). On how hot towers fuel the Hadley Cell: An observational and modeling study of line-organized convection in the equatorial trough from TOGA COARE. *Journal of the Atmospheric Sciences*, **66**, 2730–2746. https://doi.org/10.1175/2009jas3017.1

Fierro, A. O., Zipser, E. J., LeMone, M. A., Straka, J. M., & (Malkus) Simpson, J. (2012). Tropical oceanic hot towers: Need they be undilute to transport energy from the boundary layer to the upper troposphere effectively? An answer based on trajectory analysis of a simulation of a TOGA COARE convective system. *Journal of the Atmospheric Sciences*, **69**, 195–213. https://doi.org/10.1175/jas-d-11-0147.1

Fuchs, Ž., Gjorgjievska, S., & Raymond, D. J. (2012). Effects of varying the shape of the convective heating profile on convectively coupled gravity waves and moisture modes. *Journal of the Atmospheric Sciences*, **69(8)**, 2505–2519. https://doi.org/10.1175/jas-d-11-0308.1

Galarneau, T. J., Zeng, X., Dixon, R. D., Ouyed, A., Su, H., & Cui, W. (2023). Tropical mesoscale convective system formation environments. *Atmospheric Science Letters*, **24**. https://doi.org/10.1002/asl.1152

Garg, P., Nesbitt, S. W., Lang, T. J., Priftis, G., Chronis, T., Thayer, J. D., & Hence, D. A. (2020). Identifying and characterizing tropical oceanic mesoscale cold pools using spaceborne scatterometer winds. *Journal of Geophysical Research: Atmospheres*, **125**. https://doi.org/10.1029/2019jd031812

Gelaro, R., McCarty, W., Suárez, M. J., Todling, R., Molod, A., Takacs, L., et al. (2017). The Modern-Era Retrospective analysis for Research and Applications, Version 2 (MERRA-2). *Journal of Climate*, **30**, 5419–5454. https://doi.org/10.1175/jcli-d-16-0758.1

Gill, A. E. (1980). Some simple solutions for heat-induced tropical circulation. *Quarterly Journal of the Royal Meteorological Society*, **106**, 447–462. https://doi.org/10.1002/qj.49710644905

Grabowski, W. W. (2001). Coupling cloud processes with the large-scale dynamics using the Cloud-Resolving Convection Parameterization (CRCP). *Journal of the Atmospheric Sciences*, **58**, 978–997. https://doi.org/10.1175/1520-0469(2001)058<0978:ccpwtl>2.0.co;2

Grabowski, W. W., & Smolarkiewicz, P. K. (1999) CRCP. A cloud resolving convection parameterization for modeling the tropical convecting atmosphere. *Physica D: Nonlinear Phenomena*, **133**, 171–178. https://doi.org/10.1016/s0167-2789(99)00104-9

Grant, L. D., Lane, T. P., & van den Heever, S. C. (2018). The role of cold pools in tropical oceanic convective systems. *Journal of the Atmospheric Sciences*, **75**, 2615–2634. https://doi.org/10.1175/jas-d-17-0352.1

Grant, L. D., Moncrieff, M. W., Lane, T. P., & van den Heever, S. C. (2020). Shear-parallel tropical convective systems: importance of cold pools and wind shear. *Geophysical Research Letters*, **47**. https://doi.org/10.1029/2020gl087720

Greco, S., Emmitt, G. D., & Garstang, M. (2018). *Overview of YES dropsonde performance during CPEX and YES QC*. Presented at CPEX Science Team Workshop, Salt Lake City, UT. [Available online at https://cpex.jpl.nasa.gov/cpex2017/scienceteammeeting/2018/SteveGRECO_CPEX_SLC_DROP_FINAL.pdf]

Greco, S., Emmitt, G. D., Garstang, M., & Kavaya, M. (2020). Doppler Aerosol Wind (DAWN) lidar during CPEX 2017: Instrument performance and data utility. *Remote Sensing*, **12**, 2951. https://doi.org/10.3390/rs12182951

Guy, N., & Jorgensen, D. P. (2014). Kinematic and precipitation characteristics of convective systems observed by airborne Doppler radar during the life cycle of a Madden–Julian Oscillation in the Indian Ocean. *Monthly Weather Review*, **142**, 1385–1402. https://doi.org/10.1175/mwr-d-13-00252.1

Guy, N., Rutledge, S. A., & Cifelli, R. (2011). Radar characteristics of continental, coastal, and maritime convection observed during AMMA/NAMMA. *Quarterly Journal of the Royal Meteorological Society*, **137**, 1241–1256. https://doi.org/10.1002/qj.839

Hannah, W. M. (2017). Entrainment versus dilution in tropical deep convection. *Journal of the Atmospheric Sciences*, **74**, 3725–3747. https://doi.org/10.1175/jas-d-16-0169.1

Hartmann, D. L. (2016). Tropical Anvil Clouds and climate sensitivity. *Proceedings of the National Academy of Sciences*, **113**, 8897–8899. https://doi.org/10.1073/pnas.1610455113

Hartmann, D. L., Moy, L. A., & Fu, Q. (2001). Tropical convection and the energy balance at the top of the atmosphere. *Journal of Climate*, **14**, 4495–4511. https://doi.org/10.1175/1520-0442(2001)014<4495:tcateb>2.0.co;2

Heikenfeld, M., Marinescu, P. J., Christensen, M., Watson-Parris, D., Senf, F., van den Heever, S. C., & Stier, P. (2019). Tobac 1.2: towards a flexible framework for tracking and analysis of clouds in diverse datasets. *Geoscientific Model Development*, **12**, 4551–4570. https://doi.org/10.5194/gmd-12-4551-2019

Hersbach, H., Bell, B., Berrisford, P., Biavati, G., Horányi, A., Muñoz Sabater, J., et al. (2018). ERA5 hourly data on pressure levels from 1979 to present [Dataset]. Copernicus Climate Change Service (C3S) Climate Data Store (CDS). https://doi.org/10.24381/cds.bd0915c6

Heymsfield, G. M., Tian, L., Heymsfield, A. J., Li, L., & Guimond, S. (2010). Characteristics of deep tropical and subtropical convection from nadir-viewing high-altitude airborne Doppler radar. *Journal of the Atmospheric Sciences*, **67**, 285–308. https://doi.org/10.1175/2009jas3132.1

Hock, T. F., & Franklin, J. L. (1999). The NCAR GPS dropwindsonde. *Bulletin of the American Meteorological Society*, **80**, 407–420. https://doi.org/10.1175/1520-0477(1999)080<0407:tngd>2.0.co;2

Holloway, C. E., & Neelin, J. D. (2009). Moisture vertical structure, column water vapor, and tropical deep convection. *Journal of the Atmospheric Sciences*, **66**, 1665–1683. https://doi.org/10.1175/2008jas2806.1

Holloway, C. E., Wing, A. A., Bony, S., Muller, C., Masunaga, H., L'Ecuyer, T. S., et al. (2017). Observing convective aggregation. *Surveys in Geophysics*, **38(6)**, 1199–1236. https://doi.org/10.1007/s10712-017-9419-1

Houze, R. A., Jr. (1982). Cloud clusters and large-scale vertical motions in the tropics. *Journal of the Meteorological Society of Japan. Ser. II*, **60**, 396–410. https://doi.org/10.2151/jmsj1965.60.1_396

Houze, R. A., Jr. (1977). Structure and dynamics of a tropical squall–line system. *Monthly Weather Review*, **105**, 1540–1567. https://doi.org/10.1175/1520-0493(1977)105<1540:sadoat>2.0.co;2

Houze, R. A., Jr. (1989). Observed structure of mesoscale convective systems and implications for large-scale heating. *Quarterly Journal of the Royal Meteorological Society*, **115**, 425–461. https://doi.org/10.1002/qj.49711548702

Houze, R. A., Jr. (1997). Stratiform precipitation in regions of convection: A meteorological paradox? *Bulletin of the American Meteorological Society*, **78**, 2179–2196. https://doi.org/10.1175/1520-0477(1997)078<2179:spiroc>2.0.co;2

Houze, R. A., Jr. (2018). 100 years of research on mesoscale convective systems. *Meteorological Monographs*, **59**. https://doi.org/10.1175/amsmonographs-d-18-0001.1

Houze, R. A., Jr., & Betts, A. K. (1981). Convection in GATE. *Reviews of Geophysics*, **19**, 541–576. https://doi.org/10.1029/rg019i004p00541

Houze, R. A., Jr., Rasmussen, K. L., Zuluaga, M. D., & Brodzik, S. R. (2015). The variable nature of convection in the tropics and subtropics: A legacy of 16 years of the Tropical Rainfall Measuring Mission Satellite. *Reviews of Geophysics*, **53**, 994–1021. https://doi.org/10.1002/2015rg000488

Hristova-Veleva, S. M., Peggy Li, P., Knosp, B., Vu, Q., Turk, F. J., Poulsen, W. L., et al. (2020). An eye on the storm: Integrating a wealth of data for quickly advancing the physical understanding and forecasting of tropical cyclones. *Bulletin of the American Meteorological Society*, **101**. https://doi.org/10.1175/bams-d-19-0020.1

Hristova-Veleva, S., Zhang, S. Q., Turk, F. J., Haddad, Z. S., & Sawaya, R. C. (2021). Assimilation of DAWN Doppler wind lidar data during the 2017 Convective Processes Experiment (CPEX): Impact on precipitation and flow structure. *Atmospheric Measurement Techniques*, **14**, 3333–3350. https://doi.org/10.5194/amt-14-3333-2021

Huffman, G. J., Stocker, E. F., Bolvin, D. T., Nelkin E. J., & Tan J. (2019). GPM IMERG Final Precipitation 13 Half Hourly 0.1 degree x 0.1 degree V07 [Dataset]. Goddard Earth Sciences Data and Information Services Center (GES DISC). https://doi.org/10.5067/GPM/IMERG/3B-HH/07

Hunter, J. D. (2007). Matplotlib: A 2d graphics environment. *Computing in Science & Engineering*, **9**(3), 90– 95. https://doi.org/10.1109/MCSE.2007.55

Iacono, M. J., Delamere, J. S., Mlawer, E. J., Shephard, M. W., Clough, S. A., & Collins, W. D. (2008). Radiative forcing by long-lived greenhouse gases: calculations with the AER radiative transfer models. *Journal of Geophysical Research: Atmospheres*, **113(D13)**. https://doi.org/10.1029/2008jd009944

Igel, M. R., & van den Heever, S. C. (2015). The relative influence of environmental characteristics on tropical deep convective morphology as observed by CloudSat. *Journal of Geophysical Research: Atmospheres*, **120**, 4304–4322. https://doi.org/10.1002/2014jd022690

Inoue, K., & Back, L. E. (2015). Gross moist stability assessment during TOGA COARE: Various interpretations of gross moist stability. *Journal of the Atmospheric Sciences*, **72**, 4148–4166. https://doi.org/10.1175/jas-d-15-0092.1

Janiga, M. A., & Thorncroft, C. D. (2016). The influence of African easterly waves on convection over tropical Africa and the East Atlantic. *Monthly Weather Review*, **144**, 171–192. https://doi.org/10.1175/mwr-d-14-00419.1

Jenney, A. M., Houze Jr., R. A., LeMone, M., Thompson, E. J., Núñez Ocasio, K. M., Zhang, C., & Nathan, T. R. (2025). Celebrating 50 years since GATE. *Bulletin of the American Meteorological Society*, **106**. https://doi.org/10.1175/bams-d-24-0063.1

Jo, E., & Lasher-Trapp, S. (2022). Entrainment in a simulated supercell thunderstorm. Part II: the influence of vertical wind shear and general effects upon precipitation. *Journal of the Atmospheric Sciences*, **79(5)**, 1429–1443. https://doi.org/10.1175/jas-d-21-0289.1

Jury, M. R., Chiao, S., & Harmsen, E. W. (2009). Mesoscale structure of trade wind convection over Puerto Rico: Composite observations and numerical simulation. *Boundary-Layer Meteorology*, **132**, 289–313. https://doi.org/10.1007/s10546-009-9393-3

Kaufman, Y. J., Koren, I., Remer, L. A., Tanré, D., Ginoux, P., & Fan, S. (2005). Dust transport and deposition observed from the Terra-Moderate Resolution Imaging Spectroradiometer (MODIS) spacecraft over the Atlantic Ocean. *Journal of Geophysical Research: Atmospheres*, **110**. https://doi.org/10.1029/2003jd004436

Kavaya, M. J., Beyon, J. Y., Koch, G. J., Petros, M., Petzar, P. J., Singh, U. N., et al. (2014). The Doppler Aerosol Wind (DAWN) airborne, wind-profiling coherent-detection lidar system: Overview and preliminary flight results. *Journal of Atmospheric and Oceanic Technology*, **31**, 826–842. https://doi.org/10.1175/jtech-d-12-00274.1

Kiladis, G. N., Thorncroft, C. D., & Hall, N. M. (2006). Three-dimensional structure and dynamics of African easterly waves. part I: Observations. *Journal of the Atmospheric Sciences*, **63**, 2212–2230. https://doi.org/10.1175/jas3741.1

Kiladis, G. N., Wheeler, M. C., Haertel, P. T., Straub, K. H., & Roundy, P. E. (2009). Convectively coupled equatorial waves. *Reviews of Geophysics*, **47(2)**. https://doi.org/10.1029/2008rg000266

Kingsmill, D. E., & Houze, R. A., Jr. (1999). Thermodynamic characteristics of air flowing into and out of precipitating convection over the west Pacific warm pool. *Quarterly Journal of the Royal Meteorological Society*, **125**, 1209–1229. https://doi.org/10.1002/qj.1999.49712555606

Klemp, J. B., & Wilhelmson, R. B. (1978). Simulations of right- and left-moving storms produced through storm splitting. *Journal of the Atmospheric Sciences*, **35(6)**, 1097–1110. https://doi.org/10.1175/1520-0469(1978)035<1097:soralm>2.0.co;2

Kummerow, C., Barnes, W., Kozu, T., Shiue, J., & Simpson, J. (1998). The Tropical Rainfall Measuring Mission (TRMM) sensor package. *Journal of Atmospheric and Oceanic Technology*, **15(3)**, 809–817. https://doi.org/10.1175/1520-0426(1998)015<0809:ttrmmt>2.0.co;2

Lane, T. P., & Moncrieff, M. W. (2015). Long-lived mesoscale systems in a low–convective inhibition environment. Part I: upshear propagation. *Journal of the Atmospheric Sciences*, **72(11)**, 4297–4318. https://doi.org/10.1175/jas-d-15-0073.1

Lane, T. P., & Zhang, F. (2011). Coupling between gravity waves and tropical convection at mesoscales. *Journal of the Atmospheric Sciences*, **68(11)**, 2582–2598. https://doi.org/10.1175/2011jas3577.1

Lasher-Trapp, S., Jo, E., Allen, L. R., Engelsen, B. N., & Trapp, R. J. (2021). Entrainment in a simulated supercell thunderstorm, Part I: the evolution of different entrainment mechanisms and their dilutive effects. *Journal of the Atmospheric Sciences*, **78**, 2725-2740. https://doi.org/10.1175/jas-d-20-0223.1

Lawton, Q. (2024). Objective African Easterly Tracks in Reanalysis Data using "QTrack" Version 2 [Dataset]. Zenodo. https://doi.org/10.5281/zenodo.14338645

Lawton, Q. A., Majumdar, S. J., Dotterer, K., Thorncroft, C., & Schreck, C. J. (2022). The influence of convectively coupled Kelvin waves on African easterly waves in a wave-following framework. *Monthly Weather Review*, **150**, 2055–2072. https://doi.org/10.1175/mwr-d-21-0321.1

LeMone, M. A., & Zipser, E. J. (1980). Cumulonimbus vertical velocity events in GATE. Part I: Diameter, intensity and mass flux. *Journal of the Atmospheric Sciences*, **37**, 2444–2457. https://doi.org/10.1175/1520-0469(1980)037<2444:cvveig>2.0.co;2

LeMone, M. A., Barnes, G. M., & Zipser, E. J. (1984). Momentum flux by lines of cumulonimbus over the tropical oceans. *Journal of the Atmospheric Sciences*, **41**, 1914–1932. https://doi.org/10.1175/1520-0469(1984)041<1914:mfbloc>2.0.co;2

LeMone, M. A., Zipser, E. J., & Trier, S. B. (1998). The role of environmental shear and thermodynamic conditions in determining the structure and evolution of mesoscale convective systems during TOGA COARE. *Journal of the Atmospheric Sciences*, **55**, 3493–3518. https://doi.org/10.1175/1520-0469(1998)055<3493:troesa>2.0.co;2

Lindzen, R. S., & Nigam, S. (1987). On the role of sea surface temperature gradients in forcing low-level winds and convergence in the tropics. *Journal of the Atmospheric Sciences*, **44**, 2418–2436. https://doi.org/10.1175/1520-0469(1987)044<2418:otross>2.0.co;2

Liu, S., & Liang, X.-Z. (2010). Observed diurnal cycle climatology of planetary boundary layer height. *Journal of Climate*, **23**, 5790–5809. https://doi.org/10.1175/2010jcli3552.1

Madden, R. A., & Julian, P. R. (1971). Detection of a 40–50 day oscillation in the zonal wind in the tropical Pacific. *Journal of the Atmospheric Sciences*, **28**, 702–708. https://doi.org/10.1175/1520-0469(1971)028<0702:doadoi>2.0.co;2

Madden, R. A., & Julian, P. R. (1972). Description of global-scale circulation cells in the tropics with a 40–50 day period. *Journal of the Atmospheric Sciences*, **29**, 1109–1123. https://doi.org/10.1175/1520-0469(1972)029<1109:dogscc>2.0.co;2

Maddy, E. S., & Barnet, C. D. (2008). Vertical resolution estimates in version 5 of AIRS operational retrievals. *IEEE Transactions on Geoscience and Remote Sensing*, **46**, 2375–2384. https://doi.org/10.1109/tgrs.2008.917498

Markowski, P., & Richardson, Y. (2011). Mesoscale meteorology in midlatitudes (Vol. 2). John Wiley & Sons.

Martin, C., & Suhr, I. (2021). NCAR/EOL Atmospheric Sounding Processing Environment (ASPEN) software. Version 3.4.5 [Software]. [Available online at: https://www.eol.ucar.edu/content/aspen]. (Accessed November 16, 2022)

Martinez, G., Rowe, A. K., Núñez Ocasio, K. M., Moon, Z. L., & Rodenkirch, B. D. (2025). Evaluating environmental moisture relative to tropical deep convective growth using CPEX-CV airborne and satellite observations. *Journal of Geophysical Research: Atmospheres*, **130(17)**. https://doi.org/10.1029/2025jd043877

Maybee, B., Marsham, J. H., Klein, C. M., Parker, D. J., Barton, E. J., Taylor, C. M., et al. (2024). Wind shear effects in convection–permitting models influence MCS rainfall and forcing of tropical circulation. *Geophysical Research Letters*, **51**. https://doi.org/10.1029/2024gl110119

Mayta, V. C., & Adames Corraliza, Á. F. (2024). The stirring tropics: the ubiquity of moisture modes and moisture–vortex instability. *Journal of Climate*, **37**, 1981–1998. https://doi.org/10.1175/jcli-d-23-0145.1

Mazza, E., & Chen, S. S. (2021). Subsidence warming in the tropical cyclogenesis of Cindy (2017): CPEX observations and coupled modeling. *Journal of the Atmospheric Sciences*, **78**, 3385–3400. https://doi.org/10.1175/jas-d-20-0340.1

Mechem, D. B., Chen, S. S., & Houze, R. A., Jr. (2006). Momentum transport processes in the stratiform regions of mesoscale convective systems over the western Pacific warm pool. *Quarterly Journal of the Royal Meteorological Society*, **132**, 709–736. https://doi.org/10.1256/qj.04.141

Mechem, D. B., Houze, R. A., Jr., & Chen, S. S. (2002). Layer inflow into precipitating convection over the western tropical Pacific. *Quarterly Journal of the Royal Meteorological Society*, **128**, 1997–2030. https://doi.org/10.1256/003590002320603502

Minamide, M., & Posselt, D. J. (2022). Using ensemble data assimilation to explore the environmental controls on the initiation and predictability of moist convection. *Journal of the Atmospheric Sciences*, **79**, 1151–1169. https://doi.org/10.1175/jas-d-21-0140.1

Morrison, H., & Peters, J. M. (2018). Theoretical expressions for the ascent rate of moist deep convective thermals. *Journal of the Atmospheric Sciences*, **75**, 1699–1719. https://doi.org/10.1175/jas-d-17-0295.1

Morrison, H., Thompson, G., & Tatarskii, V. (2009). Impact of cloud microphysics on the development of trailing stratiform precipitation in a simulated squall line: comparison of one- and two-moment schemes. *Monthly Weather Review*, **137(3)**, 991–1007. https://doi.org/10.1175/2008mwr2556.1

Moser, D. H., & Lasher-Trapp, S. (2018). Cloud-spacing effects upon entrainment and rainfall along a convective line. *Journal of Applied Meteorology and Climatology*, **57(8)**, 1865–1882. https://doi.org/10.1175/jamc-d-17-0363.1

Muetzelfeldt, M. R., Plant, R. S., Christensen, H. M., Zhang, Z., Woollings, T., Feng, Z., & Li, P. (2025). Environmental conditions affecting global mesoscale convective system occurrence. *Journal of the Atmospheric Sciences*, **82**, 391–407. https://doi.org/10.1175/jas-d-24-0058.1

Mulholland, J. P., Peters, J. M., & Morrison, H. (2021). How does vertical wind shear influence entrainment in squall lines? *Journal of the Atmospheric Sciences*, **78**, 1931–1946. https://doi.org/10.1175/jas-d-20-0299.1

Muller, C. J., & Bony, S. (2015). What favors convective aggregation and why? *Geophysical Research Letters*, **42(13)**, 5626–5634. https://doi.org/10.1002/2015gl064260

Muller, C. J., & Held, I. M. (2012). Detailed investigation of the self-aggregation of convection in cloud-resolving simulations. *Journal of the Atmospheric Sciences*, **69(8)**, 2551–2565. https://doi.org/10.1175/jas-d-11-0257.1

Muller, C. J., Yang, D., Craig, G., Cronin, T., Fildier, B., Haerter, J., et al. (2022). Spontaneous aggregation of convective storms. *Annual Review of Fluid Mechanics*, **54**, 133-157. https://doi.org/10.5194/egusphere-egu22-11607

NASA/LARC/SD/ASDC. (2023). PISTON 2019 Research Vessel (RV) Sally Ride data [Dataset]. NASA Langley Atmospheric Science Data Center Distributed Active Archive Center. https://doi.org/10.5067/SUBORBITAL/PISTON2019-ONR-NOAA/RVSALLYRIDE/DATA001

Ni, X., Liu, C., & Zipser, E. (2019). Ice microphysical properties near the tops of deep convective cores implied by the GPM Dual-Frequency Radar observations. *Journal of the Atmospheric Sciences*, **76**, 2899–2917. https://doi.org/10.1175/jas-d-18-0243.1

Nicholls, S. D., & Mohr, K. I. (2010). An analysis of the environments of intense convective systems in West Africa in 2003. *Monthly Weather Review*, **138**, 3721–3739. https://doi.org/10.1175/2010mwr3321.1

Nowottnick, E. P., Rowe, A. K., Nehrir, A. R., Zawislak, J. A., Piña, A. J., McCarty, W., et al. (2024). Dust, convection, winds, and waves: the 2022 NASA CPEX-CV campaign. *Bulletin of the American Meteorological Society*, **105**. https://doi.org/10.1175/bams-d-23-0201.1

NSF NCAR Earth Observing Laboratory. (1993). NCAR Airborne Vertical Atmospheric Profiling System (AVAPS). NSF NCAR Earth Observing Laboratory. https://doi.org/10.5065/D66W9848

Núñez Ocasio, K. M., Evans, J. L., & Young, G. S. (2020). A wave-relative framework analysis of AEW–MCS interactions leading to tropical cyclogenesis. *Monthly Weather Review*, **148**, 4657–4671. https://doi.org/10.1175/mwr-d-20-0152.1

Padullés, R., Kuo, Y.-H., Neelin, J. D., Turk, F. J., Ao, C. O., & de la Torre Juárez, M. (2022). Global tropical precipitation relationships to free-tropospheric water vapor using radio occultations. *Journal of the Atmospheric Sciences*, **79**, 1585–1600. https://doi.org/10.1175/jas-d-21-0052.1

Parker, D. J., Burton, R. R., Diongue-Niang, A., Ellis, R. J., Felton, M., Taylor, C. M., et al. (2005). The diurnal cycle of the West African monsoon circulation. *Quarterly Journal of the Royal Meteorological Society*, **131(611)**, 2839–2860. https://doi.org/10.1256/qj.04.52

Parker, M. D. (2010). Relationship between system slope and updraft intensity in squall lines. *Monthly Weather Review*, **138(9)**, 3572–3578. https://doi.org/10.1175/2010mwr3441.1

Peters, J. M. (2016). The impact of effective buoyancy and dynamic pressure forcing on vertical velocities within two-dimensional updrafts. *Journal of the Atmospheric Sciences*, **73**, 4531–4551. https://doi.org/10.1175/jas-d-16-0016.1

Peters, J. M., Hannah, W., & Morrison, H. (2019). The influence of vertical wind shear on moist thermals. *Journal of the Atmospheric Sciences*, **76**, 1645–1659. https://doi.org/10.1175/jas-d-18-0296.1

Peters, J. M., Morrison, H., Nelson, T. C., Marquis, J. N., Mulholland, J. P., & Nowotarski, C. J. (2022). The influence of shear on deep convection initiation. Part I: theory. *Journal of the Atmospheric Sciences*, **79(6)**, 1669–1690. https://doi.org/10.1175/jas-d-21-0145.1

Pilewskie, J. A., & L'Ecuyer, T. S. (2022). The global nature of early-afternoon and late-night convection through the eyes of the A-train. *Journal of Geophysical Research: Atmospheres*, **127**. https://doi.org/10.1029/2022jd036438

Pilewskie, J. A., & L'Ecuyer, T. S. (2026). The role of convective intensity in modulating Earth's radiative balance. *Journal of Climate*, **39**, 125–144. https://doi.org/10.1175/jcli-d-24-0334.1

Pincus, R., Beljaars, A., Buehler, S. A., Kirchengast, G., Ladstaedter, F., & Whitaker, J. S. (2017). The representation of tropospheric water vapor over low-latitude oceans in (re-)analysis: errors, impacts, and the ability to exploit current and prospective observations. *Surveys in Geophysics*, **38**, 1399–1423. https://doi.org/10.1007/s10712-017-9437-z

Qian, J.-H. (2008). Why precipitation is mostly concentrated over islands in the Maritime Continent. *Journal of the Atmospheric Sciences*, **65**, 1428–1441. https://doi.org/10.1175/2007jas2422.1

Qian, J.-H., Robertson, A. W., & Moron, V. (2010). Interactions among ENSO, the monsoon, and diurnal cycle in rainfall variability over Java, Indonesia. *Journal of the Atmospheric Sciences*, **67**, 3509–3524. https://doi.org/10.1175/2010jas3348.1

Rajagopal, M., Russell, J., Skok, G., & Zipser, E. (2023). Tracking mesoscale convective systems in IMERG and regional variability of their properties in the tropics. *Journal of Geophysical Research: Atmospheres*, **128**. https://doi.org/10.1029/2023jd038563

Randall, D. A., & Fowler, L. D. (1999). Eauliq: The next generation. *Colorado State University Atmospheric Science Paper No. 673*, 65 pp.

Randall, D. A., Khairoutdinov, M., Arakawa, A., & Grabowski, W. (2003). Breaking the cloud parameterization deadlock. *Bulletin of the American Meteorological Society*, **84**, 1547–1564. https://doi.org/10.1175/bams-84-11-1547

Raymond, D. J., & Fuchs, Ž. (2007). Convectively coupled gravity and moisture modes in a simple atmospheric model. *Tellus A: Dynamic Meteorology and Oceanography*, **59(5)**, 627. https://doi.org/10.1111/j.1600-0870.2007.00268.x

Raymond, D. J., & Fuchs-Stone, Ž (2021). Emergent properties of convection in OTREC and PREDICT. *Journal of Geophysical Research: Atmospheres*, **126**. https://doi.org/10.1029/2020jd033585

Reid, J. S., Maring, H. B., Narisma, G. T., van den Heever, S., Di Girolamo, L., Ferrare, R., et al. (2023). The coupling between tropical meteorology, aerosol lifecycle, convection, and radiation during the Cloud, Aerosol and Monsoon Processes Philippines Experiment ($CAMP^2Ex$). *Bulletin of the American Meteorological Society*, **104**. https://doi.org/10.1175/bams-d-21-0285.1

Riehl, H. & Malkus, J. S. (1958). On the heat balance in the equatorial trough zone. *Geophysica*, **6**, 503-538.

Rio, C., Del Genio, A. D., & Hourdin, F. (2019). Ongoing breakthroughs in convective parameterization. *Current Climate Change Reports*, **5**, 95–111. https://doi.org/10.1007/s40641-019-00127-w

Rios-Berrios, R., Sakaeda, N., Jimenez-González, H. J., Nieves-Jimenez, A., Zayas, Y., Martin, E., et al. (2023). Observing the diurnal cycle of coastal rainfall over western Puerto Rico in collaboration with University of Puerto Rico students. *Bulletin of the American Meteorological Society*, **104**. https://doi.org/10.1175/bams-d-21-0322.1

Robe, F. R., & Emanuel, K. A. (2001). The effect of vertical wind shear on radiative–convective equilibrium states. *Journal of the Atmospheric Sciences*, **58**, 1427–1445. https://doi.org/10.1175/1520-0469(2001)058<1427:teovws>2.0.co;2

Roca, R. Ã., Brogniez, H., Chambon, P., Chomette, O., Cloché, S., Gosset, M. E., et al. (2015). The Megha-Tropiques mission: A review after three years in orbit. *Frontiers in Earth Science*, **3**. https://doi.org/10.3389/feart.2015.00017

Roca, R. Ã., Fiolleau, T., & Netz, L. (2025). Scale-dependence of tropical oceanic deep convective systems' cloud shield morphology to environmental conditions. *Journal of Geophysical Research: Atmospheres*, **130**. https://doi.org/10.22541/au.172771698.89429063/v1

Rodenkirch, B. (2024). brodenkirch/CPEXAW: March 26, 2024 Release (Version 1.0.0) [Software]. Zenodo. https://doi.org/10.5281/zenodo.10884221

Rodenkirch, B. (2025a). brodenkirch/CM1: October 9, 2025 Release (Version 1.0.0) [Software]. Zenodo. https://doi.org/10.5281/zenodo.17308731

Rodenkirch, B. (2025b). brodenkirch/CPEXCV: December 7, 2025 Release (Version 1.0.0) [Software]. Zenodo. https://doi.org/10.5281/zenodo.17850834

Rodenkirch, B. D., & Rowe, A. K. (2024). Near-storm environmental relationships with tropical oceanic convective structure observed during NASA CPEX and CPEX-AW. *Journal of Geophysical Research: Atmospheres*, **129**. https://doi.org/10.1029/2023jd039632

Rodenkirch, B. D., & Rowe, A. K. (2025). Linking In Situ Observations of Near-storm Environments to Tropical Oceanic Convective Structure from NASA CPEX-CV. *ESS Open Archive (preprint)*. https://doi.org/10.22541/essoar.176659753.32011710/v1

Rodenkirch, B. D., Rowe, A. K., & Rios-Berrios, R. (2025). Vertical Wind Shear Influences on Tropical Oceanic Convection in Idealized Numerical Model Simulations. *ESS Open Archive (preprint)*. https://doi.org/10.22541/essoar.176083561.12117786/v1

Rodriguez-Monje, Rauqel (2023). Airborne Precipitation Radar 3rd Generation (APR-3) CPEX-CV [Dataset]. NASA Global Hydrometeorology Resource Center DAAC. https://doi.org/10.5067/CPEXCV/APR3/DATA101

Romatschke, U., & Dixon, M. J. (2022). Vertically resolved convective–stratiform echo-type identification and convectivity retrieval for vertically pointing radars. *Journal of Atmospheric and Oceanic Technology*, **39**, 1705–1716. https://doi.org/10.1175/jtech-d-22-0019.1

Romps, D. M., & Kuang, Z. (2010). Nature versus nurture in shallow convection. *Journal of the Atmospheric Sciences*, **67**, 1655–1666. https://doi.org/10.1175/2009jas3307.1

Rosenfeld, D. (1999). TRMM observed first direct evidence of smoke from forest fires inhibiting rainfall. *Geophysical Research Letters*, **26**, 3105–3108. https://doi.org/10.1029/1999gl006066

Rotunno, R., Klemp, J. B., & Weisman, M. L. (1988). A theory for strong, long-lived squall lines. *Journal of the Atmospheric Sciences*, **45**, 463–485. https://doi.org/10.1175/1520-0469(1988)045<0463:atfsll>2.0.co;2

Rowe, A. K., & Houze, R. A., Jr. (2014). Microphysical characteristics of MJO convection over the Indian Ocean during DYNAMO. *Journal of Geophysical Research: Atmospheres*, **119**, 2543–2554. https://doi.org/10.1002/2013JD020799

Rowe, A. K., & Houze, R. A., Jr. (2015). Cloud organization and growth during the transition from suppressed to active MJO conditions. *Journal of Geophysical Research: Atmospheres*, **120**. https://doi.org/10.1002/2014jd022948

Russell, J. (2022). Tracked IMERG Mesoscale Precipitation Systems (TIMPS) Version 1 [Dataset]. Zenodo. https://doi.org/10.5281/zenodo.5781881

Sadowy, G. A., Berkun, A., Chun, W., Im, E., & Durden, S. (2003). Development of an advanced airborne precipitation radar. *Microwave Journal*, **46**, 84-98

Sakaeda, N., & Torri, G. (2022). The behaviors of intraseasonal cloud organization during DYNAMO/AMIE. *Journal of Geophysical Research: Atmospheres*, **127**. https://doi.org/10.1029/2021jd035749

Sakaeda, N., & Torri, G. (2023). The observed effects of cold pools on convection triggering and organization during DYNAMO/AMIE. *Journal of Geophysical Research: Atmospheres*, **128**. https://doi.org/10.1029/2023jd038635

Satoh, M., Stevens, B., Judt, F., Khairoutdinov, M., Lin, S.-J., Putman, W. M., & Düben, P. (2019). Global cloud-resolving models. *Current Climate Change Reports*, **5**, 172–184. https://doi.org/10.1007/s40641-019-00131-0

Savarin, A., Chen, S. S., Kerns, B. W., & Jorgensen, D. P. (2014). *Convective cold pool structure and boundary layer recovery time in DYNAMO*. Paper presented at 31st Conference on Hurricanes and Tropical Meteorology, American Meteorological Society, San Diego, CA. [Available online at https://ams.confex.com/ams/31Hurr/webprogram/Paper245387.html]

Saxen, T. R., & Rutledge, S. A. (1998): Surface fluxes and boundary layer recovery in TOGA COARE: sensitivity to convective organization. *Journal of the Atmospheric Sciences*, **55**, 2763–2781. https://doi.org/10.1175/1520-0469(1998)055<2763:sfablr>2.0.co;2

Saxen, T. R., & Rutledge, S. A. (2000). Surface rainfall–cold cloud fractional coverage relationship in TOGA COARE: A function of vertical wind shear. *Monthly Weather Review*, **128**, 407. https://doi.org/10.1175/1520-0493(2000)128<0407:srccfc>2.0.co;2

Schiro, K. A., Sullivan, S. C., Kuo, Y., Su, H., Gentine, P., Elsaesser, G. S., et al. (2020). Environmental controls on tropical mesoscale convective system precipitation intensity. *J. Atmos. Sci.*, **77**, 4233–4249. https://doi.org/10.1175/JAS-D-20-0111.1

Schlemmer, L., & Hohenegger, C. (2014). The formation of wider and deeper clouds as a result of cold-pool dynamics. *Journal of the Atmospheric Sciences*, **71(8)**, 2842–2858. https://doi.org/10.1175/jas-d-13-0170.1

Sherwood, S. C. (1999). Convective precursors and predictability in the tropical western Pacific. *Monthly Weather Review*, **127**, 2977–2991. https://doi.org/10.1175/1520-0493(1999)127<2977:cpapit>2.0.co;2

Skofronick-Jackson, G., Piña, A., & Chen, S. S. (2021). Convective Processes Experiment – Aerosols & Winds (CPEX-AW) field campaign collection [Dataset]. NASA EOSDIS Global Hydrometeorology Resource Center Distributed Active Archive Center. https://doi.org/10.5067/CPEXAW/DATA101

Sobel, A. H., & Bretherton, C. S. (2000). Modeling tropical precipitation in a single column. *Journal of Climate*, **13**, 4378–4392. https://doi.org/10.1175/1520-0442(2000)013<4378:mtpias>2.0.co;2

Sobel, A. H., Nilsson, J., & Polvani, L. M. (2001). The weak temperature gradient approximation and balanced tropical moisture waves*. *Journal of the Atmospheric Sciences*, **58**, 3650–3665. https://doi.org/10.1175/1520-0469(2001)058<3650:twtgaa>2.0.co;2

Sobel, A. H., Sprintall, J., Maloney, E. D., Martin, Z. K., Wang, S., de Szoeke, S. P., et al. (2021). Large-scale state and evolution of the atmosphere and ocean during PISTON 2018. *Journal of Climate*, **34**, 5017–5035. https://doi.org/10.1175/jcli-d-20-0517.1

Sobel, A. H., Yuter, S. E., Bretherton, C. S., & Kiladis, G. N. (2004). Large-scale meteorology and deep convection during TRMM KWAJEX*. *Monthly Weather Review*, **132**, 422–444. https://doi.org/10.1175/1520-0493(2004)132<0422:lmadcd>2.0.co;2

Sokolowsky, G. A., Freeman, S. W., Jones, W. K., Kukulies, J., Senf, F., Marinescu, P. J., et al. (2024). *tobac*V1.5: Introducing fast 3D tracking, splits and mergers, and other enhancements for identifying and analysing meteorological phenomena. *Geoscientific Model Development*, **17**, 5309–5330. https://doi.org/10.5194/gmd-17-5309-2024

Stephens, G. L. (1990). On the relationship between water vapor over the oceans and sea surface temperature. *Journal of Climate*, **3(6)**, 634–645. https://doi.org/10.1175/1520-0442(1990)003<0634:otrbwv>2.0.co;2

Storer, R. L., van den Heever, S. C., & L'Ecuyer, T. S. (2014). Observations of aerosol-induced convective invigoration in the tropical East Atlantic. *Journal of Geophysical Research: Atmospheres*, **119**, 3963–3975. https://doi.org/10.1002/2013jd020272

Sullivan, S. C., Schiro, K. A., Stubenrauch, C., & Gentine, P. (2019). The response of tropical organized convection to El Niño warming. *Journal of Geophysical Research: Atmospheres*, **124**, 8481–8500. https://doi.org/10.1029/2019JD031026

Tanelli, S., Durden, S. L. & Im, E. (2006). Simultaneous measurements of Ku- and Ka-band sea surface cross sections by an airborne radar. *IEEE Geoscience and Remote Sensing Letters*, **3**, 359–363. https://doi.org/10.1109/lgrs.2006.872929

The Matplotlib Development Team (2024). Matplotlib: Visualization with Python (v3.9.2) [Software]. Zenodo. https://doi.org/10.5281/zenodo.13308876

Thompson, G., Field, P. R., Rasmussen, R. M., & Hall, W. D. (2008). Explicit forecasts of winter precipitation using an improved bulk microphysics scheme. Part II: implementation of a new snow parameterization. *Monthly Weather Review*, **136(12)**, 5095–5115. https://doi.org/10.1175/2008MWR2387.1

Tiedtke, M. (1993). Representation of clouds in large-scale models. *Monthly Weather Review*, **121**, 3040–3061. https://doi.org/10.1175/1520-0493(1993)121<3040:rocils>2.0.co;2

Tobin, I., Bony, S., & Roca, R. (2012). Observational evidence for relationships between the degree of aggregation of deep convection, water vapor, surface fluxes, and radiation. *Journal of Climate*, **25**, 6885–6904. https://doi.org/10.1175/jcli-d-11-00258.1

Tomassini, L. (2018). Mesoscale circulations and organized convection in African easterly waves. *Journal of the Atmospheric Sciences*, **75**, 4357–4381. https://doi.org/10.1175/jas-d-18-0183.1

Tompkins, A. M. (2001). Organization of tropical convection in low vertical wind shears: The role of water vapor. *Journal of the Atmospheric Sciences*, **58**, 529–545. https://doi.org/10.1175/1520-0469(2001)058<0529:ootcil>2.0.co;2

Tompkins, A. M., & Semie, A. G. (2017). Organization of tropical convection in low vertical wind shears: role of updraft entrainment. *Journal of Advances in Modeling Earth Systems*, **9(2)**, 1046–1068. https://doi.org/10.1002/2016ms000802

Touzé-Peiffer, L., Vogel, R., & Rochetin, N. (2021). Detecting cold pools from soundings during EUREC4A. https://doi.org/10.5194/egusphere-egu21-1038

Turk, F. J., Hristova-Veleva, S., Durden, S. L., Tanelli, S., Sy, O., Emmitt, G. D., et al. (2020). Joint analysis of convective structure from the APR-2 precipitation radar and the DAWN Doppler wind lidar during the 2017 Convective Processes Experiment (CPEX). *Atmospheric Measurement Techniques*, **13**, 4521–4537. https://doi.org/10.5194/amt-13-4521-2020

Vaisala. (2018). Dropsonde RD41 Datasheet B211706EN-A. Vaisala.

van den Heever, S. (2019). Dropsondes observations, Clouds, Aerosol and Monsoon Processes-Philippines Experiment (CAMP^{2}Ex, 2019) [Dataset]. Colorado State University. https://doi.org/10.5067/Suborbital/CAMP2EX2018/DATA001

Vargas Martes, R. M., Adames Corraliza, Á. F., & Mayta, V. C. (2023). The role of water vapor and temperature in the thermodynamics of tropical northeast Pacific and African easterly waves. *Journal of the Atmospheric Sciences*, **80**, 2305–2322. https://doi.org/10.1175/jas-d-22-0177.1

Vömel, H., Goodstein, M., & Arendt, C. (2020). Dropsonde data quality report: Clouds, Aerosol and Monsoon Processes-Philippines Experiment (CAMP^{2}Ex, 2019). [Readme]. *National Center for Atmospheric Research Earth Observing Laboratory Doc.*, 20 pp. [Available online at https://www-air.larc.nasa.gov/cgi-bin/enzFile?c1684C5749C53F525A470B4E964F4D05ABA2f7075622d6169722f5846532f43414d503245582f323031392f5033425f41495243524146542f56414e44454e4845455645522e535553414e2f43414d503245582d64726f70736f6e6465735f5033425f52315f524541444d455f51432e706466]

Vömel, H., Goodstein, M., Tudor, L., Witte, J., Fuchs-Stone, Ž., Sentić, S., et al. (2021). High-resolution in situ observations of atmospheric thermodynamics using dropsondes during the Organization of Tropical East Pacific Convection (OTREC) field campaign. *Earth System Science Data*, **13**, 1107–1117. https://doi.org/10.5194/essd-13-1107-2021

Wilhelmson, R. B., & Chen, C.-S. (1982). A simulation of the development of successive cells along a cold outflow boundary. *Journal of the Atmospheric Sciences*, **39(7)**, 1466–1483. https://doi.org/10.1175/1520-0469(1982)039<1466:asotdo>2.0.co;2

Wing, A. A., Emanuel, K., Holloway, C. E., & Muller, C. (2017). Convective self-aggregation in numerical simulations: a review. *Surveys in Geophysics*, **38(6)**, 1173–1197. https://doi.org/10.1007/s10712-017-9408-4

Wing, A. A., Reed, K. A., Satoh, M., Stevens, B., Bony, S., & Ohno, T. (2018). Radiative–convective equilibrium model intercomparison project. *Geoscientific Model Development*, **11**, 793–813. https://doi.org/10.5194/gmd-11-793-2018

Wolding, B., Dias, J., Kiladis, G., Maloney, E., & Branson, M. (2020). Interactions between moisture and tropical convection. part II: the convective coupling of equatorial waves. *Journal of the Atmospheric Sciences*, **77**, 1801–1819. https://doi.org/10.1175/jas-d-19-0226.1

Wolding, B., Powell, S. W., Ahmed, F., Dias, J., Gehne, M., Kiladis, G., & Neelin, J. D. (2022). Tropical thermodynamic–convection coupling in observations and reanalyses. *Journal of the Atmospheric Sciences*, **79**, 1781–1803. https://doi.org/10.1175/jas-d-21-0256.1

Wolding, B., Rydbeck, A., Dias, J., Ahmed, F., Gehne, M., Kiladis, G., et al. (2024). Atmosphere–ocean coupled energy budgets of tropical convective discharge–recharge cycles. *Journal of the Atmospheric Sciences*, **81**, 3–29. https://doi.org/10.1175/jas-d-23-0061.1

Wong, S., & Dessler, A. E. (2005). Suppression of deep convection over the tropical North Atlantic by the Saharan Air Layer. *Geophysical Research Letters*, **32**. https://doi.org/10.1029/2004gl022295

Yamazaki, K., & Miura, H. (2024). Reproducibility of equatorial kelvin waves in a super-parameterized MIROC: 2. linear stability analysis of in-model kelvin waves. *Journal of Advances in Modeling Earth Systems*, **16(5)**. https://doi.org/10.1029/2023ms003837

Yano, J.-I., Chaboureau, J.-P., & Guichard, F. (2005). A generalization of CAPE into potential-energy convertibility. *Quarterly Journal of the Royal Meteorological Society*, **131**, 861–875. https://doi.org/10.1256/qj.03.188

Young, G. S., Perugini, S. M., & Fairall, C. W. (1995). Convective wakes in the equatorial western Pacific during TOGA. *Monthly Weather Review*, **123**, 110–123. https://doi.org/10.1175/1520-0493(1995)123<0110:cwitew>2.0.co;2

Yuan, T., Remer, L. A., Pickering, K. E., & Yu, H. (2011). Observational evidence of aerosol enhancement of lightning activity and convective invigoration. *Geophysical Research Letters*, **38**. https://doi.org/10.1029/2010gl046052

Yuter, S. E., & Houze, R. A., Jr. (1995). Three-dimensional kinematic and microphysical evolution of Florida cumulonimbus. Part II: Frequency distributions of vertical velocity, reflectivity, and differential reflectivity. *Monthly Weather Review*, **123**, 1941–1963. https://doi.org/10.1175/1520-0493(1995)123<1941:tdkame>2.0.co;2

Zagrodnik, J. P., McMurdie, L. A., Houze, R. A., Jr., & Tanelli, S. (2019). Vertical structure and microphysical characteristics of frontal systems passing over a three-dimensional coastal mountain range. *Journal of the Atmospheric Sciences*, **76**, 1521–1546. https://doi.org/10.1175/jas-d-18-0279.1

Zawislak, J., & Zipser, E. J. (2010). Observations of seven African Easterly Waves in the East Atlantic during 2006. *Journal of the Atmospheric Sciences*, **67**, 26–43. https://doi.org/10.1175/2009jas3118.1

Zawislak, J., Nowottnick, N., & Nehrir, A. (2022). Convective Processes Experiment - Cabo Verde (CPEX-CV) field campaign collection [Dataset]. NASA EOSDIS Global Hydrometeorology Resource Center Distributed Active Archive Center. https://doi.org/10.5067/CPEXCV/DATA101

Zhang, C. (2005). Madden-Julian Oscillation. *Reviews of Geophysics*, **43**. https://doi.org/10.1029/2004rg000158

Zipser, E. J. (1977). Mesoscale and convective–scale downdrafts as distinct components of squall-line structure. *Monthly Weather Review*, **105**, 1568–1589. https://doi.org/10.1175/1520-0493(1977)105<1568:macdad>2.0.co;2

Zipser, E. J. (2003). Some views on "hot towers" after 50 years of tropical field programs and two years of TRMM data. *Meteorological Monographs*, **29**, 49–49. https://doi.org/10.1175/0065-9401(2003)029<0049:csvoht>2.0.co;2

Zipser, E. J., & LeMone, M. A. (1980). Cumulonimbus vertical velocity events in GATE. Part II: Synthesis and model core structure. *Journal of the Atmospheric Sciences*, **37**, 2458–2469. https://doi.org/10.1175/1520-0469(1980)037<2458:cvveig>2.0.co;2

Zipser, E. J., & Lutz, K. R. (1994). The vertical profile of radar reflectivity of convective cells: A strong indicator of storm intensity and lightning probability? *Monthly Weather Review*, **122**, 1751–1759. https://doi.org/10.1175/1520-0493(1994)122<1751:tvporr>2.0.co;2

Zipser, E. J., Cecil, D. J., Liu, C., Nesbitt, S. W., & Yorty, D. P. (2006). WHERE ARE THE MOST INTENSE THUNDERSTORMS ON EARTH? *Bulletin of the American Meteorological Society*, **87**, 1057–1072. https://doi.org/10.1175/bams-87-8-1057x

Zipser, E. J., Twohy, C. H., Tsay, S.-C., Thornhill, K. L., Tanelli, S., Ross, R., et al. (2009). The Saharan Air Layer and the fate of African Easterly Waves—NASA's AMMA field study of tropical cyclogenesis. *Bulletin of the American Meteorological Society*, **90**, 1137–1156. https://doi.org/10.1175/2009bams2728.1